Preparation and Realization of a new Hypertriton Mass Experiment at MAMI

Dissertation
zur Erlangung des Grades „Doktor der Naturwissenschaften"
am Fachbereich Physik, Mathematik und Informatik
der Johannes Gutenberg-Universität in Mainz

von

Philipp Vonwirth geb. Eckert

geboren in Boppard

Institut für Kernphysik
Johannes Gutenberg-Universität Mainz
30. August 2023

Erstgutachter:	Prof. Dr. J. P.
Zweitgutachter:	Prof. Dr. W. G.
Datum der mündlichen Prüfung:	19.12.2023

Zusammenfassung

Hypertriton ist der einfachste gebundene Hyperkern, bestehend aus einem Proton p, einem Neutron n und einem instabilen Lambda-Baryon Λ. Bereits seit der Entdeckung in den 1950er Jahren sind Hyperkerne der Fokus einer weltweiten Reihe an Experimenten. Ihre Eigenschaften – wie Lebensdauer oder Bindungsenergie des Λ zum Restkern – geben wichtige Aufschlüsse über die zu Grunde liegende Wechselwirkung zwischen dem Λ und den anderen regulären Nukleonen. Diese erlauben beispielsweise Schlussfolgerungen für die Zusammensetzung von Neutronensternen. Seit den 1960er Jahren begannen daher die Studien, um Bindungsenergie, Lebensdauer und weitere Eigenschaften einiger Hyperkerne zu bestimmen. Durch seine vergleichsweise einfache Zusammensetzung galt bereits damals dem Hypertriton ein gesteigertes Interesse. Als Drei-Körper-System ist es besonders gut mit theoretischen Vorhersagen zu vergleichen.
Bereits Mitte der 1970er Jahre war ein umfangreicher Katalog an Hyper-Isotopen vermessen worden [165], meist mit der damals gängigen Emulsions-Methode. So waren es erst neuartige experimentelle Ansätze, die in den folgenden Jahrzehnten neue Bewegung in die Datenlage brachten. Ab 2010 wurden erstmals Ergebnisse mittels relativistischen Schwerionen-Kollisionen erlangt. Gleich drei unabhängige Experimente lieferten neue Werte für die Hypertriton-Lebensdauer, die 30 bis 40% kürzer waren als zuvor beobachtet [255, 12, 14]. Als dann erstmals im Jahre 2020 – nach fast 50 Jahren – die Λ-Bindungsenergie vom Hypertriton in einem ähnlichen Experiment bestimmt wurde, verstärkten sich die Zweifel am bisherigen Wissensstand. Zwar war diese Größe bereits zu Zeiten der Emulsion mit einer fast 40-prozentigen Unsicherheit angegeben worden [165],

$$B_\Lambda = 130 \pm 50\,\mathrm{keV},$$

jedoch wich der neu gemessene Wert von über $400\,\mathrm{keV}$ um mehr als 200% ab [13]. Diese unklare Gesamtsituation wurde als *Hypertriton-Puzzle* bezeichnet [239] und lieferte zwei grundlegende Motivationen für die vorliegende Doktorarbeit:

(i) Wie ist mit den einzelnen Veröffentlichungen umzugehen? Wie kann aus den verschiedenen Werten ein aussagekräftiger Mittelwert errechnet werden?

(ii) Ist es möglich, die Λ-Bindungsenergie vom Hypertriton mittels einer von den anderen Experimenten unabhängigen Methode neu zu messen?

In Bezug auf die erste Fragestellung wurde im Rahmen dieser Arbeit die Datenbank *Chart of Hypernuclides* entwickelt, um jegliche Messergebnisse der Hyperkernphysik zu sammeln und aus den verschiedenen Quellen Mittelwerte zu errechnen. In Anlehnung an die Particle Data Group [237], die es sich zur Aufgabe gemacht hat, Forschungsergebnisse aus der Teilchenphysik zusammenzufassen, wurden daher zahlreiche Algorithmen und Methoden implementiert, um Mittelwerte eines weiten Spektrums an Hyperkern-Daten korrekt errechen zu können. Inzwischen enthält die Datenbank mit etwa 600 Einträgen ein weitreichendes Abbild der Forschungsgeschichte rund um Hyperkerne. Für eine gute Erreichbarkeit wurde eine Website eingerichtet, auf der Nutzer mittels eines interaktiven User-Interfaces die Daten einsehen können. Auch umfangreiche Hintergrundinformationen zu den einzelnen Veröffentlichungen sind dort hinterlegt. Neben der reinen Auflistung der Daten bietet die Seite darüber hinaus Einblicke

in deren statistische Aufarbeitung. So werden beispielsweise neben den berechneten Mittelwerten auch Grafiken – sogenannte Ideogramme – erzeugt, die einen quantitativen Überblick über die Datenlage liefern. Die URL der Seite lautet `https://hypernuclei.kph.uni-mainz.de`. Mit mehr als 50 experimentellen Werten alleine über Hypertriton konnte eine detaillierte Analyse der Lebensdauer- und Bindungsenergie-Situation durchgeführt werden.

Die zweite Frage betreffend, wurde eine Messkampagne am A1-Aufbau des Mainzer Instituts für Kernphysik vorbereitet und durchgeführt, um die Hypertriton-Bindungsenergie mittels Zerfalls-Pionen-Spektroskopie bestimmen zu können. Mit dieser experimentellen Methode war bereits wenige Jahre zuvor das etwas schwerere Hyper-Isotop ${}^{4}_{\Lambda}\mathrm{H}$ vermessen worden [275]. Für die neue Messung wurde ein spezielles Lithium-Target-System entworfen und getestet, um die Ausbeute an relevanten Ereignissen gegenüber den früheren Messungen zu maximieren. Für das Experiment wurde schließlich das Kaon-Spektrometer KAOS verwendet, mit welchem zuletzt 2014 Hyperkernstudien durchgeführt wurden [275]. Die Messreihen fanden im Sommer und Herbst 2022 statt. Die Auswertung der Daten ist momentan im Gange und wird von den Doktoranden T. S. und R. K. durchgeführt. Ihnen ist bereits der Nachweis von ${}^{4}_{\Lambda}\mathrm{H}$ gelungen.

Abstract

Hypertriton is the simplest known hypernucleus, consisting of a proton p, a neutron n and an unstable Lambda baryon Λ. Already since the discovery in the 1950's hypernuclei have been the focus of a worldwide series of experiments. Their properties – such as lifetime and binding energy of the Λ to the regular nucleus – give important insights into the underlying forces acting between the Λ and the ordinary nucleons. Even conclusions about the composition of neutron star matter can be drawn. Therefore, since the 1960's experiments began to determine the binding energy, lifetime and other properties of many hypernuclear isotopes. The hypertriton proved to be of special interest due to its relatively simple nature. As a three-body system, it compares particularly well with theoretical predictions.
Already by the mid-1970's, an extensive catalog of hyper-isotopes had been investigated [165], mostly with the at that time usual emulsion technique. Thus, over the following decades it were novel experimental methods that brought new movement into the hypernuclear data situation. Regarding the hypertriton, the relativistic heavy ion collision offered many new results. Since 2010, there have been the first new measurements of the hypertriton's lifetime. Around these years, three independent facilities reported values that were 30 to 40% shorter than previously observed during the emulsion era [255, 12, 14]. In 2020, the Λ binding energy of the hypertriton was then finally remeasured as well – for the first time in almost 50 years. While the best result from the emulsion era was already given with a relative error of almost 40% [165],

$$B_\Lambda = 130 \pm 50\,\mathrm{keV},$$

the new value even intensified the confusion. With around $400\,\mathrm{keV}$, it was more than 200% larger [13]. This unclear data situation was summarized as the *hypertriton puzzle* [239] and lead to two fundamental motivations for the present PhD thesis:

(i) How to combine individual measurements to determine the most likely value for the lifetime and binding energy of hypernuclei?

(ii) Is it possible to re-measure the Λ binding energy of the hypertriton using a method independent to the other experiments?

Addressing the first question, a database called *Chart of Hypernuclides* has been developed to collect experimental results in hypernuclear physics and to calculate average values from the various sources. Following the Particle Data Group [237], which collects and summarizes research results from particle physics, numerous algorithms and methods have been implemented in order to correctly calculate average values of versatile sets of hypernuclear data. Meanwhile, with about 600 entries, the database contains a wide-ranging picture of the research history around hypernuclei. To make the database easily accessible, a website has been set up, where users can view the data by means of an interactive user interface. Extensive background information on the individual publications is also provided there. Furthermore, the site offers insights into the statistical processing of the data, so in addition to the calculated average values, generated figures – so-called ideograms – provide a quantitative overview of the data situation. The URL of the website is `https://hypernuclei.kph.uni-mainz.de`. With solely 50 entries about the hypertriton's properties, a detailed analysis of the lifetime and binding energy situation was performed.

Regarding the second question, a data taking campaign was prepared and performed at the A1 setup of the Mainz Institute for Nuclear Physics to determine the hypertriton binding energy via decay pion spectroscopy. This experimental method had already been applied a few years earlier to determine the binding energy of the somewhat heavier isotope ${}^{4}_{\Lambda}\mathrm{H}$ [275]. For the new measurement, a high luminosity lithium target system was designed and tested to maximize the yield of relevant events compared to the previous measurements. As in the hypernuclear studies in 2014 [275], the kaon spectrometer KAOS was used for the experiment. The data taking campaigns took place in summer and autumn of 2022. The analysis of the data is currently being performed by the PhD students T. S. and R. K.. Just recently, they have already detected the ${}^{4}_{\Lambda}\mathrm{H}$.

Personal contributions in context of this thesis

The experimental setup for Decay Pion Spectroscopy at A1

- Reactivation of the KAOS spectrometer, refurbishment of the coincidence electronics, the scintillation detectors and the involved hardware and electronics. Exchange of a vacuum window with a new solid aluminum plate. General improvements around the setup, e.g. installation of a thicker lead absorber wall and other measured for background suppression.
- Development of a new Lithium target setup together with P. Klag, J. Geratz and M. Mildenberger, involving the design of multiple aluminum parts for the experimental setup, the optimization and installation of the thermal camera system, the implementation of a dedicated motor steering program and more.
- Preparation and conduction of three beamtimes at the A1 hall, one to test the lithium target and two to take data for the hypertriton binding energy.

Other hardware-related tasks at A1

- Installation and testing of new PMT preamplifiers for the A1 spectrometers A, B and C together with P. Klag and P. Herrmann.
- Installation and testing of new NMR Probes for the A1 spectrometers A, B and C together with P. Klag.

The Chart of Hypernuclides

- Development of the *Chart of Hypernuclides*, design of the database structure, collection of data, implementation of the averaging routines and the web interface.
- Supervision of the Bachelor thesis "Systematische Sammlung und Verarbeitung von Daten aus Hyperkernexperimenten" by S. Ries [261] which addressed the expansion of the chart to also hold branching ratio data.

Other activities

- Support for P. Klag with the preparation and conduction of his undulator light interference experiments [183].
- Publication of paper about a position sensitive octagon scintillator [102].
- Contribution at several other experimental campaigns at A1 [113, 274, 301, 186].

The work was supported by the Deutsche Forschungsgemeinschaft, Grant Number PO256/7-1 and the European Union's Horizon 2020 research and innovation programme No. 824093.

Partial results of this thesis have already been published in [111, 110, 109] and have been presented at the THEIA-REIMEI 2021 seminar [104], the HADRON2021 conference [106], the PANIC2021 conference [105], the SNP school 2021 [107] and the HYP2022 conference [103].

Table of Contents

1. Dense Baryonic Matter – From Nuclei to Stars

1.1. The Hadronic Equation-of-State

One of the most basic questions in nuclear physics is the challenge of combining the four fundamental forces into one universal theoretical framework. While the *standard model* already provides an excellent description of sub-atomic particles and their dynamics, it only combines the electrical, the strong and the weak forces together. The remaining force, the gravitation, becomes negligibly low on these small scales. In contrast to the standard model, the *general relativity* (GR) from Albert Einstein describes the interaction of stellar objects, mainly influenced by gravitation due to their enormous masses. While this theory is successfully applied over a wide range of masses, observed motions of galaxies in our universe could not be explained by their visible mass alone [45], which lead to the concept of dark matter and energy [45]. Since this concept still was not yet confirmed despite many experimental efforts, also the GR itself is in question [206, 81].

Within general relativity, the so called Schwarzschild radius defines the radius of the event horizon of a black hole. It was named after Karl Schwarzschild, who retrieved this property as a solution of the general relativity in 1916. This radius reads

$$R_s = \frac{2\,GM}{c^2}, \tag{1.1}$$

with the gravitational constant G, the mass of the object M and the speed of light c. In other words, the relation $\frac{2GM}{c^2R}$ is a measure of the compactness of astrophysical objects with their respective radius R. Its maximum of 1 is then indeed given for $R = R_s$. A comparison of the parameter space of this relation is found in Figure 1.1. It illustrates several different stellar

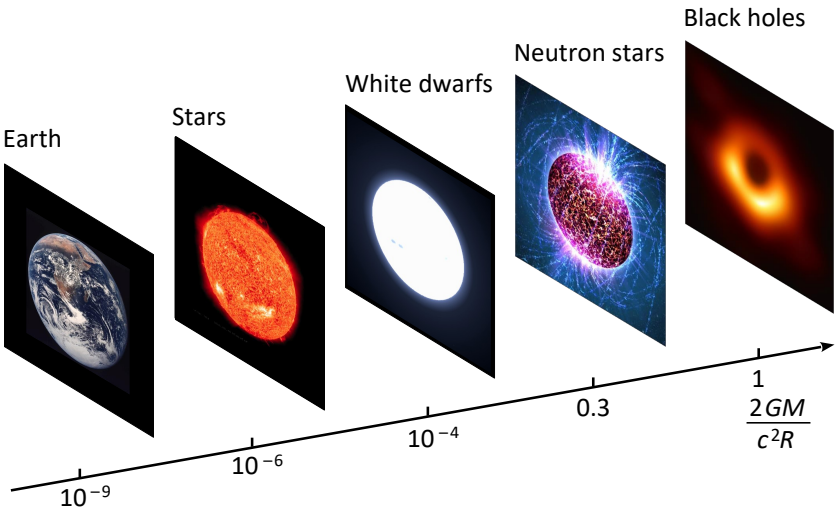

Figure 1.1.: Compactness of stellar objects in units of the Schwarzschild radius [247] (modified). While for black holes this radius is indeed reached, other objects like planets, stars and even white dwarfs lie quite far away from it. Only neutron stars with 0.3 come very close to the state of black holes.

objects sorted by their $\frac{2GM}{c^2R}$ value [247]. While for black holes, the maximum of 1 is reached, planets like the earth or stars lie many orders of magnitude below it. Even white dwarfs – possible outcomes of supernovae – reach only 10^{-4}. In contrast, neutron stars with 0.3 are, compared to the others, only a tiny fraction away from the black holes.
After all, the parameter space for studying astrophysical systems with the GR is huge. Most of the time, the success of the GR is remarkable, so a break down in the extremely weak region seems unlikely *prima facie*. However, as long as the concept of dark matter lacks a clear experimental proof, questioning the validity of the GR in extreme regimes seems natural. But also here, none of the many alternative modified gravity approaches has – despite significant progress [281] – so far proven to explain the whole set of given observations [189, 233].
As indicated in Figure 1.1, the other extreme case of gravity can be probed in the strong fields of black holes and neutron stars as well as their binary systems. For this region progress was made recently, when for the first time gravitational waves of a black hole merging event were detected by the collaborations LIGO and Virgo [4, 2]. This result opened the door for many new gravitational wave detectors like for example the space-based interferometer LISA. With these setups going into operation in the next decades, even preciser observations of gravitational waves will constrain or even refute theories of modified gravity in the strong-field regime [309, 304, 188].
In neutron stars, comparable gravitational fields are found [252], but in contrast to black holes, their structure is not hidden behind an event horizon [42, 309]. Referring to the initial question of finding a theory which unifies the four fundamental forces, neutron stars are objects which are influenced by all of them. While the electro-magnetic force plays only a minor role inside their equation-of-state (EOS), neutron stars still generate the strongest magnetic fields across the universe. Also the weak interaction is subordinate in their dynamics, but still it opens additional hadronic degrees of freedom at high densities. Despite that, neutron stars involve a multifaceted set of fundamental concepts in physics, like quantum mechanics, general relativity an thermodynamics. These properties render neutron stars to be their own specific laboratory to study fundamental physics as offered by no other object in the micro- and macro-cosmos [36, 252, 42, 35].
Ongoing studies, as the first observation of a neutron star merger by LIGO and Virgo [3] already put severe constraints on possible modifications of the GR on large distance scales and weak fields [37, 84, 117]. Ground breaking observations like these merger events bring up the hope, that gravitational-wave astronomy one day will also be able to observe the post-merger phase and by that yield a first view on the non-linear and dynamical regime of strong-field gravity in matter [309, 25, 303, 36].
In contrast, also experiments in terrestrial laboratories can contribute to a deeper understanding of the nuclear EOS and may deliver a comparison to the conclusions drawn from neutron star mergers. High energy nuclear reactions, radioactive beams mapping the chart of nuclear stability and precision studies of nuclear few body systems contribute to this task. Among these approaches, the strangeness nuclear physics is another essential protagonist. However, even after many decades of research, the determination of the EOS of dense nuclear matter and the fundamental hadronic EOS in general remain one of the biggest missions in physics.
The state of the art regarding the matter in strong-field gravity was recently summarized by E. Fonseca *et al.* [126] to the following most prominent questions:

- What is the EOS of matter at the center of neutron stars? What are the maximum masses allowed for neutron stars before they collapse to a black hole?

- What is the correct theory of gravitation in the strong-field regime? Does Einstein's general relativity break down at some point?

- What are the future prospects of gravitational-wave astronomy? How can multi-messenger measurements of neutron stars be used to test gravitation and resolve the century-long mystery of their structure?

The work presented in this thesis focuses on hypernuclear physics, the study of bound nuclear structures containing hyperons. One major aspect is the preparation and commissioning of a decay pion spectroscopy experiment at the Mainz Microtron to study light hypernuclei. The other part addresses the systematic collection of experimental information about hypernuclei and the consistent computation of average values, including a proper treatment of statistical and systematic error sources. These efforts may contribute to shed light on the role of hyperons in the interior of dense stellar objects and help to unveil the mysteries of dense hadronic matter.

1.2. Introducing Neutron Stars

Generation in supernovae

Besides the big bang itself, a supernova explosion of a supergiant star is one of the most spectacular events in the universe. Within only a few seconds, the supernova shines with a brightness equivalent to 10 billion suns, releasing an energy of 10^{44} J. During the explosion, the neutrino output can reach the order of 1% of the total neutrino output of the entire universe. In the Milky Way galaxy, these events are expected to happen once every 100 years. The result of a supernova is essentially given by the mass of the preceding star. For heavier stars, the formation of a black hole is expected, due to the total victory of the gravitational pressure. Lighter stars ranging from 10 to 25 solar masses $M_\odot$ end up in an equilibrium state between gravitation, the degeneracy pressure and the strong interaction, so-called neutron stars.

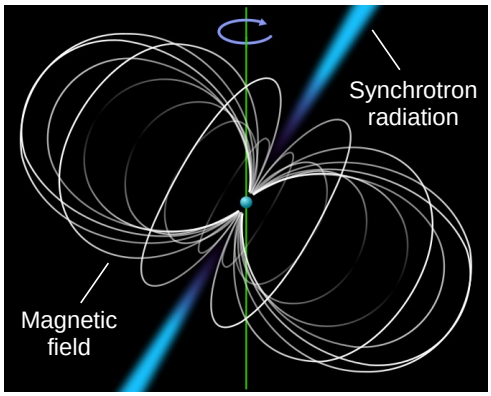

Figure 1.2.: Schematic drawing of the magnetic field of a neutron star [148]. Due to the misalignment of rotational axis and the magnetic field, synchrotron radiation is emitted along the poles of the field.

First observation of a neutron star

Already in 1933 Walter Baade and Fritz Zwicky analysed supernova explosions. They were the first to use the term *supernova* and predicted the existence of neutron stars. Years later, these stars were observed to have extremely strong magnetic fields reaching up to 10^8 T. As illustrated in Figure 1.2, this dipole field is usually not aligned with the rotational axis of the neutron stars, so that synchrotron radiation is emitted along the symmetry axis of the magnetic field [148].
In 1967 Jocelyn Bell, a student supervised by Antony Hewish discovered the first so called pulsar, a binary neutron star system bound by the gravitational force [155]. The original data is shown in Figure 1.3. The synchrotron radiation of the neutron star had pointed repeatedly towards the earth, leaving a periodical radio wave signal. It was detected with a large radio telescope at the Mullard Radio Astronomy Observatory. In the analysis, a periodicity of $1.33733(1)\,\mathrm{s}$ was observed.
During follow-up experiments the pulse timing of this neutron star was re-measured even more precisely with $1.3372795(20)\,\mathrm{s}$ still in the same year [242]. Within the following decades and the

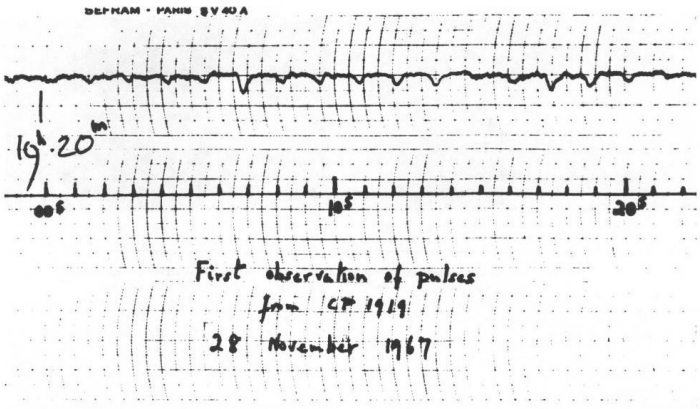

Figure 1.3.: First observation of a neutron star's radio frequency pulse signal. On top, the actual signal is seen, on the bottom a scale from 0 to $20\,\mathrm{s}$ is given. In the analysis, a period time of $1.33733(1)\,\mathrm{s}$ was found [155].

improving experimental setups, these measurements could again be improved by several orders of magnitude. With Bell's discovery, a new high precision tool was given to study neutron stars with the theory of general relativity [70].

Modern studies

Today, around 3000 pulsars are known [33], with rotational frequencies ranging from $0.1\,\mathrm{Hz}$ to close to $1\,\mathrm{kHz}$. In sum, the Milky Way is expected to be the home of 100 million neutron stars. Within the 5 decades that passed since the first discovery, many additional approaches to study the characteristics of neutron stars have been established. One of them is the study of X-rays. Figure 1.4 shows a schematic illustration of two neutron stars with an X-ray emitting "hot spot" [258]. Compared are the case of a weak gravitational field versus a strong field. In strong gravity stars, a hot spot (yellow) is visible for more than half a rotation due to the bending of the space-time around them. This is seen in the second panel, where for the weak gravity star

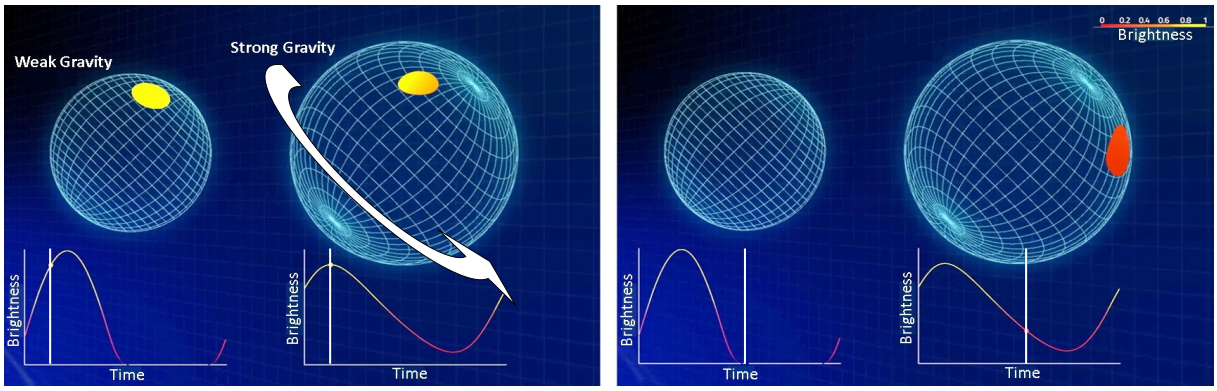

Figure 1.4.: Brightness patterns of neutron stars as indicator for their gravitational fields [258]. **Left:** two neutron stars are illustrated, a light and a heavy one, with weak and strong gravity respectively. Both stars have a bright spot, which emits detectable radiation. **Right:** due to the rotation of neutron stars, this spot will turn away at some point, so that no brightness is visible anymore for the weak gravity case. For the strong case, the gravitational field is bent so much, that the bright spot still is visible.

nothing is seen anymore, while for the strong case, still a certain intensity is remaining. The result is a characteristic brightness pattern which can offer information about both the radius as well as the mass of the neutron star. Observations like these are enabled by the STROBE-X project, a satellite-based X-ray telescope [258].

Along with the previously mentioned gravitational waves and pulsar timings, a bigger picture about neutron stars can be drawn, especially when several experimental sources are available for one and the same neutron star. This approach is followed by the Neutron star Interior Composition ExploreR (NICER) Collaboration, which collects data sets from various facilities around the world to extract information about the mass and radius of neutron stars [263].

Neutron star mass

The mass of a neutron star is one of the key elements of understanding neutron star matter. One can ask questions like, at which point this mass exceed the threshold to the complete victory of the gravitation so that it collapses to a black hole? Or which mass is at least required to keep the immense compression of neutron star matter stable? These conditions leave only a small mass range, in which neutron stars can exist.

An overview about the so far observed masses is shown in Figure 1.5 [129]. As can be seen, there are several very well determined NS masses in the range of $1.3 - 1.4\,M_\odot$. This is confirmed by the histogram representation on the right side. Slightly lighter masses down to $1.2\,M_\odot$ were observed as well, but more remarkably, also heavy neutron stars of more than two solar masses have been found. As of today, PSR J0740+6620 is the heaviest know neutron star with a mass of about 2.1 solar masses [85, 125, 263] and was observed just three years ago. This intensifies the question of how far the compressed matter still can withstand the gravitational force before the limit of the conversion to a black hole is exceeded.

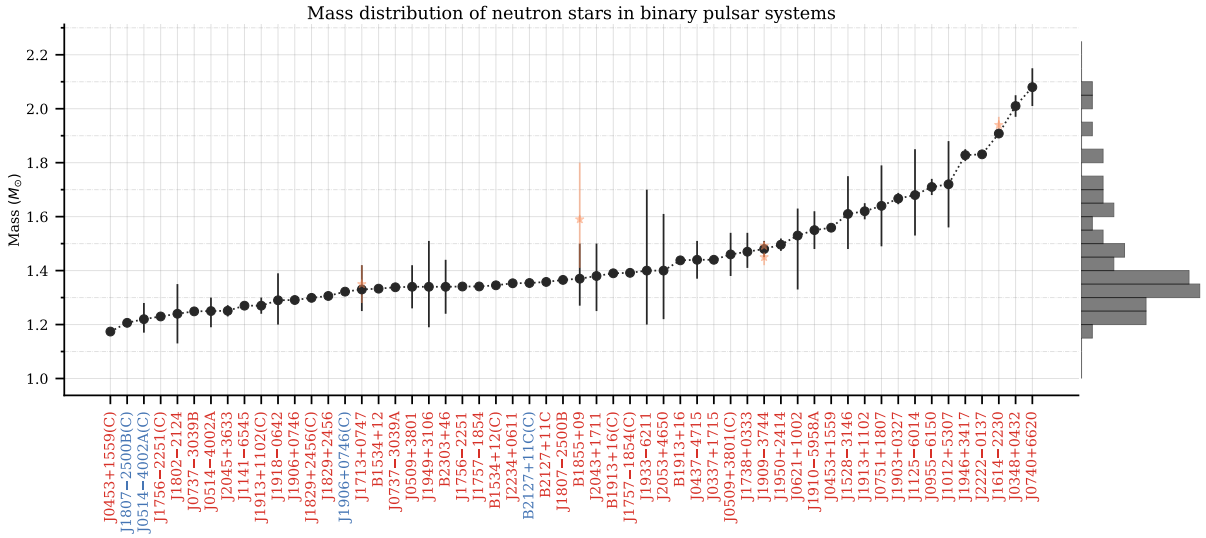

Figure 1.5.: Neutron star mass distribution in binary pulsar systems [129] (as of July 2023). The right part shows these masses in a histogram. While most of the neutron stars are of a mass between $1.2 - 1.5\,M_\odot$, there are also single cases of more than two solar masses. The orange data points denote multiple recent measurements of the same NS mass.

Mass-radius relation

The relation of the mass to the radius is another key aspect in understanding the dynamics of a neutron star, since here the compactness of the object is better represented as by the mass alone. From the theoretical side, the Tolman–Oppenheimer–Volkoff equation (TOV) allows to calculate possible pairs of mass and radius for a given specific nuclear equation-of-state [226]. It was derived in 1939 as a solution of Einstein's field equations. The TOV equation reads

$$\frac{\mathrm{d}P}{\mathrm{d}r} = -\frac{GM(r)\varepsilon(P)}{r^2c^2}\left(1+\frac{P}{\varepsilon(P)}\right)\left(1+\frac{4\pi r^3 P}{M(r)c^2}\right)\left(1-\frac{2GM(r)}{rc^2}\right)^{-1}, \tag{1.2}$$

with pressure P, radius r, mass M, the equation-of-state $\varepsilon(P)$ being the pressure dependent energy density, the gravitational constant $G = 6.67430(15) \times 10^{-11}\,\mathrm{m^3 kg^{-1} s^{-2}}$ and the speed of light $c = 299792458\,\frac{\mathrm{m}}{\mathrm{s}}$. An additional equation constrains the mass of the neutron star,

$$\frac{\mathrm{d}M(r)c^2}{\mathrm{d}r} = 4\pi r^2 \varepsilon(P). \tag{1.3}$$

The core component for the dynamics of neutron stars inside the TOV is indeed given by the equation-of-state $\varepsilon(P)$, as it determines the compressibility of the NS matter. Examples of various EOS and their resulting mass-radius relation by using the TOV equation are shown in Figure 1.6 [210, 247]. On the left side, the link between energy density and pressure is given according to several nuclear theories. As for classical systems, the pressure is mainly determined by the particles' momentum. Via a dashed line, also the threshold case of massless particles is given, where the energy would be purely of kinetic nature.
In general, it is to be distinguished between stiffer and softer EOS. A stiff equation links an increase of the energy density more strongly to an increase of pressure than the softer ones. The latter include other effects which lead to a relief of pressure. One of them may be the appearance of so called *hyperons*, baryons with strangeness, as will be discussed in the following section. A stiffer EOS prevents the compression of the neutron star to a black hole and hence allows to stabilize larger masses, while for the softer equations the threshold for the compression is

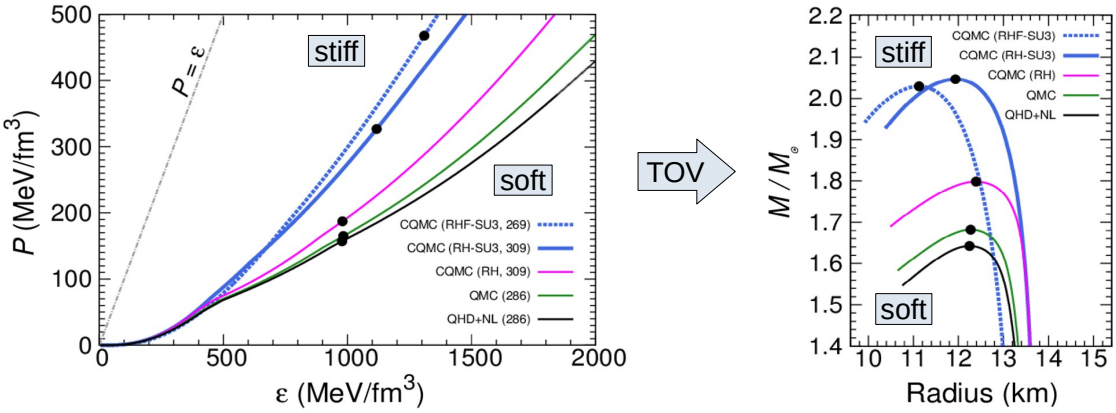

Figure 1.6.: Theoretical mass-radius relations for neutron stars [210, 247]. **Left:** different equations-of-state link the energy density ε to a pressure P. The relation $\varepsilon(P)$ acts as input parameter to the TOV equation. **Right:** resulting mass-radius relations for neutron stars, given by the TOV equation. Each energy-pressure curve translates into a new curve on which stable neutron stars are expected. For each one, the maximum mass is marked with a dot which is found in the left figure as well.

reached sooner. This can be seen on the right side of Figure 1.6. Here, the results after evaluating the EOS with the TOV equations are shown. The curves indicate mass-radius combinations at which neutron stars can exist. Here the stiffer EOS reach up to higher maximum masses, more than two solar masses, while the softer equations predict not more than $1.7\,M_\odot$.

1.3. The Hyperon Puzzle

Hyperons in neutron stars

The theoretical foundation for the various EOS depicted in Figure 1.6 is given by versatile assumptions about the internal structure of neutron stars. Besides the *traditional* neutron star, there are many other hypotheses for the composition of the inner core. One of them is the existence of hyperons, strangeness $S = -1$ and $S = -2$ baryons. This assumption was already made 8 years prior to the pulsar observation by Bell. It was Cameron in 1959, who suggested by a simple kinematic calculation, that nucleons might be transformed into hyperons at high densities of around 5 times the nuclear density ρ_0 [71]. His point is the following: Inside a regular atomic nucleus, nucleons possess a certain amount of momentum, the Fermi momentum of typically

$$p_\mathrm{F} \approx 200\,\mathrm{MeV}/c,$$

varying with the size of the nucleus. Due to degeneracy, a nucleon has to occupy higher and higher momentum shells, the bigger the nucleus gets. A density dependence of this momentum is given by

$$\rho = \frac{p_\mathrm{F}^3}{3\pi^2}, \tag{1.4}$$

so that at higher nuclear densities also the Fermi momentum is increased. It is the density of $\approx 5.5\,\rho_0$ which produces a Fermi momentum of roughly $600\,\mathrm{MeV}/c$ for neutrons inside a neutron star. Their total energy, given by $E^2 = m^2 + p^2$, exceeds then the rest energy of a Λ baryon, the lightest hyperon. As illustrated in Figure 1.7, the conversion to such a Λ becomes then energetically favorable [247].
Shortly after Cameron, Ambartsumyan and Saakyan discussed the appearance of hyperons quantitatively in a dense non-interacting gas of elementary particles and suggested, that Σ^- and Λ hyperons would be the first strange baryons to appear with increasing density [26]. Looking back at Figure 1.6, the introduction of hyperons as an additional species can reduce the Fermi pressure, once a certain energy density is exceeded. This is seen at around $500\ \mathrm{MeV/fm^3}$, so that

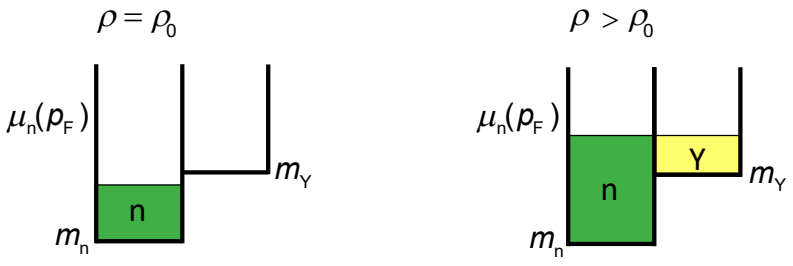

Figure 1.7.: Nuclear potential compared for normal and higher nuclear densities [247]. The appearance of hyperons is expected if the density increases beyond a certain threshold (compare to (1.4)). For interactions among the hyperons being neglected, the threshold lies at around $5\,\rho_0$ [71].

from there the equation-of-state is softened. This loss of pressure then results in a significant reduction of the maximum NS mass.

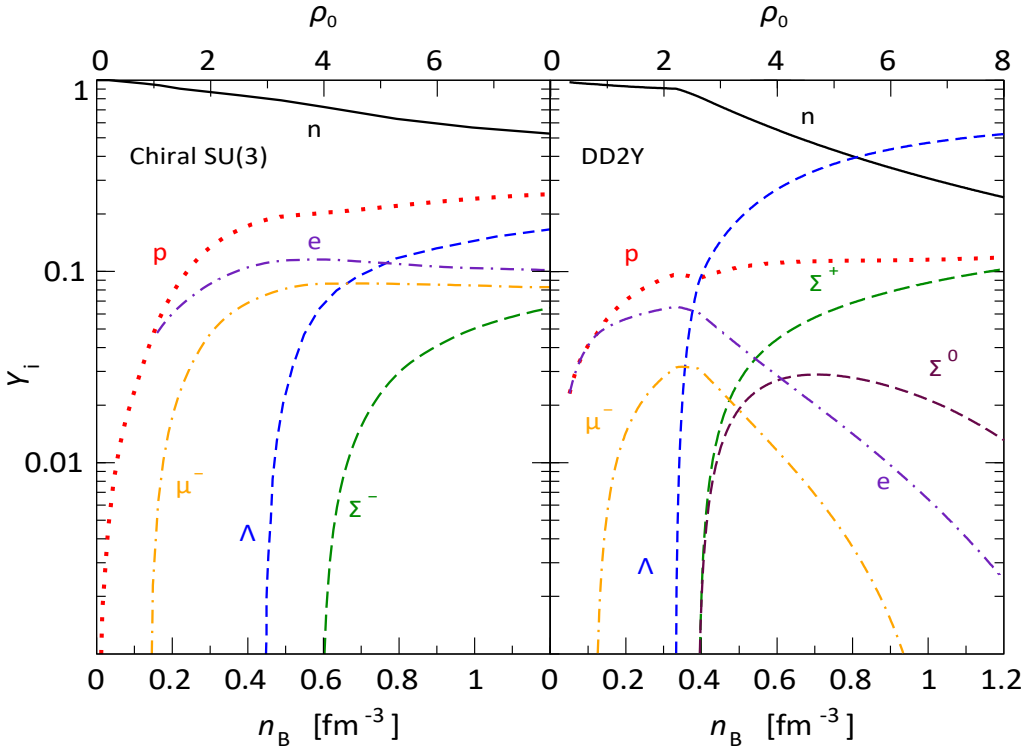

Figure 1.8.: Comparison of two exemplary models for the composition of dense nuclear matter, depending on the density [194]. The regular x-axis is given in units of nucleons per fm^3, while on top an additional scale in units of ρ_0 is given. **Left:** a model by Dexheimer *et al.* suggests the presence of the Λ hyperon at around $3\,\rho_0$. In the denser regime, it contributes with 10 to 20% to the total number of particles [95]. **Right:** in the model by Fortin *et al.* the Λ plays an even more dominant role. It appears already at $2\,\rho_0$ and overrules the neutron at around $5\,\rho_0$ [127].

Today, there is a widely shared consensus in nearly all present theoretical approaches that hyperons may appear in the inner core of neutron stars already at densities of about twice the nuclear saturation density, given by the influence of hyperon-nucleon interactions. Depending on these, different contributions of hyperons are expected. As an example, two predictions are shown in Figure 1.8 [194]. The figure presents the density dependent fractions of particles inside neutron star matter. The parametrization on the left [95] predicts the existence of the Λ at around $3\,\rho_0$. From there, with increasing density it can gain a fraction of up to 20%. The other model [127] suggests a much more prominent role of hyperons in general, but also mainly the Λ. Occurring at $2\,\rho_0$, it quickly gains influence, so that at $5\,\rho_0$ it overrules the neutron and becomes the dominant particle. In both models, also Σ baryons are expected to be present, but at higher densities and far lower quantities than the Λ. Beyond that, other models also suggest the appearance of Ξ baryons [173].

Problems with the heavy stars

A wide agreement that neutron stars cannot be heavier than two solar masses [70], was proven to be wrong after the recent discovery of the heavy neutron star PSR J0740+6620. Hence, also the appearance of hyperons was questioned despite the almost trivial argumentation by Cameron.

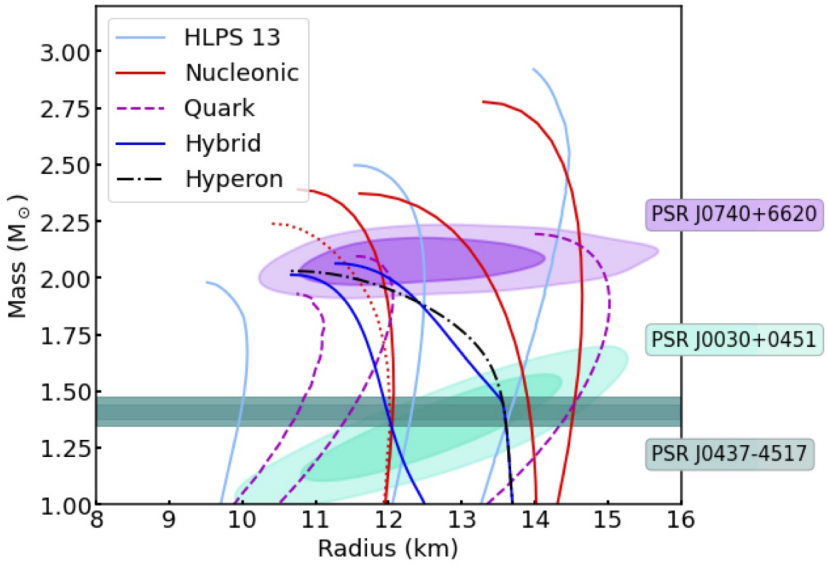

Figure 1.9.: Predictions for the mass-radius-relation of neutron stars by various theories [163]. Constraints are given by the masses and radii from three astronomical observations by NICER including the recently observed heaviest known neutron star. More details about the used EOS can be found in [302].

A compilation of the current data situation was given recently by the NICER Collaboration, as illustrated in Figure 1.9 [163]. Here, an updated version of the mass-radius plot from Figure 1.6 is shown. Additionally, the best available data for single neutron stars is drawn as probability regions. While the mass of several neutron stars may be given with quite good precision, the extraction of the NS radius remains the bigger challenge so that the data is rather scarce. Anyhow, due to the heavy PSR J0740+6620 many theories with lower maximum masses were rejected, including many of the hyperon models.

A possible solution

A step towards the understanding of the EOS may be given by studying the interaction of hyperons with other baryons. A well suited tool is given by the study of so called hypernuclei, nuclear structures which contain besides protons and neutrons also hyperons. They offer – unlike any other tool – the opportunity to study not only the baryon-baryon interaction but also the even more subtle multi-body interaction in strange baryonic systems. A more detailed introduction into the physics of hypernuclei is going to be found in following Chapter 2.
One key characteristic of hypernuclei is the energy by which the hyperon is bound to the remaining nucleus. Depending on the experimental method used to study this binding energy, the hyperon may also be observed in excited states, depending on whether it was bound to the s shell ground state or the higher shells.
Such observations are depicted in Figure 1.10 [217]. The binding energy B_Λ of the Λ on the energy shells s, p, d, f and g in several hypernuclei was plotted against $A^{-2/3}$, the mass number[1]. The experimental data contains hyper-isotopes ranging from ${}^{13}_{\Lambda}\mathrm{C}$ to ${}^{207}_{\Lambda}\mathrm{Pb}$ [150] and is plotted with circles, while two theoretical predictions are found as lines. The blue dashed line indicates a calculation just with two-body interactions, so three-body forces are ignored. In contrast, the red one takes these into account additionally. For most data points, the latter model is in

[1] Further motivation for plotting against $A^{-2/3}$ is found in Chapter A.1.3 on page 128.

much better agreement than the simpler one without three-body effects [217]. Especially for the heavier hyper-isotopes plotted on the left, the discrepancy is the strongest. To summarize, the repulsive three-body hyperon-nucleon-nucleon force prevents B_Λ from being over-estimated. Today this repulsive three-body force is known to be essential to reproduce the binding energy of hypernuclei over a wide mass range [197]. Especially the heavier hypernuclear systems show the biggest influence of three-body effects, so the remaining question is if – or rather to which quantity – the nuclear EOS is affected at high energy densities. This effect would again stiffen the EOS and allow for higher maximum masses.
Indeed, for such a scenario theoretical predictions have already been made, of which also one is still to be found within the comparison with actual neutron star data in Figure 1.9. This model – in black – allows for a maximum mass of up to $2.1\ M_\odot$ and is compatible with the experimental data. After all however, it is still impossible to exclude any of the theoretical approaches due to the limited resolution, especially for the radius of neutron stars. So until today, the expected appearance of hyperons at about two times nuclear density remains an unresolved mystery in neutron star physics, which was given the name *hyperon puzzle*.

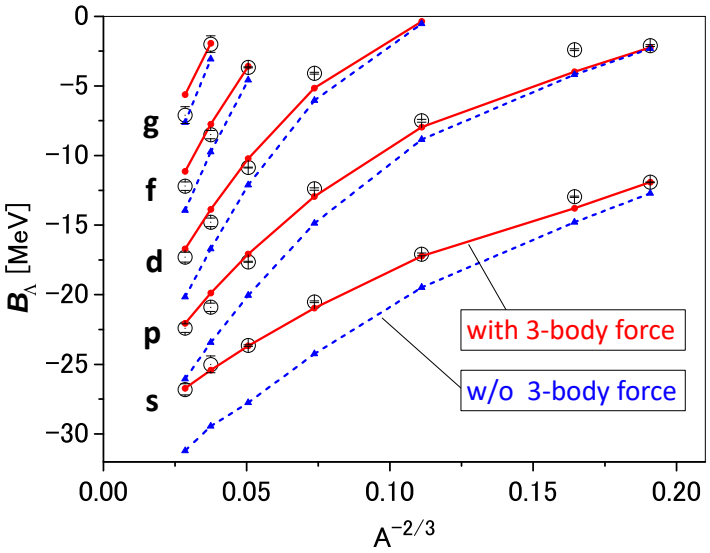

Figure 1.10.: Λ binding energies for hypernuclei ranging from ${}^{13}_{\Lambda}\mathrm{C}$ to ${}^{207}_{\Lambda}\mathrm{Pb}$ as a function of $A^{-2/3}$ [217]. The circles show experimental values [150] for the Λ bound to various nuclear energy shells, the dashed lines indicate calculations without three-body forces. The red solid lines take a phenomenological three-baryon repulsion into account.

2. Introduction to Hypernuclear Physics

2.1. Hypernuclei

While in terrestrial laboratories it still remains an experimental impossibility to study nuclear matter with a density larger than ρ_0 over a long period of time, it is indeed feasible to produce hyperons and observe bound systems with regular nucleons at ρ_0, so called *hypernuclei*.

2.1.1. Nomenclature

A hypernucleus is an atomic nucleus which is build up not only by protons and neutrons but also by one or more hyperons Y, as illustrated in Figure 2.1. Similar to the regular isotopes, hyper-isotopes are given a name according to their nuclear charge Z, while their nucleon number A is written in front of them as superscript. For hypernuclei, the information about the hyperon content is added as a subscript below the nucleon number, resulting in ${}^{A}_{Y}Z$. Here, Y denotes the explicit letters of the involved hyperons. For example, a carbon nucleus ${}^{12}\mathrm{C}$ will become ${}^{13}_{\Lambda}\mathrm{C}$ if a Λ is added. A bit more attention has to be paid if the hyperon itself carries electric charge. The bond of a Σ^- to ${}^{12}\mathrm{C}$ will result in ${}^{13}_{\Sigma^-}\mathrm{B}$.

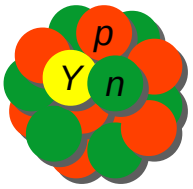

Figure 2.1.: Schematic sketch of a hypernucleus. A hyperon Y is bound to a regular nucleus.

2.1.2. Categorization in sub-species

In principle, any exotic baryon could form a bond to regular nuclear matter. However, most of these theoretically possible combinations are not observable due to their very short lifetime. Baryons which decay via the strong force for example typically live $10^{-23}\,\mathrm{s}$, which is not sufficiently long for the creation of a bound system. The same holds for electro-magnetic decays with around $10^{-20}\,\mathrm{s}$. Only weakly decaying baryons with a lifetime in the order of $10^{-10}\,\mathrm{s}$ live long enough, which is fulfilled by just a small group of strangeness-containing baryons. Practically, only the Λ, Σ and Ξ baryons in their lightest form are suited for such a bond. This leads to a categorization into at least three sub-families of hypernuclei which have their own unique characteristics and challenges for the observation in laboratories.

The Λ hypernuclei are the most common group. These are the easiest to produce and hence have already been studied intensively. Today, more than 30 different hyper-isotopes have been observed in various experiments. For the Σ and Ξ hypernuclei, the information is much more limited. This is mostly due to a lower production probability, but also some experimental methods for the creation of Λ's simply cannot be applied to these baryons at all. Only one Σ hypernucleus has been observed unambiguously so far, which is ${}^{4}_{\Sigma^+}\mathrm{He}$ [230, 213]. In case of the Ξ, only the ${}^{15}_{\Xi^-}\mathrm{C}$ system was discovered [152, 308, 220]. The experimental success of the Λ hypernuclei though allowed for the study of a fourth family, the double Λ hypernuclei. The most successful observation was the so called Nagara event, the detection of ${}^{6}_{\Lambda\Lambda}\mathrm{He}$ [289, 20]. In the scope of this thesis, mainly the single Λ hypernuclei will be addressed.

2.2. Hyperons and Strange Mesons – an Overview

2.2.1. The Λ baryon

The Λ baryon is the lightest hyperon consisting of a uds quark triplet. With $m_\Lambda = 1115.683(6)\,\mathrm{MeV}/c^2$, it is slightly heavier than the proton and the neutron. While it carries no electric charge, its strangeness is $S = -1$ and therefore its lifetime is – as typical for strange quarks – in the order of several picoseconds, $\tau_\Lambda = 263.2 \pm 2.0\,\mathrm{ps}$ [292].
The Λ was discovered in 1950 by Hopper and Biswas [158], only two years prior to the first observation of a hyperfragment. At that time, the experimental information about the Λ must have been scarce to say the least. When by the end of the 1950's a first average value for the Λ mass was published by the PDG, it was shifted by almost half an MeV to the mass we know today. This is illustrated in Figure 2.2, where the PDG literature values [237] are plotted for the last 70 years as the difference from the present m_Λ (black). For comparison, also the proton and pion masses are shown in red and blue. While during the 1960's the mass accuracy was improving year by year, it stagnated at around $100\,\mathrm{keV}$ from the 70's until the end of the 80's. During these years, hypernuclei have already been studied intensively, as indicated by the timeline in the lower part of the figure. Just by 1994, an until then unprecedented accuracy in the order of single keV was achieved, which largely satisfies the needs of hypernuclear physics. Still already in the previous years, lots of experimental data about hypernuclei was gathered, especially in the emulsion era. This data still strongly influences the overall knowledge about hypernuclei from today, so the question is raised, if a re-calibration for these values is needed [13]. This question will also be addressed in this thesis, found in Chapter 4.3.6 on page 47.
Further explanation about the timeline is going to be provided in Chapter 2.3, while the mentioned experimental facilities are going to be discussed in closer detail in Chapter 3 on page 21.

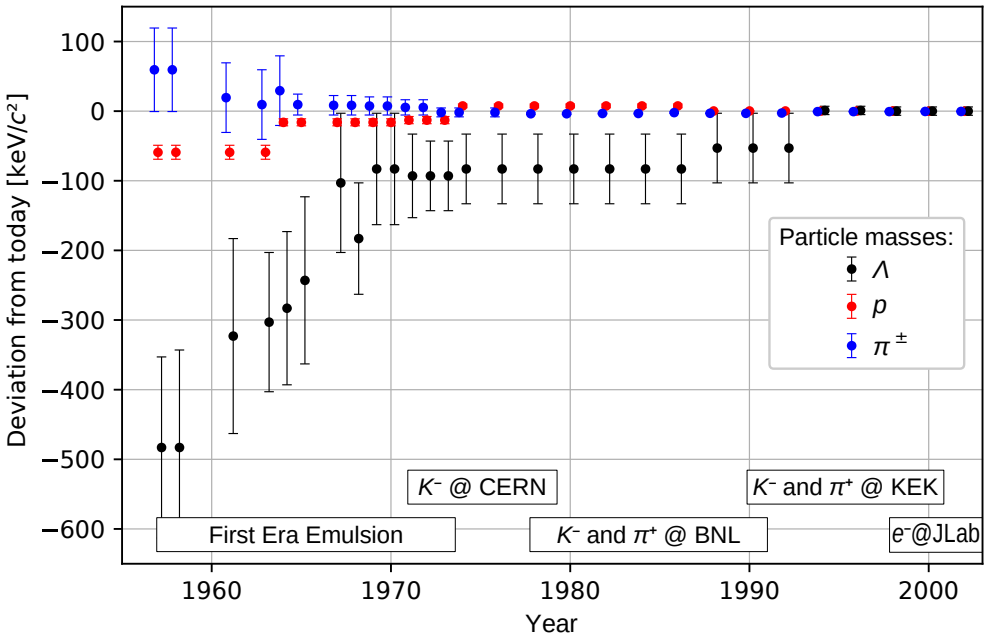

Figure 2.2.: Development of the mass literature values of proton, Λ and pion within the last 70 years, given by the PDG [237]. In the early years, especially the Λ mass (black) deviated quite significantly from the present value, almost by half an MeV in the late 1950's. During the 60's huge improvements were achieved, so that by the 70's the mass deviated roughly $100\,\mathrm{keV}$ from today's value. It took another 20 years to reach an accuracy in the order of single keV.

Λ decays

The free Λ is known to decay most likely via the emission of a π meson, the so called *mesonic weak decays*, of which two channels are possible:

$$\Lambda \rightarrow p + \pi^- \qquad 63.9\%, \tag{2.1}$$
$$\Lambda \rightarrow n + \pi^0 \qquad 35.8\%. \tag{2.2}$$

The charged decay is expected to occur around twice as often and is most frequently used for decay studies of hypernuclei. The uncharged decay though is not detectable in charge sensitive detectors, so its experimental value is limited. Beyond these two channels, there exist further decay possibilities with a summed probability of around 0.3%. These are not relevant for the physics discussed in the scope of this thesis and hence will not be discussed.
In contact with other baryons – as given in hypernuclei – additional decay channels are opened, the so called *non-mesonic weak decays*:

$$\Lambda + n \rightarrow n + n, \tag{2.3}$$
$$\Lambda + p \rightarrow n + p. \tag{2.4}$$

Additionally, also channels with one more involved nucleon have been observed. The probability of these decays strongly depends on the shape of the hypernuclear system. A strong bond of the Λ to the nucleus, as well as a huge mass number increase the chances of such decays. Therefore, they have to be evaluated for every hypernuclear isotope specifically. The appearance of these additional channels lowers the lifetime of the Λ inside the hypernucleus typically by up to 25%. A data collection about hypernuclear branching ratios is found in Chapter A.4 on page 139.

2.2.2. Other hyperons

From the first discovery of the Λ it wasn't long until other strangeness-containing baryons were found, for example the charged Ξ^- in 1952 [31]. Together with proton and neutron, they form the so called baryon octet shown on the left side of Figure 2.3 [10]. It lists all spin $J = \frac{1}{2}$ baryons in the $\{u, d, s\}$ flavor space. Inside this octet the Λ is the only particle to share its place

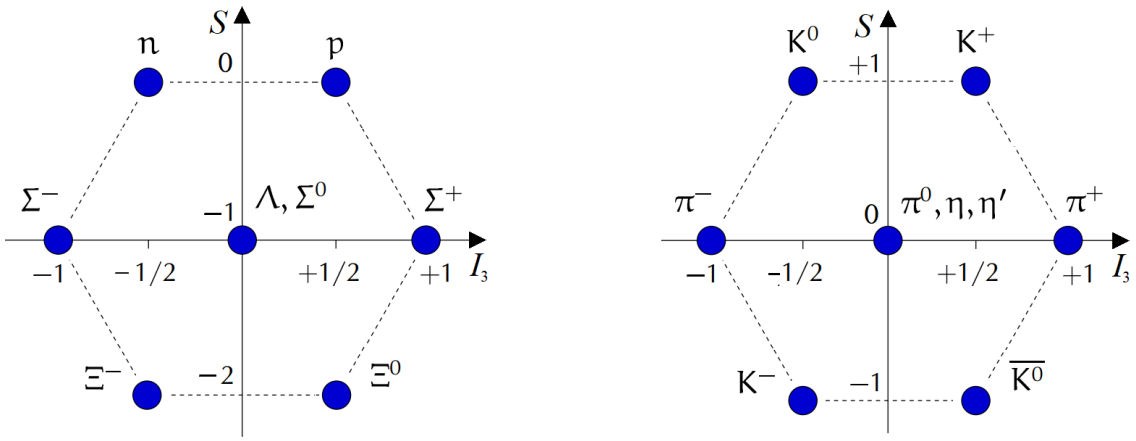

Figure 2.3.: The baryon octet and meson nonet [10]. They sort all possible spin $\frac{1}{2}$ baryons and mesons from the $\{u, d, s\}$ flavor space by their strangeness S and third isospin component I_3. Also indirectly, their charge Q is ascending from the bottom left to the top right.

with another baryon, the Σ^0. Both are to be distinguished by their isospin I, which is 0 for the Λ and 1 for the Σ^0. The latter possesses a slightly higher mass of $1189.37(7)\,\mathrm{MeV}/c^2$. Besides that, there exist two other $S = -1$ baryons, the Σ^+ and the Σ^-. They only vary in their first generation quark content, being uus and dds, respectively. The final group is given by adding another strange quark, the $S = -2$ Ξ baryons.
An overview about all these baryons is provided in Table 2.1. They all show a common property, which is the lifetime in the order of $100\ \mathrm{ps}$ and the decay channels, which all involve π mesons. The only exception is the Σ^0, which performs an electromagnetic decay into a Λ and therefore is much shorter-lived. Without this exception, all hyperons live long enough to bind with regular nucleons to form a hypernucleus. Special note is to be taken of the Ω^-, a $S = -3$ hyperon with $J = \frac{3}{2}$, where no bond was observed yet.

Table 2.1.: Overview of subatomic particles relevant for this work. Next to proton, neutron and pion, the basic strange mesons and baryons are shown. Besides their mass and lifetime literature values also their decay channels are shown [236]. For the K^+ and the Λ the least likely decay channels were omitted.

Name	**Letter**	**Quarks**	**Mass** $[\,\mathrm{MeV}/c^2\,]$	**Lifetime**	**Decay**	
Proton	p	uud	$938.27208816(29)$	$stable$	–	
Neutron	n	udd	$939.56542052(54)$	$878.4(5)\,\mathrm{s}$	$p + e^- + \bar{\nu}_e$	
Pion	π^-	$\bar{\mathrm{u}}\mathrm{d}$	$139.5704(2)$	$26.033(5)\,\mathrm{ns}$	$\mu^- + \bar{\nu}_\mu$	
Kaon	K^+	$\mathrm{u}\bar{\mathrm{s}}$	$493.677(16)$	$12.380(20)\,\mathrm{ns}$	$\mu^+ + \nu_\mu$	64%
					$\pi^+ + \pi^0$	21%
					$\pi^0 + e^+ + \nu_e$	5%
					$\pi^+ + \pi^+ + \pi^-$	6%
Lambda	Λ	uds	$1115.683(6)$	$263.2(2.0)\,\mathrm{ps}$	$p + \pi^-$	64%
					$n + \pi^0$	36%
Sigma	Σ^+	uus	$1189.37(7)$	$80.18(26)\,\mathrm{ps}$	$p + \pi^0$	52%
					$n + \pi^+$	48%
	Σ^0	uds	$1192.642(24)$	$7.4(7)\cdot 10^{-20}\,\mathrm{s}$	$\Lambda + \gamma$	
	Σ^-	dds	$1197.449(30)$	$147.9(1.1)\,\mathrm{ps}$	$n + \pi^-$	
Cascade/Xi	Ξ^0	uss	$1314.86(20)$	$290.0(9.0)\,\mathrm{ps}$	$\Lambda + \pi^0$	
	Ξ^-	dss	$1321.71(7)$	$163.9(1.5)\,\mathrm{ps}$	$\Lambda + \pi^-$	
Omega	Ω^-	sss	$1672.45(29)$	$82.1(1.1)\,\mathrm{ps}$	$\Lambda + K^-$	68%
					$\Xi^0 + \pi^-$	23%
					$\Xi^- + \pi^0$	9%

2.2.3. Strange mesons – the kaons

Kaons are a group of pseudoscalar mesons. They consist of a quark-antiquark pair with one quark from the first generation $\{\mathrm{u}, \mathrm{d}\}$ and a strange quark s. In total, four different kaons exist, the K^+ being the $\mathrm{u}\bar{\mathrm{s}}$ combination, its anti-particle K^- with $\bar{\mathrm{u}}\mathrm{s}$ and the neutral kaons K^0, $\mathrm{d}\bar{\mathrm{s}}$ and $\bar{K}^0$, $\bar{\mathrm{d}}\mathrm{s}$. They all carry a strangeness of $S = \pm 1$ and are summarized in the *meson nonet*, shown in the right side of Figure 2.3. The horizontal center line is occupied by the various pions, which only consist of first generation quarks. With a weight of almost $500\,\mathrm{MeV}/c^2$ the K^+ is three times as heavy as a pion, while its lifetime is with $12\,\mathrm{ns}$ around half the pions lifetime. The

exact values are found in Table 2.1. The K^+ most likely decays into a $\mu^+\nu_\mu$ pair ($\approx 64\%$) but also hadronic and semileptonic decay channels with involved pions are possible. The K^-, as the respective anti-particle, behaves analogously.
Charged kaons are often involved in the generation process of Λ hyperons, so that they play an important role in various hypernuclear studies. Within the experiment of this thesis for example, kaons are detected on purpose to identify Λ production reactions. The other particles, the neutral kaons and the η mesons, are in view of the present thesis not of great relevance, so information about them may be provided by the Particle Data Group [237].

2.3. Experimental History of Hypernuclear Physics

The discovery

Hypernuclear physics was born in 1953, when several independent experimental groups discovered yet unseen events in photographic emulsion plates. These were based on the usual photo plates, as used by Röntgen and Becquerel before. The emulsion is thicker and contains silver bromide grains that condense along the tracks of traversing charged particles. Once examined with a microscope, the structure of the grains gives information about the mass of the particle. In addition, also its direction and flight length can be examined to access further kinematic properties.
Figure 2.4 shows the two first ever observed hypernuclear events, the left one by Crussard and Morellet [86], the right one by Danysz and Pniewski [92]. The plates were exposed to cosmic

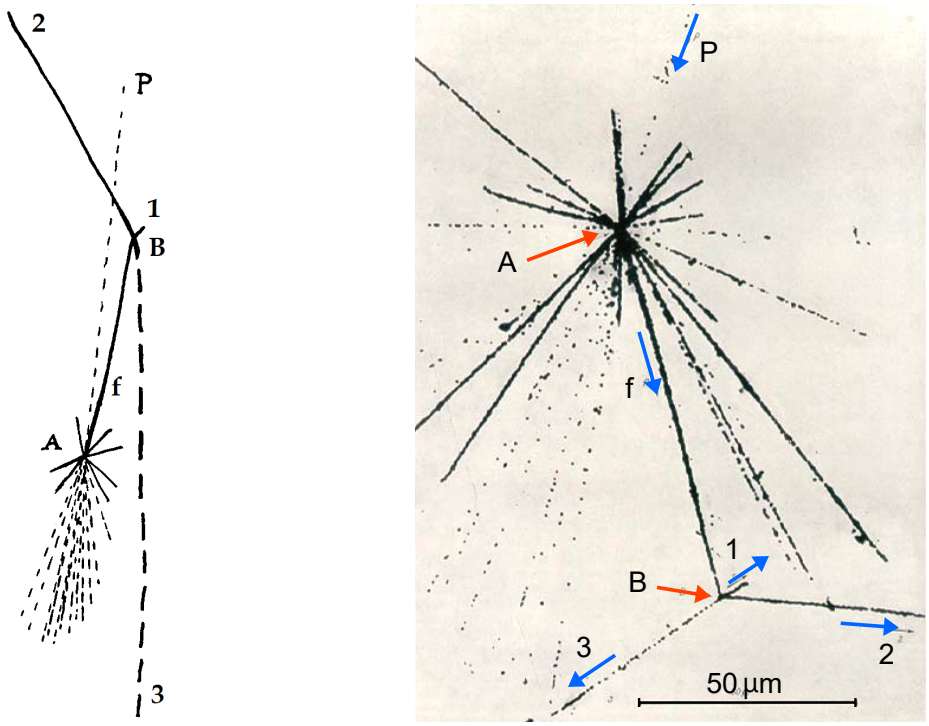

Figure 2.4.: The first hyperfragment events seen in nuclear emulsion. **Left:** drawing of an event published by Crussard and Morellet in January 1953 [86]. **Right:** event submitted by Danysz and Pniewski in December 1952 and published in march 1953 [92]. In both pictures an incident cosmic ray P interacts at A with a heavy nucleus in the nuclear emulsion. A produced hyperfragment f decays at B into three charged particles.

radiation, causing an energetic particle P to traverse the plate. In both cases, a violent fragmentation was triggered, once a nucleus was hit, generating a primary star in the emulsion, A. One of the fragments f traveled several μm through the emulsion, until a secondary star was observed, B. A similar event was also detected by Tidman and co-workers [295] and they were initially called *connected stars*.

The secondary fragment was estimated to be stopped within the emulsion in about $10^{-12}\,\mathrm{s}$ and to release an energy of 140 to $180\,\mathrm{MeV}$. By that, the first hypothesis of a decay of an excited ordinary nuclear fragment already could be excluded – decays of excited states in the order of $100\,\mathrm{MeV}$ were known to live only around $10^{-20}\,\mathrm{s}$. Furthermore, the fact that the unknown fragment was stopped, drawn from the momentum distribution of the emitted bodies 1, 2, 3, ruled out the possibility of a secondary collision between the fragment and another nucleus in the emulsion. The random coincidence of two events was discarded as well by Tidman et al. [295] and Ciok et al. [79] because of an extremely small probability [86, 92]. Finally, the experimentalists were left with two possibilities, being (i) the capture of a meson like a pion coming from an atomic orbit or (ii) a bound system of the recently observed [264, 279] heavy V_0^1 particle and other nucleons [92].

In both events from Figure 2.4 three bodies were emitted, while one of them left a weaker track than the others, 3, indicating the presence of a pion. As a consequence, a pionic atom as the origin of these connected stars could be discarded. Analysing a two-body decay of another secondary star, Bonetti and co-workers also excluded a capture of a heavier meson as the trigger of the secondary decay [56] leaving only possibility (ii). The V_0^1 particle was soon renamed to Λ baryon, as it is known today and – as suggested by Goldhaber [131] – such unique fragments were later called *hyperfragments*.

The first experimental era – Emulsion studies

In the following years, strangeness- and hypernuclear physics became a subject of continued interest. Especially the binding energy between the Λ baryon and the remaining nucleus were already investigated in the 60's and early 70's of the last century. In addition, also the lifetime and branching ratios for the different decay channels were determined. The state-of-the-art methods were again the emulsion technique [165, 53, 132, 250] but also bubble chamber experiments were performed [177, 128]. The experimental setups were improved by making use of hadron beams at accelerators instead of cosmic rays. For example, proton and pion beams were used at the Brookhaven Cosmotron [131] but also reactions with stopped Σ^- baryons originating from K^- interactions were analysed [130]. These resulting Λ binding energy values B_Λ gave the first hints about the behavior of nuclear systems besides the proton and neutron degrees of freedom.

By that time, experimentalists also started to investigate the lifetimes of the hypernuclear isotopes, by evaluating their flight lengths in the emulsion matter. The achievable accuracy with that procedure was limited though so that most of the published values were scattering strongly and had errors ranging from at least 25% to more than 100%. Better suited were the available techniques for analysing the branching ratios of different decay channels of hypernuclei.

By the mid of the 70's already thousands of hypernuclear events from several facilities were collected and compiled to average values. The most cited compilation is the one by M. Jurič from 1973 [165]. It contains averaged binding energy values for various hyper-isotopes with a nucleon number A ranging from 3 to 12. This compilation was seen as the best available source of information for many decades and marked the end of the first experimental era of hypernuclear physics.

The second era – Missing mass experiments with kaon beams

By the end of the 1970's, the first spectroscopic studies have been performed. They followed a new approach, the study of hypernuclei in their generation process via the missing mass technique using kaon beams. More information about this technique is provided in the following Chapter 3. Two facilities were pioneering such studies, the Brookhaven National Lab BNL and the CERN [249, 248, 68, 67]. This approach was chosen due to a special kinematic behavior of generated Λ's, which is illustrated in Figure 2.5. Here one can see various curves for different production reactions of hyperons [223, 38]. They link the momentum of the incident beam particle to the recoil of the generated hyperon. Only for the reactions $Kn \rightarrow \pi\Lambda$ and $Kn \rightarrow \pi\Sigma$ an absolute minimum of 0 in the recoil of the hyperon is found. The corresponding beam momenta received the name *magic momentum*, since they allow for a maximized binding probability of the produced hyperon to the remaining nucleus. All other reactions – using protons, pions and gammas as beam particle – transfer at least $200\,\mathrm{MeV}/c$ to the hyperon. Therefore, kaons were used as beam particles, despite the great efforts and challenges involved in their handling, compared to the other particles. These are mainly given by the short lifetime of the kaons.

The principle of the experiments at CERN is seen in Figure 2.6 [249, 248]. An initial proton beam hit a primary target PT. From here, various fragments and mesons were produced, of which the kaons were extracted via an element separator (E.SEP.). After a short section for focusing the beam with various quadrupole magnets Q and other components, a thick target, e.g. $10\,\mathrm{mm}$ carbon, was used to produce hypernuclei. Inside the hit nucleus, the kaon reacted with a neutron to a Λ and a π^-. A quark flow diagram of this reaction is found in Figure 3.2 on page 24. The outgoing pion was then detected in the following pion spectrometer. The beam line was designed as compact as possible to take the short kaon lifetime into account.

Contrary to the previous emulsion experiments, here the actual generation process of the hypernucleus was investigated. This opened a till then unknown spectrum of excited states in hypernuclei. In general, a hypernucleus can be produced in various states, depending on which neutron from the nucleus was transformed into the hyperon and to which shell it was bound.

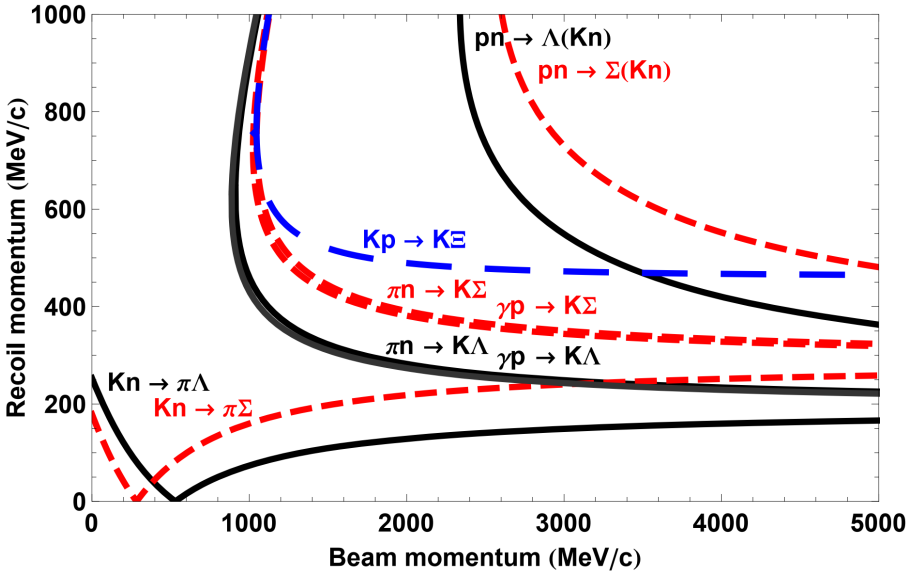

Figure 2.5.: Hyperon recoil momentum for various generation reactions dependent on the momentum of the incident beam particle [223], adapted from [38]. Remarkably, only two reactions allow for the production of recoil-free hyperons, one being the $Kn \rightarrow \pi\Lambda$ reaction.

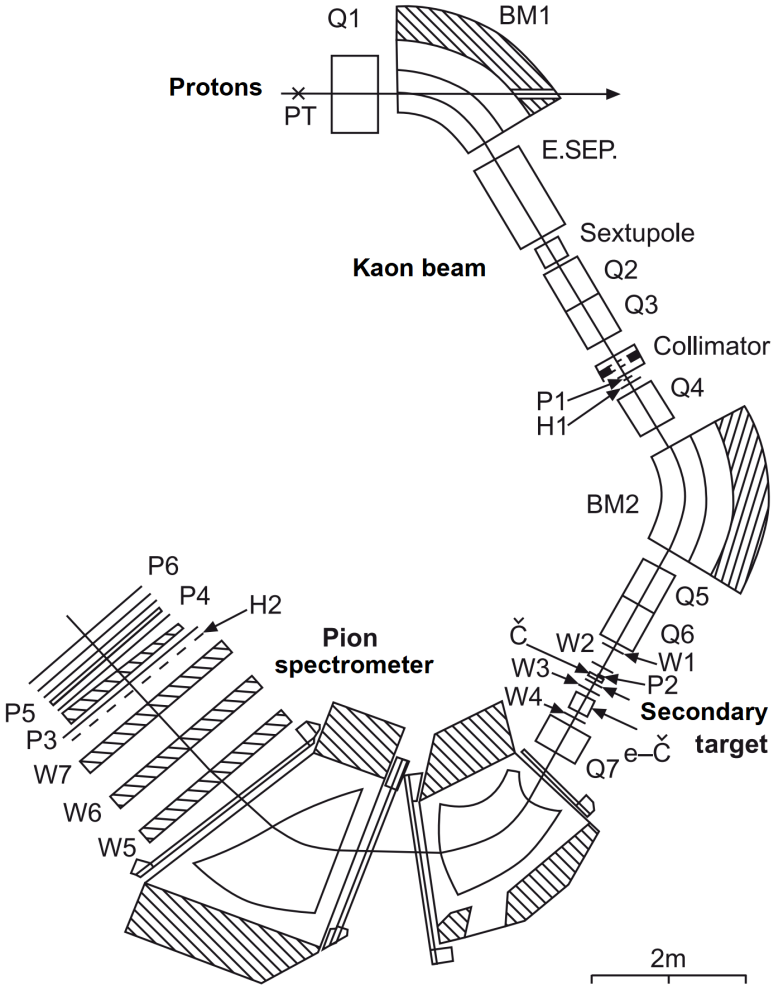

Figure 2.6.: Experimental setup of the second era experiments at CERN [249, 248]. Kaons were produced off a primary target PT and focused onto a secondary carbon target. The outgoing pions from the production process $K^- n \rightarrow \Lambda\pi^-$ were detected in a dedicated spectrometer under forward angles.

This excitation may be strongly unstable, but due to studying the products of the production process, it still can be observed in the resulting spectrum. One of these is shown in Figure 2.7, the missing mass spectrum of ${}^{12}_{\Lambda}\mathrm{C}$ [248]. Besides the ground state binding energy at roughly $11\,\mathrm{MeV}$, a much stronger peak for an excited state was found at around 0. Besides this carbon hypernucleus, also other excitation spectra of oxygen, sulfur, calcium and bismuth hypernuclei were observed in these new studies.

Still, these results were far from perfect, since they were hampered with a variety of problems. For example, only Λ hypernuclei have been observed unambiguously. Despite the kinematic possibility, Σ hypernuclei could not be observed due to a lower production probability. Also the kaon beam intensity and precision was limited, since the production off the primary target was rather inefficient. As a consequence, a thick target had to be used to allow for enough hypernuclear reactions. At the same time, also the momentum of the produced pions was distorted due to the straggling in the thick target. Finally, the results of these studies were limited in terms of resolution and could not compare to the accuracy achieved in the emulsion experiments.

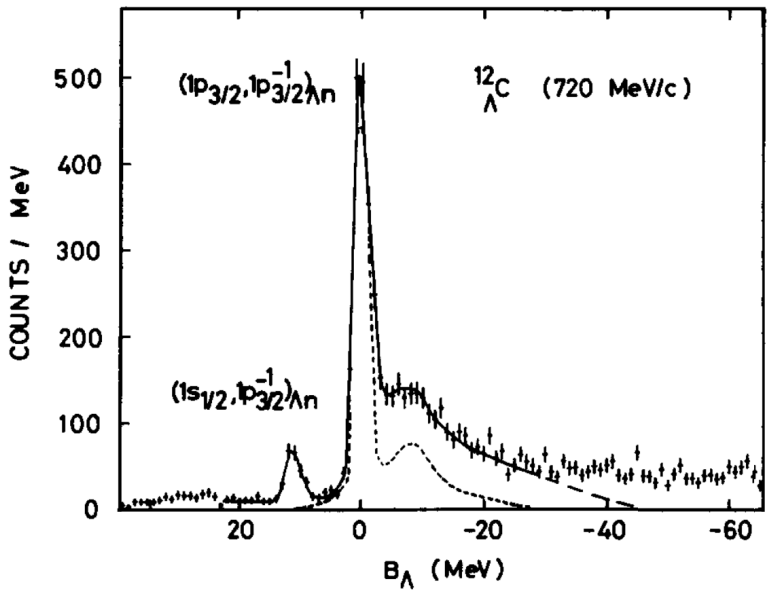

Figure 2.7.: Excitation spectrum of $^{12}_{\Lambda}\mathrm{C}$ during the second era K^- experiments at CERN [248]. While in the first era emulsion experiments only the ground state of hypernuclei could be observed – here at $B_\Lambda \approx 11\,\mathrm{MeV}$ – excited states became accessible for the first time, as the one seen here at around $0\,\mathrm{MeV}$.

The third era until today – Various approaches

In the 1990's, when new spectroscopic experimental methods became available, further characteristics of hypernuclei became accessible. For example, Tamura was able to observe missing mass spectra of heavier hypernuclei [291], e.g. the one to see in Figure 2.8 [150]. For this yttrium hypernucleus, not only one excited state was observed besides the ground state Λ binding energy, but information about a whole level structure was gained, where the Λ was bound to even higher shells. Results like these are a prime example of information that contributed to the experimental data shown previously in Figure 1.10 on page 10.
Not only kaon beams have been used in the more recent studies, but a whole spectrum of beam particles, pions, gammas and even electrons has been utilized. Since 2010, the heavy ion collision became another valuable source of information about hypernuclei. For example, the ALICE Collaboration at the LHC was able to extract lifetime as well as binding energy data about lightest hypernuclei just recently [119].

Summary

The history of hypernuclear physics shows that the experimental possibilities during each period had a large influence on the available data and accuracy. Like already indicated in Figure 2.2 on page 12, there have been several decades where just single facilities with unique experimental methods coined the progress in hypernuclear physics. These individual experiments each led to a deeper level of confidence about the methods themselves but in some cases also spotted discrepancies.
The unique – but also challenging – characteristic of hypernuclear physics is, that still today it remains a non-trivial to the experimentalists to overrule the accuracy of the results published from the first era of emulsion, even 50 years later. This is in deep contrast to, for example, the accuracy of the particle masses shown in Figure 2.2. While in the 1960's the masses of pion and

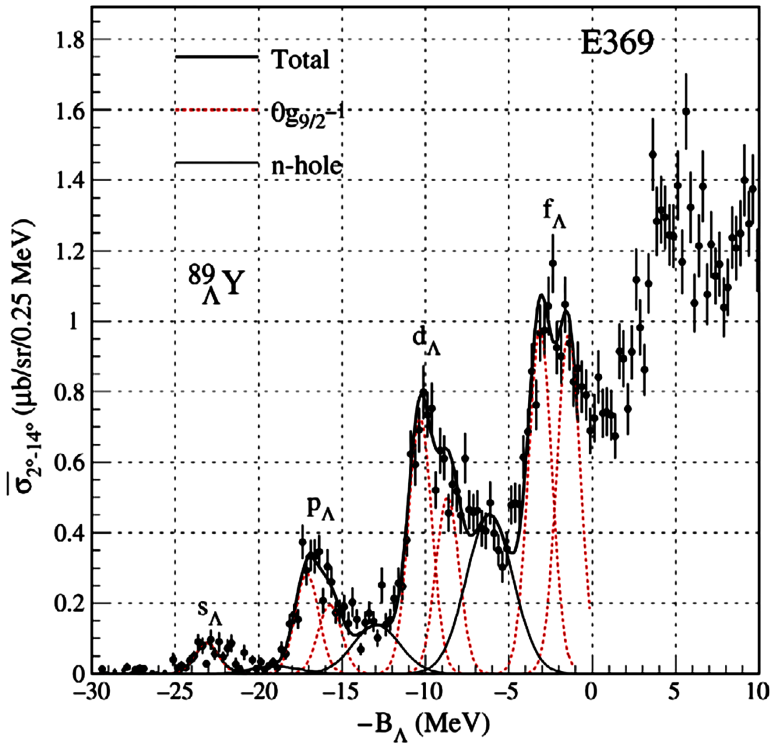

Figure 2.8.: Missing mass spectrum of ${}^{89}_{\Lambda}\mathrm{Y}$ observed by H. Tamura in stopped K^- reactions [150]. This spectrum shows several distinct peaks indicating the Λ to be bound to different shells of the remaining ${}^{88}\mathrm{Y}$ nucleus.

Λ were known only with roughly $100\,\mathrm{keV}/c^2$, the $1\,\mathrm{keV}/c^2$ scale is reached today for both of them. On the one hand, this keeps all the successfully explored techniques relevant for new improvements to gain even better results. On the other hand, it is more important to consider the complete picture of data than in other areas of physics, even if 50 years old. A more detailed description of the explored experimental methods is to be found in the following Chapter 3.

3. How to study Hypernuclei

3.1. Two Fundamental Principles

While in the previous Chapter 3 already several experimental methods to study hypernuclei were mentioned, a more detailed and complete description is going to be found in this chapter. The focus lies on the masses of Λ hypernuclei. Generally, two different phases allow to study hypernuclei. One is the production process and the other the decay. These are depicted schematically in Figure 3.1. Here it is to note, that for the production (left) a scenario was chosen, where a regular nucleus ${}^{A}Z$ is transformed to a hypernucleus. This is not the only possibility for the generation of hypernuclei, since at central heavy ion collisions, entirely new hyper-isotopes can hadronize out of the collision. More about that is going to be described in Section 3.3.3 on page 29. Apart from that, usual decay scenarios are depicted in the center and right of Figure 3.1. In the first case, a hypernucleus de-excitates to its ground state via the emission of gamma rays, while in the latter, the Λ itself decays. All scenarios are described in the following.

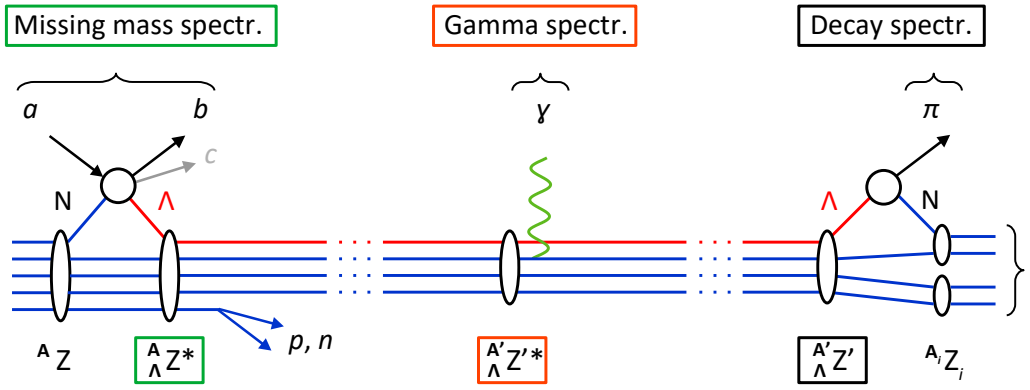

Figure 3.1.: Two fundamental methods to study hypernuclei, the production and the decay spectroscopy. **Left:** production of a hypernucleus with an incident beam particle b, an outgoing particle p and the produced hypernucleus, possibly in an excited state. Studying this nucleus is enabled by the missing mass technique, the determination of the kinematic properties of b and p (and c, if more particles are outgoing). **Center:** decay of the possible excitation via the emission of γ rays resulting in a ground state hypernucleus. **Right:** decay of the hypernucleus. The Λ decays back into a nucleon under the emission of a decay pion. Depending on the circumstances, this decay can be of two-body nature so that the spectroscopic study of this pion alone can be sufficient to extract the mass of the initial hypernucleus.

Missing mass spectroscopy

The production, shown on the left of Figure 3.1, is initiated by an incoming particle a which reacts with a nucleon N of a nucleus in the target. This results in the generation of a Λ and another particle b. By knowing the kinematic properties of a and b, the generated hypernucleus

can be studied via the missing mass technique. Due to the conservation of energy and momentum, the sum of fourvectors before the reaction (a + target nucleus) has to be equal to the four vectors afterwards (b + hypernucleus), which can be solved for the hypernucleus. It is to be noted, that in some cases a third particle c may also be involved, which then additionally has to be taken into consideration. This missing mass method was for example used during the previously described kaon experiments in the second era of hypernuclear physics, see Chapter 2.3 on page 15. As already shown in Figure 2.7 and Figure 2.8, the results of these experiments yield excellent excitation spectra, while the appearance of the ground state mass may be suppressed by the production cross section.
Within the missing mass spectroscopy, the generated hyper-isotopes are always pre-determined by the used target nuclei. On the one hand, this limits the experimentally accessible hypernuclei to a certain group, but on the other, these can be produced and examined regardless of their stability. The biggest challenge in such experiments is that two – or in some cases even three – particles have to be observed and studied for a proper result of the missing mass. By that, in general, a high resolution is hard to achieve.

Decay spectroscopy

The other possibility is given by the decays of hypernuclei, shown on the center and the right of Figure 3.1. In the first case, γ ray spectroscopy allows for the observation of excitation spectra of hypernuclei, compare to Figure 4.1 on page 39. In the second case, the hypernucleus finds its end by the decay of the Λ back into a nucleon under the emission of a pion. In case of two-body decays, the spectroscopic study of the pion can be sufficient to extract the mass of the preceded hypernucleus. An example for decay studies are the emulsion experiments. Contrary to the missing mass spectroscopy, here only the ground state can be studied, since typically the hypernucleus lives much longer than its excitations.
Generally, there are many possible outcomes of hyperfragments off the same initial target isotope due to the decay of the excitation. This usually causes the emission of several nucleons, so that afterwards a lighter hyper-isotope is given in its ground state. By that, for example, it was possible to study various hyper-isotopes within one type of emulsion plate. A downside, however, is that heavy hypernuclei most likely split up into lighter isotopes, so that they are rare to be found in decay studies. The even bigger problem is given by the fact that for higher mass numbers multi-body decays will take over, which also might involve neutrons. These are, due to their lack of charge, not detectable by many spectrometer types. This limits the method of decay spectroscopy to low mass number hypernuclei.

In the following, the various spectroscopic approaches are going to be explored in deeper detail and some of the involved experimental facilities are introduced. While most of them can be categorized clearly to one of the two main principles, there are also several combined studies, which investigate the hypernucleus both during production *and* decay.

3.2. Missing Mass Spectroscopy

While with the emulsion technique all participating particles, including the hypernucleus, are visible, the principle of missing mass spectroscopy aims to gain information by studying all surrounding particles, but not the hypernucleus itself. This is possible by the conservation of energy E and momentum p. By knowing these properties for the initial state particles – usually an accelerated beam particle and a resting target nucleus – the energy and momentum is already determined for the final state system. The detection and spectroscopy of the outgoing particles then enables to study the remaining modified target nucleus.
In hypernuclear physics, there were already several experiments exploring different methods of the missing mass spectroscopy. An overview is given in Figure 3.2, where possible quark flow diagrams for the creation of Λ baryons off regular nucleons are shown [223]. Depending on the incident particle, they may be grouped into strangeness exchange reactions, where a K^- already carries the required strange quark, or strangeness production reactions, where this quark needs do be created during the reaction. Another exotic version of the missing mass spectroscopy is the strangeness electro-production. It uses the energy transfer from the virtual photon given by an electron beam, to generate an $\mathrm{s\bar{s}}$ pair. Unique for this technique is the presence of two outgoing particles, the scattered electron and a produced kaon. Both of these particles need to be studied as precise as possible for a proper missing mass resolution. In the following, the details about these reactions and their application in the past are going to be described.

3.2.1. The (K^-, π^-) reaction – Strangeness exchange

The quark flow diagram of this reaction, 1. in Figure 3.2, is the most trivial one. The incoming K^- already carries strangeness so that, when it reacts with a neutron, this strange quark only needs to be exchanged with one down quark to generate a Λ. At the same time, the kaon is transformed into a π^-. By knowing the kinematic properties of these two mesons, sufficient information is given to study the hypernuclear system.
Due to the incoming strangeness, this reaction has a comparably high cross section, as seen in Figure 3.3 on page 25. Here, in a 2D space of cross section and momentum transfer on the created Λ, the regions for the various production reactions are shown [150]. The strangeness exchange reaction is found in the upper left at *in flight* (K^-, π^-) and is not to be confused with the *stopped* (K^-, π^-) reaction. The latter is part of the decay pion spectroscopy section found in Chapter 3.3.2 on page 28. Concerning the *in flight* region, the momentum transfer on the Λ can even reach zero for a certain kinematic condition, as already observed before in Figure 2.5. It is given for a kaon momentum of around $530\,\mathrm{MeV}/c$, the so called *magic momentum*. This condition maximizes the probability for binding the Λ to the remaining nucleons to finally create a hypernucleus.
The challenge of experimenting with this reaction arises from the generation and handling of a K^- beam. It has to be produced off a primary target and then collected for the use at a secondary beam line. The beam intensity is limited as well as the achievable precision for the beam energy. Experiments with the (K^-, π^-) reaction were primarily performed at CERN in the 1970's [118, 68, 67, 248], compare to the second era of hypernuclear physics described in Chapter 2.3.

3.2.2. The (π^+, K^+) reaction – Strangeness production

With this type of reaction, a π^+ beam acts as incoming particle to transfer enough energy to a nucleus so that strangeness is produced. This is shown at 2. in Figure 3.2, where a $\mathrm{d\bar{d}}$ pair is converted to an $\mathrm{s\bar{s}}$ pair. Analogously to 1., a neutron from the target nucleus was transformed to a Λ baryon. According to Figure 3.3, the cross section of such a reaction may roughly be three

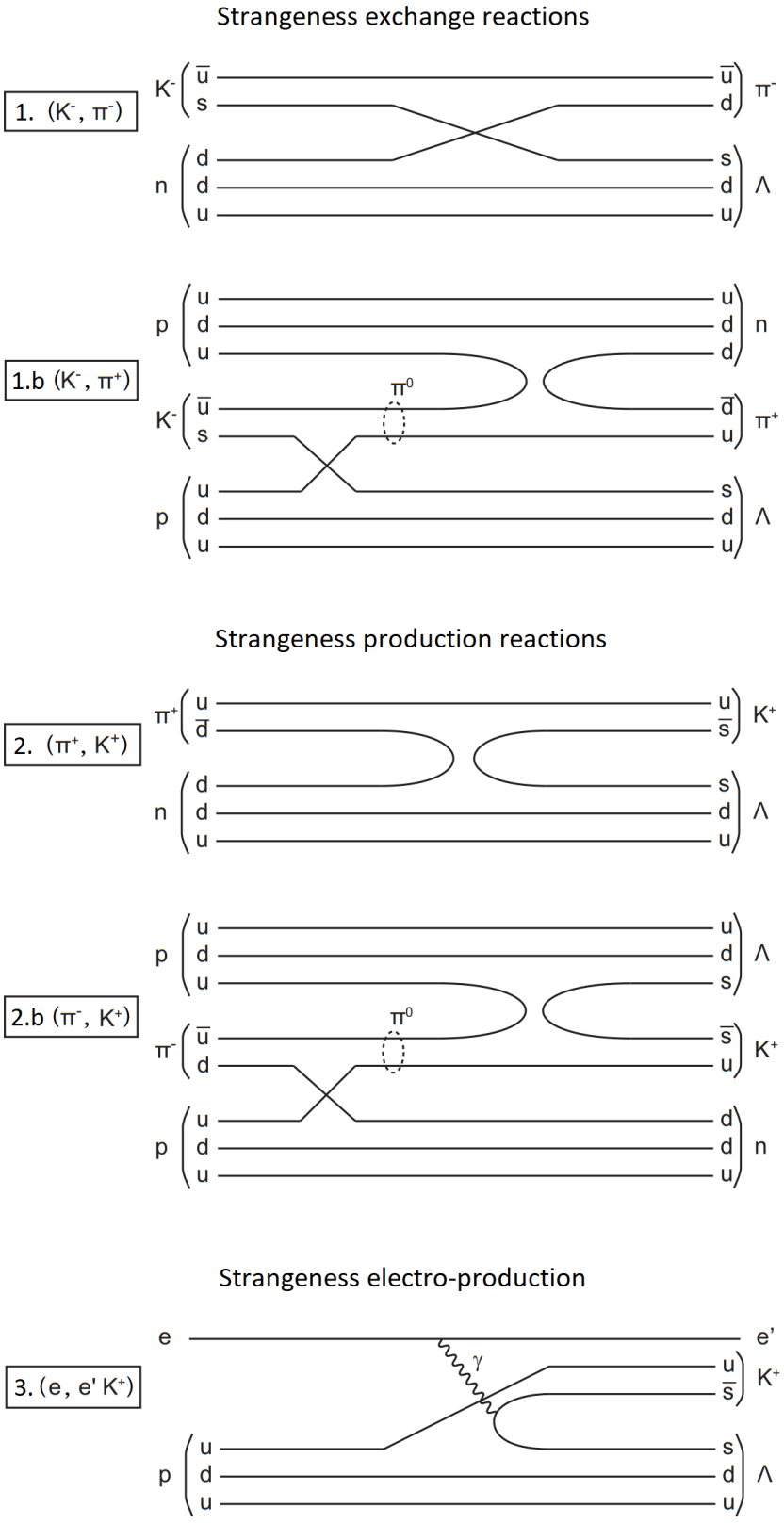

Figure 3.2.: Different Λ production mechanisms off target nuclei as quark flow diagram. Modified, adapted from [223].

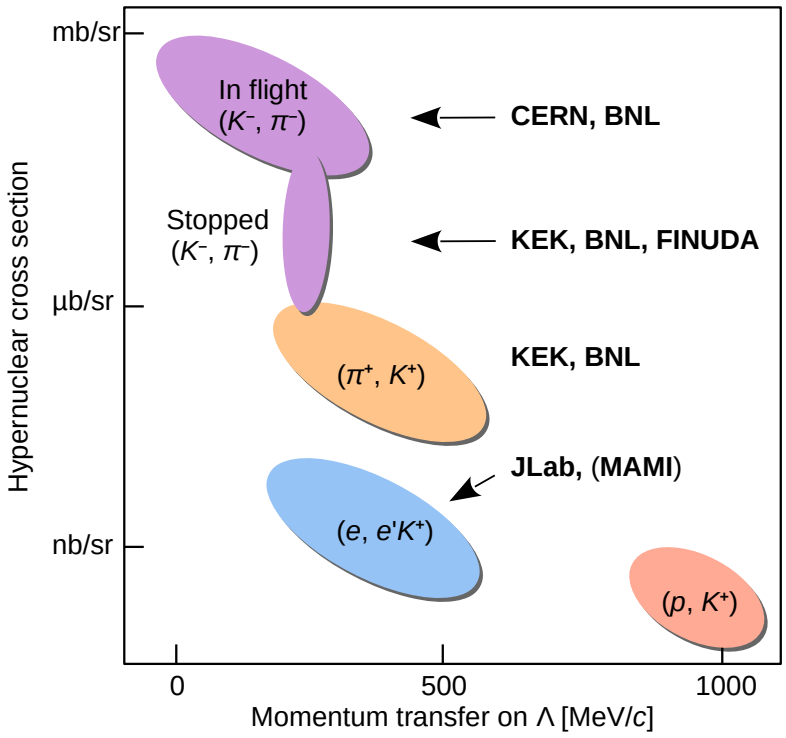

Figure 3.3.: Comparison of several missing mass reactions in terms of cross section and momentum transfer on the hypernucleus. The text labels name the experimental facilities which are associated with these reactions. Adapted from [150], modified and updated.

orders of magnitude smaller than for the experiments with kaon beams. Also the momentum transfer is limited to at least $200\,\mathrm{MeV}/c$, so the binding probability of the Λ to the remaining nucleus is decreased. This reaction still has other advantages which are that a pion beam is easier to produce and handle experimentally so that higher intensities are possible. This compensates for the decreased cross section.
Another critical aspect of this method though is the detection of the emitted kaons. Due to their short lifetime of around $12\,\mathrm{ns}$, their mean flight length $c\tau$ is limited to just $3.7\,\mathrm{m}$. In order to detect most of these kaons before their decay, the flight length in the spectrometer has to be kept as short as possible. At KEK in Japan for example, the Superconducting Kaon Spectrometer (SKS) was developed, which uses extremely large magnetic fields of around $3\,\mathrm{T}$ to allow for a compact spectrometer design. Experiments with this spectrometer were performed mainly in the 1990's and 2000's [149, 168]. Even prior to that, similar experiments were conducted at the AGS of the Brooklyn National Lab (BNL) ranging from the 1970's to the 1990's [208, 241].

3.2.3. The $(e, e'K^+)$ reaction – Strangeness electro-production

The reaction is found at 3. in Figure 3.2. While the quark flow diagram is not too much different from 2. – in both cases an incoming particle induces the production of an $s\bar{s}$ pair – a fundamental difference is given by the fact that a proton is converted into a Λ instead of a neutron. Experimentally the electro-production has two main disadvantages compared to 2., one being the even lower cross section. This can be seen in Figure 3.3, where it is again a factor of 100 lower than for the (π^+, K^+) reaction. Another challenge is given by the amount of final state particles. While for all the other reactions in Figure 3.2 only one outgoing particle needs to be detected in order to compute the missing mass, the electro-production method requires the detection of the

scattered electron in addition. This, again, lowers the detection probability and adds another source of inaccuracies. Despite all these downsides, there is one major advantage, namely the achievable luminosity and precision with electron beams. While for the other reaction types radioactive beams have to be produced and collected at a primary target, electron beams are comparably easy to generate, even in high intensity, purity and brilliance.
The Jefferson Lab (JLab) in the United States was the first facility to successfully produce and detect hypernuclei by using this method in the early 2000's [211, 97]. Here, the dedicated High-resolution Kaon Spectrometer (HKS) was developed and installed so that around the 2010's one was able to determine the binding energies of several light hypernuclei including ${}^{7}_{\Lambda}\mathrm{He}$, ${}^{9}_{\Lambda}\mathrm{Li}$, ${}^{10}_{\Lambda}\mathrm{Be}$ and ${}^{12}_{\Lambda}\mathrm{B}$ [143, 219, 293]. Additionally, excitation energies for the Λ being bound to different energy shells were observed as well [140].
Also at MAMI hypernuclei are produced by the (e, e', K^+) reaction, but in contrast to JLab, the study focuses on their decay products instead of the outgoing particles from the generation process. Therefore, MAMI is going to be described in the section *Decay Pion Spectroscopy* on page 28.

3.2.4. The (K^-, π^+) reaction – Kaon induced double charge exchange

This type of reaction, 1b. in Figure 3.2, combines the strangeness exchange mechanism with an additional charge exchange with another proton inside the nucleus, so that the process reduces the nuclear charge by two units. It hence allows for the study of neutron rich hypernuclei. The downside of this procedure is the even lower production cross section. At FINUDA, one experiment aiming at this goal was performed around 2012. The experimentalists used a ${}^{6}\mathrm{Li}$ target and instead of a π^- in the generation process it was looked for a π^+. The expectation was the production of a heavy hydrogen hyper-isotope,

$$ {}^{6}\mathrm{Li}(K^-, \pi^+){}^{6}_{\Lambda}\mathrm{H}. \tag{3.1} $$

Finally, three events were found [16] which potentially were true ${}^{6}_{\Lambda}\mathrm{H}$ events. However, when the same experiment was repeated at the Japan Proton Accelerator Research Complex (J-PARC), no evidence for ${}^{6}_{\Lambda}\mathrm{H}$ was found [157]. Until today it remains unclear if this hypernucleus is actually bound. Still, with more experiments and higher luminosities, new hyper-isotopes may be explored in the future.

3.2.5. The (π^-, K^+) reaction – Production with double charge exchange

This reaction is found as 2b. in Figure 3.2. It combines the strangeness production reaction of 2. with an additional charge exchange. Analogously to the previously described 1b. reaction, a pp pair is converted to $n\Lambda$, removing two nuclear charges from the hypernucleus. The only experiment to be performed so far is the search for ${}^{10}_{\Lambda}\mathrm{Li}$ in 2005 [265] which did not find any evidence. Similar to 1b., the potential of this method lies in future studies with improved luminosity.

3.3. Decay Spectroscopy

Now, the focus is shifted to the versatile decay spectroscopy approaches. These are in the most cases based on the charged mesonic weak decay of the Λ inside the hypernucleus, $\Lambda \rightarrow p + \pi^-$.

3.3.1. Emulsion and bubble chamber

Both of these methods are based on the same principle, the optical visualization of particle tracks inside a certain medium. While in the first case a material comparable to a film of an analog camera is used, where the particle tracks directly leave discolorations, the second method replaces this medium with a critical helium liquid. A traversing particle would trigger evaporation bubbles along its way which then could be photographed. Since this method did only find limited application in hypernuclear physics, the following description will more focus on the emulsion technique.
After the first observations in the 1950's (compare to Figure 2.4 on page 15), it did not take long until the systematic production and study of hypernuclei began. For example at the Argonne ZGS [311] a K^- beam was used to re-generate events in the previously observed *connected stars* shape. The irradiated emulsion plates (or photos of them) had to be scanned completely by hand so that from hundreds of thousands of samples, a set in the order of thousand hypernuclear events was found until the mid of the 1970's. An example of such an event is found in Figure 3.4. While this particular event was recorded and analysed just a few years ago at J-PARC [267], it nicely depicts the generation and decay of a hypertriton nucleus in the same fashion as in the decades before. It shows an incoming K^- which eventually hits a nucleus of

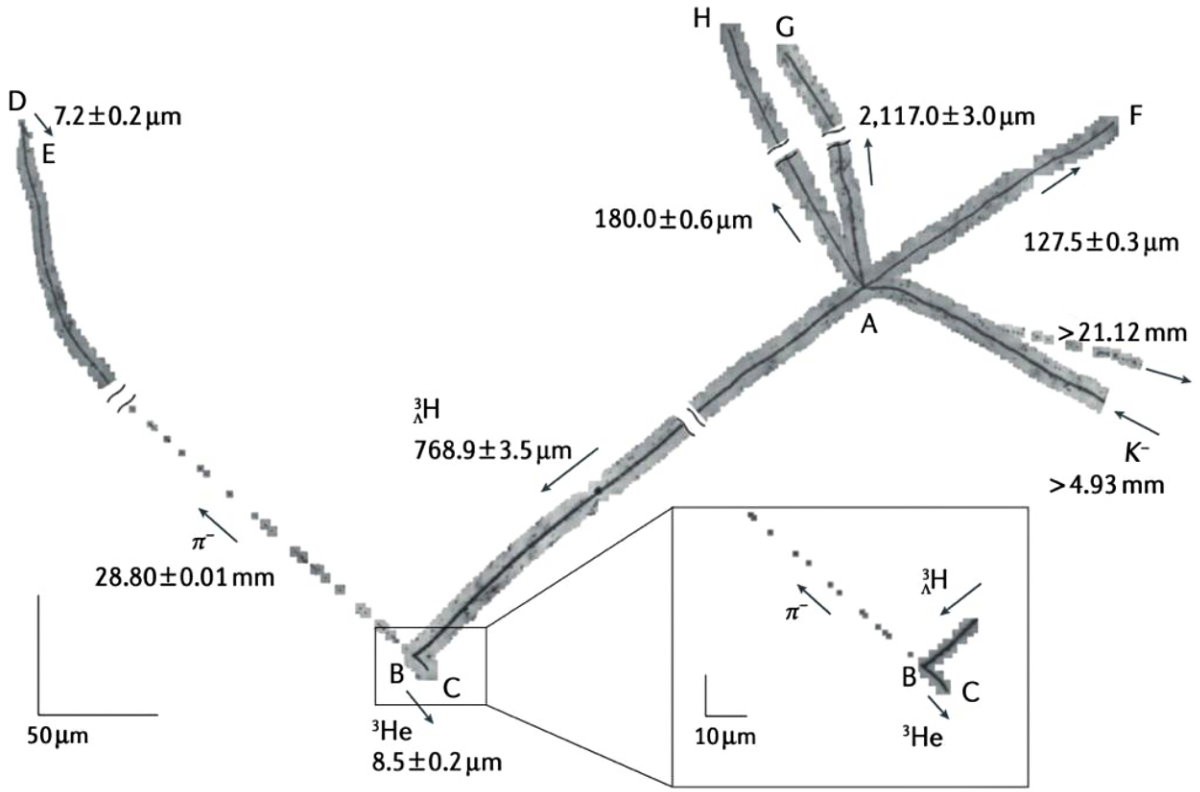

Figure 3.4.: Hypertriton emulsion event taken at J-PARC [267] with generation point A and decay point B.

the emulsion in point A and causes a multi-body fragmentation. While at some point most of the fragments are stopped inside the emulsion, one track is observed to produce a secondary decay at B. By that, the event is almost identical to the first observed hypernuclear events in Figure 2.4. For the evaluation, the challenge is to determine the flight lengths of the fragments inside the emulsion as well as their angle so that the kinematics can be reconstructed. A key element is to know the amount of deposited kinetic energy of every particle along its track as accurately as possible, because then the initial energy of the fragments becomes accessible. Another important aspect is the doubtless identification of the participating isotopes. It is possible by investigating the patterns of energy loss and the restrictions given by the conservation of energy and momentum. Finally, the mass of the hypernucleus m_{hyp} can be determined from the sum of the masses m_i of all decay products and their kinetic energies Q_i,

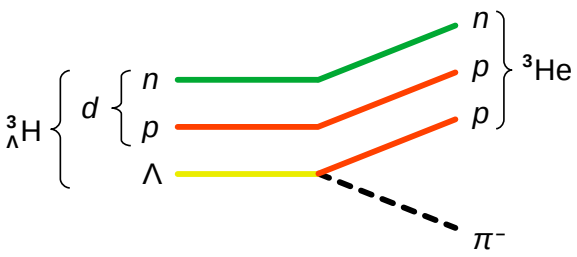

Figure 3.5.: Sketch of a hypertriton two-body decay. The Λ inside the hypernucleus decays into a proton$-\pi^-$ pair, leaving behind a ^{3}He nucleus.

$$m_{\text{hyp}}c^2 = \sum_i m_i c^2 + Q_i. \tag{3.2}$$

From here, the binding energy of the Λ to the non-strange core is given by

$$B_\Lambda = (m_{\text{core}} + m_\Lambda - m_{\text{hyp}})c^2, \tag{3.3}$$

where m_{core} and m_Λ are the masses of the nuclear core in its ground state and the Λ hyperon, respectively. In case of the hypertriton, the lightest known hypernucleus, m_i holds the mass of the pion and the ^{3}He nucleus, while m_{core} is given by the deuteron d, as illustrated in Figure 3.5. Together with the Λ mass, four literature values are needed in total for the final calculation.
Besides the binding energy also the lifetime of the hypernucleus was extracted in early emulsion (and bubble chamber) experiments. By evaluating the kinematics of all particles at point A in Figure 3.4 as well, the initial velocity of the hyperfragment was extracted and by analysing the flight length, also statements about its lifetime were made [174, 177, 54]. These results though were far from the accuracy to be achieved in the binding energy studies.
Until the mid of the 1970's the binding energies of various hyper-isotopes ranging from $^3_\Lambda$H to $^{15}_\Lambda$N were determined by emulsion experiments [165]. While for some of these isotopes they even today remain the only or at least the most accurate source of information, the old data has its particular downsides. Many values have been published without any estimation of their systematic errors, many data resources have gone lost and many involved mass literature values are outdated. Furthermore the averaging techniques are irreproducible from today's view. The method of a truncated mean was frequently used, where iteration-wise outliers were excluded until a consistent set of data remained. For these reasons, new experiments are needed to cross check and verify or even discard the old data. Discussions about a re-calibration of emulsion data [13] are addressed in Chapter 4.3.6 on page 47.

3.3.2. Decay pion spectroscopy

The $(K^-_{\text{stop}}, \pi^-)$ reaction – Kaon induced decay pion spectroscopy

In contrast to the *in flight* method, where the pion from the generation process is studied, the *stopped* (K^-, π^-) spectroscopy focuses more on the decay of the hypernucleus. The method makes use of the fact that the generated hypernucleus is usually stopped inside the target material, so that it is at rest once the Λ decays. Such a decay will – as in the emulsion – most

likely emit another π^-. If the remaining nuclear fragment stays bound together, the decay is of a two-body nature, so that solely the π^- carries all information about the initial hyperfragment. This eliminates the drawbacks of a missing mass study where all in- and outgoing particles are needed to be known precisely. Especially the disadvantages of the kaon beam become irrelevant. Still, the particles from the generation process can be detected in coincidence to act as a background suppression.
Experiments like these where performed at KEK [291], BNL [78, 203, 288] and FINUDA [18, 19]. The FINUDA experiment e.g. operates at the e^+e^- storage ring DAΦNE, where Φ mesons are produced from e^+e^- annihilations. These have a chance of 49% to decay into K^+K^- pairs, so that a secondary K^- beam can be used for experiments at fixed targets. A solenoid magnet spectrometer offers 2π acceptance to detect both pions, the one from the generation process and the decay pion in coincidence. While the first one is expected to carry around $260 - 290\,\mathrm{MeV}/c$, the decay pion is – depending on the hyper-isotope – emitted mono-energetically within the range of $90 - 140\,\mathrm{MeV}/c$. With that technique, the masses of many light hypernuclei were measured successfully.

Electron induced decay pion spectroscopy

This method is based on the strangeness electro-production process, 3. in Figure 3.2 on page 24. Initially, an electron hits a target nucleus and generates an $s\bar{s}$ pair, resulting in the conversion of a proton to a ΛK^+ pair. But also here, similar to the previously described K_{stop} method, only the precise spectroscopy of the later emitted decay pion is sufficient to gain information about the mass and binding energy of the hypernucleus. In addition, the detection of the K^+ in coincidence with the decay pion can acts as tag for strangeness production events to suppress other background.
Experiments like these are performed at the Mainz Microtron MAMI since 2012. Here, the dedicated kaon spectrometer KAOS is used for the detection of kaons in forward direction. Additionally, the magnetic spectrometers of the A1 Collaboration are utilized to observe the momentum of the decay pions. The data taking campaigns of the past resulted in a successful binding energy measurement of the light hypernucleus ${}^{4}_{\Lambda}\mathrm{H}$. A more detailed description of the reaction mechanism is found in Chapter 7.1 on page 81 while additional information about the experimental results are provided in Chapter 7.2 on page 83.
The new experiment at A1 which was prepared and conducted within the scope of this thesis aims to determine the binding energy of the even lighter ${}^{3}_{\Lambda}\mathrm{H}$. More information about a new target system, the conception of the measurement and the actual data taking is found in the Chapters 8 and 9.

3.3.3. Heavy ion collision

So far, all experimental methods had in common that a target nucleus was transformed into a hypernucleus during a strangeness production or exchange reaction by an incoming particle. This is not the case in heavy ion collisions. Instead of single particles, whole nuclei (*heavy ions*) are accelerated and brought to collision with either a target or another accelerated ion. The reactions to be expected there are much more violent due to a higher center of mass energy compared to the other approaches. A pictorial view of such a reaction is given in Figure 3.6 [297]. On the left side, two rapidly approaching ions are illustrated. The character of the collision will mainly be determined by the impact parameter b. Depending on b, only some of the nucleons in the ions will take part at the collision, the *participants*, while some others may stay mostly unaffected, the *spectators.* Both of these groups offer unique ways to study hypernuclei, as discussed in the following.

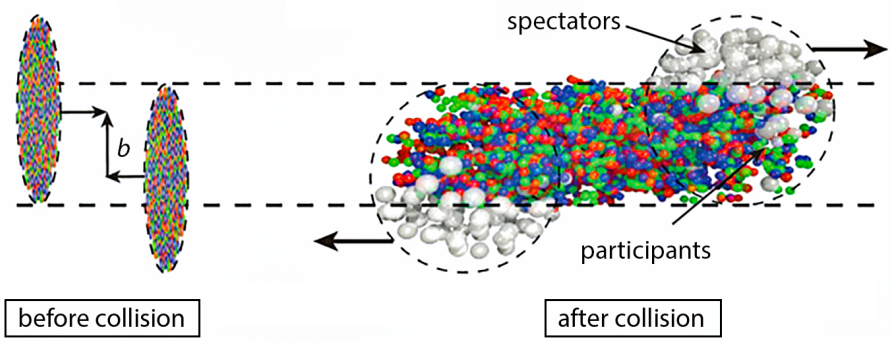

Figure 3.6.: Pictorial view of a collision of two relativistic heavy ions [297] (modified). **Left:** two ions before the collision with impact parameter b. **Right:** after the collision the spectator nucleons remain mostly unaffected while particle production takes place in the participant zone.

Central collisions

This approach focuses on the study of the hot participant zone. In this phase space region many particles are created including kaons and hyperons. The latter can form hypernuclei by the combination with other nucleons. This procedure is often modeled by a coalescence process. Figure 3.7 shows an invariant yield spectrum obtained by gold-lead and gold-platinum collisions in dependence of the mass number A of the produced fragments [284, 32]. The data (black) is compared to two theoretical models, one only including regular nucleons (red) and the other including hyperons (green). It is observed that model and data are in a good qualitative agreement, all showing the same tendency of a strong decline towards higher fragment mass numbers. In fact, from all three sources a penalty factor of roughly 50 for every added nucleon was extracted for the yield. For this reason, the central collision method is best suited for the study of light hypernuclei.

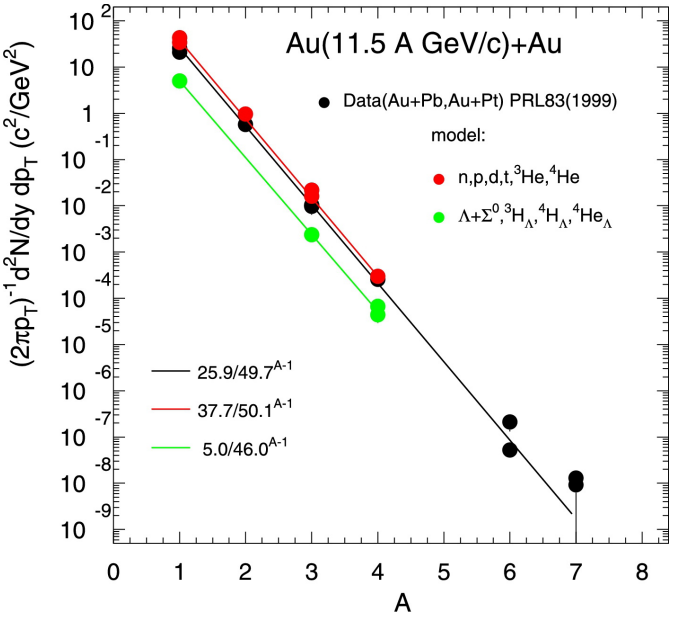

Figure 3.7.: Mass dependence of the invariant yields of light fragments and hyperfragments predicted for central Au + Au collisions at $11.5\,A\,\mathrm{GeV}/c$ [284]. The black dots represent experimental data for Au + Pb collisions [32]. The lines are empirical interpolations of the results.

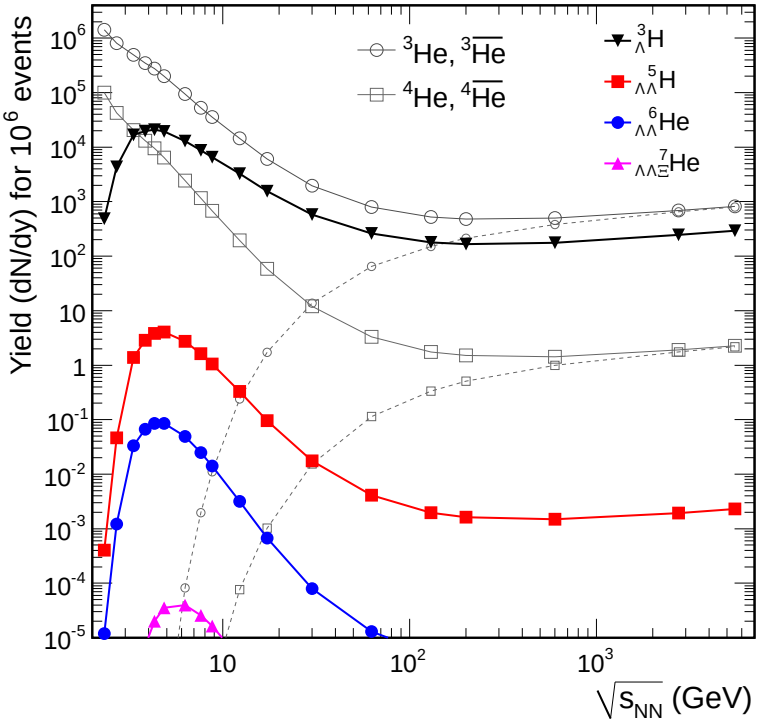

Figure 3.8.: Predicted yields for the production of hypernuclei in central collisions dependent on the center of mass energy [30]. The yields of the ^{3}He and ^{4}He nuclei are included for comparison, along with the corresponding anti-nucleus (small symbols and dashed lines).

This trend is also confirmed by the statistical model calculations shown in Figure 3.8, where the yields of various (hyper)-fragments are plotted in dependence of the center of mass energy [30]. In black, the appearance of the hypertriton is shown. Compared to other heavier hyper-isotopes, its yield tops them by many orders of magnitude. For comparison, also two non-strange isotopes are plotted, ^{3}He and ^{4}He. To the $A = 3$ nucleus, the hypertriton yield is quite similar, especially in the high energy region. Its yield suffers only from a small penalty, roughly a factor of three, given by the likelihood of producing a hyperon. The hypertriton still strongly dominates the production of ^{4}He, which is suppressed even more by the mass number penalty (compare to Figure 3.7). The figure also illustrates the transition from the rather peripheral collisions to the pure central collisions. The peripheral behavior is found for low energies. Here, a peak structure for the hyper-isotopes is observed, due to the fact that a certain threshold energy is required for the generation of hyperons. The helium isotopes in contrast can also result from collisions at even lower energies. With rising $\sqrt{s}$, all yields are observed to decline, due to a more violent fragmentation of the nuclei. This decline is compensated by the more and more occurring generation of new nucleons and hyperons together with their anti-particles, so that the yields converge to an almost straight line, which slowly increases with $\sqrt{s}$.
Experiments in the high energy region were already performed in the 2010's by the ALICE Collaboration at the LHC as well as the STAR Collaboration at BNL. Both of these two experiments are able to perform a unified lifetime and binding energy study. It was the STAR Collaboration to extract the first lifetime value for hypertriton from gold-gold collisions in 2010 [6], soon to be followed by enhanced studies with larger data sets [14, 5]. By 2020, the first binding energy measurement was published [13].
Since 2016 also the ALICE Collaboration provides experimental information about the hypertriton by studying lead-lead central collisions with large center of mass energies $\sqrt{s_{NN}} = 5.5\,\text{TeV}$.

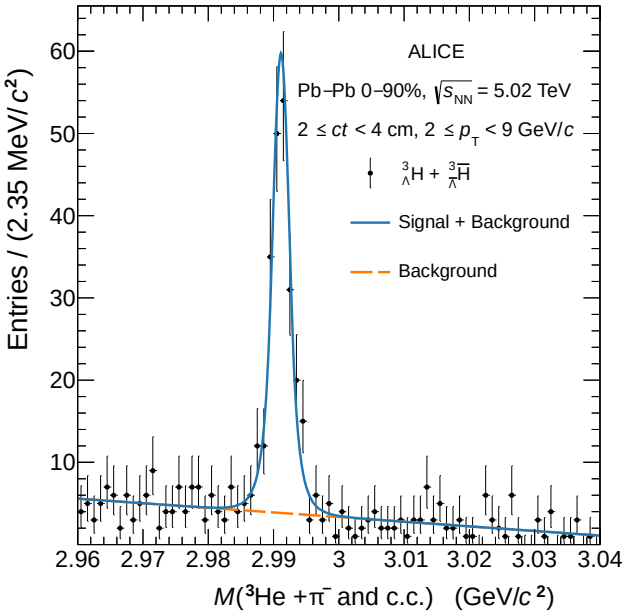

Figure 3.9.: Hypertriton and anti-hypertriton events observed by the ALICE Collaboration in the recent evaluation of Pb+Pb collisions at LHC from 2022 [24].

While in the recent years mainly the lifetime could be extracted [12, 8], a new data set from 2018 offered the identification of roughly 200 hypertriton and anti-hypertriton events in a mass spectrum, shown in Figure 3.9 [24].

Peripheral collisions

This method focuses on the detection of the spectator nucleons, which can form a new isotope after the impact. Other than in the hot participant zone, the spectators are only moderately excited. Here, hyperons are not produced by primary collisions but rather by the re-scattering of strange hadrons emerging from the participant zone [65, 64]. This process can be described by transport models, as shown in the left of Figure 3.10. The figure shows the predicted spatial coordinates, in which Λ hyperons are absorbed by other nucleons [65]. This is possible, if the momentum with respect to one of the spectator nucleons is sufficiently low. For the result in the figure, A. Botvina simulated 2×10^4 Au + Au collisions with $20\,A\,\mathrm{GeV}$ at an impact parameter of $8.5\,\mathrm{fm}$. As can be seen, the major amount of absorptions is caused by the scattering of hyperons with other nucleons (blue dots). At the same time, direct nucleon nucleon and pion-nucleon reactions (red circles and red dots) play a comparably minor role, since in these cases, the kinetic energy of the resulting hyperons is too high. The same reason causes the suppression of absorptions in the hot participant region in the center. Here, also the nucleons possess a very high kinetic energy, so that generally fewer absorptions are found.
The yields of these spectator hyperfragments can be described by a statistical multi-fragmentation model [122, 66, 55], which was extended for systems including hyperons around 10 years ago [62, 198]. In peripheral collisions, hypernuclei with larger mass numbers are not necessarily suppressed like in the coalescence process found in central collisions (compare to Figure 3.7). This model also was utilized for the design of the new target system for the hypertriton experiment of this thesis. More details are found in Chapter 8.1 on page 91.
In the right of Figure 3.10, the yields of $^3_\Lambda\mathrm{H}$ and $^4_\Lambda\mathrm{H}$ are compared depending on their rapidity [60]. A high rapidity indicates the appearance of these hyper-isotopes inside the projectile

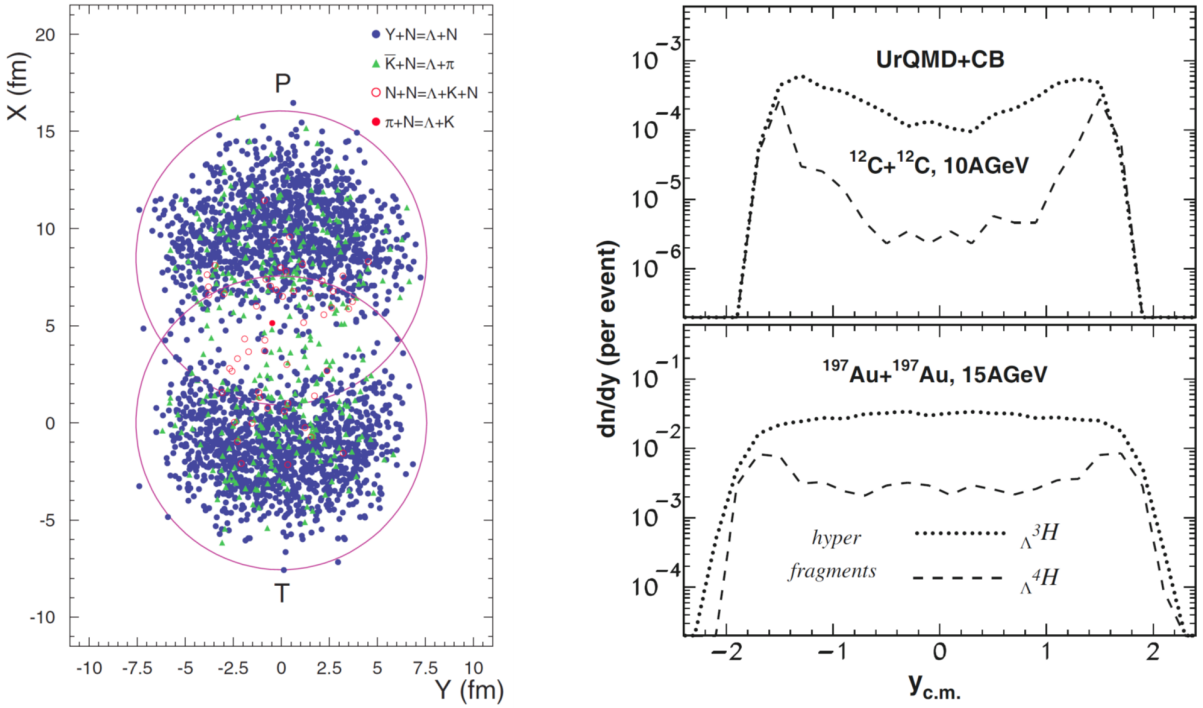

Figure 3.10.: Production of hyperfragments in heavy ion collisions. **Left:** spatial distribution of points, where a Λ is bound to other nucleons. This was simulated with the Dubna cascade model for Au + Au collisions at $20\,A\,\mathrm{GeV}$ with an impact parameter of $8.5\,\mathrm{fm}$ [65]. The circles P and T mark the outer shapes of the projectile and target nuclei. The processes of creating the absorbed hyperon, such as interactions of secondary hyperons, antikaons, nucleons, and pions with nucleons, are indicated by different symbols. **Right:** rapidity distribution of ${}^{3}_{\Lambda}\mathrm{H}$ and ${}^{4}_{\Lambda}\mathrm{H}$ hyperfragments (dotted and dashed lines respectively) in symmetric carbon and gold collisions, averaged over all impact parameters [60].

nucleus, a negative rapidity in the target nucleus and in the region around zero – the so called mid-rapidity – the coalescence is found. As can be seen, the formation of ${}^{4}_{\Lambda}\mathrm{H}$ is strongly reduced with respect to ${}^{3}_{\Lambda}\mathrm{H}$ at mid-rapidity, while at projectile or target rapidity similar yields are expected for both isotopes. Another advantage of the hypernucleus production in the peripheral region is, that exotic hypernuclei can be generated by the use of extreme projectile nuclei. For example, beams of unstable nuclei with oddly high neutron numbers could stimulate the production of neutron rich hyper-isotopes such as ${}^{6}_{\Lambda}\mathrm{H}$ [59].
Experiments studying the peripheral region have been performed for example by the HypHI Collaboration at the GSI, Darmstadt. Here, ${}^{6}\mathrm{Li}$ ions with an energy of $2\,A\,\mathrm{GeV}$ were sent on a carbon target and hypernuclei could be detected by the observation of their decay pions in a magnetic spectrometer. In addition, a segmented detectors close to the target allowed for a good vertex reconstruction. In that fashion, combined lifetime- and binding energy measurements could be performed for the light isotopes ${}^{3}_{\Lambda}\mathrm{H}$ and ${}^{4}_{\Lambda}\mathrm{H}$ [255, 254].

3.3.4. Gamma ray studies

Another unique method of studying hypernuclei are the observation of gamma rays. These can be emitted during the de-excitation process of newly generated hypernuclei. With germanium detectors, an excellent resolution of single keV can be achieved. Missing mass experiments in contrast usually deliver an accuracy in the order of $100\,\mathrm{keV}$.
In the recent years, precision gamma-ray spectroscopy has been successfully performed for p-shell Λ hypernuclei at the KEK PS and at the BNL AGS with the use of the germanium detector array Hyperball. An example of these observations is given in Figure 4.1 on page 39, where excited states of ${}^{4}_{\Lambda}\mathrm{H}$ and ${}^{4}_{\Lambda}\mathrm{He}$ [305] are shown and compared.

3.4. Summary

With all these available experimental techniques a versatile set of data about various hypernuclei was already obtained. By focusing on the binding energy of light hyper-isotopes, an overview about the data situation is found in Figure 3.11 in form of a hypernuclear chart. It shows all hyper-isotopes ranging from a single Λ up to heavy carbon hypernuclei. Analogously to a regular nuclear chart, the nuclei are sorted by their neutron number on the x axis and their proton number on the y axis. Isotopes in gray have been observed experimentally without any doubt, while the white ones still remain hypothetical. The isotopes inside the black frame have already been observed by the first era emulsion experiments. In addition, the color code around the element name indicates if it was studied with other experimental approaches as well, as described in the legend. Bold colors were used if such an experiment was already performed, while pale colors emphasize the possibility. In general, the previously described experimental methods can be grouped into sub-categories, depending on whether a neutron or a proton is converted to a Λ or even the double charge exchange $pp \rightarrow n\Lambda$. These reactions offer different possibilities for the generation of hypernuclei off a stable target nucleus. For example, a ${}^{12}\mathrm{C}$

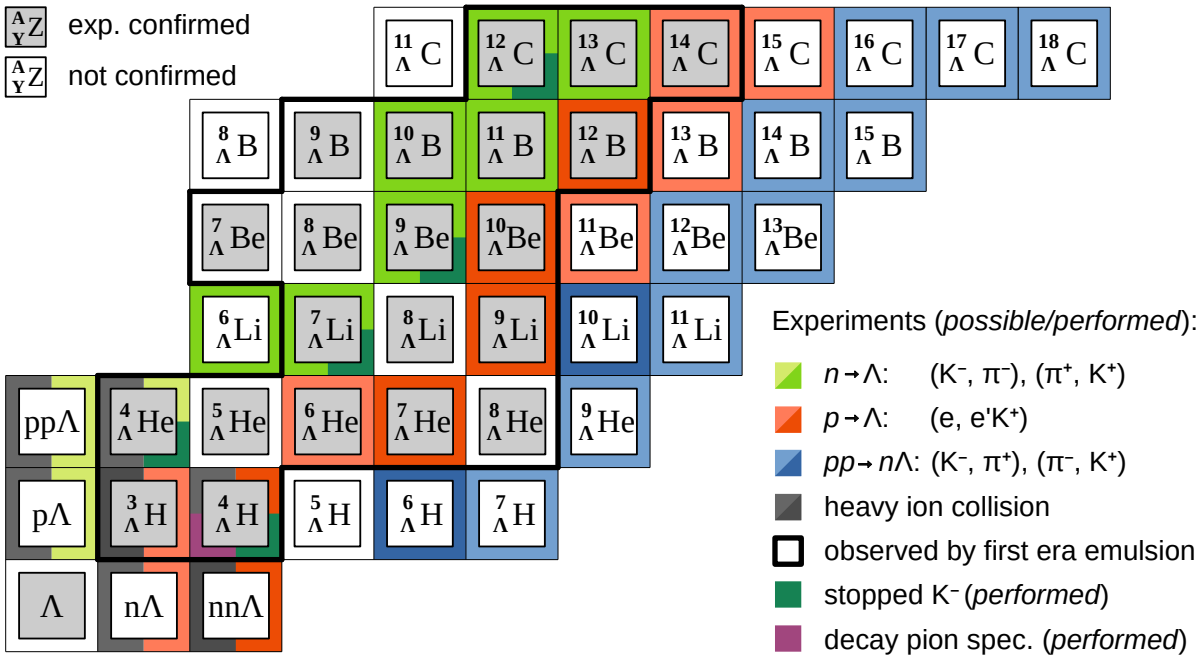

Figure 3.11.: Overview about the data situation regarding binding energies of light Λ hypernuclei and further experimental possibilities.

target would offer to study ${}^{12}_{\Lambda}\mathrm{C}$ via an $n \to \Lambda$ reaction, ${}^{12}_{\Lambda}\mathrm{B}$ via a $p \to \Lambda$ reaction and ${}^{12}_{\Lambda}\mathrm{Be}$ via the double charge exchange. By evaluating the available target nuclei, a wide coverage in the colors green, red and blue is observed. However, some hyper-isotopes remain impossible to study by these methods, such as the isobars with mass number 5 and 8. The available experimental information about them still is solely given by the first era emulsion.
For small hypernuclei, the heavy ion central collisions are able to contribute data as well, indicated as dark gray. So far however, the hypertriton was the only isotope for which reliable binding energy data could be delivered so far. Still, these are not the only possible experimental techniques. The stopped K^- approach as well as other decay pion spectroscopy methods open the possibility to study hypernuclei more independently of the initial target nucleus – during the fragmentation process mentioned in Chapter 3.1 on page 21, several nucleons may be emitted from the hypernucleus, so that a completely new isotope is created. The same holds for the peripheral collisions. As a consequence, only the actually performed experiments are shown in the figure.
One observation is, that until today, the old emulsion experiments play a very prominent role in the present binding energy data situation. There is not a single hyper-isotope, which was newly discovered after the emulsion era, despite several experimental efforts, e.g. for ${}^{10}_{\Lambda}\mathrm{Li}$ and ${}^{6}_{\Lambda}\mathrm{H}$. While these two require a relatively rare double charge exchange reaction, other heavier hypernuclei might still be accessible by the $p \to \Lambda$ methods.
Another interesting region is to be found at mass number 2 and 3. While hypertriton is known as the simplest bound hypernucleus, the existence of similar $A = 3$ and even smaller systems is still not entirely excluded. Various experimental approaches would allow for deeper studies. A more detailed discussion about these isotopes is going to follow in Chapter 5.1 on page 55. Indeed, there are various experiments proposed around the globe, not only to study characteristics of Λ hypernuclei but also the even more exotic double Λ hypernuclei and more. These are going to be summarized in the following section.

3.5. Ongoing and Planned Experiments

An overview about the experiments to be performed in the following 5 years is given by the world map in Figure 3.12 [247]. Several facilities around America, Europe and Asia are going to conduct new studies around the subject of hypernuclei. Besides the previously described experimental approaches – found here as the points 1., 2., 3. and 4. – there are further activities at several facilities which involve the study of final state interaction, also known as femtoscopy $(5.)$ as well as scattering experiments with hyperons $(6.)$. These are also mentioned for the sake of completeness, but go beyond the scope of this discussion. More information is found in [169, 238]. In the following, the experiments with the methods 1. to 4. are going to be introduced briefly. Some experiments involving the hypertriton will be discussed in deeper detail later on in Chapter 5.4 on page 66.

STAR at RHIC

The STAR Collaboration intends to perform a new fixed target study (STAR-FXT), where energies of $\sqrt{s_{NN}} = 2.9 - 5.3\,A\,\mathrm{GeV}$ are to be covered. In this region, the production of hypernuclei is expected to be maximal for central collisions, as shown before in Figure 3.8 [30]. This is expected to increase the number of observed hypertritons by more than one order of magnitude compared to the previous studies at $7 - 200\,A\,\mathrm{GeV}$ [14], bringing the detailed study of $A = 4$ hypernuclei within reach. Furthermore, yet unknown systems like the double hypernucleus ${}^{4}_{\Lambda\Lambda}\mathrm{H}$ could be discovered – if bound.

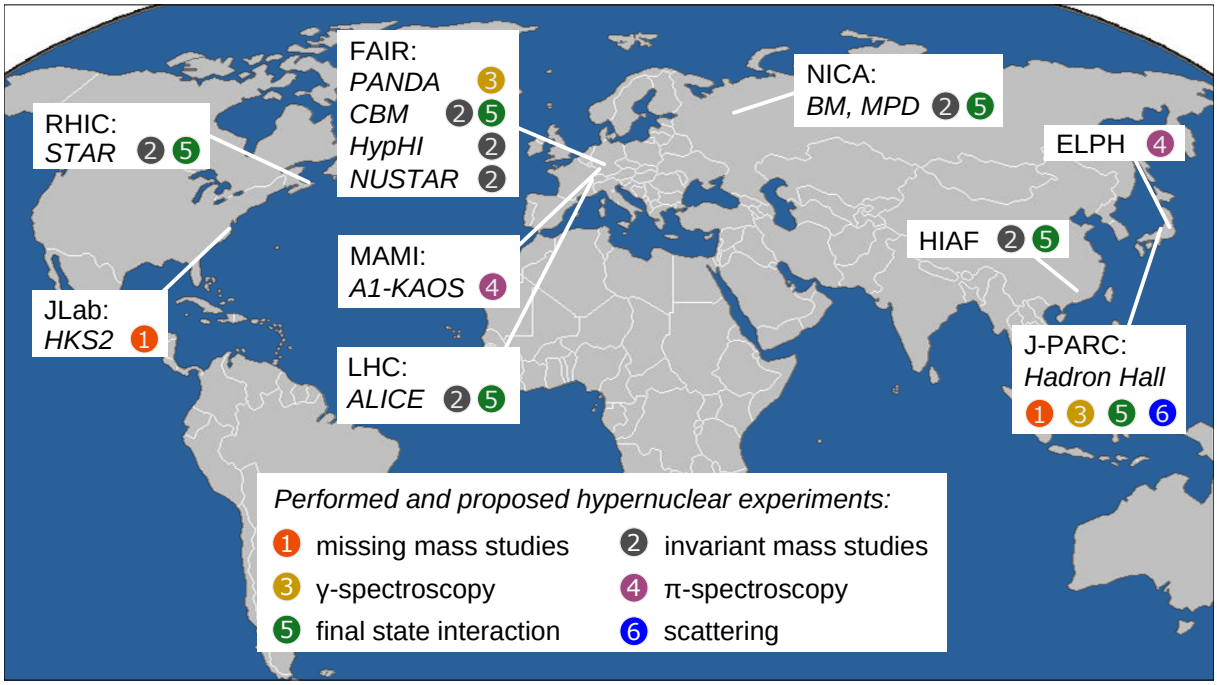

Figure 3.12.: Global map of planned or already operational facilities studying properties of hypernuclei [247] (modified).

HKS2 at JLab

A new measurement of the hypertriton mass with an accuracy of less than $100\,\mathrm{keV}$ has been proposed at JLab Hall A [141]. The experiment will make use of the missing-mass technique via the $(e, e'K^+)$ reaction with a $4.2\,\mathrm{GeV}$ electron beam. The binding energy is reconstructed from the scattered electron and the K^+, both detected in the High Resolution Spectrometer (HRS) and the High resolution Kaon Spectrometer (HKS) respectively. While the hypertriton is foreseen to be produced off a $^3\mathrm{He}$ target, ${}^4_\Lambda\mathrm{H}$ is also to be studied at $^4\mathrm{He}$. In addition, heavier calcium and lead targets are going to be utilized as well.

FAIR

The Facility for Antiproton and Ion Research (FAIR) in Darmstadt, Germany is currently under construction and will supply many new hypernuclear experiments:

- The PANDA experiment [232] aims for the study of double hypernuclei. Their production is going to be achieved by the absorption of Ξ hyperons in nuclear matter so that after their decay $\Xi p \to \Lambda\Lambda$ double hypernuclei are created. Emitted gamma rays during the absorption process are observed via the dedicated Germanium detector PanGeA to provide yet unrivaled information on the structure of double Λ hypernuclei. Furthermore, PANDA is going to study X-rays from heavy hyperatoms [283] as well as the exclusive production of hyperon-antihyperon pairs close to their production threshold in $\bar{p}$-nucleus collisions.

- The Compressed Baryonic Matter experiment CBM [73] will focus on versatile nuclear studies with the new CBM detector. Together with high luminosities and extreme trigger rates it can access rare events such as multi-strange hyperons and hypernuclei with high statistics. So besides single Λ hypernuclei, the CBM Collaboration expects to measure about 3000 ${}^5_{\Lambda\Lambda}\mathrm{H}$ and 60 ${}^6_{\Lambda\Lambda}\mathrm{He}$ per week.

- The HypHI Collaboration [269, 255, 256, 257] continues the exploration of hypernuclei in peripheral collision reactions at the fragment separator Super-FRS. Using the excellent momentum resolution of the Super-FRS beam line, they aim at a significant improvement of the invariant mass resolution. This will allow to address the question of the existence of a neutral $nn\Lambda$ system for which a hint was already observed before by HypHI in 2013 [257], see Figure 5.3 on page 57. New data was already taken in early 2022 and the analysis is ongoing. It will also deliver new lifetime information about the light isotopes ${}^{3}_{\Lambda}\mathrm{H}$ and ${}^{4}_{\Lambda}\mathrm{H}$ [112].
- In addition, a unique experiment to probe the Λ halo of ${}^{3}_{\Lambda}\mathrm{H}$ has been proposed by Obertelli *et al.* [23] at NUSTAR. The experiment will be performed at the R3B spectrometer. More information about hypertriton's halo character is found in Chapter 5.3.1 on page 63 followed by a detailed description of this experiment in Chapter 5.4.3 on page 67.

ALICE at LHC

During the LHC Run3 and Run4 in the upcoming years, ALICE will again record the results of high energetic heavy ion central collisions and increase the data sets by a factor of larger than 50. This will allow for more precise mass and lifetime measurements for the lightest hypernuclei. Also information about the hypertriton decay channels is expected to be obtained [24]. Since at the energies ALICE uses, the formation probability of heavier hypernuclear systems like ${}^{4}_{\Lambda}\mathrm{H}$ or ${}^{4}_{\Lambda\Lambda}\mathrm{H}$ is expected to be at least two orders of magnitude below the ${}^{3}_{\Lambda}\mathrm{H}$ production, their observation is still questionable.

NICA

NICA is a heavy ion accelerator at Dubna, Russia, which is going to be used for two different hypernuclear experiments:

- The fixed target experiment for studies of Baryonic Matter (BM) will perform heavy ion reactions in the beam energy range corresponding to $\sqrt{s_{NN}} = 2 - 6\,A\,\mathrm{GeV}$ [172, 286]. About 900 hypertritons will be reconstructed within a run time of one month. In contrast to ALICE, this experiment can also detect fragments at beam rapidity with good acceptance, making it a well suited tool to study hypernuclei in peripheral collisions at rather high energy. That way, also heavier hypernuclei become accessible.
- The Multi Purpose Detector MPD is a 4π detector which will observe heavy ion collisions in the region of $\sqrt{s_{NN}} = 4 - 11\,A\,\mathrm{GeV}$ [282, 307, 277, 7]. For example, at $\sqrt{s_{NN}} = 5\,A\,\mathrm{GeV}$ about 120 ${}^{3}_{\Lambda}\mathrm{H}$ events are expected to be reconstructed in 1 million central Au+Au collisions, corresponding to about 1 h of run time [307, 182, 160]. Assuming a similar reconstruction efficiency as for the hypertriton, a few ${}^{5}_{\Lambda\Lambda}\mathrm{H}$ events may be reconstructed per week. Depending on the amount of background, this double hypernucleus could be detectable in a long period of running.

Both experiments were planned to be committed in late 2022 and their evaluation is yet to be performed.

HIAF

The so called booster ring is currently under construction [312] at the High Intensity heavy-ion Accelerator Facility in Huizhou, China. Its scientific program involves the investigation of light hypernuclei in collisions of ${}^{20}\mathrm{Ne}$ + ${}^{12}\mathrm{C}$ at a projectile energy of $4.25\,A\,\mathrm{GeV}$, and later studies shall also involve hypernuclei with double strangeness [121].

ELPH

This experiment at the Tohoku University, Japan, plans to utilize a photon beam to produce ${}^{3}_{\Lambda}\mathrm{H}$ off a ${}^{3}\mathrm{He}$ target [216] and to determine its lifetime via a start-stop measurement. As a proof of principle, the collaborations plans to measure the free Λ lifetime in a pilot run at first [214]. More information about the experiment is provided in Chapter 5.4.2 on page 67.

Hadron Hall at J-PARC

- The P73/P77 Collaboration at J-PARC plans to measure the ${}^{3}_{\Lambda}\mathrm{H}$ lifetime with a K^{-} beam [21, 22]. The lifetime is going to be determined event-wise by the time difference between the incoming kaon and the detected decay pion of ${}^{3}_{\Lambda}\mathrm{H}$. In a pilot run [22] the decay of ${}^{4}_{\Lambda}\mathrm{H}$ was already studied to demonstrate the feasibility of this measurement. In 2022, a preliminary value of $190 \pm 8\,\mathrm{ps}$ (stat.) was announced for ${}^{4}_{\Lambda}\mathrm{H}$, but with yet unknown systematic errors [200].
- Another aspect of the Extension Project at J-PARC is focusing on γ-ray spectroscopy of hypernuclei at the K1.1 beam line [306]. A high resolution Germanium detector array can then be used to search for γ-ray transitions especially for ${}^{3}_{\Lambda}\mathrm{H}$, in case an excited state of the hypertriton is bound.
- Furthermore, the J-PARC E07 Collaboration plans to analyse hypertriton decays in emulsion plates. Using Monte Carlo simulations and machine learning techniques, the statistical and systematic errors for the hypertriton binding energy has been estimated to be approximately $30\,\mathrm{keV}$ each [191, 218, 267].

4. Systematic Averaging of Hypernuclear Data

4.1. Motivation

The field of hypernuclear physics is a multi-faceted topic and has already been studied for more than 70 years, as mentioned before in Chapter 2.3 on page 15. Still today, the influence of more than half a century old data is strongly present for many hypernuclei despite several new experiments which have been performed since then. So far, a unified basis, where all this data is stored and averaged – similar to the PDG – was nonexistent. This circumstance was addressed in this thesis, to answer the following questions:

- What is the complete set of available data?
- Can an average be determined reliably? If yes, how?
- How is old data to be treated? Should a re-calibration due to outdated particles masses be performed (see Figure 2.2 on page 12)?
- What is to be done about missing systematic errors?

Especially for subtle effects, an accurate determination of the best value for a physical quantity is crucial. One example is the charge symmetry breaking within the binding energy of the $A = 4$ systems ${}^{4}_{\Lambda}\mathrm{H}$ and ${}^{4}_{\Lambda}\mathrm{He}$. The reported binding energy values scatter for the first hypernucleus between 2.04 and $2.35\,\mathrm{MeV}$, while for the latter between 2.20 and $2.44\,\mathrm{MeV}$, so that their difference does not appear obviously. Only after the averaging process, which is going to be presented in the following, their binding energies could be separated to be

$$\overline{B}_{\Lambda}({}^{4}_{\Lambda}\mathrm{H}) = 2.169 \pm 0.042\,\mathrm{MeV} \tag{4.1}$$

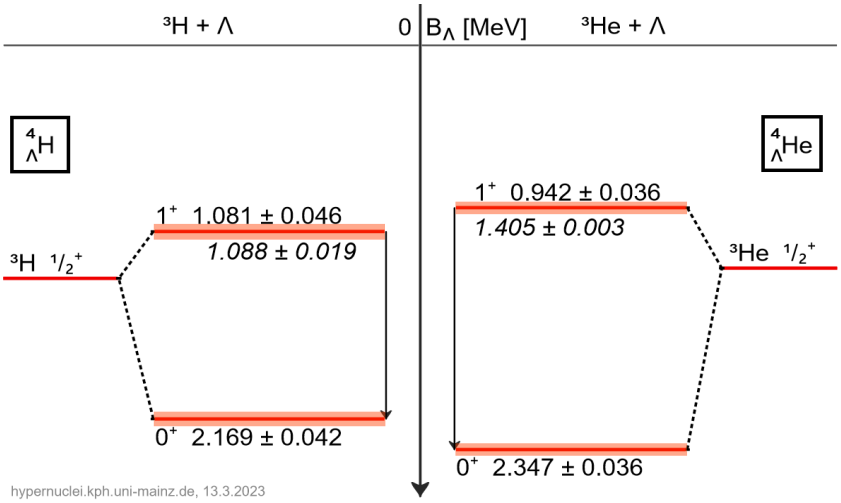

Figure 4.1.: Energy level scheme for ${}^{4}_{\Lambda}\mathrm{H}$ in comparison with ${}^{4}_{\Lambda}\mathrm{He}$ [101]. On the y axis, the Λ binding energy is found. From bottom to top the different states of the two hypernuclei are shown, starting with the ground state binding energy. For the following levels, also the γ transition energy is displayed in italic characters.

and

$$\overline{B}_\Lambda({}^4_\Lambda\mathrm{He}) = 2.347 \pm 0.036\,\mathrm{MeV}. \tag{4.2}$$

These values differ by more than $4\,\sigma$, so that the charge symmetry breaking effect is truly noticeable. The result is depicted in Figure 4.1. Here, not only the ground state of ${}^4_\Lambda\mathrm{H}$ and ${}^4_\Lambda\mathrm{He}$ is shown, but also their respective 1^+ excited states. As one can see, the binding energy of these states differs even less from each other, only $140\,\mathrm{keV}$. But still, after the evaluation a difference of around $3\,\sigma$ was found.
In the following, the whole framework behind the averaging of hypernuclear data will be described. The data situation of the hypertriton is – with the help of the presented averaging techniques – going to be examined in Chapter 5.2 on page 58.

4.2. Introduction to the Chart of Hypernuclides

Now, that many facets of hypernuclear physics were introduced, it is time to take a closer look at the *Chart of Hypernuclides*, one of the core components of this thesis. The goal of this project is to create a unified basis, where all experimental information about hypernuclei is to be stored and averaged. By that, the discussions about single data points and their treatment, as they were performed frequently in the past, may come to an end. The chart combines three core components:

- **The database** – a frame structure to store relevant information about measurements in a unified fashion
- **The averaging techniques** – reliable methods of computing average values and automated application of additional data treatment
- **The website** – a user interface for a maximized accessibility around the world with visualization and assessment of the available data

The website is currently hosted by the Institute for Nuclear Physics, Mainz and is found at `https://hypernuclei.kph.uni-mainz.de`. A screenshot of the website's user interface is seen at Figure 4.2. Here, four main elements are seen. The top left box offers an overview about the available hypernuclei in form of a hypernuclear chart. Once, a hypernucleus is selected there, a table about its properties is opened at the bottom. In this case, ${}^4_\Lambda\mathrm{H}$ was selected, so that in the middle box some general information about the components of this hyper-isotope is displayed. The table rows can also be opened to provide more information about the hypernucleus' properties. If one does so, an ideogram of the clicked data will be shown in the top right box. It illustrates the present data situation.

An in-depth explanation of the whole *Chart of Hypernuclides* project is found in the appendix in **Chapter A**, starting from page 123. This includes a detailed description of the user interface and all its characteristics in **A.1** and additional thoughts about the ideograms in **A.2**. Also the database structure is to be found in **A.3**. Here, the underlying framework in which measurements are stored is listed and described. Finally, all branching ratio results are found in **A.4**.
The remaining core component is the computation of average values and the further data treatment techniques. These are going to be discussed in the following Section **4.3**. They have already been published in [111]. The results obtained with the *Chart of Hypernuclides* about lifetimes and binding energies are provided in **4.4**. Finally, a detailed discussion about the lifetime and binding energy situation of ${}^4_\Lambda\mathrm{H}$ is found in **4.5**.

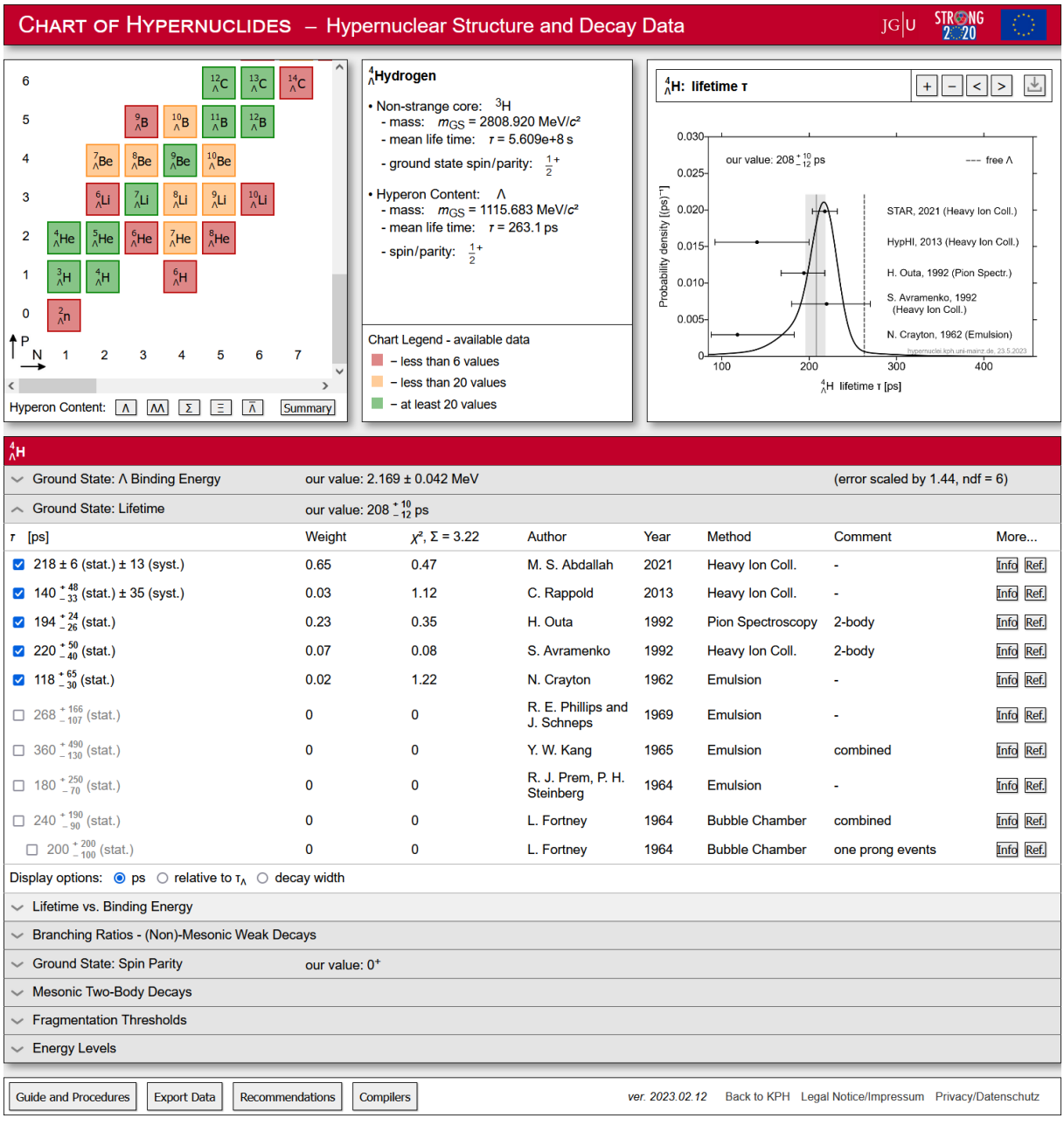

Figure 4.2.: Screenshot of the *Chart of Hypernuclides* website [101]. The lifetime of ${}^{4}_{\Lambda}\mathrm{H}$ was selected.

4.3. Computation of Averages

4.3.1. Nomenclature

At first, a data point with a mean value and errors of statistical and systematic nature will be named as

$$\mu \pm \sigma_{\text{stat}} \pm \sigma_{\text{syst}}. \tag{4.3}$$

Thereby it is possible for a value to have the systematic error consisting from several sources. These are added in squares to form the overall systematic error,

$$\sigma_{\text{syst}} = \sqrt{\sigma_{\text{syst1}}^2 + \sigma_{\text{syst2}}^2 + \dots}\,. \tag{4.4}$$

Since for the calculation of averages the differentiation between statistical and systematic errors is not of any meaning anymore, they both are added as well to form the total error

$$\sigma = \sqrt{\sigma_{\text{stat}}^2 + \sigma_{\text{syst}}^2}. \tag{4.5}$$

If this is applied to a whole set of data which is to be averaged, one ends up with N measurements, each with

$$\mu_i \pm \sigma_i. \tag{4.6}$$

This will be the starting point for the following discussion about ways to average data and how it is finally done in the *Chart of Hypernuclides*.

4.3.2. The arithmetic mean

The simplest form of averaging is the arithmetic mean. All values contribute equally, so that the formula for a mean value $\bar{x}$ simply reads

$$\bar{x} = \frac{1}{N} \sum_{i=0}^{N} \mu_i. \tag{4.7}$$

While being applicable in many situations, it is not suited for the purpose of evaluating averages inside the chart, since the aspect of varying accuracy σ_i is completely ignored.

4.3.3. The error weighted mean

This method includes the errors σ_i of the data points into the averaging procedure. The idea is to assign a weight w to every measurement. The smaller the error is, the larger shall be the resulting weight of this measurement. A widely used approach is the following,

$$w_i = \frac{1}{\sigma_i^2}. \tag{4.8}$$

These weights then can be normalized so that their sum adds up to one,

$$w_i' = \frac{w_i}{\sum_j w_j}. \tag{4.9}$$

From here, the average value is calculated quite analogously to the arithmetic method from (4.7). Each value gets multiplied by its weight and the resulting sum is the average,

$$\bar{x} = \sum_i w_i' \, \mu_i. \tag{4.10}$$

In a similar fashion, also an error for the average value is found. Here, the errors are added in squares, multiplied again by their weights,

$$\bar{\sigma} = \sqrt{\sum_i {w'_i}^2 \, \sigma_i^2}. \tag{4.11}$$

This procedure already is a solid starting point for evaluating averages, however, it still has some downsides, which need to be addressed. One important point is the reliability of handling asymmetric error intervals. While these are almost non-existent among the hypernuclear binding energy data, they frequently appear in lifetime measurements.
Another characteristic of this method is the behavior of the resulting error $\bar{\sigma}$. The nature of (4.11) is to return an error $\bar{\sigma} \leq \min \sigma_i$, tending to decrease for more contributing data points. This becomes obvious, when inserting the formulas for weight (4.8) and (4.9) back into (4.11). The result is

$$\bar{\sigma} = \left(\sum_i \left(\frac{1}{\sigma_i} \right)^2 \right)^{-\frac{1}{2}}, \tag{4.12}$$

where at first the inverse errors σ_i are added in squares. This sum grows bigger, the more data points are included. Then, the square root together with the inverse is taken. By that, the result will always be smaller than any of the contributing errors. Only for the case of $N = 1$, the errors will be the same. This behavior might seem to make sense at first glance. Why should the average error exceed the contributing errors, doesn't more data mean better results? The answer is, that the distribution of the μ_i is at that point not considered for the calculation. Especially, when one or more values in the data set were reported with too small errors, the error weighted mean method might under-estimate the error of the average. A solution is given by the *error scaling* method, described in 4.3.5.

4.3.4. Error weighted mean with asymmetric errors

To address the situation of asymmetric errors, $\pm\sigma \rightarrow {}^{+\sigma_+}_{-\sigma_-}$, a procedure described by R. Barlow [39] is used. This approach aims to parameterize an asymmetric Gaussian-like probability density function *pdf* for each data point and to find the average via the maximum likelihood method.

Definition

Barlow describes two similar models, a so called linear variance and a linear σ model. From them, the latter proved to be more stable and hence was chosen to be applied in the *Chart of Hypernuclides*. A description of the linear variance model is still to be found in Chapter A.5.2 on page 142. For the linear σ model, the corresponding *pdf* is defined via

$$pdf(x) = \frac{1}{\sigma(x)\sqrt{2\pi}} \mathrm{e}^{-\frac{1}{2}\left(\frac{x-\mu}{\sigma(x)}\right)^2}, \tag{4.13}$$

which is fairly similar to a normal Gaussian distribution. The only important difference is that the error σ was replaced by the function $\sigma(x)$. By that, the width is continuously varied, generating an asymmetric distribution in the form of a skewed Gaussian. This $\sigma(x)$ is defined as a linear function in x,

$$\sigma(x) = \sigma_1 + \sigma_2(x - \mu) \tag{4.14}$$

with the parameters

$$\sigma_1 = 2\,\sigma_+\sigma_-/(\sigma_+ + \sigma_-) \tag{4.15}$$

and

$$\sigma_2 = (\sigma_+ - \sigma_-)/(\sigma_+ + \sigma_-). \tag{4.16}$$

These two are defined so that $\sigma(x - \sigma_-) = \sigma_-$ and $\sigma(x + \sigma_+) = \sigma_+$. By this definition, also the case of a symmetric error $\sigma = \sigma_+ = \sigma_-$ is covered, σ_2 will then be 0 and σ_1 will just be σ so that $\sigma(x) = \sigma$.

The average value

Analogously to the calculation for the symmetric case, each measurement needs to receive a weight which reads

$$w_i = \frac{\sigma_{1,i}}{(\sigma_{1,i} + \sigma_{2,i}(\bar{x} - \mu_i))^3}. \tag{4.17}$$

From there, the normalization is performed according to (4.9) and the weighted sum would lead to the average as in (4.10). The resulting equation can be written as

$$\bar{x} \sum_i w_i = \sum_i \mu_i w_i. \tag{4.18}$$

The only difference, however, is that in this case the weights depend on the average $\bar{x}$ itself, making the equation unsolvable analytically. To find the solution, the value has to be determined numerically in an iterative approach. A proper starting value is given by the arithmetic mean of all μ_i, and from there, fortunately, the search converges quite quickly. The approximation was observed to improve by one order of magnitude for each iteration. Hence, within 5 iterations, an accuracy of 10^{-5} is reached. This is fully sufficient for the application in the *Chart of Hypernuclides*.

The errors

Also the error intervals of this average $\bar{\sigma}_+$ and $\bar{\sigma}_-$ need to be determined numerically. For them, the log-likelihood function becomes relevant. It is defined as the logarithm of the likelihood function, which is simply the multiplication of the contributing *pdf*'s. The result is

$$\ln L = -\frac{1}{2} \sum_i \left(\frac{x - \mu_i}{\sigma_i(x)} \right)^2, \tag{4.19}$$

where the remaining additional terms originating from the pre-factors are neglected. The logarithm of the likelihood function is preferable to the function itself due to computational reasons. It breaks multiplications and exponents down to mostly simple additions while still providing the same physical importance as the likelihood function.
$\ln L$ peaks at the average $\bar{x}$ which was already determined previously. Now the function will be used to extract the error intervals. Equivalent to a true Gaussian function, the $1\,\sigma$ interval is given by the points, where the exponent reaches $-\frac{1}{2}$. Analogously, it is to look for the points, where

$$\ln L(\bar{x}) - \ln L(\bar{x} \pm \bar{\sigma}_\pm) = -\frac{1}{2}. \tag{4.20}$$

A good initial value is this time given by the error weighted mean procedure in (4.12). Here, a separate starting value for both error components is derived. With these, this iterative approximation is observed to converge quickly as well. Again, one order of magnitude in accuracy is gained per iteration. For the errors, 10^{-3} is sufficient, so another 6 iterations are needed. Overall, the quick convergence is rendering the procedure applicable for real time processing on the website.

Further improvement

Still, also this method has its limits. It was noticed that the handling of strongly asymmetric errors ($\sigma_+ > 1.5\,\sigma_-$ and vice versa) is problematic. In such cases the function $\sigma(x)$ becomes quite steep so that it quicker reaches zero. This leads to a pole in the *pdf* from (4.13). If this pole is too close to the location of the average, the related measurement will receive either an oddly high or even a negative weight. Also the other direction of $\sigma(x)$ which is continuously rising, can cause problems. If it rises too strongly, it will suppress the negative exponent in the probability density function Eq. (4.13), leading to a slower falling or even non-converging *pdf*. To prevent this from happening, measurements with such extreme errors are treated with a modified version of the function $\sigma(x)$ which reads

$$\sigma'(x) = \begin{cases} \sigma_-, & \text{if } x \leq \mu - \sigma_- \\ \sigma_+, & \text{if } x \geq \mu + \sigma_+. \\ \sigma(x), & \text{otherwise} \end{cases} \tag{4.21}$$

Here, the parameter σ gets fixed to the constant values outside of the $1\,\sigma$ interval and is only varied inside.

It was C. Rappold who was the first to apply the described averaging methods to hypernuclear data in 2013 [255]. He computed the lifetime averages for ${}^{3}_{\Lambda}\mathrm{H}$ and ${}^{4}_{\Lambda}\mathrm{H}$. In contrast to the approach that was described before, he used both the linear variance and the linear σ model from which he took the average for the final results. Also, he did not use the modified $\sigma'(x)$ from Eq. (4.21). However, especially within the ${}^{4}_{\Lambda}\mathrm{H}$ lifetime data, there is one data point with a very asymmetric error, $\tau({}^{4}_{\Lambda}\mathrm{H}) = 360\,^{+490}_{-130}\,\mathrm{ps}$ by Kang from 1965 [171]. Here, $\sigma_+ \approx 3.8\,\sigma_-$. When reproducing the calculation by Rappold, it was observed, that this measurement received an oddly high weight of around 5%, while it was truly overruled by newer experiments. This was due to the steep $\sigma(x)$ quickly reaching 0 in combination with the high mean value, compared to the today known ${}^{4}_{\Lambda}\mathrm{H}$ lifetime value of around $200\,\mathrm{ps}$. That way, the $\sigma(x)$ was evaluated relatively far away from the $360\,\mathrm{ps}$ where it had reached an oddly low quantity, resulting in an over-estimated weight.

It was also observed, that the situation with the linear variance model is even worse. Here, the error intervals are processed in the form of their squares, emphasizing their asymmetry even more. For Kang's value, the pole was then moved so close to the region where the average is computed, that the measurement broke the algorithm. Rappold had to remove this value manually from the calculation at that point. While technically the linear variance model is less complicated, it still was decided to only use the linear σ model in the *Chart of Hypernuclides* due to its greater reliability. Finally, with the addition of the modified σ' function, the weight of Kang's data point was re-evaluated to be only 1%.

Summary

The linear σ model improved the procedure of averaging by making it capable of handling asymmetric errors. The method was observed to work quite reliably, only the cases of largely asymmetric errors was still critical. This was improved by the σ' function. However, the procedure is still not complete. For example, the second downside of the error weighted mean procedure, described in Chapter 4.3.3, was not yet addressed. So far, the method still is not capable of taking into account, how the data points are distributed and if errors may be under-estimated. This and more will be addressed in the following section.

4.3.5. Further data treatment

In total, four more additional procedures were implemented. They each treat further special cases to achieve the goal of a maximized reliability of the averaging routines, so that they can be applied automatically without concerns.

Error scaling

This procedure finally addresses the distribution of the data points and the under-estimation of errors. It was adopted from the PDG [236]. To quantify the amount of scattering of the data points, a χ^2 value is computed,

$$\chi^2 = \sum_i^N w_i(\mu_i - \bar{x})^2, \tag{4.22}$$

including the un-normalized weights w_i from (4.8). If this χ^2 exceeds the number of degrees of freedom ($ndf =$ number of contributing measurements $N - 1$), it is likely, that for at least one of the measurements the error was underestimated. Then, a scaling factor S is computed

$$S = \sqrt{\chi^2/ndf}. \tag{4.23}$$

For $1 < S < 2$, the data situation still is considered as sufficiently consistent and the error of the average is multiplied by S. This leads to a χ^2 value equal to its statistically expected value, $\chi^2 = ndf$. The procedure is also known as Birge ratio algorithm and is used when handling discrepant data [294]. For $S \geq 2$, unknown effects are assumed to be in place and the average cannot be determined reliably. In that case, the error will still be scaled up and the resulting average value will be displayed at the website, but it will not be recommended. Only for $S \leq 1$, no treatment will be applied.

Shared systematic errors

The treatment of shared systematic errors was again adopted from the PDG [236]. It focuses on measurements originating from the same experimental apparatus, since they would likely carry the same systematic shifts in the data. When averaging these, however, their systematic error would be reduced without that shift to be countered by other data. The starting point for the correction is a data set with varying mean values and statistical errors but with only one and the same systematic error,

$$\mu_i \pm \sigma_{\mathrm{stat}\,i} \pm \sigma_{\mathrm{syst}} \tag{4.24}$$

From there, a scaled systematic error is computed,

$$\sigma_{\mathrm{syst}\,i} = \sigma_{\mathrm{syst}} \cdot \sigma_{\mathrm{stat}\,i} \left(\sum_j \frac{1}{\sigma^2_{\mathrm{stat}\,j}} \right)^{\frac{1}{2}}. \tag{4.25}$$

Within the PDG review, this method is described as follows:

"This procedure has the advantage that, with the modified systematic errors [...]*, each measurement may be treated as independent and averaged in the usual way with other data."* – PDG [236]

Exclusion of data

Because the general goal of the *Chart of Hypernuclides* is to gather as much data and information as possible, it is even more important to extract the truly relevant experiments, from which a reliable average can be calculated. Therefore, irrelevant values are excluded from the averaging procedure. This applies to all measurements which received a weight of less than 2%. Their weights will be set to zero and the calculation is repeated.
Additionally, also outliers are treated in a similar fashion. Here, measurements with weights of up to 5% and an unusually high contribution to the χ^2 value are excluded as well. The explicit threshold was chosen to be

$$\frac{\chi_i^2}{w_i'} > 120. \tag{4.26}$$

That way, a measurement with 5% weight is tolerated up to a χ^2 contribution of 6. A value with 2.5% is already sorted out at $\chi_i^2 = 3$. The rationale of both of these procedures is, that otherwise these measurements would dilute or enlarge the overall χ^2 sum and by that influence the scaling factor S from (4.23).

Missing systematic errors

The remaining treatment is to try to equip measurements with proper systematic errors. This is relevant since in hypernuclear physics, there are many published values which are lacking this error component. Especially the early binding energy measurements using the emulsion technique were often reported without that information. As a consequence, following the estimation by D. H. Davis [94, 93], all emulsion values from before 1980 have been assigned an error of $\sigma_{\text{syst}} = 40\,\text{keV}$ if none other was given.

Summary

With these four additional treatments, all facets of the averaging procedure were explained. So far, there are no more known issues which would justify the need for furthermore corrections. After all, the complete data in the chart's database was observed to be treated without any problems or exceptions. In the following, there is one more possible treatment described, which on purpose was not included to the averaging algorithm.

4.3.6. Ongoing discussion about the re-calibration of data sets

Outdated particle masses in emulsion data

As already mentioned in Chapter 2.2.1, there have been attempts to re-calibrate old binding energy data due to the changes of many mass literature values [13]. Indeed, from the first observation of a hypernucleus in 1952 it wasn't long until the first papers about their properties were published. An example is a hypertriton binding energy measurement from 1957 [300]. This is now 66 years ago. Apart from questioning the available experimental setups and state-of-the-art analysis tools, the knowledge about mass literature values was truly different. This was already emphasized in Figure 2.2 on page 12.Especially the pion and Λ masses deviated by several $100\,\text{keV}$ during the 50's and 60's. In addition, due to the fact that still today many hypernuclear properties rely mostly on data from the 1970's and older, the discussion started about if or how the old data might be corrected.
One suggestion was given by J. Adams *et al.* from the STAR Collaboration in 2020 [13]. In emulsion experiments, usually a released kinetic energy Q is determined from the track lengths

inside the emulsion plate. If all the contributing tracks are uniquely assigned to particles, the hypernucleus can be identified and the binding energy is extracted via

$$B_\Lambda = m_{\text{before}} - m_{\text{after}} - Q, \tag{4.27}$$

compare to the description of the emulsion technique in Chapter 3.3.1 on page 27 and the equations (3.2) and (3.3). For a two-body decay of hypertriton,

$${}^{3}_{\Lambda}\text{H} \rightarrow {}^{3}\text{He} + \pi^- \tag{4.28}$$

the equation reads

$$B_\Lambda = m_\Lambda + m_d - m_{^3\text{He}} - m_{\pi^-} - Q. \tag{4.29}$$

This last formula explicitly contains four particle masses which had to be taken from literature. The approach from STAR intends to compare all the involved masses to the present values and to add the overall difference to the calculation. Thereby, for example, the hypertriton binding energy value by Gajewski from 1967 [132] would be shifted from $B_\Lambda = 200 \pm 120\,\text{keV}$ to $B_\Lambda = 410 \pm 120\,\text{keV}$. Also other values were re-calibrated, including the emulsion works of Bohm [53] and Jurič [165].
What is missing in Ref. [13] however, is the famous compilation value for the hypertriton binding energy of $130 \pm 50\,\text{keV}$, which was determined by Jurič by combining the data from all the three mentioned references. As described before, the truncated mean method was used, meaning that iteration-wise some outlier events were excluded from the data by hand, until a trust-worthy set remained. Surely, this method was the state-of-the-art at that time and its strength was to exclude events which might have been interpreted incorrectly. From today's perspective though, it is impossible to reproduce which value from which data set was exactly excluded. This also marks the limit of the re-calibration possibilities of these compilation values. The only option would then be to ignore them and to proceed with the initial references. From there, the next question arises. If not specified explicitly which particle masses were in use, they are simply unknown.
Another obscurity is the procedure of how the emulsion plates were calibrated. Some have observed free Λ decays to extract the Λ mass and link it to the literature value of that time. If the Λ was believed to be lighter than it actually was, the released energy during the decay in the emulsion plate would have been calibrated to underestimated values in order to achieve the literature mass. By that, the deviation in this mass would also directly affect the resulting Q values from the hypernuclear decays. Considering again Eq. (4.29), these shifts would cancel out each other to a certain level, if not almost completely.

The KEK and FINUDA spectrometer data

Not only emulsion values were considered to be re-calibrated, also spectroscopic data from experiments at FINUDA and KEK was questioned. Both of these experiments studied the (π^+, K^+) reaction – compare to Chapter 3.2.2 on page 23 – so that the binding energy of multiple hyper-isotopes was observed successfully. However, by using a secondary pion beam, the absolute resolution was limited due to large uncertainties in the actual beam energy. This lead to the idea to calibrate all data sets by coupling the binding energy of one specific hypernucleus to the respective value obtained in emulsions. In that fashion, the uncertainty was expected to vanish for all observed binding energies. It was decided, to perform this calibration with the emulsion binding energy of ${}^{12}_{\Lambda}\text{C}$, a hypernucleus to be rather easily produced by the (π^+, K^+) at a ${}^{12}\text{C}$ target (compare to Figure 3.11 on page 34).
After this calibration, though, further discrepancies were observed, for example, when E. Botta compared the binding energies obtained at FINUDA with the ones from KEK [58]. She found

that across multiple hypernuclei, a mean offset of $0.6\,\mathrm{MeV}$ is given, as seen in the left of Figure 4.3. A similar result was observed by T. Gogami [140], when he compared the KEK data to the emulsion values, seen on the right of Figure 4.3. Also he observed a difference of about half an MeV. As a consequence, Gogami suggested, that the original emulsion value of ${}^{12}_{\Lambda}\mathrm{C}$ was wrong. It was given initially with $10.76 \pm 0.19\,\mathrm{MeV}$ [96], relying on 6 single events of which two had even been questioned several years before [165]. Today, the binding energy of this hypernucleus is computed to be $11.34 \pm 0.13\,\mathrm{MeV}$ by the *Chart of Hypernuclides*, but still huge discrepancies in the data are given, see Table 4.2.

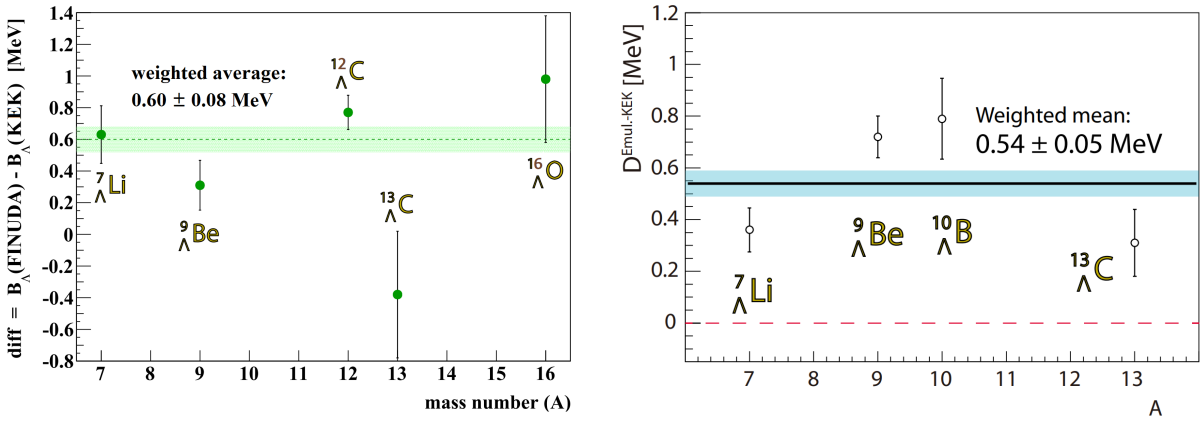

Figure 4.3.: Re-calibration efforts for spectroscopic data of the FINUDA and KEK experiments. **Left:** comparison of FINUDA and KEK data by E. Botta [58]. **Right:** comparison of KEK and emulsion data by T. Gogami [140]. Both authors found systematic offsets in the extracted Λ binding energies in the order of half an MeV.

Conclusion

To summarize the situation, it remains still unclear, if or how a comprehensive calibration could be performed. While certainly some effects are present for the emulsion values given by the differences in the particle masses, it is not believed, that the rather simple approach of STAR [13] can address this issue properly. In contrast, a detailed inspection of each hyper-isotope is expected to be more promising, as it was demonstrated by Gogami for the case of the ${}^{12}_{\Lambda}\mathrm{C}$ hypernucleus [140].
After all, the process of re-calibrating data sets requires as much information about the experiment as possible and should mainly be taken into account by the associated experts. The *Chart of Hypernuclides* therefore rather aims to collect data as thoroughly as possible to allow for detailed discussions about discrepancies, so that a consistent and widely agreed method for a re-calibration may be elaborated in the future.

4.4. Data Collection and Resulting Average Values

Now, that the complete set of routines for calculating averages was explained, the results of a comprehensive data collection are going to be presented. Every of the following average values was received from the *Chart of Hypernuclides*.

Lifetime values

For the lifetimes, only data about the Λ hypernuclei is available. A total of 56 values is distributed over 9 different hyper-isotopes, which are listed in Table 4.1. This table lists their average value and the involved references being included to the average. Obsolete sources, which were excluded during the calculation were omitted. These are still to be found on the chart's website. For the lifetime data sets, no inconsistencies were found at all. The averages are reliable and no error scaling needed to be applied. For the both hydrogen hypernuclei, a detailed discussion of the lifetime data is presented in Chapter 5.2.2 on page 60 ($^{3}_{\Lambda}\mathrm{H}$) and Chapter 4.5 on page 52 ($^{4}_{\Lambda}\mathrm{H}$), including explicit listings of all data points found in the tables 5.2 and 4.4, respectively.

Table 4.1.: List of all evaluated lifetimes from the *Chart of Hypernuclides* [101]. Together with isotope and value, also the included references are displayed. Obsolete referenced were omitted. No error scaling correction was applied.

Isotope	Lifetime τ [ps]	References
$^{3}_{\Lambda}\mathrm{H}$	242 ± 9	[24, 5, 298, 8, 12, 255, 174, 177, 176]
$^{4}_{\Lambda}\mathrm{H}$	$208\ ^{+\ 10}_{-\ 12}$	[5, 255, 227, 34, 83]
$^{4}_{\Lambda}\mathrm{He}$	250 ± 18	[235, 228, 240]
$^{5}_{\Lambda}\mathrm{He}$	274 ± 9	[168, 288]
$^{9}_{\Lambda}\mathrm{Be}$	201 ± 31	[147]
$^{11}_{\Lambda}\mathrm{B}$	206 ± 11	[234, 147]
$^{12}_{\Lambda}\mathrm{C}$	212 ± 7	[48, 147]
$^{27}_{\Lambda}\mathrm{Al}$	203 ± 10	[234]
$^{28}_{\Lambda}\mathrm{Si}$	206 ± 11	[234]

Binding energy values

A total of 286 binding energy values was added to the database, providing experimental information about 34 isotopes of Λ hypernuclei. The evaluated averages are shown in Table 4.2, analogously to the lifetime table. Also, if an inconsistency or other problems were observed, these are summarized in a short comment. In 13 cases, the error scaling correction had to be applied and in four of these cases, the inconsistency within the data was so hefty that the resulting average value is not recommended. Two other nuclei, the $^{6}_{\Lambda}\mathrm{H}$ and the $^{6}_{\Lambda}\mathrm{Li}$, were just hardly observed by one respective experiment so that their existence is lacking further confirmation. Here, again, the average value is to be questioned. For the other isotopes, the binding energy values were computed reliably without any further treatment.
Again, an explicit analysis of $^{3}_{\Lambda}\mathrm{H}$ and $^{4}_{\Lambda}\mathrm{H}$ is found in the chapters 5.2.1 on page 58 and 4.5. All the collected binding energy values are listed in the tables 5.1 and 4.3, respectively.

Table 4.2.: List of all evaluated Λ binding energies from the *Chart of Hypernuclides* [101]. Together with hyper-isotope and value, also the included references are displayed. Excluded references were omitted.

Isotope	B_Λ [MeV]	References	Comment
${}^{3}_{\Lambda}\mathrm{H}$	0.164 ± 0.043	[24, 13, 165, 177, 76, 204, 28, 250]	
${}^{4}_{\Lambda}\mathrm{H}$	2.169 ± 0.042	[276, 290, 165, 53, 132, 83]	error scaled by 1.44, $ndf = 6$
${}^{6}_{\Lambda}\mathrm{H}$	4.000 ± 1.100	[16]	existence not verified
${}^{4}_{\Lambda}\mathrm{He}$	2.347 ± 0.036	[291, 153, 165, 132, 260, 83]	error scaled by 1.09, $ndf = 5$
${}^{5}_{\Lambda}\mathrm{He}$	3.102 ± 0.030	[165, 132, 83, 250]	
${}^{6}_{\Lambda}\mathrm{He}$	4.180 ± 0.108	[244]	
${}^{7}_{\Lambda}\mathrm{He}$	5.064 ± 0.332	[143, 219, 53, 132, 83, 250]	error scaled by 3.30, $ndf = 6$, value not recommended
${}^{8}_{\Lambda}\mathrm{He}$	7.160 ± 0.701	[165]	
${}^{6}_{\Lambda}\mathrm{Li}$	4.500 ± 0.500	[44]	existence not verified
${}^{7}_{\Lambda}\mathrm{Li}$	5.619 ± 0.060	[58, 19, 165, 132, 83]	error scaled by 1.50, $ndf = 4$
${}^{8}_{\Lambda}\mathrm{Li}$	6.767 ± 0.053	[165, 132, 83]	error scaled by 1.24, $ndf = 2$
${}^{9}_{\Lambda}\mathrm{Li}$	8.370 ± 0.071	[142, 299, 244, 132, 83]	
${}^{7}_{\Lambda}\mathrm{Be}$	5.160 ± 0.089	[165]	
${}^{8}_{\Lambda}\mathrm{Be}$	6.818 ± 0.060	[165, 132]	
${}^{9}_{\Lambda}\mathrm{Be}$	6.614 ± 0.072	[58, 19, 165, 132, 83]	error scaled by 1.83, $ndf = 4$
${}^{10}_{\Lambda}\mathrm{Be}$	8.793 ± 0.247	[140, 72]	error scaled by 1.80, $ndf = 1$
${}^{9}_{\Lambda}\mathrm{B}$	8.290 ± 0.184	[244]	
${}^{10}_{\Lambda}\mathrm{B}$	8.485 ± 0.250	[58, 149, 165]	error scaled by 3.73, $ndf = 2$, value not recommended
${}^{11}_{\Lambda}\mathrm{B}$	10.25 ± 0.06	[58, 165, 132]	
${}^{12}_{\Lambda}\mathrm{B}$	11.43 ± 0.06	[293, 165, 132]	error scaled by 1.31, $ndf = 2$
${}^{12}_{\Lambda}\mathrm{C}$	11.34 ± 0.13	[19, 17, 291, 241, 78, 243, 69, 118]	error scaled by 3.93, $ndf = 7$, value not recommended
${}^{13}_{\Lambda}\mathrm{C}$	11.80 ± 0.16	[58, 150, 18, 72, 132, 83]	error scaled by 2.16, $ndf = 4$, value not recommended
${}^{14}_{\Lambda}\mathrm{C}$	12.17 ± 0.33	[72]	
${}^{15}_{\Lambda}\mathrm{N}$	13.59 ± 0.15	[58, 165]	
${}^{16}_{\Lambda}\mathrm{N}$	13.79 ± 0.16	[88]	
${}^{16}_{\Lambda}\mathrm{O}$	13.00 ± 0.09	[58, 18, 291, 241]	error scaled by 1.02, $ndf = 3$
${}^{28}_{\Lambda}\mathrm{Si}$	16.41 ± 0.28	[149, 241]	error scaled by 1.70, $ndf = 1$
${}^{32}_{\Lambda}\mathrm{S}$	17.50 ± 0.50	[43]	
${}^{40}_{\Lambda}\mathrm{Ca}$	18.70 ± 1.10	[241]	
${}^{51}_{\Lambda}\mathrm{V}$	19.97 ± 0.26	[159, 241]	
${}^{52}_{\Lambda}\mathrm{V}$	21.88 ± 0.60	[145]	
${}^{89}_{\Lambda}\mathrm{Y}$	22.87 ± 0.32	[159, 149, 241]	
${}^{139}_{\Lambda}\mathrm{La}$	23.80 ± 1.00	[149]	
${}^{208}_{\Lambda}\mathrm{Pb}$	26.50 ± 0.50	[149]	

Additionally, from all the results of Table 4.2, the website offers to generate summary plots, similar to the one displayed in Figure 1.10 on page 10. These are found along with a brief discussion in Chapter A.1.3 on page 128.

Further data in the chart

Besides the lifetime and binding energy, even more properties about hypernuclei are found in the *Chart of Hypernuclides*. This includes another 115 branching ratios values. This data was collected together with Bachelor student S. Ries and the resulting averages along with a discussion are already found in her thesis [261]. Details about the branching ratios are still to be found in the appendix, Chapter A.4 on page 139, including tables with the resulting average values and a description of the various channels in Table A.1.
138 excitation energies were collected as well. An example of these was given in Figure 4.1. The other entries are to be found on the website itself [101]. The same holds for binding energy values addressing hypernuclei with a different hyperon content. Here, the data is rather scarce. In total, 7 more isotopes are found there.

4.5. Detailed Analysis of ${}^{4}_{\Lambda}\mathrm{H}$

The ${}^{4}_{\Lambda}\mathrm{H}$ possesses one more neutron than the hypertriton and can therefore be seen as a member of the lightest hypernuclei, along with ${}^{4}_{\Lambda}\mathrm{He}$. Despite their similar composition compared to the hypertriton, their properties differ quite strongly. With around $2\,\mathrm{MeV}$ their Λ binding energy is more than a factor of 10 larger than the one of the hypertriton. The data situation of ${}^{4}_{\Lambda}\mathrm{H}$ is summarized in the following.

${}^{4}_{\Lambda}\mathrm{H}$ binding energy

For this hypernucleus, a set of 9 binding energy values is given. These are dominated by old emulsion values, but also the newer techniques of pion and decay pion spectroscopy are available. From these, the binding energy of ${}^{4}_{\Lambda}\mathrm{H}$ was evaluated to be

$$\overline{B}_{\Lambda}({}^{4}_{\Lambda}\mathrm{H}) = 2.169 \pm 0.042\,\mathrm{MeV}. \tag{4.30}$$

For this average, a total of 7 measurements was included. These values, together with the two obsolete ones are listed explicitly in Table 4.3. The resulting ideogram is depicted in Figure 4.4. At first glance, the two peak structure of the probability density curve appears prominently. Almost symmetrically it raises steeply to the first maximum, then to form a local minimum at the center and then to raise again. Due to the location of these maxima, it is quickly seen, that the emulsion values from Jurič and Bohm cause this behavior. They both are the values with the smallest errors of only $57\,\mathrm{keV}$ but lie quite far apart from each other with 3.8 standard deviations. By comparing the ideogram to Table 4.3, one can see that these two values dominate the average value with an added weight of more than 50%. Therefore, also the respective χ^2 contribution of around 5 is tremendous. The other values seem to be less in conflict with each other, their χ^2 values are well between 0 and 2. After the two emulsion values, the next biggest influence with around 25% is given by the two recent values from A1. Comparing with the ideogram, they are compatible very well with the resulting average. These values together with the 4 others are still not able to compensate for the tension given by the two emulsion values though. The resulting χ^2 sum of 12.5 is too high given the *ndf* of just 6. The reduced χ^2 – χ^2_{red} – is with 2.08 strongly above 1, so a scaling factor of 1.44 had to be applied.

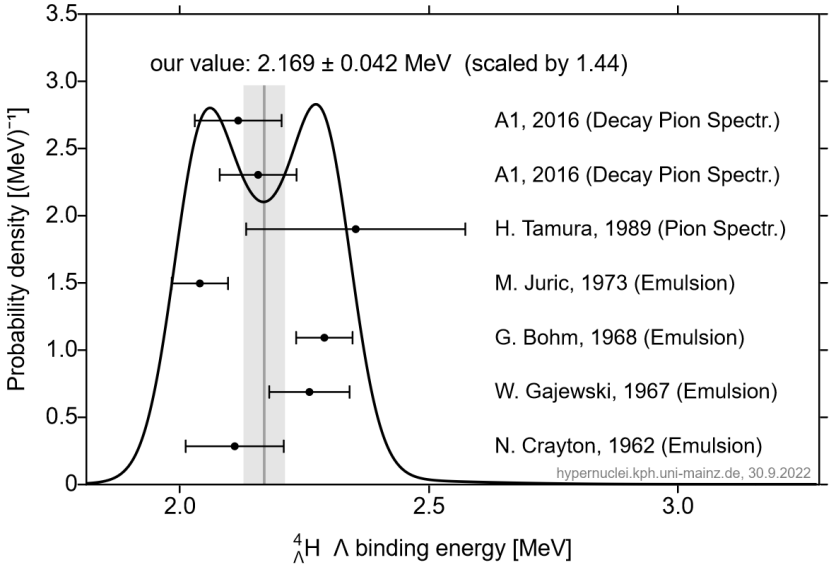

Figure 4.4.: Measurements contributing to the average of the ${}^{4}_{\Lambda}$H binding energy [101]. The emulsion values of Jurič and Bohm dominate the average. Their values lead to a two peak structure. The newest values from A1 fit to the average very well.

Table 4.3.: List of reported ${}^{4}_{\Lambda}$H binding energy values. The measurements before 1980 were assigned with an additional systematic error of $40\,\mathrm{keV}$ as suggested by Davis [94, 93], as far as no other was given.

Reference	**Year**	B_Λ [keV]	w	χ^2	**Method**	**Comment**
F. Schulz [275]	2016	$2117 \pm 14 \pm 86$	0.11	0.36	Pion Spec.	reanalysis of [114]
F. Schulz [275]	2016	$2157 \pm 5 \pm 77$	0.14	0.03	Pion Spec.	
H. Tamura [290]	1989	2353 ± 220	0.02	0.70	(K^-, π^-)	
M. Jurič [165]	1973	$2040 \pm 40 \pm 40$	0.26	5.22	Emulsion	with three-body events of [53, 132]
G. Bohm [53]	1968	$2290 \pm 40 \pm 40$	0.26	4.55	Emulsion	two-body only
W. Gajewski [132]	1967	$2260 \pm 70 \pm 40$	0.13	1.27	Emulsion	two-body only
N. Crayton [83]	1962	$2110 \pm 90 \pm 40$	0.09	0.36	Emulsion	
M. Raymund [260]	1964	$1780 \pm 160 \pm 40$	–	–	Emulsion	bad χ^2 to w ratio
Y. Prakash [250]	1961	$2010 \pm 230 \pm 130$	–	–	Emulsion	low weight
Our average:	2023	2169 ± 42	1	12.5	$ndf = 6$	scaled by 1.44

${}^{4}_{\Lambda}$H lifetime

For the lifetime, again, 9 values are available. These are rich in variety, originating from emulsion, bubble chamber, pion spectroscopy and heavy ion collision experiments. The explicit list is found in Table 4.4. Here it is observed that already 4 of these values are sorted out by low weight. This includes the bubble chamber value from Fortney and three other emulsion values. The resulting ideogram is found in Figure 4.5. The probability curve shows a distinct maximum as well as a long tail down to short lifetimes. The main attention is immediately caught by the newest STAR value from 2021. With its small error it seems to be responsible for the peak. Cross checking with the exact values in Table 4.4 confirms this assumption. The value alone receives

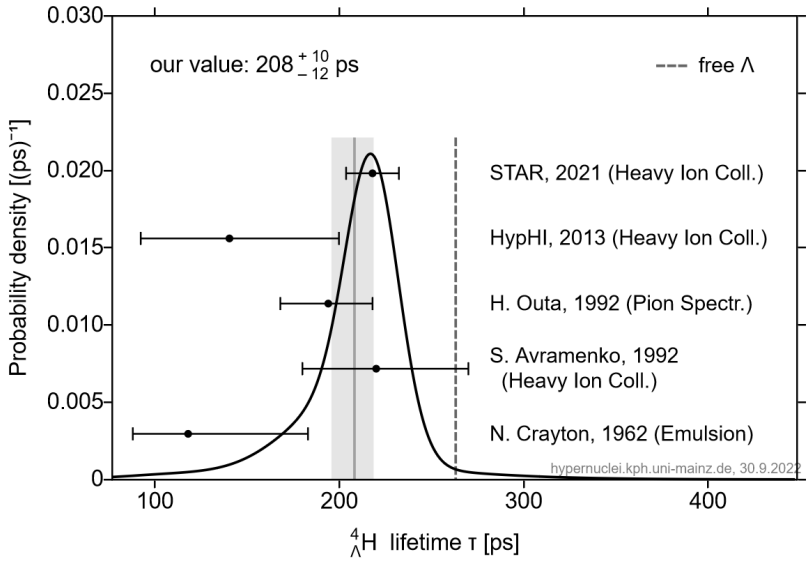

Figure 4.5.: Ideogram showing all contributing lifetime values to the average for ${}^{4}_{\Lambda}\mathrm{H}$ [101]. It is dominated by the recent STAR measurement. During the analysis, no ambiguities were observed.

a weight of 65% being the undisputed main influence to the average. The second strongest is with 23% the value by Outa. They both are compatible within 1σ with the average value of

$$\overline{\tau}({}^{4}_{\Lambda}\mathrm{H}) = 208^{+10}_{-12}\,\mathrm{ps}. \tag{4.31}$$

Overall, there is no measurement which lies in great tension with this average. The χ^2 contributions are scattering around 1 and the sum of 3.22 is below the *ndf* of 4. Therefore, no further correction was applied.

Table 4.4.: List of reported ${}^{4}_{\Lambda}\mathrm{H}$ lifetime values. Many of the older values were excluded due to low weight. The data set is dominated by the newest STAR value from 2021.

Reference	**Year**	**Lifetime τ** [ps]	w	χ^2	**Method**	**Comment**
M. S. Abdallah [5]	2021	$218 \pm 6 \pm 13$	0.65	0.47	Heavy ion	
C. Rappold [255]	2013	$140 \,^{+\,48}_{-\,33} \pm 35$	0.03	1.12	Heavy ion	
H. Outa [227]	1992	$194 \,^{+\,24}_{-\,26}$	0.23	0.35	Pion Spec.	
S. Avramenko [34]	1992	$220 \,^{+\,50}_{-\,40}$	0.07	0.08	Heavy ion	
N. Crayton [83]	1962	$118 \,^{+\,65}_{-\,30}$	0.02	1.22	Emulsion	
R. E. Phillips, J. Schneps [240]	1969	$268 \,^{+166}_{-107}$	–	–	Emulsion	low weight
Y. W. Kang [171]	1965	$360 \,^{+490}_{-130}$	–	–	Emulsion	low weight
R. J. Prem, P. H. Steinberg [251]	1964	$180 \,^{+250}_{-\,70}$	–	–	Emulsion	low weight
L. Fortney [193]	1964	$240 \,^{+190}_{-\,90}$	–	–	Bubble ch.	low weight
Our average:	2023	$208 \,^{+\,10}_{-\,12}$	1	3.22	$ndf = 4$	

5. The Hypertriton and other Light Systems

Now, that the *Chart of Hypernuclides* was introduced and its capabilities were already shown in case of the ${}^{4}_{\Lambda}\mathrm{H}$ hypernucleus, it is time to move on to a in-depth description of the even smaller hypertriton system. It is the main focus in the context of this thesis and the performed decay pion spectroscopy experiment.
In Section **5.1**, the hypertriton is going to be introduced along with other $A = 3$ hypernuclear systems. Followed by **5.2**, the data situation regarding lifetime and binding energy of ${}^{3}_{\Lambda}\mathrm{H}$ is reviewed and put into historical context. **5.3** introduces the so-called *hypertriton puzzle*, a frequently used term to summarize ambiguities in the experimental data, and emphasizes the extraordinary halo character of the hypertriton. Finally, in Section **5.4**, some of the upcoming hypertriton experiments are depicted in closer detail.

5.1. The $A = 3$ Hypernuclei

5.1.1. Overview

Within isospin space, four different three-body single Λ hypernuclei are to be distinguished. As shown in Figure 5.1, these are separated into an isospin $I = 0$ singlet and an isospin 1 triplet [247, 245]. From these, only the hypertriton on the left is so far known to be bound. Many references reported a spin-parity assignment of $J^{\pi} = 1/2^{+}$ to this hypernucleus [89, 190, 91, 177, 174], on the one hand due to its low Λ binding energy in the order of $100\,\mathrm{keV}$ and on the other due to the observed decay branching ratio [101]

$$R_3 = \frac{\Gamma({}^{3}_{\Lambda}\mathrm{H} \to \pi^- + {}^{3}\mathrm{He})}{\Gamma({}^{3}_{\Lambda}\mathrm{H} \to \pi^- + \quad X\ )} = 0.36 \pm 0.03. \tag{5.1}$$

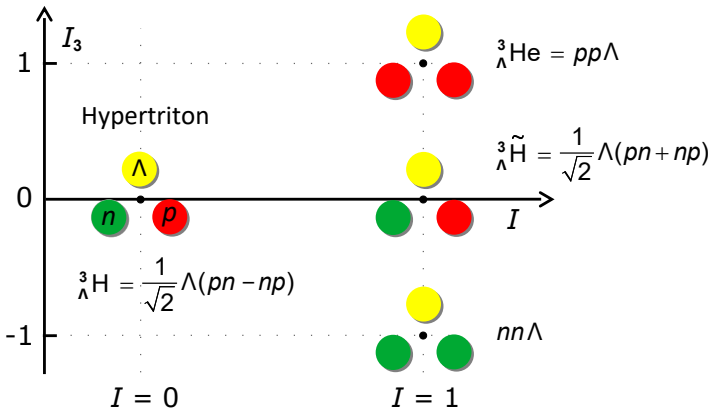

Figure 5.1.: Isospin representation of $A = 3$ hypernuclei [247, 245]. Only the $I = 0$ hypertriton is known to be bound and was observed in various experiments. Due to a recent experiment at HypHI, also hints for the neutral $nn\Lambda$ system were found [257], which need further experimental confirmation (compare to Figure 5.3 on page 57).

It describes the proportion of pure two-body decays with negative pions to all mesonic decays via π^- of the hypertriton. One of the assignments was performed by Bertrand already in 1970 [46], based on a theoretical calculation performed by Dalitz in 1959 [90]. There he calculated the value of R_3 once for a $J = 1/2$ hypertriton and additionally for $J = 3/2$, depending on the p wave amplitude contribution of the pions in free Λ decays. This is seen in Figure 5.2 [46]. The latter quantity was in the following years determined by Overseth to be quite small with $\frac{p^2}{p^2+s^2} = 0.126 \pm 0.006$ [231]. Together with the R_3 which was measured by Bertrand to be around 0.4, he found great agreement with the $J = 1/2$ case.

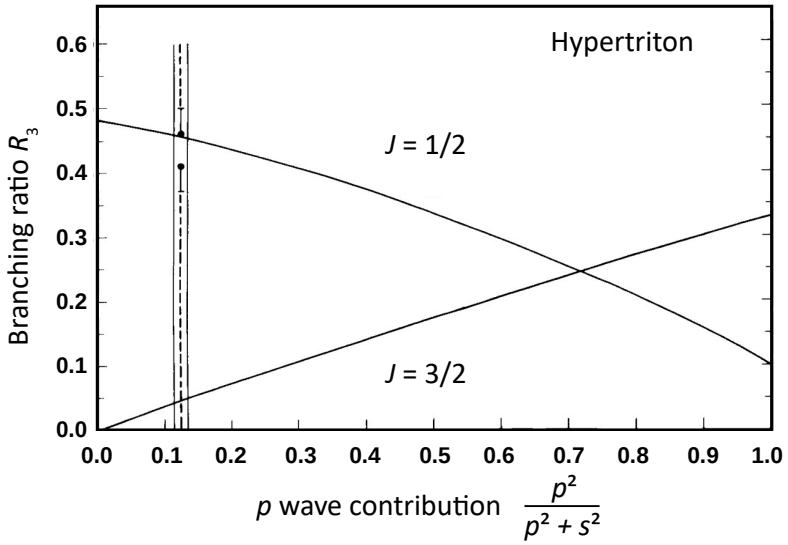

Figure 5.2.: Theoretical prediction of the connection between the R_3 branching ratio and the p wave contribution in free Λ decays for the hypertriton [46] (modified). By assuming the two different spin settings of $\frac{1}{2}$ and $\frac{3}{2}$, two different behaviors are found. The data which was available by 1970 already strongly indicated the spin $\frac{1}{2}$ setting.

So far, the $J^\pi = 1/2^+$ ground state was the only observed level in hypertriton. A hypothetical excited state ${}^3_\Lambda\mathrm{H}^*(I = 0,\ J^\pi = 3/2^+)$ would exceed the $\Lambda - d$ threshold, as many theories imply [99, 135, 209, 136, 296, 224, 77, 273, 272]. For the $I = 1$ triplet, no clear experimental evidence was found either. Only the neutral $nn\Lambda$ system may exist, as recent studies observed structures which can be interpreted as such [257]. These are shown in the following.

5.1.2. The neutral nnΛ

In 2013, invariant mass studies by HypHI reported events that may be interpreted as the bound $nn\Lambda$ state [257], shown in the left part of Figure 5.3. As indicated by the orange fit functions, a bump structure above background was observed. Consistent with the measured binding energy of about $1\,\mathrm{MeV}$, also the observed lifetime matches the typical range for a weak decay. However, when at JLab the $nn\Lambda$ state was sought by missing-mass spectroscopy via the ${}^3\mathrm{H}(e, e'K^+)$ reaction, no such structures were observed [287]. This is shown in the right part of Figure 5.3. Here, no significant peak was found. Therefore, only upper limits of the $nn\Lambda$ production cross-section were obtained.
Following the vague observation by HypHI, the search for the $nn\Lambda$ system in the ${}^6\mathrm{Li}$ + ${}^{12}\mathrm{C}$ reaction was repeated with an improved setup in the new studies in early 2022. The evaluation has yet to reveal, if the observed structure really corresponds to a bound $nn\Lambda$ system. The experiment is explained in more detail in Section 5.4.4 on page 68.

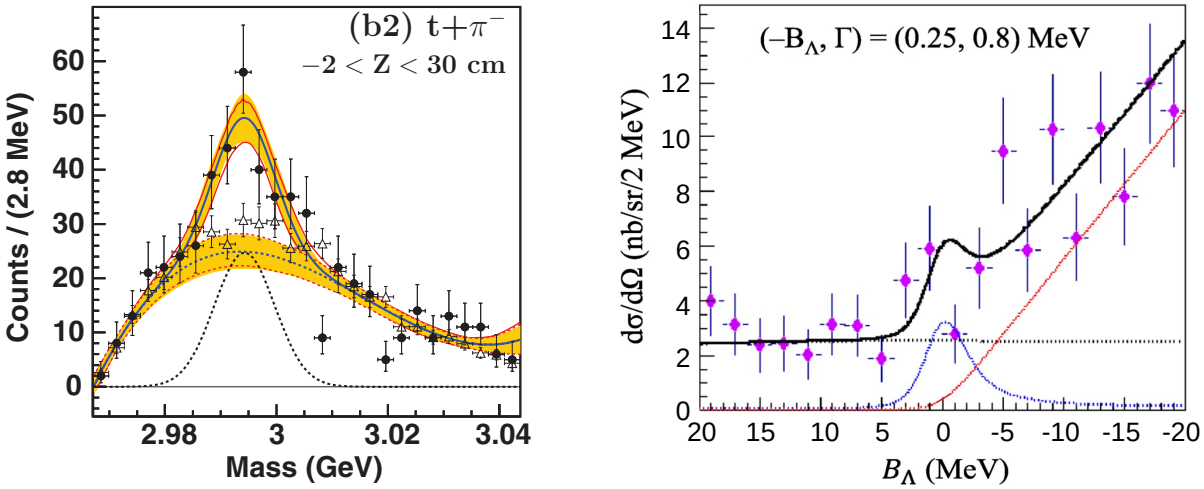

Figure 5.3.: Data situation for the $nn\Lambda$ system. **Left:** invariant mass spectrum observed from ^{3}H - π^- coincidences measured by HypHI in ^{6}Li - ^{12}C collisions at 2 A GeV [257]. The clear triangles represent the background distribution while the black dots describe the actual data. The broad bump may be caused by two-body decays of the $nn\Lambda$. **Right:** missing mass distribution measured in the ^{3}H $(e, e'K^+)$ reaction at JLab [287]. No significant structures indicating the presence of the $nn\Lambda$ state were observed.

5.1.3. The hypertriton

Since also for the smaller hypernuclei $n\Lambda$ and $p\Lambda$ there is no experimental evidence, after all, the hypertriton remains the simplest known hypernucleus. Hence it enables for the unique and most basic opportunity to study a system with three distinguishable particles and offers to compare theoretical predictions to actual experimental data.
Compared to its simplicity, however, the hypertriton became one of the most controversial hypernuclei due to a contradictory data situation for both its lifetime and its Λ binding energy. The community around hypernuclear physics was surprised mainly, when the first new measurement of the binding energy in 2020 – almost 50 years after the emulsion experiments – delivered a value more than three times larger than previously assumed [13]. The doubts had initially started by new lifetime measurements in the 2010's which pointed towards lower values than expected. While being compatible to the higher binding energy, the question arose whether the dynamics of the hypertriton were understood at all, resulting in the term *hypertriton puzzle* to summarize the unsatisfactory situation.
As a consequence, many new experiments around the world at versatile facilities were proposed and are partly already evaluated. But also in the next few years, many more studies will help to clear up the ambiguities. One of them is the decay pion spectroscopy experiment at the Mainz Microtron which was performed within the scope of this thesis.

In the following, the data situation for the hypertriton is going to be discussed in detail, also by making use of the results elaborated with the *Chart of Hypernuclides*.

5.2. Experimental Status of the Hypertriton

5.2.1. $^{3}_{\Lambda}$H binding energy

Emulsion data by Jurič

The results from the emulsion experiments by Jurič actually stem from three different first era experiments from which one was performed by himself. The other originate from previous publications of Bohm [53] and Gajewski [132]. In total, around 200 uniquely identified hypertriton events were collected and averaged to the widely known binding energy value of $130 \pm 50\,\mathrm{keV}$. Each author analysed both two-body and three-body events, $^{3}_{\Lambda}\mathrm{H} \rightarrow \pi^{-} + {}^{3}\mathrm{He}$ and $^{3}_{\Lambda}\mathrm{H} \rightarrow \pi^{-} + p + d$. The individual values are shown in the left panel of Figure 5.4 [11]. The published B_Λ values show a relatively wide spread from -100 to even $300\,\mathrm{keV}$, while still being consistent with each other due to the errors in the order of 100 to $200\,\mathrm{keV}$. In total, 176 two-body events and 46 three-body events are given. As a green band, the evaluated average by Jurič is shown. Within his analysis, he again applied selection criteria to the data by Bohm and Gajewski so that he ended up with a set of 204 events, which are shown in the histogram on the right side of Figure 5.4 [11].

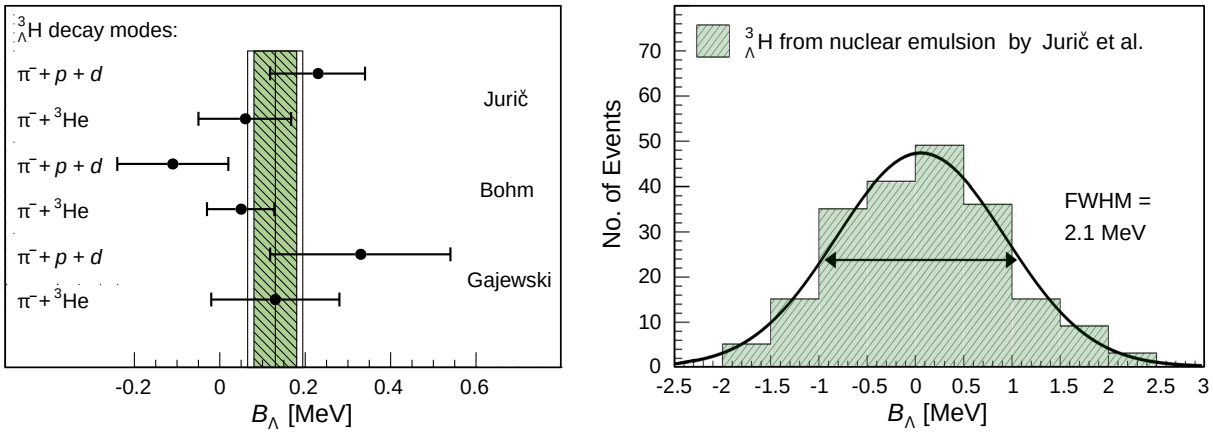

Figure 5.4.: Detailed consideration of the contributing data to Jurič's hypertriton binding energy value [11] (modified). **Left:** binding energies given by three emulsion experiments [165, 53, 132] separated by their decay channel, with purely statistical errors, 222 events in total. The mean value was evaluated to $B_\Lambda = 0.13 \pm 0.05\,\mathrm{MeV}$, shaded with the green band. **Right:** binding energy distribution of the combined data set. From the initial 222 events 204 were selected by Jurič and coworkers. The resulting width of $2.1\,\mathrm{MeV}$ is more than ten times larger than the extracted value itself.

The FWHM of the distribution is $2.1\,\mathrm{MeV}$ which corresponds to a standard deviation of $\sigma = 0.89\,\mathrm{MeV}$, if the distribution was Gaussian. Then, it would be allowed to determine the mean value with a statistical uncertainty of $\Delta B_\Lambda = 0.89\,\mathrm{MeV}/\sqrt{204} = 0.06\,\mathrm{MeV}$. Problematic is on the one hand, that the actually published error of $50\,\mathrm{keV}$ is $\sim 17\%$ smaller and on the other, that the treatment of systematic errors was ignored. Following the recommendation of Davis [94, 93], a systematic error of $40\,\mathrm{keV}$ was added to the value (compare to Chapter 4.3.5 on page 46), so that the total error is increased to $\pm 64\,\mathrm{keV}$. This error is shown as the white box in the left figure. How reliable the resulting value of $130 \pm 64\,\mathrm{keV}$ actually is though can hardly be told 50 years later. Today it depends on new experiments to rather confirm or refute the old data.

New data collection

With the literature study which was involves in the process of filling the database of the *Chart of Hypernuclides*, several more experiments from the first era were found besides the references involved in Jurič's value. One example is the earlier compilation provided by Prakash from 1961 [250]. These values were not included in Jurič's data set, but without any good reason to ignore them, they have to be included for the calculation of a new average value. Here, again, all emulsion values without any systematic error were treated with the $40\,\mathrm{keV}$ by Davis.
All these binding energy measurements are summarized in Table 5.1. In sum, besides Jurič's value, 4 more emulsion experiments as well as one bubble chamber experiment are found. Additionally to the values from the early days, two new data points were given recently by heavy ion collision experiments at STAR [13] and ALICE [24]. While $B_\Lambda = 102 \pm 63\,(\mathrm{stat.}) \pm 67\,(\mathrm{syst.})\,\mathrm{keV}$ by ALICE is in quite good agreement with the $130\,\mathrm{keV}$, the value by STAR is more than three times larger, being $B_\Lambda = 406 \pm 120\,(\mathrm{stat.}) \pm 110\,(\mathrm{syst.})\,\mathrm{keV}$. At the same time, it is four times larger than ALICE's value and they lie apart by roughly two standard deviations.
Despite this situation, an average value was calculated successfully from the data set by making use of the Chart's routines, found in Chapter 4.3. The resulting average [101] reads

$$\overline{B}_\Lambda({}^3_\Lambda\mathrm{H}) = 164 \pm 43\,\mathrm{keV}. \tag{5.2}$$

The respective weights and the compatibility of the data points with the average are also listed in the table. In addition, the data is visualized in the form of an ideogram, shown in Figure 5.5. Here, the contributing data points, the resulting average and its error as well as the summed up probability distribution is seen. The latter shows one maximum, which seems to be supported by just the newest ALICE value together with Jurič's value. The distribution also reveals a long tail pointing towards higher binding energies, mostly given by the new value of STAR.
While Jurič's binding energy value was the golden standard for a long time, it still today is the main influence on the average value with 44%, followed by ALICE's value which earns another 21%. The other weight is distributed quite smoothly across the other measurements. Considering the χ^2 values, only the STAR value is peaking out with 2.21. With the other values being moderate, the χ^2 sum is smaller than the ndf, so that no further treatment needed to be applied. After all, the hypertriton binding energy still is afflicted with a relative error of more than 25% [101]. How precise the resulting average actually is, remains hard to quantify, again due to the strong influence of the old data.

Table 5.1.: List of reported ${}^3_\Lambda$H binding energy values. The measurements before 1980 were assigned with an additional systematic error of $40\,\mathrm{keV}$ as suggested by Davis [94, 93].

Reference	**Year**	B_Λ [keV]	w	χ^2	**Method**	**Comment**
ALICE *prelim.*	2023	$102 \pm 63 \pm 67$	0.21	0.46	Heavy ion	
J. Adam [13]	2020	$406 \pm 120 \pm 110$	0.07	2.21	Heavy ion	
M. Jurič [165]	1973	$130 \pm 50 \pm 40$	0.44	0.29	Emulsion	includes [53, 132]
G. Keyes [177]	1970	250 ± 310	0.02	0.08	Bubble ch.	
K. Chaudhari [76]	1969	$240 \pm 120 \pm 40$	0.11	0.36	Emulsion	
C. Mayeur [204]	1966	$320 \pm 170 \pm 40$	0.06	0.79	Emulsion	
R. G. Ammar [28]	1962	$160 \pm 180 \pm 200$	0.03	0.00	Emulsion	includes [83]
Y. Prakash [250]	1961	$40 \pm 170 \pm 40$	0.06	0.51	Emulsion	incl. [27, 195, 300]
Our average:	2023	164 ± 43	1	4.69	$ndf = 7$	

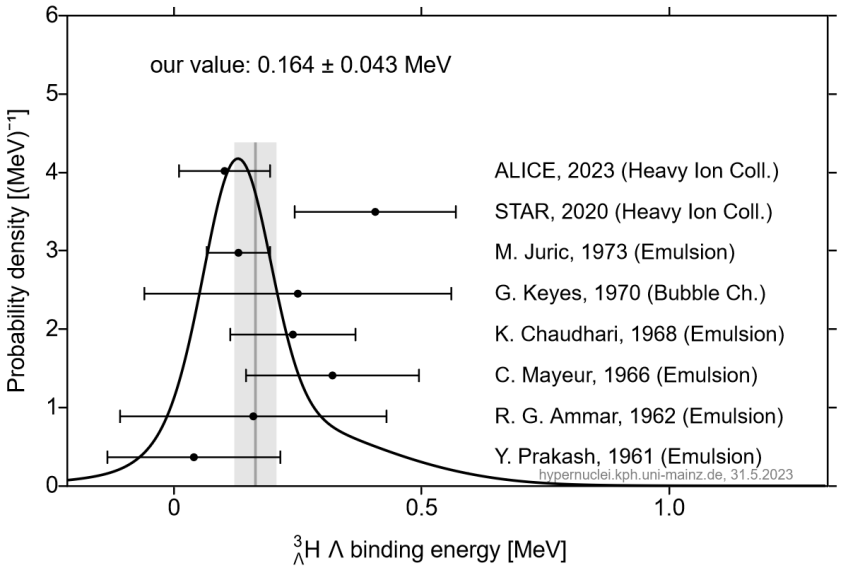

Figure 5.5.: Binding energies contributing to the average value of ${}^{3}_{\Lambda}\mathrm{H}$ [101]. While the newest value of STAR pointed towards a higher binding energy, the recent result of ALICE again supports the hypothesis of a low binding energy.

Further concerns

In contrast to the small systematic error assigned to the emulsion data, Gogami *et al.* observed discrepancies to newer results obtained with the (π^+, K^+) reaction in 2016 [140]. These are ranging from 400 to $800\,\mathrm{keV}$ and affected for example the ${}^{10}_{\Lambda}\mathrm{Be}$ binding energy data. While this was only observed for p-shell hypernuclei, it again raised the question if and to which degree offsets are also found for the smaller s-shell hypernuclei like the hypertriton. Independently, also the discussion about the re-calibration of the old emulsion data due to the outdated mass literature values [13, 192] intensified the distrust in the given data. While these procedures were not implemented into the *Chart of Hypernuclides* as described in Chapter 4.3.6 on page 47, they would have a huge impact on the ${}^{3}_{\Lambda}\mathrm{H}$ binding energy, scaling the value up by a factor of 2 to 3.
To summarize, the data situation of the hypertriton Λ binding energy is far from being perfect. Several flaws are given by the doubtful quality of the first era data, be it their reproducibility, systematic error or even shifts due to outdated literature values. At the same time, also the new data does not seem to contribute to a consistent picture as well. Answers will hopefully be given by new upcoming experiments. Some of them will be introduced in Section 5.4.

5.2.2. ${}^{3}_{\Lambda}\mathrm{H}$ lifetime

For the lifetime of the hypertriton, a rich set of data is available. It includes 18 different values from various experiments. The older values from the 1970's and earlier were performed with the emulsion and bubble chamber technique, while the newer stem from heavy ion collision experiments. The data is shown in Table 5.2 and an average value of

$$\overline{\tau}({}^{3}_{\Lambda}\mathrm{H}) = 237\,{}^{+10}_{-\ 9}\,\mathrm{ps} \tag{5.3}$$

is computed. Similar to the binding energy of the hypertriton, its lifetime also fell into the focus of hypernuclear physicists after a series of measurements between 2013 and 2018 claimed lower and lower lifetime values than initially indicated by theories and the first era experiments.

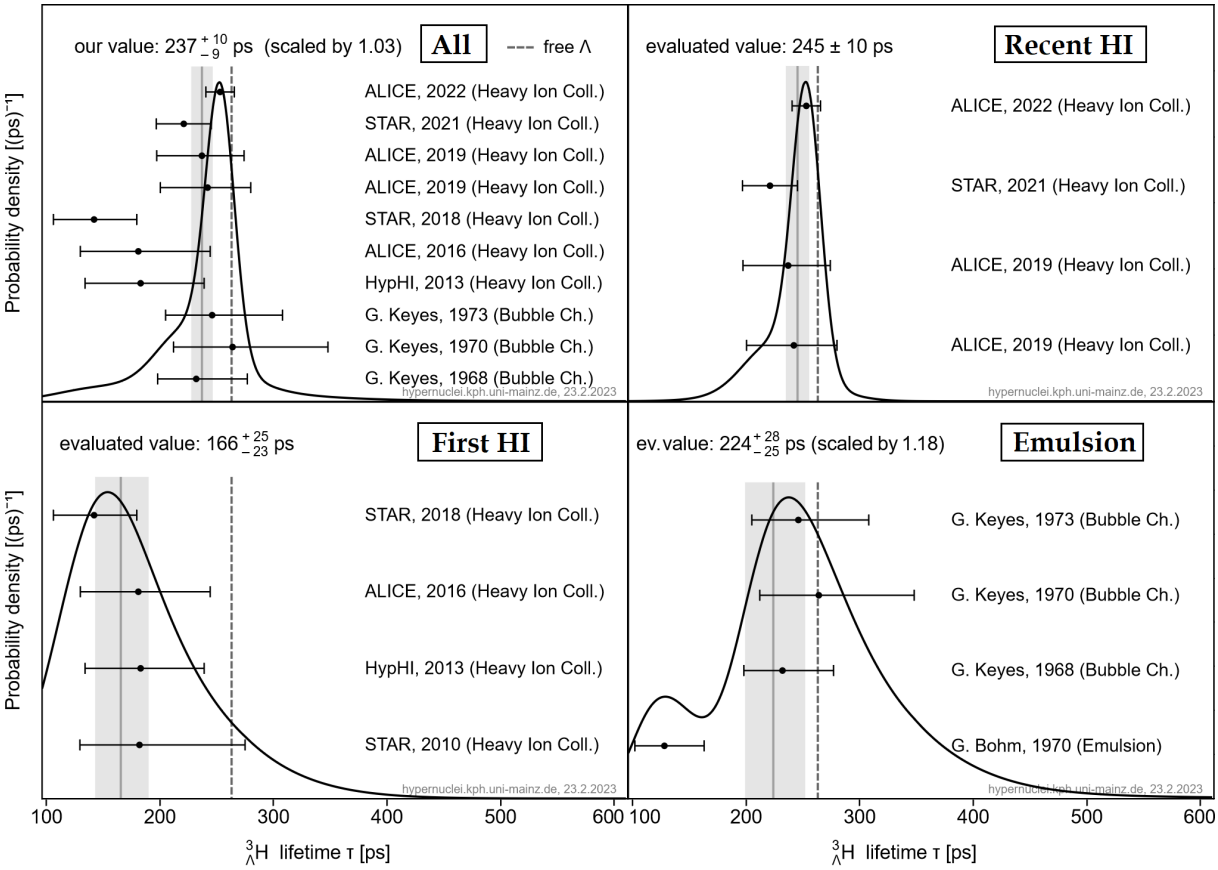

Figure 5.6.: Multiple ideograms depicting the data situation of the hypertriton lifetime. Different data sets have been selected: **Top left:** all relevant data sets with the overall average of 237^{+10}_{-9} ps. **Top right:** latest data from heavy ion collision experiments, 245 ± 10 ps. Only slightly higher than the overall average. Also the probability distribution looks very similar, indicating the strong presence of these values in the overall average. **Bottom left:** earlier heavy ion collision data. With just 166^{+25}_{-23} ps the result is three standard deviations lower than in the other cases. **Bottom Right:** data from first era imaging experiments: 224^{+28}_{-25} ps. All figures were generated with the *Chart of Hypernuclides* [101].

The present data situation is illustrated in Figure 5.6, where four different ideograms about this lifetime are shown. The one in the top left depicts the complete set of data while the top right only shows the recent heavy ion collision values, the bottom left the earlier heavy ion values and the bottom right the first era data. All ideograms share the same lifetime scale, so that the differences between these data sets are quickly observed visually. Comparing the top ideograms, the resulting probability curve appears almost identical despite the fact, that in the right one, only a fraction of the data set is used. This is explained by the strong weight of 78% the four recent values receive in the overall calculation. The exact numbers are found in Table 5.2. Also the average values are nearly identical and lie close to the free Λ lifetime (dotted line).

The values from the first heavy ion collision experiments draw a completely different picture. Their average value is found to be around 70 ps lower than the others, being equivalent to three standard deviations, given the error of ≈ 24 ps. The old data at the bottom right in contrast was usually hampered by low statistics [54, 174], so these early measurements did not yet allow for too specific conclusions. Still, the average value is more in favor of the long lifetime.

Facing again the complete set of data in Table 5.2, many values were excluded from the average

calculation, mainly due to large uncertainties which result in low weights. Another observation is the distribution of the χ^2 values, where especially the STAR value from 2018 strongly peaks out with 5.55. The resulting χ^2 sum hence slightly exceeds the ndf of 9, so that an additional scaling of the error by 1.03 needed to be applied. A description of the selection and scaling procedures is to be found in Chapter 4.3.5 on page 46.
While in the recent years great improvements about the lifetime of the hypertriton were achieved, it still remains unanswered why the first heavy ion results differed so much and so consistently from the recent ones.

Table 5.2.: List of reported ${}^3_\Lambda$H lifetime data. Many values are available, also many were excluded for several reasons. From the remaining data, the recent ALICE value dominates the average with more than 50%. The resulting error of the average had to be scaled up by 1.03 to address slight ambiguities in the data set.

Reference	**Year**	**Lifetime τ** [ps]	w	χ^2	**Method**	**Comment**
ALICE [24]	2022	$253 \pm 11 \pm 6$	0.53	1.63	Heavy ion	
M. S. Abdallah [5]	2021	$221 \pm 15 \pm 19$	0.14	0.44	Heavy ion	
S. Trogolo [298]	2019	$237 \,^{+\,33}_{-\,36} \pm 17$	0.06	0.00	Heavy ion	
S. Acharya [8]	2019	$242 \,^{+\,34}_{-\,38} \pm 17$	0.05	0.02	Heavy ion	
L. Adamczyk [14]	2018	$142 \,^{+\,24}_{-\,21} \pm 29$	0.05	5.55	Heavy ion	
J. Adam [12]	2016	$181 \,^{+\,54}_{-\,39} \pm 33$	0.02	0.73	Heavy ion	
C. Rappold [255]	2013	$183 \,^{+\,42}_{-\,32} \pm 37$	0.03	0.87	Heavy ion	
G. Keyes [174]	1973	$246 \,^{+\,62}_{-\,41}$	0.04	0.04	Bubble ch.	
G. Keyes [177]	1970	$264 \,^{+\,84}_{-\,52}$	0.03	0.24	Bubble ch.	
G. Keyes [176]	1968	$232 \,^{+\,45}_{-\,34}$	0.05	0.02	Bubble ch.	
B. I. Abelev [6]	2010	$182 \,^{+\,89}_{-\,45} \pm 27$	–	–	Heavy ion	low weight
S. Avramenko [34]	1992	$240 \,^{+170}_{-100}$	–	–	Heavy ion	low weight
G. Bohm [54]	1970	$128 \,^{+\,35}_{-\,26}$	–	–	Emulsion	bad χ^2 to w ratio
R. Phillips, J. Schneps [240]	1969	$285 \,^{+127}_{-105}$	–	–	Emulsion	low weight
Y. W. Kang [171]	1965	$80 \,^{+190}_{-\,30}$	–	–	Emulsion	low weight
R. Prem, P. Steinberg [251]	1964	$90 \,^{+220}_{-\,40}$	–	–	Emulsion	low weight
L. Fortney [193]	1964	$63 \,^{+\,50}_{-\,30}$	–	–	Bubble ch.	low weight
M. M. Block [193]	1964	$105 \,^{+\,20}_{-\,18}$	–	–	Bubble ch.	[1]
Our average:	2023	$237 \,^{+\,10}_{-\,\,9}$	1	9.53	$ndf = 9$	scaled by 1.03

[1] This value is lacking of a systematic error. In addition the group's cross check value of the free Λ lifetime of 236 ± 6 ps published in [51] is too low given the error interval. This systematic shift is expected to also affect the hypertriton lifetime and hence it is neglected.

5.3. The Hypertriton Puzzle

As shown in the previous section, both the bubble chamber and emulsion data from the 1960's and 1970's were – albeit with large uncertainties – consistent with the picture of a weakly bound, almost free Λ inside the hypertriton. This perspective was more and more doubted when the first series of heavy-ion collision experiments found consistently a lifetime which is about 30-40% shorter than the free Λ lifetime. The combination with its weak Λ binding energy and low mass number became one of the most intriguing puzzles in hypernuclear physics [134, 87]. The basic principle – a lowered lifetime due to close contact with many other nucleons (compare to *Λ decays* in Chapter 2.2.1 on page 12) – did not seem to apply anymore. This situation was referred to as the *hypertriton puzzle*. With STAR's large binding energy value from 2020 [13] the story seemed to take another turn towards the "strong-bound, short-lived" hypothesis. Only with the most recent heavy ion data, which supports the initial picture, the situation has eased.
In the following, a detailed description of the unique hypertriton system is to be found aside of the results of theoretical predictions and their comparison to the present data situation.

5.3.1. The ultimate halo nucleus?

The hypertriton system is – as it is composed of a $\Lambda - d$ pair – unique in terms of the spatial distribution of the nucleons. While the proton and neutron in the deuteron are known to be bound with $B_d \approx 2.2\,\mathrm{MeV}$, the bond of the Λ is comparably low with only $B_\Lambda \approx 0.16\,\mathrm{MeV}$. It is therefore implied that the proton and neutron are located relatively close to each other while the Λ is found at greater distances, forming a so-called *halo* around the deuteron. More quantitatively, the characteristic radius of a two-body s-wave halo system is given by

$$\langle r^2 \rangle = \hbar^2/(4\mu B), \tag{5.4}$$

where μ is the reduced mass of the system and B the binding energy [120, 262, 196]. For the Λ in ${}^{3}_{\Lambda}\mathrm{H}$ this corresponds to a radius of $\sqrt{\langle r^2 \rangle} \approx 10\,\mathrm{fm}$, while for the deuteron only $R \approx 3\,\mathrm{fm}$ are expected. This puts the hypertriton on the same size scale as a lead nucleus.
A comparison of the hypertriton to other halo systems is given in Figure 5.7 [262]. Here, the halo size $< r^2 >$ divided by the core size R^2 is evaluated for several halo nuclei and plotted against their binding energy B scaled by $\mu R^2/\hbar^2$. Compared to other nuclear halo systems, the hypertriton's size proportion is outstanding. It is only topped by the ${}^{4}\mathrm{He}_2$ molecule. This makes the ${}^{3}_{\Lambda}\mathrm{H}$ one of the most impressive halo system in nuclear physics [262]. This structural appearance is supported by modern structure calculations of the hypertriton, as the two ones shown in Figure 5.8 [313, 221]. Here, the predicted density distributions of the nucleons N and the hyperon Λ are shown. They both provide a similar geometrical picture as illustrated in the sketch on the left side [245].
Following these circumstances, the contact of the Λ with the nucleons is limited, so that its behavior is expected to be comparable to that of the single free Λ [99]. Only if the Λ was bound strongly, the chances of non-mesonic weak decays would be enhanced, lowering the lifetime of the hypernucleus (compare to Chapter 2.2.1 on page 12). For the hypertriton, in fact, all available calculations of the ${}^{3}_{\Lambda}\mathrm{H}$ lifetime predict values which deviate no more than about 10% from the free Λ decay [91, 259, 47, 253, 201, 187, 146, 139, 167]. For example, Gal and Garcilazo obtained a value of 10% lower by solving three-body Faddeev equations [133]. By also including the pion final-state interaction, the value is reduced to about 84% τ_Λ which is consistent with the recent heavy ion data.

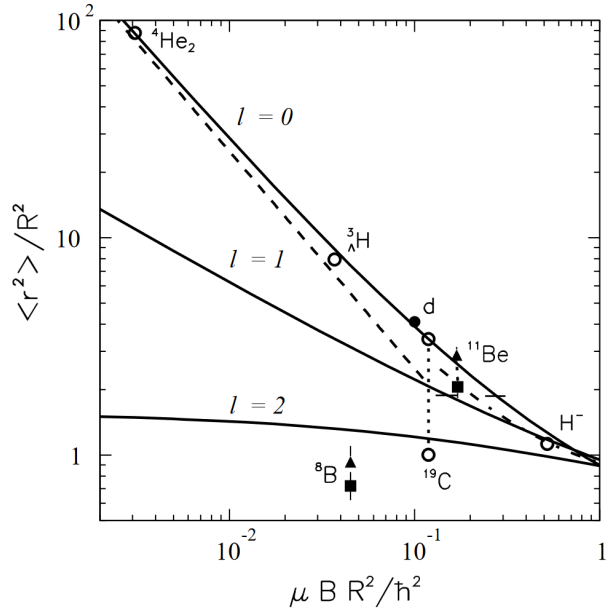

Figure 5.7.: Size comparison of the hypertriton to multiple other halo systems [262]. The fraction of the halo size $< r^2 >$ to the core size R^2 is plotted against the scaled binding energy.

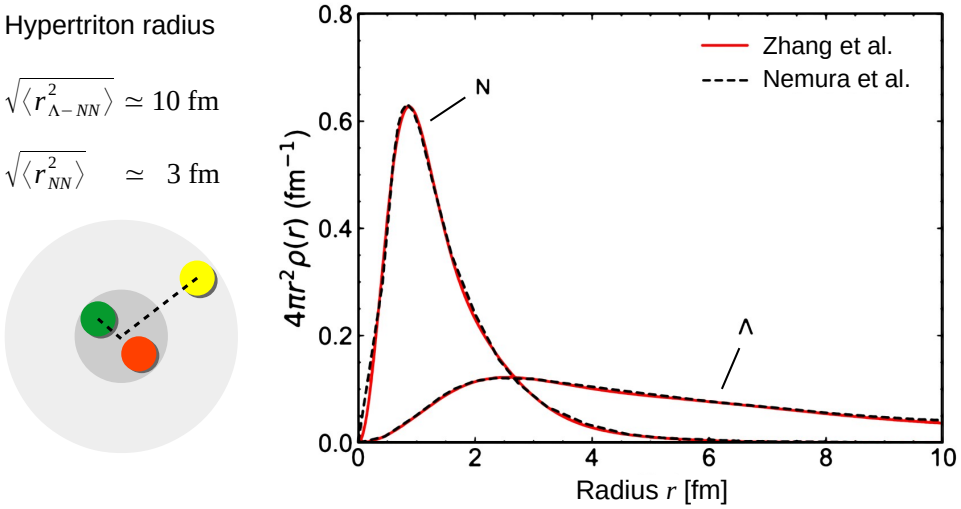

Figure 5.8.: Distribution of the nucleons and the hyperon inside hypertriton. **Left:** geometrical picture as quasi-two-body bound system with a deuteron as core and a Λ-halo [245] (modified). **Right:** density distributions of the nucleons (N) and the Λ hyperon in hypertriton as functions of the distance r from the center-of-mass of proton and neutron [313]. Black dashed lines are theoretical results from [221], red solid lines show results from [313].

5.3.2. Connection between lifetime and binding energy

Beyond the predictions about the lifetime alone, modern microscopic three-body calculations make it possible to connect hypertriton's lifetime with its binding energy [156, 239].

Figure 5.9 shows the folded lifetime and binding energy probability distribution given by the *Chart of Hypernuclides* as a contour plot. As determined by the individual distributions (Figure 5.5 and the top left of Figure 5.6), a peak is found at their respective maxima, being at a comparably low binding energy and a long lifetime. Still for both properties, a small tail pointing towards the "strong-bound and short-lived" hypothesis is found.

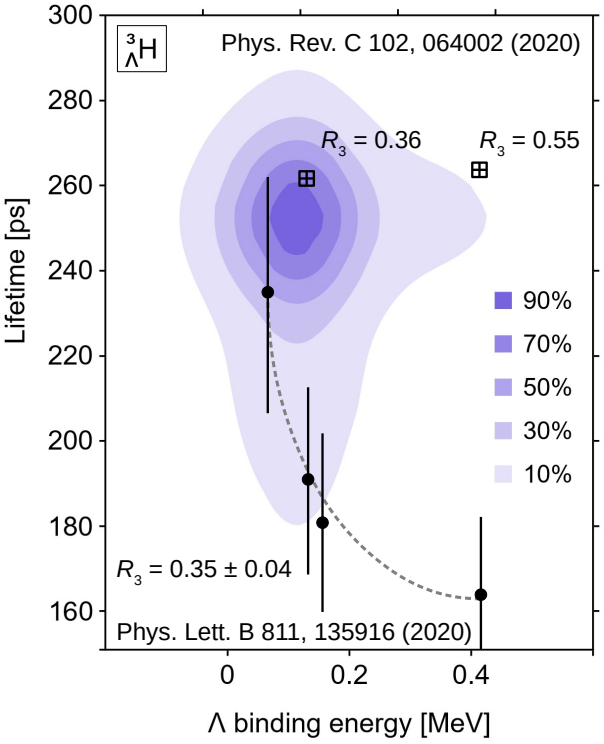

Figure 5.9.: Contour plot of the *pdf* folding integral for the binding energy and lifetime data of hypertriton [101] compared with two model predictions [156, 239]. While for both properties a tail points towards the "strong-bound and short-lived" hypothesis, the maximum is found at low binding energies and long lifetimes. The theories seem to confirm this behavior.

The contour is compared to two recent theories, one by Hildebrand and Hammer [156] and one by Pérez-Obiol *et al.* [239]. The first prediction is given by the quadratic boxes, and if a branching ratio of $R_3 = 0.36$ is used as input, a quite satisfying consensus with the contour's maximum is found. This R_3 value is so far the best estimate from the given experimental information, so the data point which uses $R_3 = 0.55$ seems rather non-physical. This needed to be assumed to re-create a system with the binding energy being as large as published by STAR in 2020 [13]. A closer look reveals that the lifetime prediction is compatible with the free Λ lifetime, which seems to be an over-estimation compared to the contour. An explanation might be given by the fact that for these calculations pionic final state interactions were not taken into account. According to [133, 239] these could reduced the lifetime by about 10%.

Also the other theoretical model – constraint with the physical R_3 value – predicts a data point close to the contours maximum. For larger binding energies like the STAR value, the system would have to be shorter-lived by around 30%, but these data points seem rather unlikely due to the given data situation.

5.3.3. Is the puzzle solved?

With the newest heavy ion data, the best estimate for the lifetime has moved closer to the free Λ lifetime and also the tendency of a stronger binding energy could not be confirmed by the recent ALICE data. Anyway, the experimental status on both of hypertriton's properties still is dissatisfactory for multiple reasons. The *hypertriton puzzle* has more turned into a quantitative problem, calling for precision studies, on the experimental as well as on the theoretical side.

5.4. Upcoming ${}^{3}_{\Lambda}$H Experiments

In this section, some of the upcoming hypertriton experiments are going to be explained in closer detail. Besides continued efforts at the heavy ion facilities, some unique and so far not explored approaches are going to be applied.

5.4.1. Modern emulsion experiment at J-PARC

As proposed by Liu *et al.* [192, 191], the modern emulsion experiment from J-PARC may allow for a new measurement of the hypertriton binding energy with statistical and systematic uncertainties of about $30\,\mathrm{keV}$ each. An example for a hypertriton event from this experiment was already shown in Figure 3.4 on page 27. Recently, a proof of concept was started with the analysis of ${}^{4}_{\Lambda}$H events from the same sample of emulsion plates. A preliminary result is shown in Figure 5.10 [266]. Here, many single events are plotted, more than 50 in total. These are fitted

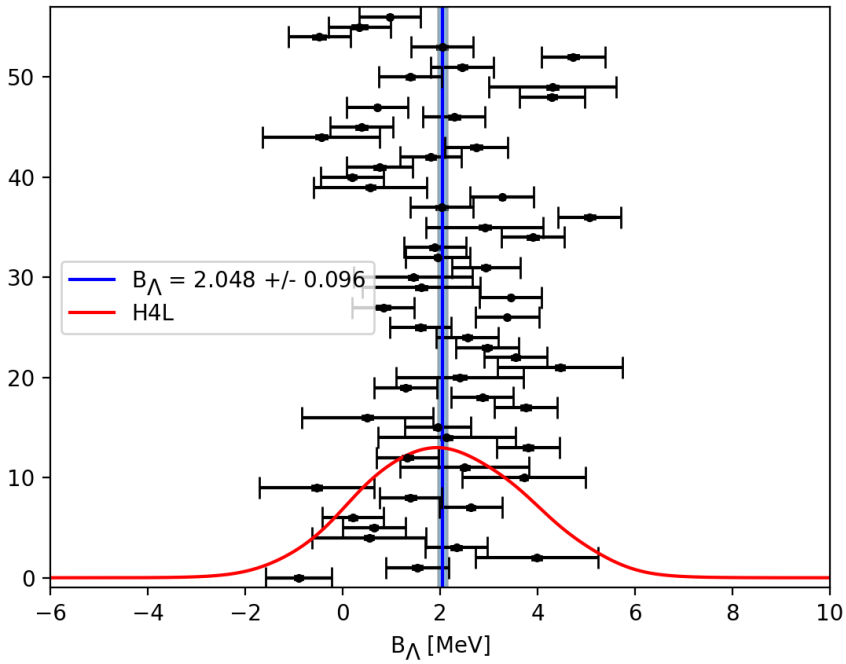

Figure 5.10.: Preliminary result for the evaluation of ${}^{4}_{\Lambda}$H events in emulsion samples [266].

with a Gaussian in red and the resulting average is marked with the blue band. The given error of roughly $100\,\mathrm{keV}$ is right now purely of statistical nature. It is expected to decrease strongly with the progressing analysis, since right now only 0.4% of the sample were analysed. The average seems to be compatible with Chart's value of $2.169 \pm 0.042\,\mathrm{MeV}$ [101].
However, the systematic error is yet unknown. Compared to the first era emulsion experiments, many improvements have been applied to the emulsion setup. One is the implementation of long-lived radioactive nuclei into the emulsion. These produce their own decay events in the material which can act as a well defined energy loss monitor. Another is the analysis via machine learning approaches, which guarantee a faster scan of the plates compared to the analysis by hand from the 1970's. Still there is a wide spread observed in the single data points, currently at a FWHM of around $4\,\mathrm{MeV}$. The continued analysis efforts have to show, which accuracy actually is to be expected and how well the method also can be adopted for the hypertriton.

5.4.2. Start-Stop measurement at ELPH

An example for a unique new experiment is the study at ELPH, where the hypertriton lifetime is going to be determined by a start-stop measurement. The setup is shown schematically in

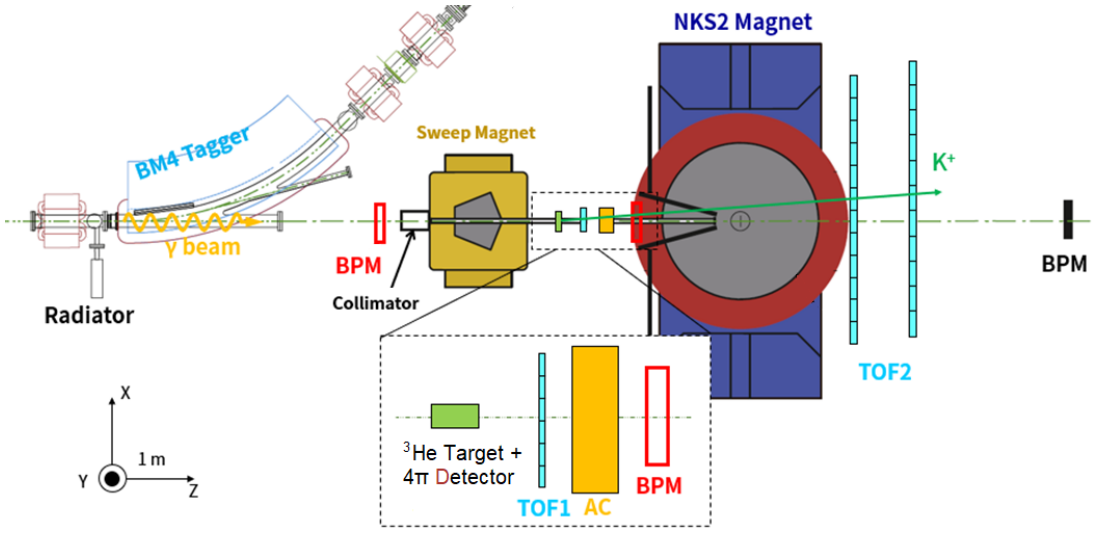

Figure 5.11.: Sketch of the hypertriton lifetime experiment at ELPH [214].

Figure 5.11 [214]. On the left, a photon beam is produced off the synchrotron electron beam. These photons are tagged and collimated to hit the target cell in the center. This cell holds $^{3}\mathrm{He}$ as target material, so that the reaction

$$^{3}\mathrm{He}(\gamma, K^{+})^{3}_{\Lambda}\mathrm{H} \tag{5.5}$$

can take place. The emitted kaon is studied by multiple detector components, one being a drift chamber inside of the NKS2 magnet to determine the kaon momentum with $\Delta p/p \approx 10^{-3}$. Additionally, the time-of-flight scintillators TOF1 and TOF2 offer to measure the kaon's flight time, so that its time of production at the target can be extracted. Together with the NKS2 magnet, TOF2 also enables for a rough kinematic study, so that hypertriton events can be separated from background by their missing mass. Finally the Aerogel-Čerenkov detector AC improves the kaon identification. The target cell is surrounded by a 4π detector to register the emitted decay pions of the hypertriton. By that, the hypertriton lifetime can be extracted from the time difference between the kaon emission and the pion detection [214]. The detector setup is planned to be operational by early 2024 so that the data taking is expected within the same year.

5.4.3. Halo experiment at NuStar

This experiment aims to directly probe the halo character of ${}^{3}_{\Lambda}\mathrm{H}$, by studying its absorption behavior in nuclear matter. Therefore, a $^{12}\mathrm{C}$ beam with $2\ A\,\mathrm{GeV}$ will hit a $^{12}\mathrm{C}$ target to produce various hyperfragments including ${}^{3}_{\Lambda}\mathrm{H}$ at around projectile rapidity [63]. About $10\,\mathrm{cm}$ behind this target, these fragments will then pass a secondary carbon target, as the first one $5\,\mathrm{cm}$ thick. The hyperfragments will be detected by measuring their pionic two-body decay.
A simulated result of this method is shown in Figure 5.12 [23]. The x-axis denotes the decay vertex on a centimeter scale, on which also the two targets are marked with light gray bars. Inside the targets, on the one hand hyperfragments are produced, which increases the ${}^{3}_{\Lambda}\mathrm{H}$ rate, but on the other, also absorptions may take place. Some hypertritons lose their rapidity and

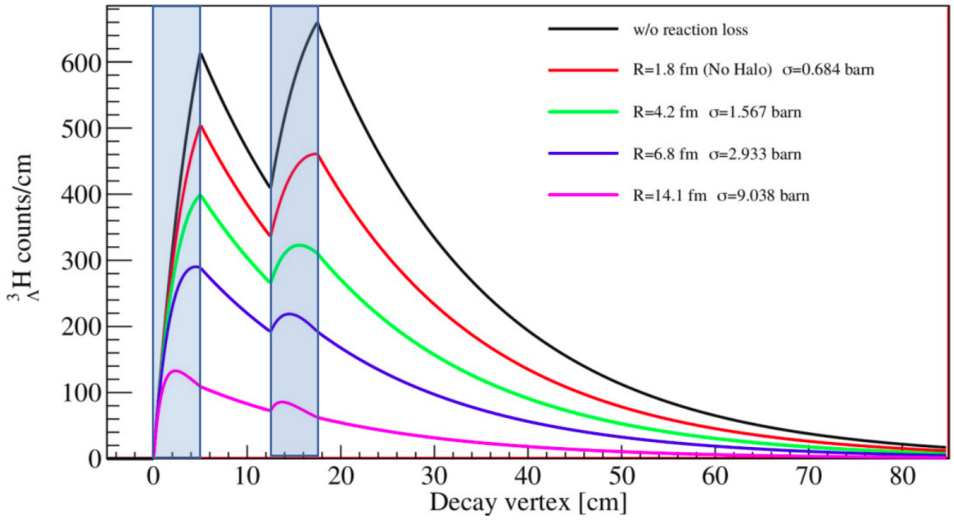

Figure 5.12.: Simulated data of the hypertriton radius experiment at GSI [23]. Two thick targets will be used (shaded areas), in which a traversing beam will produce hypertritons.

therefore their decay products are not boosted forward anymore, while others collide with target nuclei which causes their destruction. In consequence, the amount of detected hypertriton decays under forward direction will significantly decrease, the more hypertritons are absorbed. In the simulation, various radii for the hypertriton were assumed which are linked to different absorption cross sections. At first glance, the count rates for the most extreme cases, a radius of $14\,\mathrm{fm}$ and non-interacting hypertriton (basically $R = 0$) differ strongly by around a factor of 6. However, by observing the absolute rate, still a strong influence of the not exactly known hypertriton production cross section is given. Therefore, this experiment makes use of two targets, to study their relative count rate. As one can see, for small hypertriton radius, the count rate at the second target may even exceed the one of the first target, while for the large radii the first target is stronger. By evaluating this relation, the study can be performed without knowing the production cross section [23].

5.4.4. Lifetime study at WASA-FRS HypHI

From January till March 2022, the WASA-FRS HypHI experiment was performed at GSI to measure the hypertriton and $^4_\Lambda$H lifetime, as well as to re-examine the hints for the $nn\Lambda$. The beam line of the experiment is depicted in Figure 5.13 [268, 112]. On the top, the beam line with incoming beam, WASA detector and the following fragment separator are shown. On the bottom, a closeup of the setup is given. From the left, ^{6}Li projectiles at $1.96\,A\,\mathrm{GeV}$ are hitting a diamond target with a thickness of $9.87\,\mathrm{g/cm^2}$, where hyperfragments including $^3_\Lambda$H are produced. While the decay pions from two-body decays are observed by WASA, the residual nuclei after the decay are selected and measured by the FRS [112].
The strength of this experiment is the combined use of the close-to-4π detector WASA (Wide Angle Shower Apparatus) and the precise fragment separator. While WASA allows for the detection of as much decay pions as possible, FRS acts as a great background suppressor, since only ^{3}He fragments will be detected (besides small background by fragments with equal A to Z ratio). Furthermore, WASA is capable of a combined pion momentum and decay vertex study, allowing for a lifetime extraction with an expected accuracy of $8\,\mathrm{ps}$. While for the hypertriton the invariant mass resolution may not be sufficient compared to other studies, it will shed light on the question, if the previously observed $nn\Lambda$ structure is real (compare to Figure 5.3 on page 57).

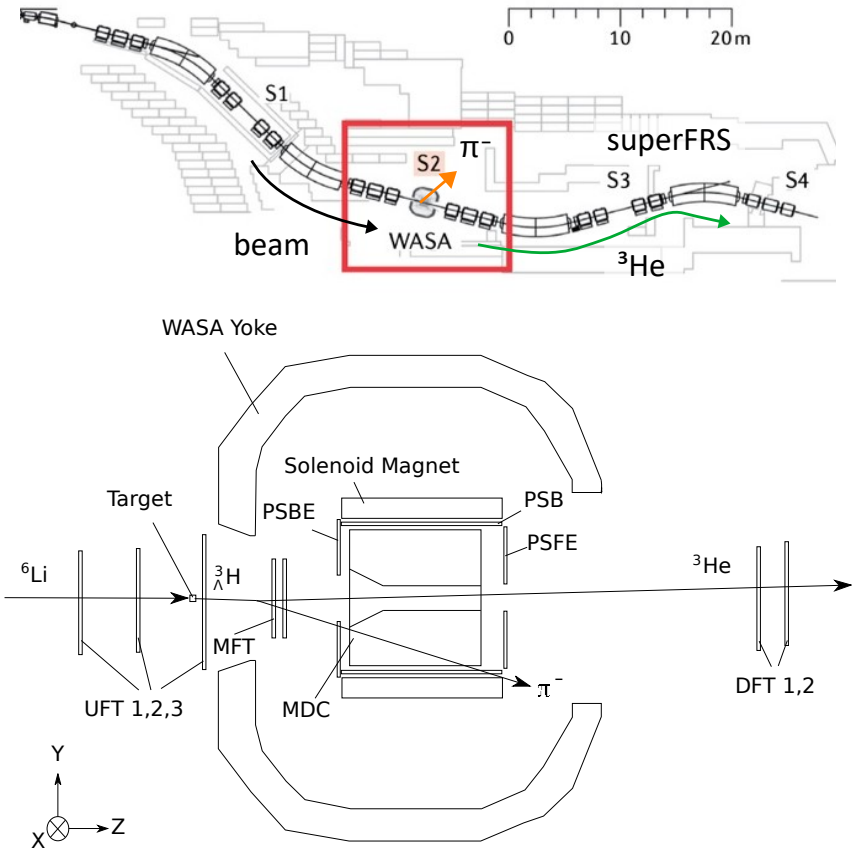

Figure 5.13.: Sketch of the improved HypHI experiment at GSI with the WASA detector [268, 112]. **Top:** schematic view of the beam line. **Bottom:** detailed view of the interaction region, the beam enters from the left and hits a target just in front of the WASA detector. The decay pions are going to be observed with WASA, whereas the remaining ${}^{3}\mathrm{He}$ fragment is going to be identified with the FRS fragment separator.

5.4.5. JLab missing mass experiment

At JLab, the first attempts of studying the lightest hypernuclei via the $(e, e'K^{+})$ reaction were performed already in the early 2000's by Dohrmann *et al.*, but the results remained rather unclear [97, 98]. Only wide and flat bump structures were observed, mostly due to a resolution limited to around $2\,\mathrm{MeV}$. However, these experiments acted as a proof of principle for the upcoming study.

Much work has been done in improving the overall resolution, by enhancing the beam stability and calibration runs so that now 65 to $100\,\mathrm{keV}$ may be reached [144]. Another major change is the installation of the new PCS magnet (seen in the left of Figure 5.14). It acts as a charge sensitive particle separator, so that the scattered electron as well as the produced kaon are bent away from the beam line. Only after that, they are respectively detected in the spectrometers HRS and HKS. Hence the PCS magnet effectively allows for studying these particles at lower angles than it was initially possible by the space requirements of the two spectrometers. At lower angles, the Λ production cross section is maximized.

The direct production of the hypertriton is going to be performed with a ${}^{3}\mathrm{He}$ target. By that it is still questionable, in which configuration the hypernucleus will be created. Simulations indicate, that an excited state with spin $\frac{3}{2}$ may be favored by a factor of 8 [144, 202], as shown

in Figure 5.14. However, until now it remains unknown, if such an excited state exists. Other than that, the production of ground state hypertritons is not impossible, but it seems strongly suppressed. The results of the experiment have to show, if the extraction of the ground state and excited state binding energies is successful.

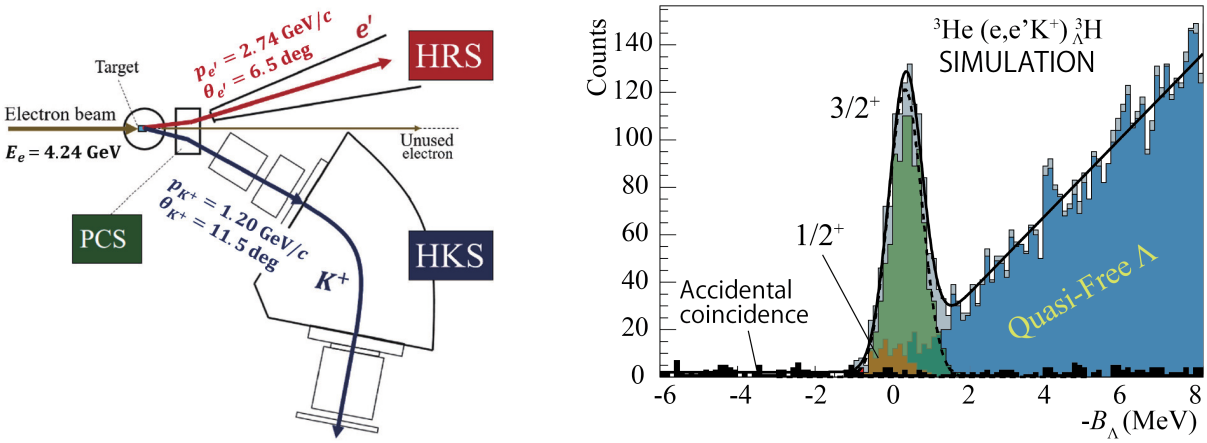

Figure 5.14.: Planned hypertriton experiment at JLab. **Left:** experimental setup [144], showing the incoming electron beam on the left. As it hits the target, the electron may get scattered and a kaon produced. With the PCS magnet they are bent towards the spectrometers HRS and HKS. **Right:** simulation results of the expected missing mass spectrum [144]. If the yet unknown $\frac{3}{2}^+$ state exists, it would be strongly favored in the production [202].

5.4.6. Summary

Various facilities will probe the characteristics of the hypertriton so that within the next 5 years the data situation may have improved significantly. A summary of all planned and yet to be evaluated experiments is found in Table 5.3. Finally, also the MAMI data taken within this thesis will contribute to bring further clarification in the near future. In the following chapters, the preparation and commissioning of this experiment will be described.

Table 5.3.: Summary of the upcoming hypertriton experiments. For the expected accuracy, statistical and systematic error estimates are added in squares.

Facility	Property	Exp. Method	Accuracy	Ref.
ALICE	B_Λ and τ	Central collisions	< 25 ps	[80]
STAR	B_Λ and τ	Central collisions		
HypHI	τ	Peripheral collisions	8 ps	[112]
NuStar	halo character	Peripheral collisions	–	[23]
JLab	B_Λ and excitation	$^3\mathrm{He}(e,e'K^+)^3_\Lambda\mathrm{H}$	65 keV	[144]
J-PARC E73	τ	$^3\mathrm{He}(K^-,\pi^0)^3_\Lambda\mathrm{H}$	30 ps	[199]
ELPH	τ	$^3\mathrm{He}(\gamma,K^+)^3_\Lambda\mathrm{H}$	10 ps	[214]
J-PARC E07	B_Λ	Emulsion	42 keV	[192]
MAMI	B_Λ	Decay pion spectroscopy	20 keV	*this work*

6. Introducing the A1 Collaboration at MAMI

6.1. The Mainz Microtron

The MAMI is the electron accelerator of the Institute for Nuclear Physics at the Johannes-Gutenberg University Mainz. It is set up as a multi stage race track microtron (RTM) with normal conducting linear accelerators. The RTM principle foresees to guide a particle beam through the same accelerator section for multiple times which allows for compact and energy efficient designs.
A floor plan of the facility is shown in Figure 6.1 [276]. The first stage, MAMI-A is located together with the electron source in the hall on the left. It consists of a small linear accelerator section and two following RTMs. This setup delivers a maximum electron energy of $180\,\mathrm{MeV}$ and purely acts as pre-accelerator for the second stage MAMI-B, where the RTM-3 is operating. It delivers electrons with an energy ranging from 180 to $855\,\mathrm{MeV}$, depending on the number times, the beam was passed through the RTM3. This energy range is quantized to 90 turns. From there, the beam can directly be guided to the experiments at the X1, A2 and A1 halls.
For even higher energies the final stage MAMI-C was added in the late 2000's. This so called "Harmonic Double Sided Microtron" HDSM accelerates the electrons up to a final energy of $1.6\,\mathrm{GeV}$ [166] to be used for experiments at A2 and A1.
In general, a huge variety of beam currents is possible at the MAMI facility, ranging from almost single electrons with $10\,\mathrm{pA}$ up to $100\,\mu\mathrm{A}$. At the same time it also delivers a high spatial resolution of several tenth of a millimeter and a stable beam energy, so that the accelerator is well-suited for high precision experiments. Several groups of physicists as well as international cooperation partners are performing experiments at MAMI with very versatile setups. One of them is the A1 Collaboration, where also hypernuclear studies are performed.
Next to A2, a new hall for the MESA project is under construction. It will house the new independent Mainz Energy-recovering Superconducting Accelerator, which will give the opportunity for new experiments with low energy electron beams at highest intensities of up to $1\,\mathrm{mA}$. For later phases, currents of even $100\,\mathrm{mA}$ are planned [285].

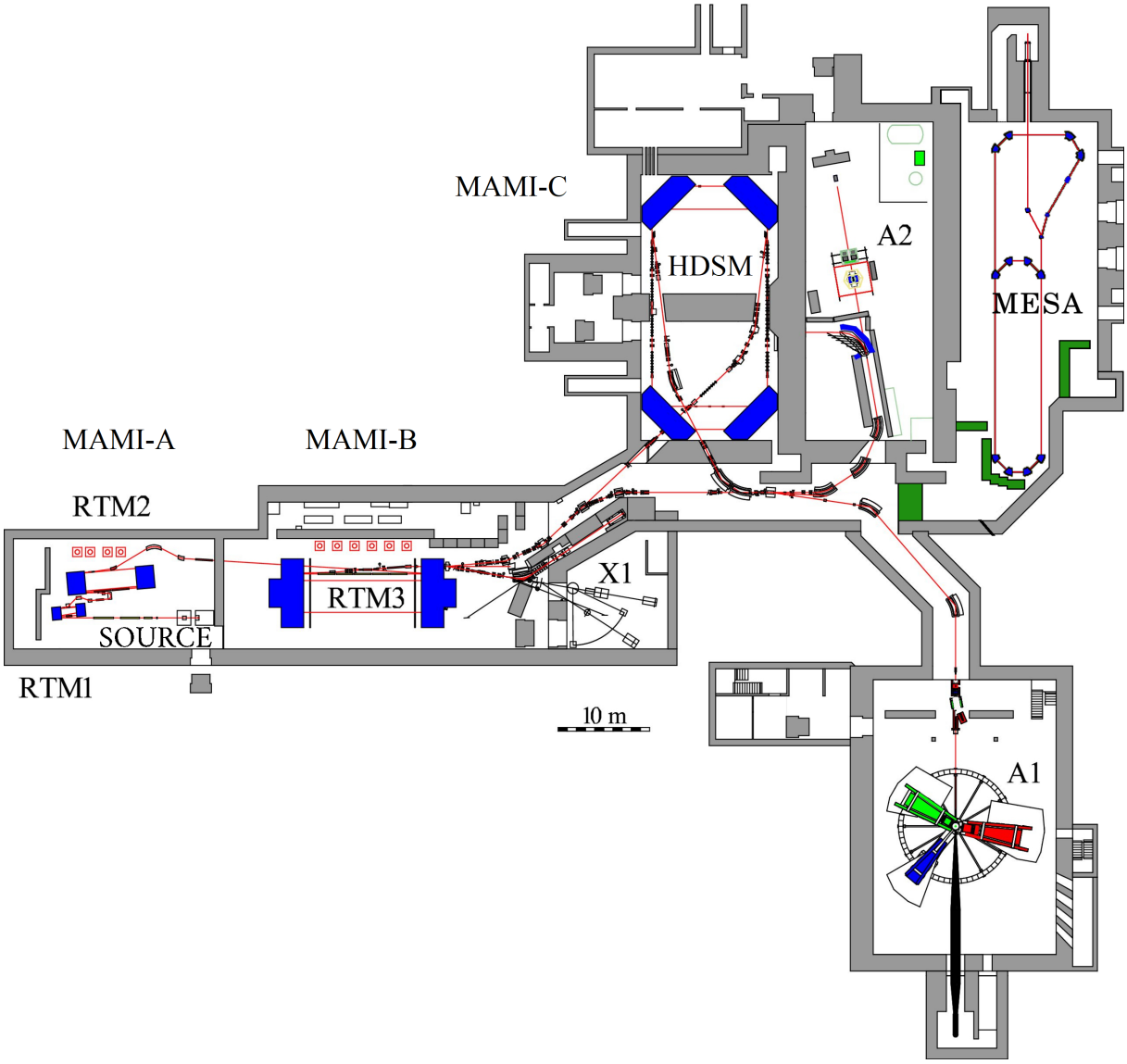

Figure 6.1.: Floor plan of the Mainz Microtron and the connected experiments [276]. On the left, the beam source is located, where the electrons are collected and accelerated in a small linear section. After that, two Race Track Microtrons (RTM1 and 2) bring the beam to an energy of 180 MeV. The next section is the RTM3, also known as MAMI-B. It can deliver electrons ranging from 180 to 855 MeV directly to the experiments X1, A2 and A1. Another possibility is to use the Harmonic Double Sided Microtron (HDSM or MAMI-C) as the final stage to gain energies up to 1.6 GeV.
Next to the A2 hall, a new complex is under construction to house the completely new MESA accelerator which will allow for experiments with high intensity electron beams.

6.2. The A1 Collaboration

Since the early 1990's, the A1 Collaboration operates at MAMI and possesses a rich history of various electron scattering experiments. Besides hypernuclear physics, they range from form factor measurements and experiments with polarized electrons [113] to tests of a new jet target system for future studies at MESA [274].

6.2.1. The spectrometers A, B and C

As shown in Figure 6.2, the setup of the A1 experiment essentially consists of the three magnetic spectrometers A (red), B (blue) and C (green), which can be arranged around the target on a circular track [1]. Below the yellow platforms the magneto-optical systems can be seen, which for SpekA and SpekC are composed of a quadrupole, a sextupole and two dipole magnets. The former two serve to focus the incoming particles, while the latter bend them upwards on a circular path. By that, the particles will be separated by their momentum. SpekB in contrast uses only one inhomogeneous dipole magnet ("clam shell"), but principally works analogously. In all three cases, the momentum of the particles is determined by observing the position and direction of these particles after they traversed the dipole magnets. The known optical character of the magnet systems additionally allows to reconstruct their initial momentum vector. The spectrometers can be set to different momentum ranges based on the field strength of the magneto-optics.

Detector system

The upper part of the spectrometers houses the detector system which consists of three different components. These are shown as a sketch in Figure 6.3 [41]. Starting with two vertical drift chambers (VDC), the position and the direction of the particle is determined, from which the momentum is extracted. This is followed by two scintillator planes (dE and ToF), which trigger the data readout, determine the flight time and provide a criterion for particle identification based on their energy loss spectra. The planes consist of a row of paddles, which are read out on both sides by photomultiplier tubes[1]. The dE plane has a thickness of $3\,\mathrm{mm}$ and is the first plane to be crossed by the particle. The following ToF layer is $10\,\mathrm{mm}$ thick. Over the last years, the efficiency of the scintillator planes has decreased so that the involved photomultipliers were equipped with new preamplifiers, which was started already several years ago [108] and was finished within the scope of this thesis. Finally, the particles pass the Čerenkov detector. It is filled with a gas of an optical index of refraction close to 1. By that, it allows for the distinction between electrons and the other particles, since they are significantly faster even with the same momentum due to their low mass of only $511\,\mathrm{keV}/c^2$. By that, only electrons generate light in the gas of the Čerenkov radiator. This light is also observed with photomultipliers.

Optical properties

In Table 6.1 the spatial and optical properties of the spectrometers are listed [52, 10]. The main advantage of the A1 facility is the flexibility of the angular and momentum ranges to be covered. Depending on the spectrometer, even 7° forward angles and up to 160° backward angles can be studied. This makes the entire structure capable of being used for a set of very different experiments. In addition, the high momentum resolution in the range of 10^{-4} as well as the angle resolution of $3\,\mathrm{mrad}$ make the spectrometers interesting for measurements in the regime of high precision. In comparison, the experiments at heavy ion accelerators have to rely on

[1] With the exception of the dE paddles from Spec. B, these are only read out on one side.

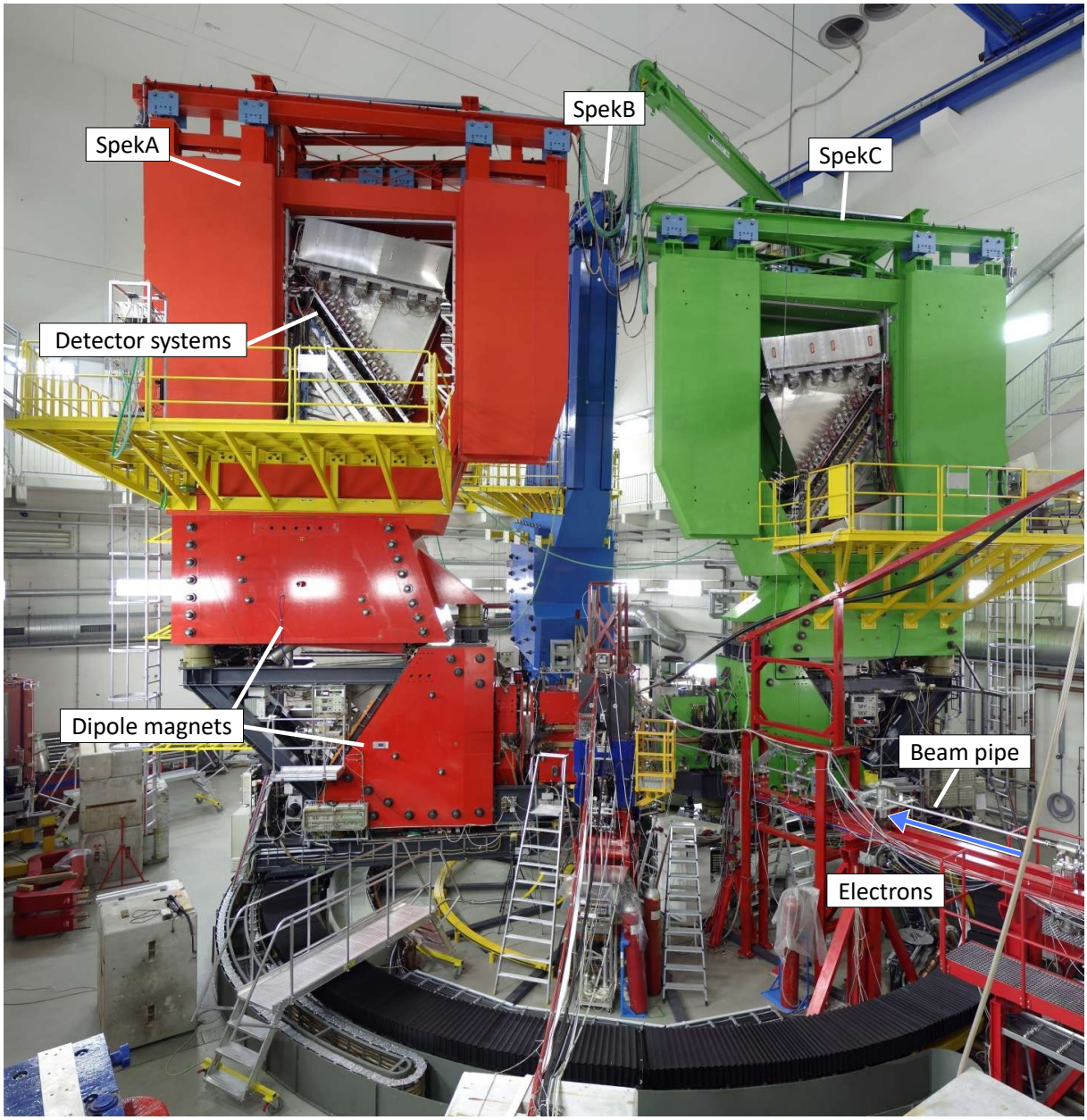

Figure 6.2.: Spectrometer hall of the A1 Collaboration with the three spectrometers A (red), B (blue) and C (green) [1]. Coming from the bottom right, the beam line enters the hall as a thin tube on a red support structure. At the center of the circular track, the target chamber is located. The concrete doors of SpekA and C are opened so that parts of the internal detector systems are visible.

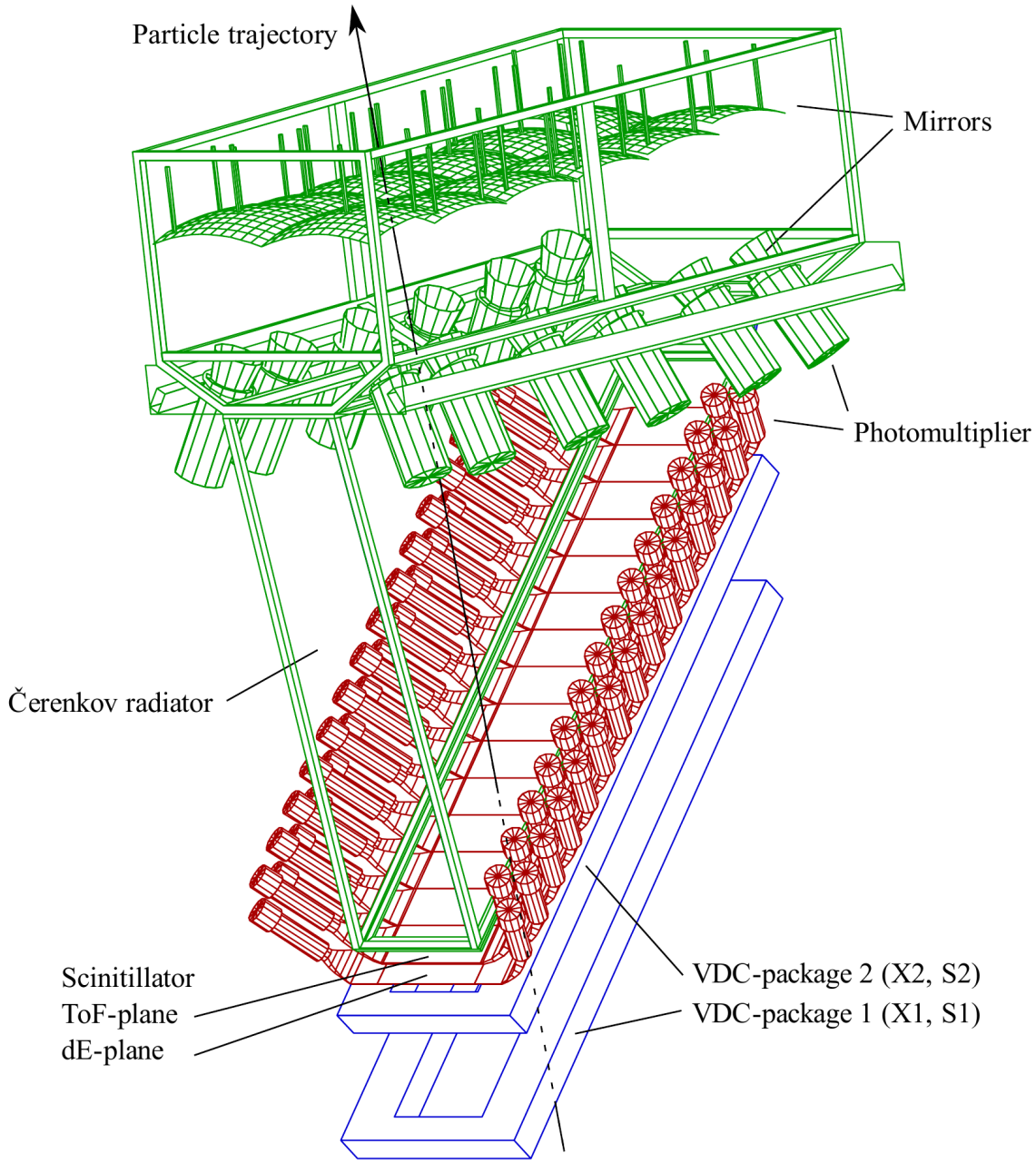

Figure 6.3.: Sketch of the three-part detector system inside the A1 spectrometers [41]. It starts with two layers of vertical drift chambers (VDC, blue) to determine the position of the particle and to reconstruct its vector. Together with the dipole magnets, the origin and the momentum of the particle is extracted. Followed by two scintillator planes (red), the flight time and characteristic energy loss is recorded. Finally, a gas Čerenkov detector (green) is used for further particle identification.

Table 6.1.: Optical and spatial properties of the A1 spectrometers [52, 10].

Spectrometer		A	B	C	KAOS
Magnet configuration		QSDD	D	QSDD	D
Variable central angle	[°]	$18 - 160$	$7 - 62$	$18 - 160$	$0 - 40$
Max. central momentum	[MeV/c]	665	810	490	1400
Momentum acceptance	[%]	20	15	25	50
Momentum resolution		10^{-4}	10^{-4}	10^{-4}	10^{-1}
Solid angle acceptance	[msr]	28	5.6	28	10.4
Angle resolution	[mrad]	3	3	3	–
Length of central track	[m]	10.75	12.03	8.53	5.3
Length of target acceptance	[mm]	50	50	50	–

large statistics to extract a precise mean value out of broad distributions. An example of this is the hypertriton mass spectrum of ALICE in Figure 3.9 on page 32. A drawback of the A1 spectrometers though is the low solid angle acceptance. It is limited for all spectrometers to only several msr, so that generally high statistics will harder be achievable. Also the length of the central track of around 10 m is not ideal especially when studying unstable particles. Here, the probability of a decay before the proper detection is increased.

6.3. The Kaon Spectrometer KAOS

Figure 6.4.: KAOS installed within the A1 setup. It allows for detecting particles under 0° forward angles and is best suited for observing kaons.

By the year 2007 the A1 setup was enhanced by a fourth spectrometer, the kaon spectrometer KAOS. Initially built at the GSI as meson spectrometer at SIS in 1991 [278], it was brought to Mainz and equipped with new detector systems [10]. A picture is shown in Figure 6.4. Here one can see KAOS installed in between the other A1 spectrometers. In contrast to them, KAOS is not fixed to the circular track, but can be moved freely, resting on polished metal plates. Its setup differs quite strongly from the other spectrometers. The magneto-optics just consist of one homogeneous dipole magnet which bends the incoming particles within the horizontal plane.

During its first years at MAMI, KAOS was designed as another high precision spectrometer, enabling for the spectroscopic study of kaons. This was hardly possible before, when only the other spectrometers were available. Due to the short lifetime of kaons, being just 12.3 ns, their classical mean flight length is only $c\tau = 3.7$ m. KAOS, with its central track length of only 5.3 m, is therefore far better suited than A, B and C with tracks of around 10 m. Additionally its design as in-beam-line spectrometer offered the capability of covering the 0° forward angle, where the kaon creation

is maximized. This made KAOS outstanding for hypernuclear studies.

After the transfer from the GSI, KAOS was equipped with layers of horizontal drift chambers (HDC) as well as two planes of scintillator paddles and a Čerenkov detector to allow for the identification and kinematic analysis of incoming particles, similar to the other spectrometers. However, due to the simpler magnet setup, the achievable momentum resolution was not as precise as compared to the more complex designs of A, B and C. While they offer 10^{-4} in momentum accuracy, KAOS was limited to 10^{-3}. To also detect scattered electrons at low angles in coincidence with a kaon or another positively charged particle, an additional scintillator fiber detector was developed and installed to the "other side" of the spectrometer, separating it into the *Electron Arm* and the *Hadron Arm* [137]. Nevertheless, the success of this detector setup was limited by issues with too high rates especially under forward angles.

To address the previous rate issues and to improve the kaon identification, the detector systems in KAOS were re-arranged again by 2012 [116]. In the hadron arm, the drift chambers were removed to offer space to add another scintillator layer and another Čerenkov detector. The rate issues were addressed by installing a lead absorber plate within the acceptance. By that, the momentum resolution of KAOS was almost lost, being only roughly 10^{-1} today. Despite that, KAOS was by then well suited to participate at *decay pion spectroscopy* experiments. A basic description of the concept of studies like these was already given in Chapter 3.3.2 on page 28, while more information about the experimental technique to study hypernuclei at A1 is going to be given in Chapter 7.

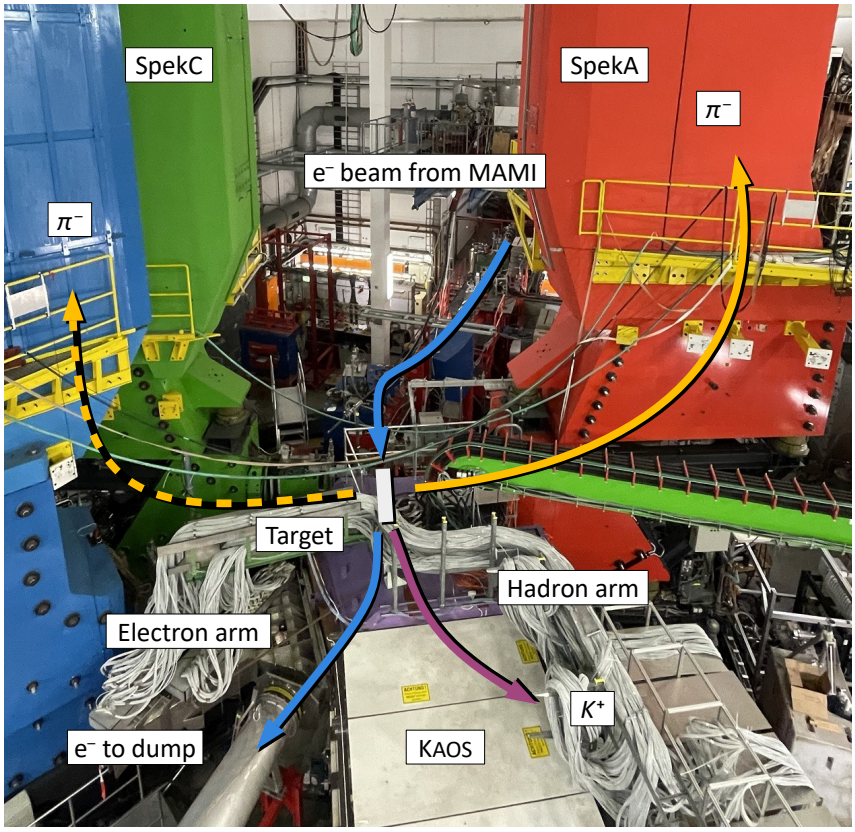

Figure 6.5.: Experimental setup for the decay pion spectroscopy experiment of this thesis. Inside KAOS, the electrons are bent into the beam dump, while kaons and other positively charged particles can enter the spectrometer. The decay pions are detected either by SpekA or SpekC. A precise sketch of the setup is found in Figure 9.1 on page 110.

Figure 6.5 shows KAOS in operation together with the spectrometers A and C. Here, several particle tracks are illustrated. The incoming beam hits the target and among others, kaons are produced. KAOS covers the forward angle so that the kaons are detected in the hadron arm. At the same time, most of the electron beam passes the target mostly undisturbed and enters KAOS as well. Within the same magnet, the electrons are bent towards the electron arm, where the exit beam pipe leads to the beam dump. The other spectrometers A and C wait for incoming decay pions of hypernuclei which might have formed during the creation process of the kaon.

6.3.1. Installation of KAOS to the beam line

For the use as in-beam-line spectrometer, the electron beam of MAMI is curved by two prechicane magnets to $17°$, so that KAOS – also resting at $17°$ – bends the incoming beam back into the beam dump via its dipole magnet. This unique installation requires an exact placement of KAOS. Since KAOS is not fixed to the circular spectrometer track, it needs to be installed quite carefully with the help of workshop members. The spectrometer then rests independently on three feet and needs to be pushed into the correct position. A sketch of this setup is found in Figure 9.1 on page 110. The complete process of aligning the spectrometer is described in the appendix in Chapter B.1 on page 143. Afterwards, measures to protect the spectrometer from radiation need to be taken, which are also described there.

6.3.2. Spectrometer design

A sketch of KAOS is shown in Figure 6.6 [9]. Here it is depicted from a top view. The heart of the spectrometer is the dipole magnet on the left side. It allows for the momentum dependent separation of incoming particles. These enter through the entrance window and traverse the spectrometer's nose as well as the collimator box. Then, the magnetic field is reached. Usually, a positive polarization of the magnet is used. That way, positive particles will enter the hadron arm in the upper part of the figure, while electrons and other negative particles enter the electron arm.
The hadron arm is the important part for the experiments of this thesis. It contains a total of three scintillator planes and two aerogel Čerenkov detectors. A positive particle will leave the magnet and the vacuum chamber through a large vacuum window before it faces a lead absorber wall. This wall proved to be crucial for the suppression of background by positrons [116]. After that, a double layer of scintillator paddles is located, the walls G and I. From there, the two aerogel Čerenkov detectors are following until the final scintillator wall H is reached.
Next to the exit flange, a $0°$ tube is found. It is connected to the vacuum chamber and allows uncharged particles like gammas and neutrons to pass into a separate beam dump. The installation of this setup is explained in the appendix, Chapter B.2 on page 144.

6.3.3. Detector setup

Scintillator walls G & I

The walls G and I each consist of 15 scintillator paddles. Each of them is manufactured from BC408 plastic scintillator material [49] and their dimension is $470 \times 20 \times 75\,\mathrm{mm}^3$. They all are read out from both ends, at the top and bottom by 2" PMTs of the type R1828 from Hamamatsu. They are usually supplied with roughly $-2000\,\mathrm{V}$ by the LeCroy 1440 HV power supply [215]. Both walls are installed quite close to each other right behind the lead wall, so that they are the first detectors to be hit by the particles. This places them also quite near to sources of unwanted radiation like the $0°$ tube and the exit flange. The double wall setup was hence chosen

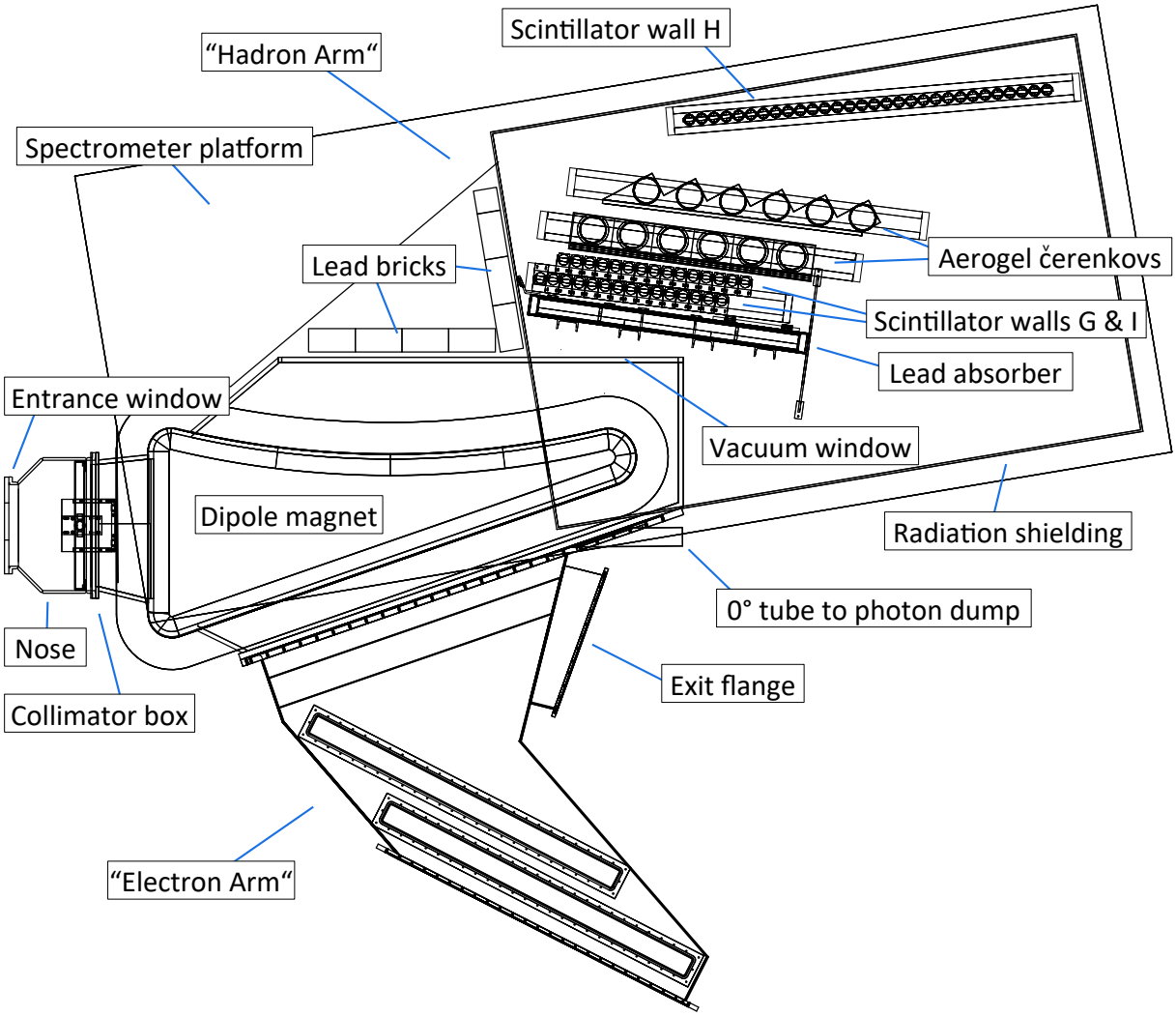

Figure 6.6.: Sketch of the KAOS spectrometer, top view [9] (modified). From the left, the particles and the remaining beam pass through the entrance window and the collimator box. From there, charges will be separated by the dipole magnet. The negative particles, mainly electrons, will pass towards the so called *Electron Arm* and eventually into the exit flange, which leads them to the beam dump. Positive particles enter the *Hadron Arm*, where they leave the vacuum chamber through a window until they enter the detector systems. To suppress incoming positrons, a lead absorber has to be passed at first. After that, the two scintillator walls G and I are placed, to be followed by two aerogel Čerenkov detectors and another scintillator wall H. The 0° tube is another flange foreseen for uncharged particles like gammas and neutrons. They will be caught in a separate beam dump.

to suppress single wall hits by background as well as double wall hits of particles which cannot originate from the target due to their hit pattern [116].

Aerogel Čerenkov detectors

The two Čerenkov detectors installed in KAOS are named "AC2" and "AC1" from upstream. Each layer consists of 6 units. Its purpose is to separate kaons from pions and positrons, so that silica aerogel with a refractive index of $n = 1.055$ was chosen as radiator material. By that, the momentum threshold of the Čerenkov radiation is $420\,\mathrm{MeV}/c$ for pions, while being $1560\,\mathrm{MeV}/c$ for kaons [215]. Each unit is – similar to the scintillators – read out with Hamamatsu PMTs from top and bottom. Similar to the G-I walls, also the Čerenkov detector was doubled to suppress undesired background events.

Scintillator wall H

This wall is the final detector component in KAOS and consists of 30 plastic scintillator paddles. The size of one paddle is larger compared to G and I being $580 \times 20 \times 70\,\mathrm{mm}^3$. The scintillator material and the used PMTs are the same as at G/I. The wall is installed in a larger distance to the other detectors to approximately match the focal plane position of the magnet [215]. The wall H is not exposed to as much radiation as the walls G and I, so here a single wall is sufficient. Also due to the distance to the other scintillators, the setup allows for flight time studies.

6.3.4. Trigger setup

Logic

Each of the walls G, I and H can be selected as triggering plane, but also logic junctions between the layers are possible. For example, to suppress background from other sources, only events with simultaneous signals in G AND I AND H can be selected as triggers. This system was already improved for the previous experiments, that only events with a physically possible hit combination in all scintillator walls are considered as true triggers [116]. This system is the so called track trigger. It was mainly used during the data taking within this thesis.

Hardware

The PMT signals are split already at the readout base of the PMTs, so that one branch of cables enters the trigger section. There, the signal is evaluated with constant fraction discriminators (CFD) and the relative timing is measured with Time-to-Digital Converters (TDC) [10]. If the CFDs find a signal to be strong enough, it is sent to an FPGA chip, which evaluates the incoming hit patterns. At this unit, the different trigger configurations can be selected. From there, the KAOS trigger signal is emitted to enter the coincidence logic described in Chapter 9.1 on page 111. The other branch of scintillator signal cables is delayed and sent to analog-to-digital converters (ADC) for the data readout.

7. Hypernuclear Physics at MAMI

This chapter addresses the experimental concept of hypernuclear studies via decay pion spectroscopy at the A1 setup. While in Section **7.1** the explicit method is introduced, the focus is shifted in **7.2** towards the studies which have already been performed in the past. These experiments delivered valuable binding energy data but still were hampered with several problems. Therefore, in the final Section **7.3**, the improvements for the new hypernuclear experiment of this thesis are summarized.

7.1. Decay Pion Spectroscopy at A1

7.1.1. The principle

Hypernuclei are investigated in several different ways, as already summarized in Chapter 3. Among them, a relatively new method was pioneered at MAMI around 10 years ago, which is the spectroscopy of decay pions at electron accelerators [115, 116]. This method allows for the determination of the mass and binding energy of a hypernucleus by studying its decay. While in general, a hypernucleus can decay via various decay channels – compare to the listing of branching ratio values in Chapter A.4 on page 139 – only the charged mesonic two-body decay is of interest here. This is the case, when the Λ inside the hypernucleus decays into a proton under the emission of a pion

$$\Lambda \rightarrow p + \pi^{-}, \tag{7.1}$$

and the remaining nucleons stay bound together. Such a decay was already illustrated for the case of the hypertriton in Figure 3.5 on page 28. Since for two-body decays the decay momenta are shared equally between both participants, the momentum of the decay pion offers all the kinematic information relevant to extract the mass of the hypernucleus. This excludes the possibility of studying multi-body decays, as it is possible for example in emulsion experiments. With the low solid angle acceptance of the A1 spectrometers, the probability of detecting more than one decay body would simply be too low. Also the other possible two-body decay, where the Λ decays into uncharged particles,

$$\Lambda \rightarrow n + \pi^{0}, \tag{7.2}$$

cannot be observed by the magnetic spectrometers due to the missing charge of the π^0. If indeed a charged mesonic two-body decay was observed, the reconstruction of the initial hypernucleus is simple. First starting with the conservation of energy, the energy of the hypernucleus has to be equal to the energy of its decay products,

$$E_{\mathrm{hyp}} = E_{\mathrm{nucl}} + E_{\pi}. \tag{7.3}$$

With the energy being composited of the mass and the momentum of a particle, $E = \sqrt{m^2 + p^2}$, the formula can be rewritten to

$$m_{\mathrm{hyp}} = \sqrt{m_{\mathrm{nucl}}^2 + p_{\pi}^2} + \sqrt{m_{\pi}^2 + p_{\pi}^2}, \tag{7.4}$$

if the hypernucleus is assumed to be at rest before the decay, $p_{\mathrm{hyp}} = 0$. Furthermore the absolute momenta of the decay products then are identical, $p_{\mathrm{nucl}} = p_{\pi}$. The only other variables are then

the masses of the decay products, m_{nucl} and m_π, which are found in literature. So after all, the mass of the hypernucleus relies solely on the determination of the pion momentum. In a final step, the hypernuclear mass is converted to the Λ binding energy,

$$B_\Lambda = m_\Lambda + m_{\mathrm{ns}} - m_{\mathrm{hyp}} \tag{7.5}$$

with the Λ mass m_Λ and the mass of the non-strange isotope the Λ was bound to m_{ns}.

7.1.2. Reaction process

With MAMI's electron beam, the underlying process for the generation of a hypernucleus is the so-called strangeness electro-production. By that, the electron transfers enough energy to a proton in a target nucleus, that an $\mathrm{s\bar{s}}$ pair is created. This reaction was already depicted in the quark flow diagram in Figure 3.2 on page 24, process 3. One of the proton's up quarks is exchanged with the s quark to form a Λ, while the remaining $\mathrm{u\bar{s}}$ pair forms a K^+,

$$e + p \rightarrow e' \Lambda K^+. \tag{7.6}$$

Another representation of this process is given in Figure 7.1 [276]. Here, the production is found on the left. For this process to happen, a certain threshold electron energy is required, given by the center of mass energies of the system before and after the electron scattering. A resulting threshold of $E_{\mathrm{thr}} \approx 780\,\mathrm{MeV}$ is found for the case of resting proton, Λ and kaon by solving

$$m_\Lambda^2 + m_K^2 \stackrel{!}{=} m_p^2 + E_e^2. \tag{7.7}$$

This requirement is fulfilled by MAMI's capability of delivering electrons up to $1.6\,\mathrm{GeV}$. After the generation of the Λ, it has to stay bound to the target nucleus to form a hypernucleus. The probability is maximized if the kaon takes as much of the forward momentum induced by the electron as possible. By that, the Λ will be comparably slow and the chance of escaping the nuclear potential is minimized.

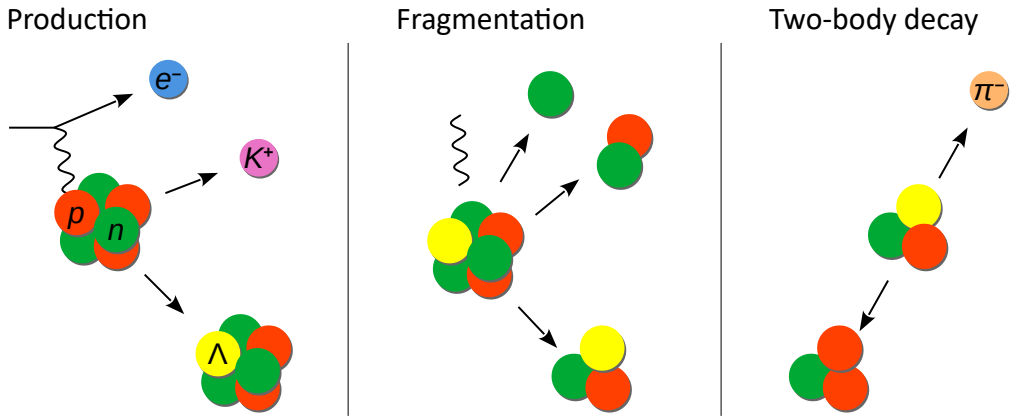

Figure 7.1.: The schema of decay pion spectroscopy with electron beams [276] (modified). In the first step, a proton is converted to a Λ via strangeness electro-production. By that, a K^+ is emitted, leaving behind a highly excited hypernucleus. Secondly, this excitation is going to decay via the emission of several nucleons and possibly γ rays, until the hyperfragment reached its ground state. In the final step, the Λ baryon itself is going to decay weakly via a two-body decay. The decay pion carries all the necessary kinematic information to determine the mass of the hypernucleus.

The emerged hypernucleus is then found in a highly excited state, due to the nature of the nuclear energy shells. Before the reaction the target nucleus was present in its ground state with protons and neutrons filling their energy shells up to a certain level. Afterwards, one proton was removed from its energy scheme, leaving a hole. Additionally, the Λ finds a series of holes beneath the state it was created in. The consequence is a violent de-excitation via the emission of several nuclear fragments, until eventually a hypernuclear isotope in its ground state is formed. This process is shown in the middle of Figure 7.1.
Also during this process, the fragments will lose their kinetic energy inside the target material, similar to the behavior in the emulsion. This is possible due to the comparably long Λ lifetime. The final two-body decay – shown on the right – then takes place at rest. The emitted decay pion will be detected by the A1 spectrometers to reconstruct the mass of the hypernucleus.
After all, the probability of such a formation of a hypernucleus is strongly suppressed compared to background events generated by other processes. To have a chance to still extract the rare hypernuclear events in the data taking and the later analysis, KAOS is used to detect the emitted kaon from the generation process in coincidence with the decay pions in the other spectrometers. In that way only "strangeness tagged" events will be recorded. In the later analysis, the detector setup of KAOS furthermore allows for a more precise extraction of the true kaon events to suppress the background once more.

7.2. The Previous Hypernuclear Experiments at A1

After the method of decay pion spectroscopy was established at A1, several data taking campaigns were performed between 2012 and 2014 to observe the decays of the light hypernuclear isotopes ${}^{3}_{\Lambda}\mathrm{H}$ and ${}^{4}_{\Lambda}\mathrm{H}$ [116, 276]. During that time, beryllium targets were used, together with the previously described SpekA-SpekC-KAOS configuration. More details about the specific setup are going to be provided in Chapter 8.2.1 on page 93.
A result of these campaigns is shown in Figure 7.2. Here one can see the resulting decay pion momentum spectrum of SpekC [276]. While showing a relatively constant background level across the whole acceptance, a single peak was observed at around $133\,\mathrm{MeV}/c$. Due to this distinct value it was associated with the decay pions of ${}^{4}_{\Lambda}\mathrm{H}$, as they were already observed before

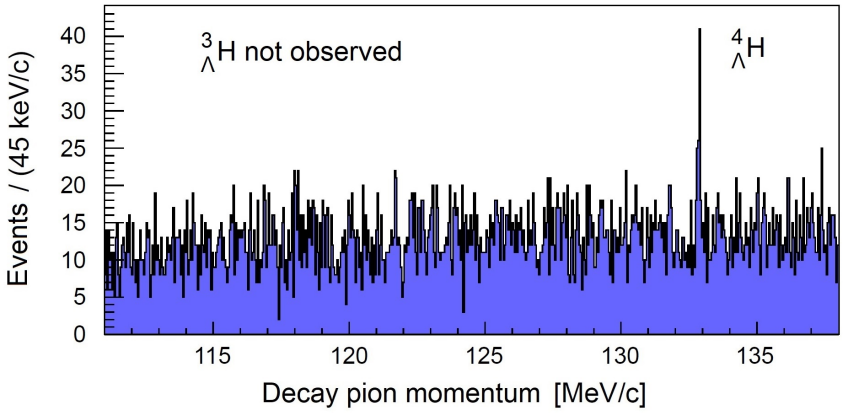

Figure 7.2.: Result of the previous hypernuclear beamtimes from 2012-2014 [276] (modified). The spectrum shows the momentum of the detected decay pions. While there is quite some background coming from free Λ decays, multi-body decays and accidental coincidences, a single peak was observed at $133\,\mathrm{MeV}/c$ confirming the presence of ${}^{4}_{\Lambda}\mathrm{H}$. However, no indication for ${}^{3}_{\Lambda}\mathrm{H}$ was found.

at $132.6 \pm 0.3\,\mathrm{MeV}/c$ in decay studies at KEK [290]. From the analysis of this peak it was possible to extract a new ${}^{4}_{\Lambda}\mathrm{H}$ binding energy value of

$$B_\Lambda = 2.157 \pm 0.005\,(\text{stat.}) \pm 0.077\,(\text{syst.})\,\mathrm{MeV}. \tag{7.8}$$

The result is in great agreement with the combined average value of all ${}^{4}_{\Lambda}\mathrm{H}$ binding energies, $\overline{B}_\Lambda({}^{4}_{\Lambda}\mathrm{H}) = 2.169 \pm 0.042\,\mathrm{MeV}$, which was elaborated in Chapter 4.5 on page 52 before. For the value of (7.8), 68 ± 12 events were found in total, which was sufficient to reduce its statistical error down to just $5\,\mathrm{keV}$. The systematic error, however, was strongly dominating in this result, being with $77\,\mathrm{keV}$ 15 times larger than the statistical component [275].

No hypertriton observed

Despite the success with ${}^{4}_{\Lambda}\mathrm{H}$, it is quickly seen in the spectrum of Figure 7.2, that this peak is the only structure above background level, meaning that the hypertriton was not observed. These decay pions were expected at around $114\,\mathrm{MeV}/c$, which was on purpose covered by the spectrometers. However, none of the experimental campaigns delivered evidence for the decays of ${}^{3}_{\Lambda}\mathrm{H}$.

Limitation by calibration

Aside of the hypertriton issue, also the systematic error of (7.8) was unsatisfying. It was mainly caused by the absolute calibration of the A1 spectrometers. In general, the magnetic field in the spectrometer optics has to be linked to a particle momentum. This is usually performed with elastic electron scattering[1]. According to Ref. [249], when knowing the energy of the incoming electron E, the mass of the target nucleus M and the scattering angle θ, the energy of the scattered electron is determined by

$$E' = \frac{E}{1 + \frac{E}{M}(1 - \cos\theta)}. \tag{7.9}$$

The spectrometer which is to be calibrated will then detect a peak of the elastically scattered electrons in a momentum spectrum, similar to the one in Figure 7.2. With (7.9), this peak can be directly linked to its correct momentum. This procedure can be repeated for various energies, so that the spectrometer gets calibrated over a wide momentum range. One crucial aspect is the precise determination of the magnetic field inside the spectrometer magnets at any calibration point which is usually done with NMR probes. Then, after the calibration, solely the magnetic field value provides the momentum information.
At MAMI, the critical point of this procedure is the energy of the incoming electron beam E. This energy can only be determined with an accuracy of $\Delta E = 160\,\mathrm{keV}$. This problem is known to originate from the method of measuring itself, because the beam energy's spread and instability is observed to be much smaller. This was demonstrated for example by Philipp Herrmann [154], as he set up and tested a new in-beam-line spectrometer to re-measure the beam energy. One of his results is shown in Figure 7.3. He was able to compare the energy measurement of MAMI to his own extracted values over the coarse of several hours. The points of MAMI in blue scatter within a range of around $100\,\mathrm{keV}$ while the points of Herrmann in purple appear more like an even line. After all though, also Herrmann's setup suffered from remaining systematic uncertainties – in this case $305\,\mathrm{keV}$ [154] – so the offset in the determined beam energy is not physical. Still he was able to proof the excellent beam quality of MAMI.

[1] At MAMI's energies, energy and momentum are almost identical for electrons due to their low mass.

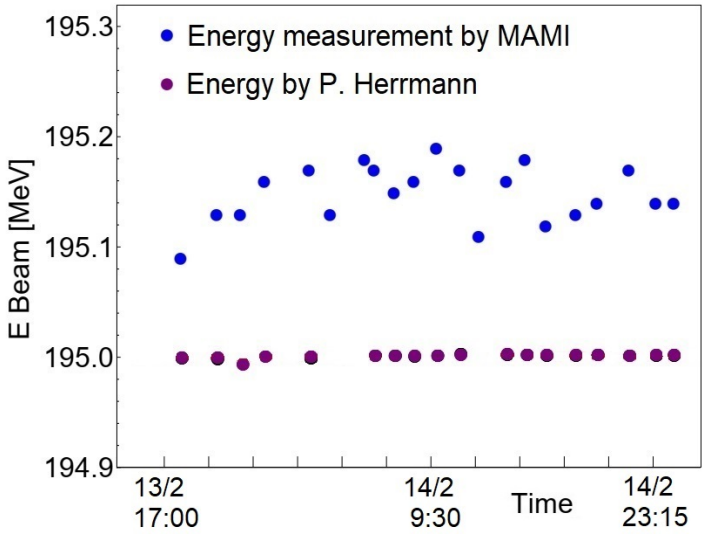

Figure 7.3.: Beam energy measurements of Philipp Herrmann compared with energy measurements by MAMI [154] (modified). The values of Herrmann scatter at least one order of magnitude less than the ones by MAMI, so MAMI operates more stable and precise as their energy measurements indicate. The energy difference between both methods is mainly given by systematic uncertainties in the purple data.

7.3. Optimizations for the new Experiment

The two previously described issues had to be addressed for a success of the new hypernuclear experiment prepared and committed within the scope of this thesis. They summarized to (i) the missing hypertriton peak and (ii) the comparably large systematic error component. The following improvements and new approaches around the experimental setup were elaborated:

- **New spectrometer calibration** – an improved beam energy measurement via undulator light interference by Pascal Klag to reduce the systematic error of a new spectrometer calibration
- **Noise reduction** – better radiation shielding of KAOS to suppress random background events and limiting KAOS' low momentum acceptance to reduce the count rate by undesired particles
- **Lithium as Target Material** – exchange of the target nucleus to a lighter isotope to enhance the yield of hypertriton fragments
- **High luminosity target** – design of a new target concept to be operated with lower beam current for less background around the whole beam line as well as larger overall luminosity

Each of the measures is going to be described in the following. Thereby it is to be noted that the latter two points in the list received a new chapter, hence they are described in Chapter 8. High Luminosity Lithium Target starting from page 91.

7.3.1. New spectrometer calibration

To further investigate the given systematic error of (7.8), a quantification of the relevant error sources needs to be done at first. While the uncertainty in the spectrometer calibration seems to be the biggest contribution, it is far from being the only one. The investigation is started by taking the derivative of the decay pion spectroscopy mass formula (7.4) with respect to the pion momentum,

$$\frac{\mathrm{d}}{\mathrm{d}p_\pi} m_{\mathrm{hyp}} = p_\pi (m_{\mathrm{nucl}}^2 + p_\pi^2)^{-\frac{1}{2}} + p_\pi (m_\pi^2 + p_\pi^2)^{-\frac{1}{2}}. \tag{7.10}$$

According to the Gaussian error propagation, the mass error of the hypernucleus will then be

$$\Delta m_{\mathrm{hyp}} = \frac{\mathrm{d}}{\mathrm{d}p_\pi} m_{\mathrm{hyp}} \cdot \Delta p_\pi, \tag{7.11}$$

with the error of the pion momentum Δp_π. From here, the error of the momentum itself has to be examined. It is composed of several sources, the most important being

- the calibration of the spectrometers, mainly given by the uncertainty of the beam energy ΔE, and
- the reproducibility of the magnetic fields in the spectrometer optics ΔB.

Spectrometer calibration

As described before, the calibration at A1 is usually performed via elastic electron scattering. For that, (7.9) links the energy of the scattered electron E' to the initial energy E and the scattering angle θ. To find the achievable accuracy $\Delta E'$, two derivatives of (7.9) were computed, one with respect to the initial energy and the other to the scattering angle. For simplification, the substitution

$$U := \frac{E}{M}(1 - \cos\theta) \tag{7.12}$$

was used. The results read

$$\frac{\mathrm{d}E'}{\mathrm{d}E} = (1+U)^{-1} - U(1+U)^{-2}, \tag{7.13}$$

$$\frac{\mathrm{d}E'}{\mathrm{d}\theta} = -\frac{E^2}{M}\sin\theta(1+U)^{-2}. \tag{7.14}$$

With these, two new equations for $\Delta E'$ are given, with the first being

$$\Delta E'(\Delta E) = \frac{\mathrm{d}E'}{\mathrm{d}E} \cdot \Delta E. \tag{7.15}$$

Here it was found that the error in the initial beam energy translates almost identically into the scattered energy, $\Delta E' \approx \Delta E$, only weakly dependent on the other parameters θ, M and E. A different observation was made for the angular error dependency,

$$\Delta E'(\Delta\theta) = \frac{\mathrm{d}E'}{\mathrm{d}\theta} \cdot \Delta\theta. \tag{7.16}$$

In this case, a small scattering angle and a heavy target nucleus are favorable. Here the spectrometers, with their intrinsic resolution of $\Delta\theta = 3\,\mathrm{mrad}$, can achieve a negligible angular error of $0.4\,\mathrm{keV}$. For that a rather small scattering angle of $40°$, an electron energy of $180\,\mathrm{MeV}$ and a heavy target nucleus like $^{181}\mathrm{Ta}$ ($M \approx 168\,\mathrm{GeV}/c^2$) need to be used. In contrast to that, the error would become as large as $75\,\mathrm{keV}$ if a light proton target under $80°$ was used. So while the angle is quite easily handled by the design of the calibration experiment, the main error source remains the initial beam energy.

The undulator light interference method

The challenge of determining MAMI's beam energy with yet unseen precision is going to be addressed by a novel undulator light interference setup which is currently under development by Pascal Klag [183, 185]. A photo of his setup is shown in Figure 7.4. Here, the two undulators can be seen together with the electron beam pipe being placed within their gap. They are located at the X1 beam line, in between the RTM3 and the X1 hall (compare to the floor plan of MAMI at Figure 6.1 on page 72). These undulators generate an alternating magnetic field so that the electrons in the beam pipe emit synchrotron radiation of a specific wavelength. The undulators act as two sources, so that, depending on the distance between them, a periodic interference pattern is generated. Via an additional optical setup in the X1 hall, Klag is possible to observe this pattern with a CMOS camera. From that, he extracts the energy of the incoming electrons via the following ratio

$$\gamma^2 = \frac{1}{2}\frac{\lambda_{\mathrm{osc}}}{\lambda_{\mathrm{rad}}}. \tag{7.17}$$

Here, the relativistic γ factor of the electrons is linked to the wavelength of the interference pattern λ_{osc} and the wavelength of the synchrotron radiation λ_{rad}. The setup is designed to operate at the minimal MAMI-B energy of $180\,\mathrm{MeV}$ so that the spectrometer calibration can be done as close as possible to the decay pion momenta of $110 - 140\,\mathrm{MeV}/c$. First tests at MAMI have shown, that an accuracy in the beam energy of $18\,\mathrm{keV}$ is possible [184, 183], which overrules the old MAMI procedure by almost one order of magnitude.

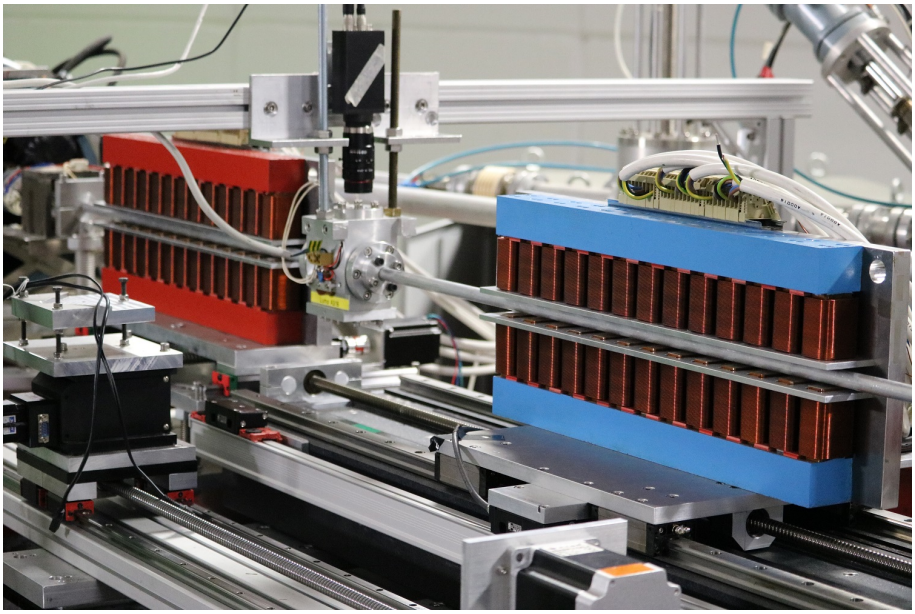

Figure 7.4.: Undulator setup developed by P. Klag. Two undulators (red and blue) generate an alternating magnetic field. Inside their gap, the beam pipe is located, so that the passing electrons emit synchrotron radiation. By varying the distance between the undulators, an intensity interference pattern can be observed with a dedicated monochromator setup (not seen). This pattern will give the opportunity to extract the absolute beam energy value with a precision of better than 10^{-4} [184, 183, 185].

Reproduction of the magnetic field

After a calibration via elastic scattering, the observed energy would be linked to the magnetic field which was set in the spectrometers. The calibration can then only be as good as the magnetic field can be reproduced in future. For this, each spectrometer magnet is equipped with an NMR probe which precisely measures the field via the Nuclear Magnetic Resonance effect. Especially for the purpose of a precise calibration, a new NMR system was installed to the A1 spectrometers within this thesis. Details about that are found in the appendix at Chapter B.4. This NMR device offers an absolute precision of $5\,\mu\mathrm{T}$ and a relative precision of $0.5\,\mu\mathrm{T}$. Due to the calibration with the electron beam the relative precision should be sufficient for finding the correct magnetic field again, since the true absolute value is then not of interest anymore. However, even in the case of having to rely on the absolute precision, the resulting error ΔB would be quite small. The fields for calibrating and measuring will be larger than $100\,\mathrm{mT}$ so that even in the worst case the relative accuracy in ΔB would still be $\leq 5 \cdot 10^{-5}$. Since in magnetic spectrometers the field is proportional to the momentum, $B \propto p$, this error translates linearly to the momentum resolution, so that here the error contribution at $p = 180\,\mathrm{MeV}$ is $\Delta p \leq 9\,\mathrm{keV}$.

Summary for the hypernuclear mass

Now, where the two remaining error sources for the calibration are given, a realistic estimation of the overall systematic error can be provided.

- An initial electron energy with $\Delta E = 18\,\mathrm{keV}$ can be achieved by the undulator setup. These translate almost identically to the energy of the scattered electron $\Delta E'$. Since this calibration is to be performed at $E = 180\,\mathrm{MeV}$, the electrons are highly relativistic so that $E \approx E' \approx p$. Additionally, the angular error was found to be negligible so that the resulting momentum error is also $\Delta p \approx 18\,\mathrm{keV}$.
- Another contribution is given by the NMR device for the magnetic field in the spectrometers, in the worst case $\Delta p = 9\,\mathrm{keV}$.

With the quadratic addition of these two values, a final error in the momentum of $\Delta p = 20\,\mathrm{keV}$ is found. From here, the expected systematic error for the mass of the hypernucleus can be computed via (7.10). With the decay pion momentum of hypertriton of $\approx 114\,\mathrm{MeV}/c$, the pion mass from Table 2.1 and the $^3\mathrm{He}$ mass of $2808.391\,\mathrm{MeV}/c^2$, the result for the systematic error component reads

$$\Delta m_{\mathrm{hyp}} = 14\,\mathrm{keV}. \tag{7.18}$$

This accuracy would improve the previous $77\,\mathrm{keV}$ by more than a factor of 5.

7.3.2. Noise reduction

Now the focus is shifted towards the actual detection of the hypertriton, which is started with improved absorbers around KAOS to ensure for less background in the resulting momentum spectra.

Thicker lead wall in KAOS' acceptance

The lead wall can be seen at Figure 7.5 and is used to prevent positrons from entering KAOS' detector systems. Initially it was separated into three separate regions of varying thickness. For the low momentum acceptance it was chosen to be $8\,\mathrm{cm}$ thick, in the center $10\,\mathrm{cm}$ and at the high momentum end $12\,\mathrm{cm}$. By that, the momentum-specific energy loss of the kaons was taken

into account [116]. After all though it turned out that the high momentum section does not cover the momentum acceptance at all, but rather acts as a shield for radiation coming from the photon and exit beam pipes. Hence also parts of the mid-momentum range were only covered with the thinnest plate. Additionally in first beam tests in 2022, it was observed that in the low momentum channels the highest rate was observed, so that it was decided to add another $2\,\mathrm{cm}$ of lead to the thinnest section. So for the final data taking beamtime, the wall was equally $10\,\mathrm{cm}$ thick.

Figure 7.5.: Lead absorber plate from inside KAOS to suppress positrons.

New vacuum window in KAOS

After the first beamtime, a leakage problem occurred at the large kapton vacuum window inside KAOS which resulted in its complete rupture. It had to be replaced by a new window and for a better reliability it was chosen to be a solid aluminum plate instead. By that, the vacuum chamber was sealed successfully and $1\,\mathrm{cm}$ of aluminum was added to the overall absorber mass.

Concrete blocks

$50\,\mathrm{cm}$ thick concrete blocks were placed behind KAOS, which are seen in Figure B.2 on page 145 and schematically in Figure 9.1 on page 110. These blocks ensured for more radiation shielding towards the electron beam dump, which is known to be the source of background particles, especially neutrons.

Switching off hot trigger paddles in KAOS

As already mentioned, during the first data takings with KAOS in 2022 it was observed that especially the scintillators in the low momentum region produced more rate than the other paddles. This may be given by remaining positrons regardless of the lead wall. This problem was already known in the previous experiments, where consequently the first paddle row of G and I was disabled. For the new experiment, also the second paddle of G/I was unplugged. Thereby, less noise was recorded in the data. The loss of acceptance could then be compensated by a higher luminosity.

8. High Luminosity Lithium Target

In this chapter, a detailed description of the developed lithium target is to be found. In Section **8.1**, lithium is analysed in terms of its hyperfragment yields and compared to the previously used beryllium. The following **8.2** introduces the new design concept as high luminosity target as well as the challenges of handling pure lithium. This also involves the setup of a thermal camera surveillance system, which is described in Section **8.3**. Finally, a dedicated target test beamtime is presented in **8.4**.

8.1. Lithium as Target Material

As already mentioned, in the previous experiments $^{9}\mathrm{Be}$ targets were in use [114, 275]. For this isotope, a calculation of the expected hyperfragment yields was performed before. The underlying routine is based on a framework which initially was used for predicting the fragmentation of ordinary nuclei in heavy ion reactions [61]. The model was later enhanced to also handle hyperfragments [62]. Since in principle, an excited system of spectator nuclei in heavy ion collisions behaves similar to a nucleus being excited by an electron beam, this model was utilized for the hyperfragment yield predictions at MAMI [276].
The outcome of this calculation is seen in Figure 8.1. After the strangeness electro-production reaction, the $^{9}\mathrm{Be}$ nucleus is transformed into a highly excited $^{9}_{\Lambda}\mathrm{Li}^{*}$ hypernucleus [276]. Depending on the excitation energy, it can fragment into several different hyper-isotopes. The most likely are the $^{7}_{\Lambda}\mathrm{He}$ (red) and the $^{4}_{\Lambda}\mathrm{H}$ (blue). Compared to the latter, the hypertriton is expected to occur one or two orders of magnitude rarer. Since in the recent experiments only around 68 $^{4}_{\Lambda}\mathrm{H}$ events were observed, the absolute yield of hypertriton events might have been well below 10, making it invisible within the background (compare to Figure 7.2 on page 83). Also, none of the more prominent hyper-isotopes $^{6}_{\Lambda}\mathrm{He}$, $^{7}_{\Lambda}\mathrm{He}$ and $^{7}_{\Lambda}\mathrm{Li}$ was observed, which supports the assumption that the excitation energy during the experiment must have been larger than $50\,\mathrm{MeV}$, so that their production also got suppressed [246].

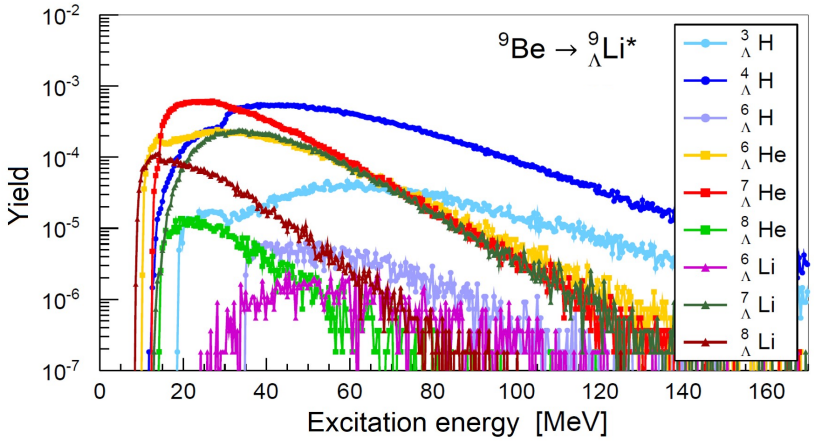

Figure 8.1.: Production probabilities of several hyperfragments off a $^{9}\mathrm{Be}$ target from a statistical fragmentation model [62]. Figure from [276].

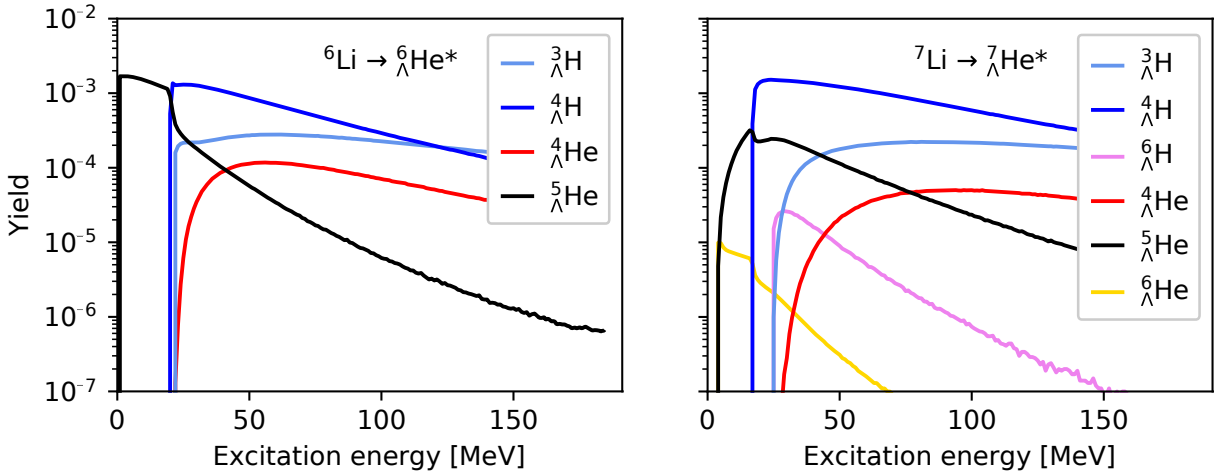

Figure 8.2.: Production probabilities of several hyperfragments off lithium nuclei [62]. The two stable isotopes contained in natural lithium are shown, ^{6}Li on the left and ^{7}Li on the right. In natural lithium, the latter isotope dominates with $\approx 92\%$.

As can be seen in Figure 8.1, the many other hyper-isotopes might have diluted the hypertriton production. Therefore, the fragmentation model was also evaluated for lithium as target nucleus. The results are presented in Figure 8.2 [62]. In this case, the main stable isotope is ^{7}Li, but also a small quantity of ^{6}Li ($\approx 8\%$) is found naturally, so both fragmentation calculations are shown. At first glance, the two spectra seem a lot clearer than the one of ^{9}Be, simply by the fact that the heavier hyperfragments cannot be produced anymore. At the same time, the yield of $^4_\Lambda$H is elevated, crossing the 10^{-3} at moderate excitation energies. This was not observed for the beryllium target. Even more importantly, the hypertriton yield falls into the region between 10^{-4} and 10^{-3}, around one order of magnitude larger than before. Furthermore, no great difference was observed between the two lithium isotopes, so that natural lithium would be well suited as target material.
From this observation, it was decided to perform the experiment of this thesis indeed with a lithium target. This however required the design of a completely new target system, as lithium is far from being handled as easily as beryllium. All the important details around this target are to be discussed thoroughly in the following section.

8.2. New Target Design

8.2.1. The previous beryllium target

For a proper comparison to the new design, the previous beryllium target is introduced briefly. The orientation of this target as well as the placement of the A1 spectrometers was quite unique in the past experiments, as can be seen on the left side of Figure 8.3. The target normal was rotated to the electron beam by $54°$, so that for the beam the actual target thickness was raised by a factor of around 1.7. However, to keep the momentum straggling of the outgoing decay pions into the spectrometers A and C as low as possible, SpekC was placed at $126°$ to directly face the target. The same was not possible for SpekA, since the forward driveway was blocked by KAOS. An angle of around $90°$ was the least possible. This meant, that SpekA saw an enhancement in the thickness of around 1.3. For the experiment, actually two beryllium targets with area densities of $X = 23\,\mathrm{mg/cm^2}$ and $X = 47\,\mathrm{mg/cm^2}$ were in use. The thin target was operated with a beam current of $I = 43\,\mu\mathrm{A}$, the thick one with $26\,\mu\mathrm{A}$. The luminosity of these targets can be calculated via

$$\mathcal{L} = \frac{N_\mathrm{A}}{m_\mathrm{mol}} \cdot I \cdot X, \tag{8.1}$$

where $N_\mathrm{A} = 6.022 \cdot 10^{23}\,\frac{1}{\mathrm{mol}}$ is the Avogadro constant and m_mol the molar mass of the target material. The beam current I needs to be converted to electrons per second with $1\,\mu\mathrm{A} \mathrel{\widehat{=}} 6.24 \cdot 10^{12}\,\frac{e^-}{\mathrm{s}}$. By that, for the previous studies the maximum luminosity is found for the thicker target with

$$\mathcal{L}_\mathrm{Be} = 8.7 \cdot 10^{35}\,\frac{1}{\mathrm{cm^2 s}}. \tag{8.2}$$

Here, the molar mass of beryllium $m_\mathrm{mol} = 9.012\,\frac{\mathrm{g}}{\mathrm{mol}}$ was used together with the thickness enhancement of 1.7. Overall, an integrated luminosity of $956\,\mathrm{fb}^{-1}$ was gathered within the last experiment [276].

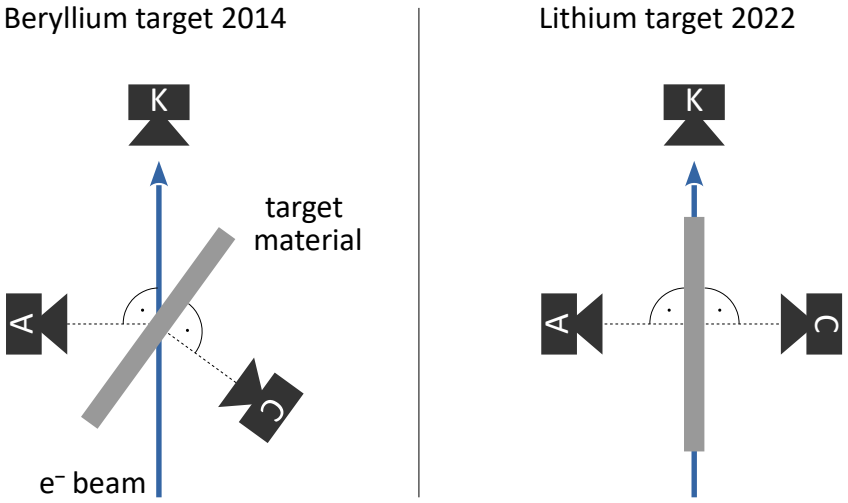

Figure 8.3.: Comparison of the previous beryllium target and the new design with lithium. **Left:** the beryllium foil was rotated to the normal of the electron beam by $54°$. **Right:** with the new approach, the target is rotated by the full $90°$, so that it is completely traversed by the electron beam. SpekA and C are now placed at around $90°$ and see the minimum momentum straggling for the pions. KAOS is kept at the same position.

8.2.2. The concept of the lithium target

The new lithium target is designed completely different. As can be seen in the right of Figure 8.3, the lithium is rotated by the full $90°$ so that it aligns with the electron beam. By that, the amount of target material is drastically enlarged. Still, by being thin perpendicular to the beam, both the spectrometers A and C can see the target without any thickness enhancements, in contrast to the old design. There, the thickness was limited in order to protect the momentum resolution of the decay pions. With more material to pass, their momentum would suffer stronger statistical losses. To compensate for that, comparably high beam currents were used for the old design. This lead to elevated radiation levels in the experimental hall, causing large background rates, frequent crashes of surrounding devices and other technical issues. The new target design therefore aims to keep a comparably high luminosity by using only a fraction of the beam current.

Material and geometry

Lithium naturally occurs in two stable isotopes, which is 7.6% ^{6}Li and 92.4% ^{7}Li. It is the third lightest element and has a density of only $\rho = 0.534\,\frac{\mathrm{g}}{\mathrm{cm}^3}$. This low quantity will be important for the target geometry, as described soon. The molar mass is $m_{\mathrm{mol}} = 6.94\,\frac{\mathrm{g}}{\mathrm{mol}}$.
It was decided to perform the experiment with the natural isotope mixture, since their similar hypernuclear yield behavior did not justify the need for purified samples (compare to Figure 8.2 on page 92). The target is designed to have a length of $l = 45\,\mathrm{mm}$, equivalent to an area density of $X = \rho \cdot l = 2.4\,\frac{\mathrm{g}}{\mathrm{cm}^2}$. By that, the available target acceptance length from SpekA and C of $50\,\mathrm{mm}$ is used properly. Following (8.1), for this target design a luminosity of

$$\mathcal{L}_{\mathrm{Li}} = 14.3 \cdot 10^{35}\,\frac{1}{\mathrm{cm}^2\mathrm{s}} \tag{8.3}$$

is easily reached with a beam current of just $I = 1.1\,\mu\mathrm{A}$. This result is not only almost twice as large as for the previous target, the beam current is also reduced by a factor of 20. Later during the experiment, the beam current of $1.1\,\mu\mathrm{A}$ turned out to be the maximum to be handled properly by the detectors. Beyond that, dead time issues and random coincidences became dominating. More about that is described in Chapter 9, starting at page 109.
While the in-beam length of the target is maximized, the perpendicular direction still has to be kept as narrow as possible to limit the amount of momentum smearing, the decay pions would suffer from. In this dimension, the lithium was chosen to be $0.75\,\mathrm{mm}$ thin. For this value, it was taken into consideration, that the electron beam is not point like, meaning that it has a Gaussian shaped intensity distribution. For narrower targets, a certain amount of electrons would then be lost by missing the target, so for that reason it cannot be arbitrarily thin. Indeed, the remaining thickness will cause momentum smearing, but here the low density of the lithium becomes useful. The target can be wider as if it was made from denser materials. By assuming the average decay pion has to traverse half of that material, the resulting area density is $20\,\frac{\mathrm{mg}}{\mathrm{cm}^2}$. This is almost the same as for the previous beryllium targets. Depending on the thickness and the angle of observation, values between 11 and $31\,\frac{\mathrm{mg}}{\mathrm{cm}^2}$ were achieved.

After all, the doubled luminosity alone won't be the changing factor between the two experiments. The main advantage of the new design rather is the lower required beam intensity. Being a factor of 20 lower, the amount of background in the A1 hall is reduced. This will already suppress false trigger events in the scintillators of all spectrometers and also reduce random coincidence events. The same holds for the whole beam line in general. There will be fewer sources of elevated radiation levels and hence the accelerator will run more stable. Finally, for lithium a larger yield of the light hydrogen hyper-isotopes is expected.

Challenges of the new design

Besides the positive aspects of the material choice and new geometry, there are certain disadvantages which needed to be addressed:

- **High reactivity of lithium** – in general, as an element from the first group of the periodic system, the alkali metals, pure lithium is very reactive with a huge variety of other elements and molecules. This includes oxygen and nitrogen from the ambient air as well as water. While the first two will cause the formation of white dust at the surface over the course of several days, the reaction with water proceeds much more violently. Therefore, pure lithium is usually stored inside a protective oil or argon gas. The actual working procedure with this material in scope of this experiment is found in the appendix in Chapter B.3.

- **Low melting point of 180°C** – especially when irradiating the target with a particle beam, a certain amount of heat will be deposited in the lithium material. To prevent it from melting, a new frame to hold and cool the target was manufactured by Bachelor student Marten Mildeberger [205]. It is described in the following Section 8.2.3. To indeed observe the deposited heat at the target, an additional thermal camera system was developed together with Bachelor student Julian Geratz [138]. It shall act as temperature monitor and detect hit patterns by the electron beam as well. This setup will be explained in Chapter 8.3.

- **Alignment of target to beam** – The usual procedure of alignment at A1 – the careful and precise orientation via a theodolite – cannot be applied to the lithium target because of its reactivity with ambient air. At the same time, it requires a better alignment than many other commonly used targets. This is due to the slim design of the target. A slight offset of the beam to the left or right would already result in many electrons passing by the sides. Even once aligned, the position still has to be checked frequently since drifts of the beam of already $100\,\mu\mathrm{m}$ can lead to a significant drop of the luminosity. In addition, also the rotation of the target has to exactly match the beam direction, otherwise the long lithium stripe will only be partially traversed. This situation was addressed via the installation of two motors inside the target chamber to correct the target position during the experiment, described in Section 8.2.4.

8.2.3. Target frame with cooling system

Based on the requirements, a copper frame was designed together with Bachelor student Marten Mildeberger [205]. It is shown in Figure 8.4. This frame fixes the lithium plate from top and bottom via two copper holders. They are screwed into the main frame to press the lithium on tightly to guarantee a proper thermal contact. The blocks were half the way colored with infrared absorbing black paint so that later on an orientation is given in the thermal images. In the upstream direction, there are two bars to support the structure. Again, they were also painted black, this time to prevent disturbances in the images by reflections on the pure metal surfaces. The pipe on the left connects the top and bottom bases of the frame which both are traversed by coolant. That way the lithium can be cooled at both ends. From the bottom base, the cycle can be connected to the existing target chamber's cooling water pipes (seen on the right side). The system is completed by the Lauda MC 250 cooler, which is then connected to the target chamber via swadge lock and placed on the hall floor. During the beamtimes, the cooling temperature was set to $5\,^{\circ}\mathrm{C}$, and a water-isopropanol mixture was used.
On top of the copper frame, the usual A1 target ladder is placed. In there, additional targets are stored, an Al_2O_3 screen for beam position checks as well as carbon and tantalum targets for calibration purposes. This whole target setup is mounted onto a set of two step motors, one rotational and one linear. These allow for the alignment of the target, even once the chamber was closed and evacuated.

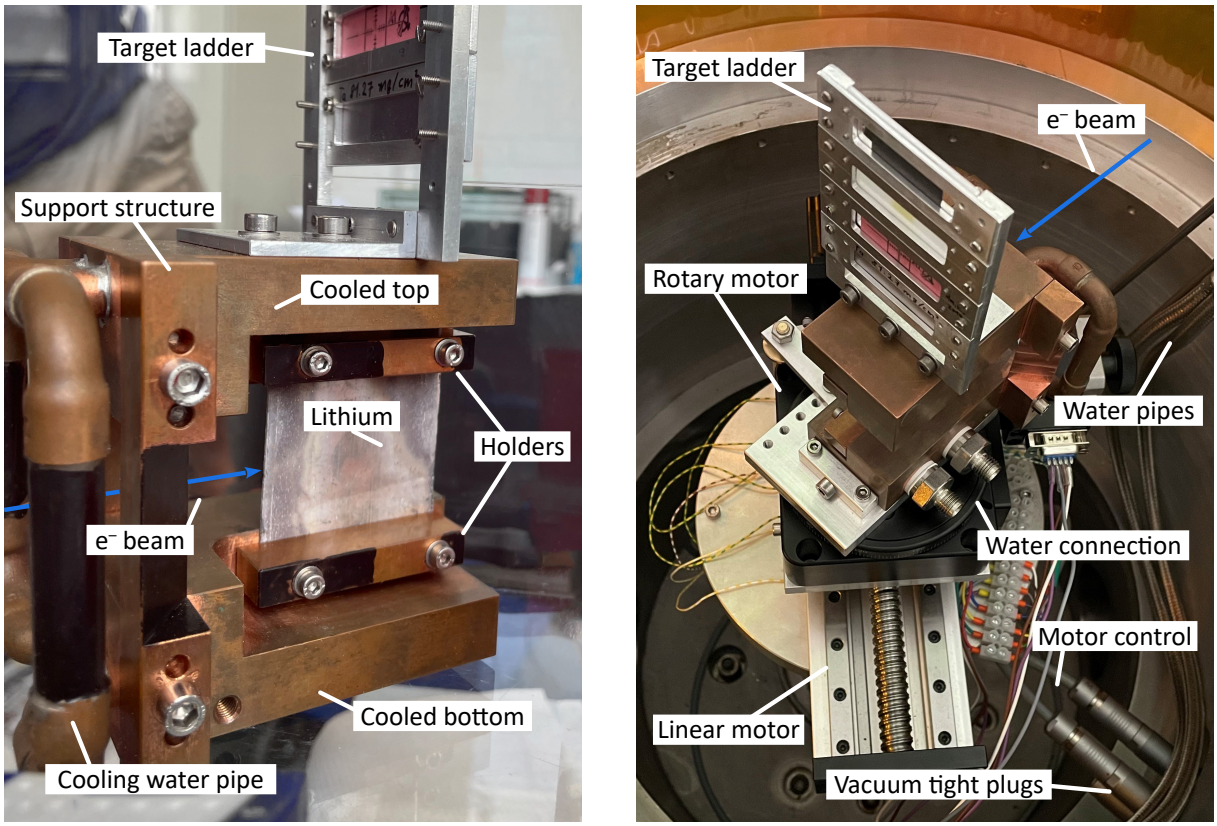

Figure 8.4.: High-luminosity lithium target designed for the new hypertriton experiment [205]. **Left:** the lithium sheet in the center has a thickness of $2.4\,\mathrm{g/cm^2}$ in beam direction. In the left part of the setup, pipes for the cooling liquid can be seen. **Right:** the copper frame inside the target chamber, additional A1 targets are mounted in an aluminum ladder on top. Below the frame, a rotary and a linear stepper motor are located.

8.2.4. Target motors and control via a GUI program

The linear motor allows to move the target to the left and right from the electrons point of view, while the rotary one allows for the left-right rotation. Both motors can be seen on the right of Figure 8.4. To control and stir these motors, a simple GUI program was developed. It is written in python with the tkinter extension for the interface. A screenshot of the program is given in Figure 8.5. It shows a grid of buttons and a status sketch as well as further details in the lower corners. The target is depicted as a gray bar which is placed in reference to the electron beam (blue line). The position of the target can be changed by pressing the *move ...* or *rotate ...* buttons. Then, the chosen amount of steps at *Steps to go* will be driven. It is to be noted that the linear motor has a step conversion of $4\,\mathrm{mm}$ per $10\,000$ steps, while the rotary motor does $1°$ per $10\,000$ steps. Once actually an amount of steps was driven, the sketch will be updated accordingly. That way, it is easily visible, how the target is located and if it is hit. This, of course, is only possible after a calibration of the target-to-beam position.

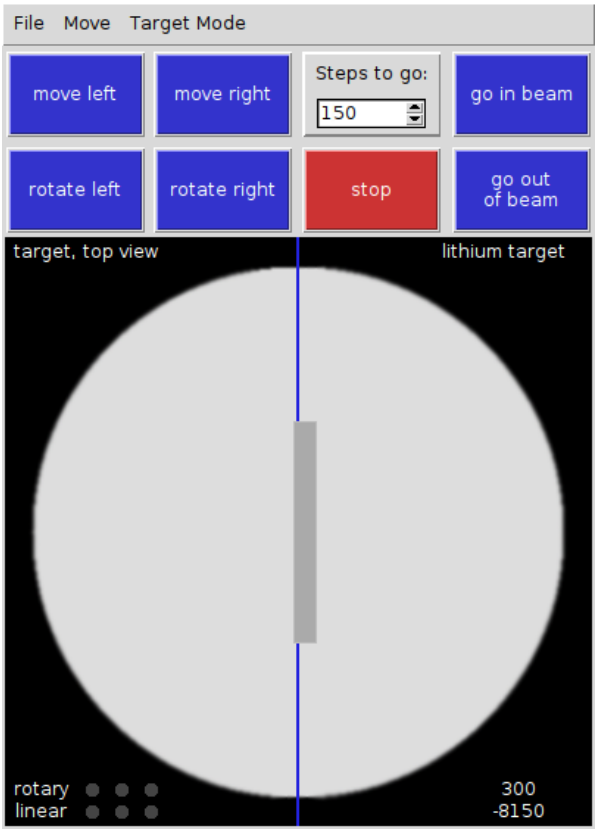

Figure 8.5.: The Target Control GUI.

Once ensured that the target is completely traversed by the electron beam, e.g. via the thermal cam surveillance or the trigger rate in the spectrometers, the set point can be marked as ideal by clicking *File* → *Save as "in beam lithium"*. Once this point exists, it can be reached immediately from any other position by pressing *go in beam*. Analogously, also a defined *out of beam* position can be saved and requested.
At the bottom right of the GUI, the raw positions of the two motors are shown as step values. On the left, there are three status lamps indicating if any of the position indicator switches is pressed. These limit the drive way of the motors to avoid damages and allow to re-calibrate the coordinate system of the motors in case of a loss. This is done by *Move* → *Do reference run*.

8.3. Video Surveillance with Thermal Cameras

Together with Bachelor student Julian Geratz a thermal camera system was developed [138]. It is based on the Flir Lepton thermal camera module [124], seen in the left part of Figure 8.6. It consists of a breakout board and the main camera chip. Its geometry is quite tiny, being as large as a cent coin. In this figure, one can see the two parts inserted into a 3D printed holder. The camera has a field of view of $50°$ and a resolution of 60×80 pixels. The chip is designed to observe long wave infrared radiation with wave lengths from $8\,\mu\text{m} - 14\,\mu\text{m}$, equivalent to a temperature range from -10 to $140°\text{C}$.

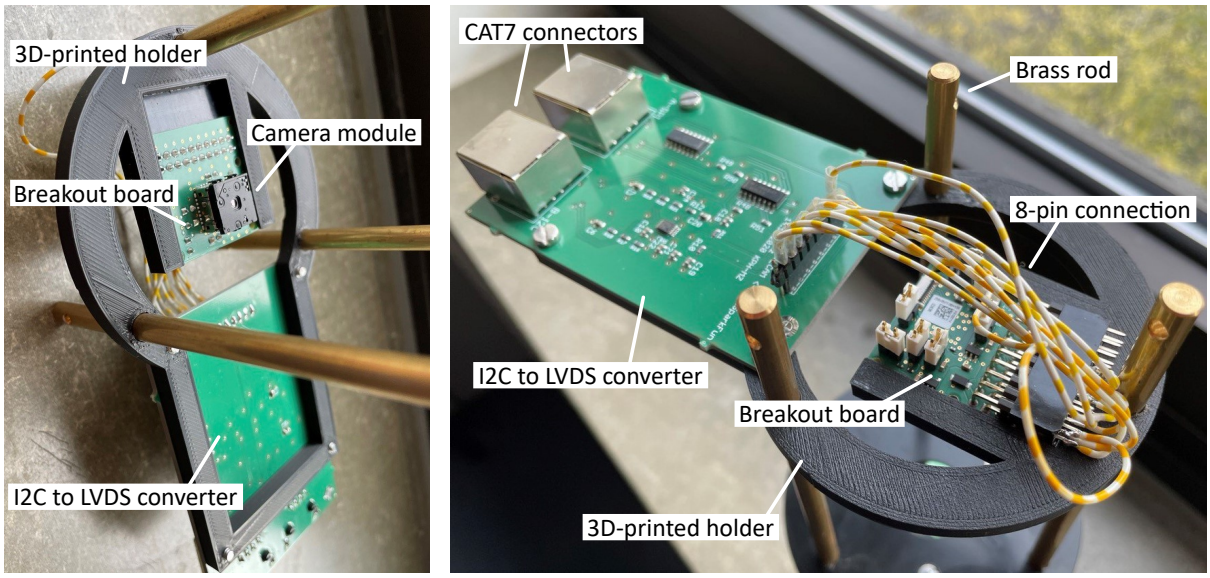

Figure 8.6.: Thermal camera setup with holder construction [138]. **Left:** the module is placed on its breakout board in a 3D printed holder frame. **Right:** back side of the construction, the breakout board is connected to Geratz' converter via 8 pins.

Lens system

Due to the wide field of view, the camera would have to be put very closely to the object it shall observe, especially for small objects like the lithium target. The idea to install the camera module inside the target chamber right next to the target was quickly discarded due to concerns about radiation damages. So the other option was to install the camera at a greater distance and develop an additional lens system to shrink the field of view. This was done via a set of 4 infra red transparent GaAs lenses. Following calculations by P. Klag, the focal lengths of these were set to $50\,\text{mm}, 2 \times 75\,\text{mm}$ and $100\,\text{mm}$.
Placing the camera outside of the target chamber also implies to have an infrared transparent window in the chamber wall. Normal glass usually isn't transparent for thermal radiation, so a solution was found by using one of the lenses as window. The construction is shown in Figure 8.7. On the left there is the aluminum flange to fit on the target chamber. It has a central hole and two grooves for the lens and an additional holder to be placed in. The connection between lens and flange is sealed with a rubber ring. This construction is seen on the right side. The flange also has three more threaded blind holes. They are used to insert brass rods which will act as holder for the remaining lenses and the camera. The complete construction will be

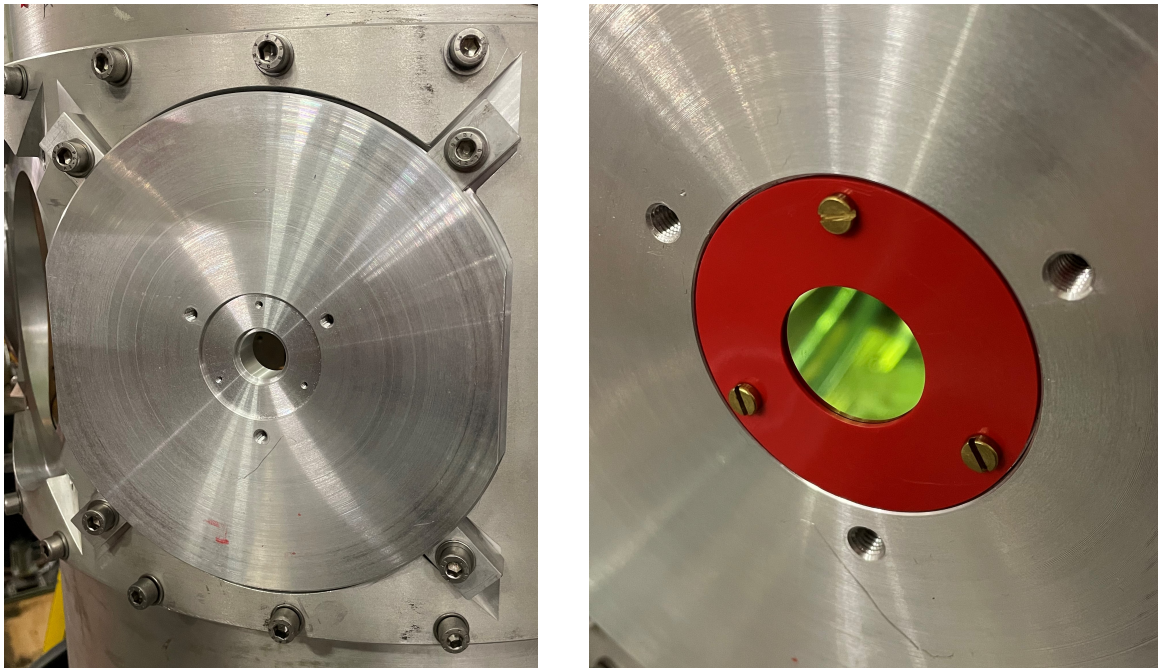

Figure 8.7.: Dedicated flange to mount the thermal camera system. **Left:** flange on the target chamber with a central hole for the thermal camera to look through and two cylindrical milling grooves for the first lens to be placed in with an additional holder plate. **Right:** these two parts are inserted. The GaAs lens is not transparent to optical light.

shown in Figure 8.10 on page 101. This setup was installed twice, on the one hand to observe the target from both sides and on the other to offer redundancy in case of radiation damages. The focus, sharpness and zoom of the lens system is dependent on the distances between the optical elements. In Figure 8.8 an overview about the parts and their order is given. Together with the students Jonas Klingelhöfer and Christian Helmel a test bench was set up to derive the combination with the best magnification and sharpness [180]. A solution was found with $d_1 = 255\,\mathrm{mm}$, $d_2 = 134\,\mathrm{mm}$, $d_3 = 53\,\mathrm{mm}$, $d_4 = 13\,\mathrm{mm}$ and $d_5 = 22\,\mathrm{mm}$. Here, the distance d_1 was already fixed by the diameter of the target chamber.

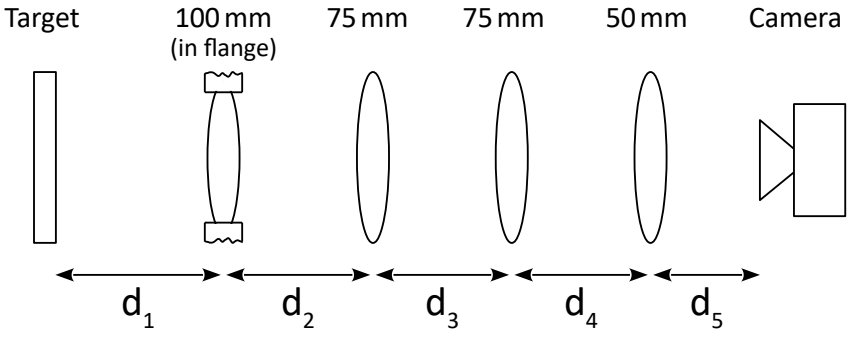

Figure 8.8.: Sketch of the thermal lens setup. A total of 4 lenses is used to focus the camera's field of view onto the target. Their focal lengths are noted on top. Depending on the distances $d_1 - d_5$, the resulting image will vary in focus and sharpness. The first lens is attached directly to the target chamber, so its position is predefined.

A resulting thermal image taken with the fully installed system is shown in Figure 8.9. Here one can see the raw image of the lithium target on the left and a more illustrated version of it on the right. The outer circular shape marks the limits of the hole in the aluminum flange, so the outer region shows parts of this flange. The region of interest is the inner circle, depicting the structures inside the target chamber. The main object inside there is indeed the lithium target. In this picture it is hit partially by the electron beam, so that the left region is warmed up.
Also the transition from hot to cold towards the top and bottom is visible. These are the regions where the cooled copper frame is located. As mentioned in Chapter 8.2.3, black marks were made on the frame to give a sense of orientation. These marks clearly show the cold temperature, while the blank copper parts mostly reflect the ambient temperature. Another detail is found on the right side, which is the partially covered thermal lens of the second camera setup on the other side of the target chamber. A more detailed analysis of the thermal images is found in Section 8.4 on page 102.

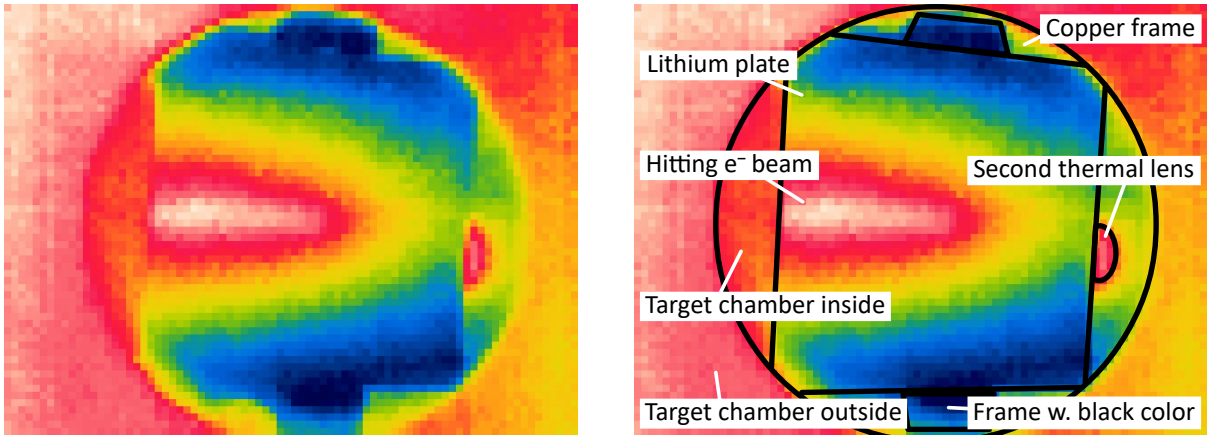

Figure 8.9.: Thermal image of the lithium target while being irradiated with $2\,\mu A$ beam electrons. **Left:** raw picture, many structures are visible, the image is sharp, the contrast high. **Right:** the same picture with additional lines and descriptions. The main image is found inside the inner circle. Here, most of the place is filled by the lithium plate. It is partially warmed by the traversing beam electrons. Also other details are found, for example the thermal lens of the second camera setup of the back side of the target chamber. Also the copper frame is partially visible. Its observed temperature varies strongly due to the applied black paint. Outside of the big circle, mainly the outer wall of the target chamber is visible.

Connection to a raspberry pi

The camera is addressed via a set of pins with the I2C protocol. Usually, this camera can directly be operated with a raspberry pi. It was found though that the signal transmission only works for several centimeters free of disturbances. However, since the camera will be located very close to the target chamber, it is of interest to use a cable of several meters length to keep the pi safe from radiation. Therefore, Klag and Geratz developed converter boards to change the signals to LVDS (Low Voltage Differential Signals) which proved to be much more reliable [138]. Then, close by the pi, a second converter changes the signal back to I2C. Figure 8.6 already showed the converter board mounted to the camera holder and the two CAT7. The completely installed setup is seen in Figure 8.10, where the outgoing CAT7 cables are plugged to the raspberry pi, seen on the right side. Here, the second conversion board is seen. In fact, by that effort the possible cable length was enhanced to at least $5\,\mathrm{m}$.

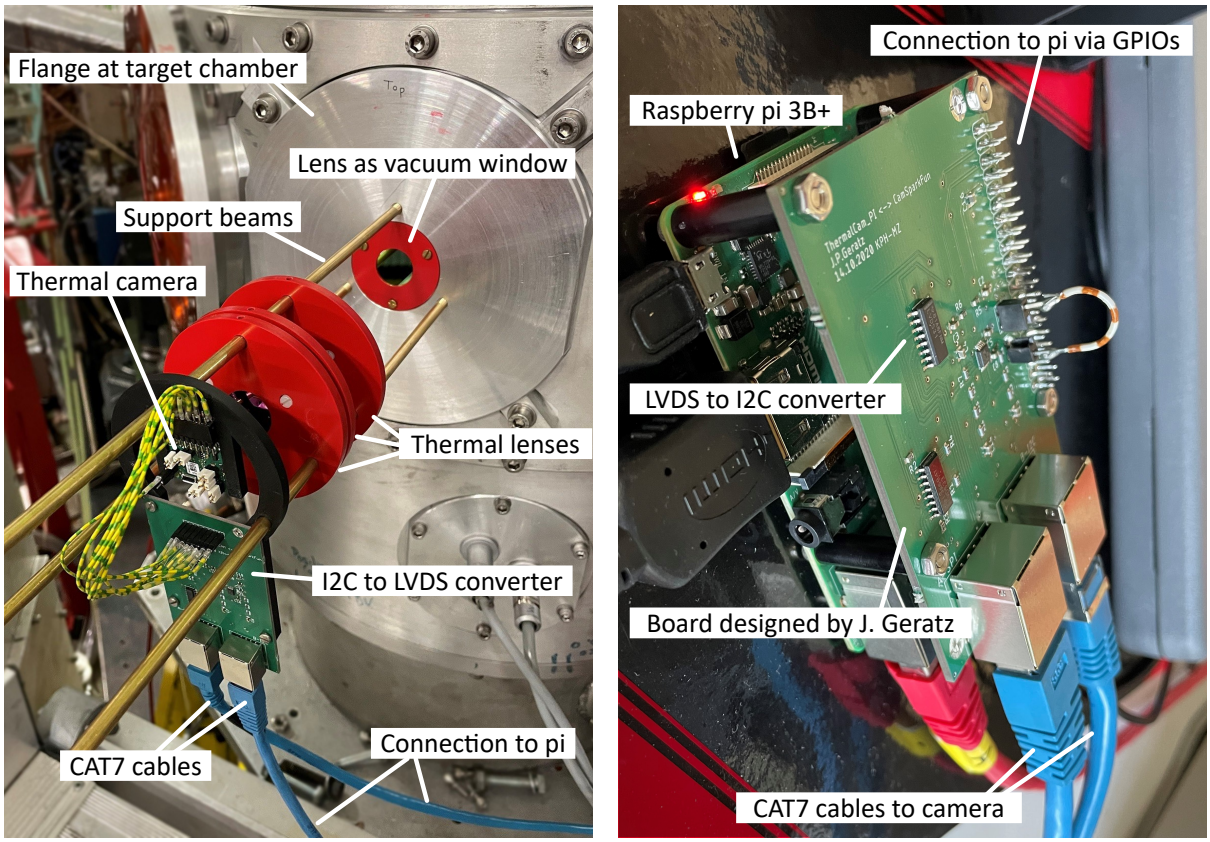

Figure 8.10.: Fully installed thermal camera system. **Left:** additional to the flange lens there are three more lenses stacked onto brass beams followed by the thermal camera on its 3D-printed holder. It also contains the I2C to LVDS converter board to allow for a disturbance free signal transmission. **Right:** connected via two CAT7 cables, a raspberry pi is located a few meters away to be safe from radiation damages. It has its own conversion board to change the signal back to I2C. This board is plugged to the pi via the GPIO connectors.

8.4. Target Test Beamtime

From the 27th to the 29th of April 2022 a beamtime was performed to test the lithium target together with the involved new hardware and proof the overall functionality. A series of tests was performed which are described in the following.

Experimental setup around the target chamber

The beamtime was solely performed with the spectrometers A and C, while KAOS was not installed at that time. Their angle and momentum setting is found in Table 8.1. The central momentum was already set to $120\,\mathrm{MeV}/c$, a value close to the final setting in the following hypernuclear beamtimes. Initially it was also planned to already use the MAMI-C energy of $1508\,\mathrm{MeV}$, but it was not available at that time though. So the maximum MAMI-B energy of $855\,\mathrm{MeV}$ was used instead.
The beamtime was shared with another group of physicists from the PANDA Collaboration, so it was not possible to install each component like foreseen for the final setup. Still, the two thermal cameras where mounted, one at $115°$ and the other at $145°$. The latter one was furthermore equipped with a periscope designed by Geratz to overcome space issues and to observe the target with a camera placed out of the scattering plane by around $20\,\mathrm{cm}$. A top view of the target chamber is given in Figure 8.11. While this figure does not depict the actual setup of the test beamtime but rather the one of the later hypernuclear beamtimes, it still nicely illustrates the used components. During the test experiment it was quickly observed that the angle of $145°$ is slightly too steep to observe the lithium properly. The main issue was rather not the geometric angle under which the target was looked at, but it was problematic due to the support structure and cooling water pipes of the copper frame. These where partially visible in the pictures and disturbed the dynamics via reflections of the emitted thermal radiation. Later on, this problem was solved by changing the angle of this camera and – as mentioned before – painting the reflective areas of the frame with infrared absorbing paint. With these improvements, better pictures were taken in the following beamtime.

Thermal images

Two shots which were taken during the first hypernuclear beamtime are given in Figure 8.12 [109]. The left panel shows target and beam misaligned so that only the left side is warmed up. This picture was already discussed in Figure 8.9. The geometrical relation is also depicted below, where the beam (blue arrow) hits the target only partially. In the right panel, beam and target are aligned, so that the full length is warm. From these pictures, a maximum temperature of $28°\mathrm{C}$ was observed for a beam current of $2\,\mu\mathrm{A}$, which proved the applicability of this target setup.

Table 8.1.: Spectrometer and camera settings for the lithium target test beamtime.

Object	Angle	Comment
Spectrometer A	$78°$	central momentum $120\,\mathrm{MeV}/c$
Spectrometer C	$90°$	central momentum $120\,\mathrm{MeV}/c$
KAOS	*not used*	
Cam 1	$145°$	regular setup
Cam 2	$115°$	periscope setup

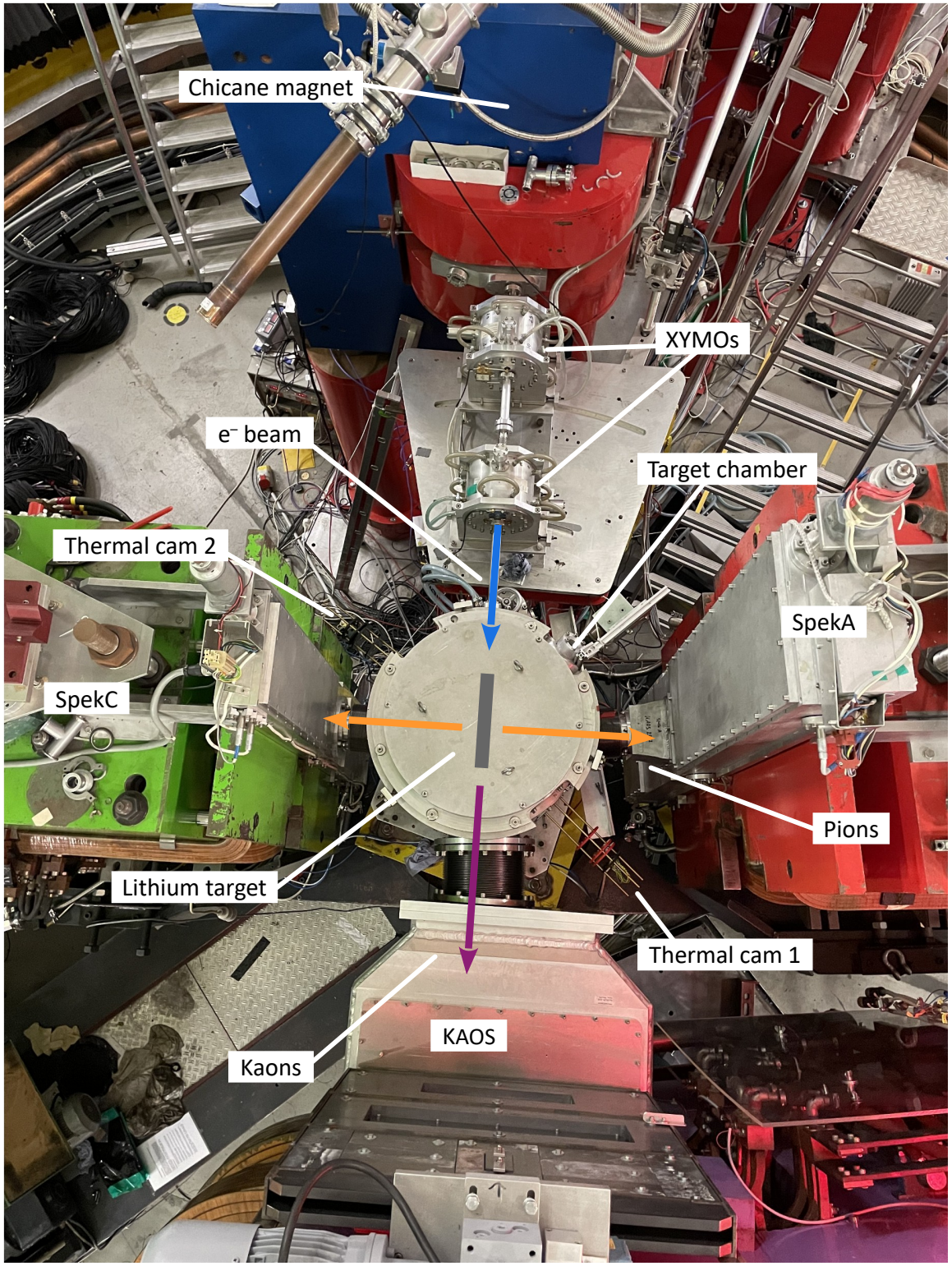

Figure 8.11.: Top view of the target chamber. One can see the arrangement of the A1 spectrometers A, C and KAOS during the first hypernuclear beamtime. From the top, the electron beam leaves the pre-chicanes and enters the target chamber. Inside, the lithium target is placed. KAOS is flanged to the chamber to catch the emitted kaons from the Λ generation process. At around 90° A and C are placed to detect the decay pions. There are also two thermal cameras attached to the chamber, one on the left at a large backward angle, one on the right at a small angle.

Within the first test beamtime, it was still possible to take images especially with the telescope camera. In particular interesting are pictures of the standard target ladder sitting on top of the copper frame, as shown in Figure 8.13 (Photos of the ladder found in Figure 8.4 on page 96). The left one shows two targets in their aluminum holder which are distinguishable due to their different reflective behavior and thermal emission. The right one shows the carbon target in its frame being hit by the electron beam. A spot of roughly $1\,\mathrm{cm}^2$ is warmed up. This proves on the one hand the reliability of the periscope setup and on the other the general usability of the thermal camera for other target systems than the lithium stripe.

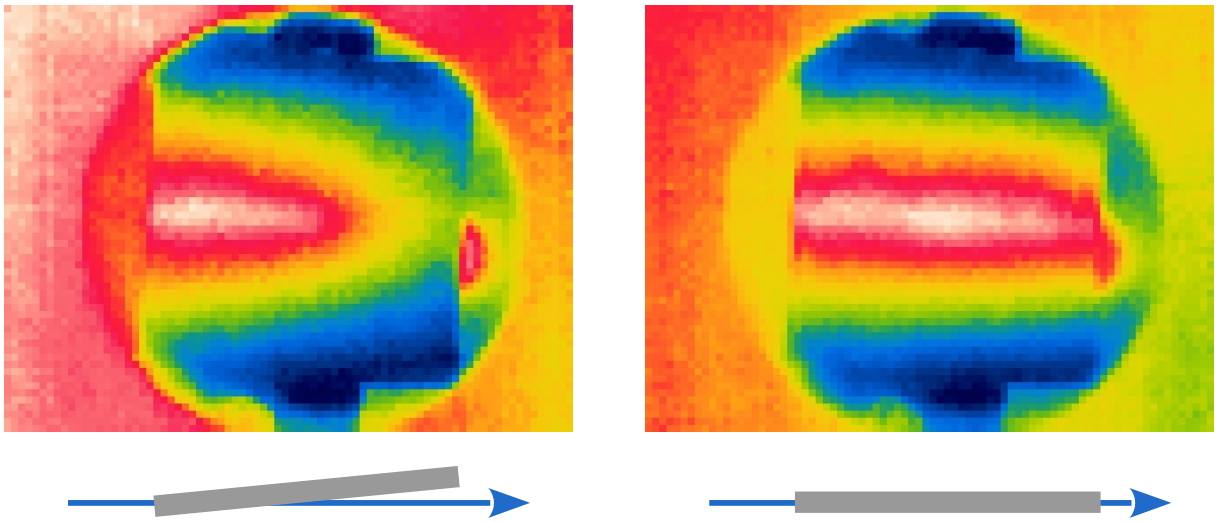

Figure 8.12.: Thermal images of the lithium target during the hypernuclear beamtime with a 1.5-GeV electron beam [109]. The orientation of the target is schematically depicted at the bottom. **Left:** target and beam are misaligned, the lithium was only partially heated (already shown in Figure 8.9). **Right:** correct alignment, the heat is equally distributed. In both cases a beam intensity of $2\,\mu\mathrm{A}$ was used and the maximum temperature only reached $28°\mathrm{C}$.

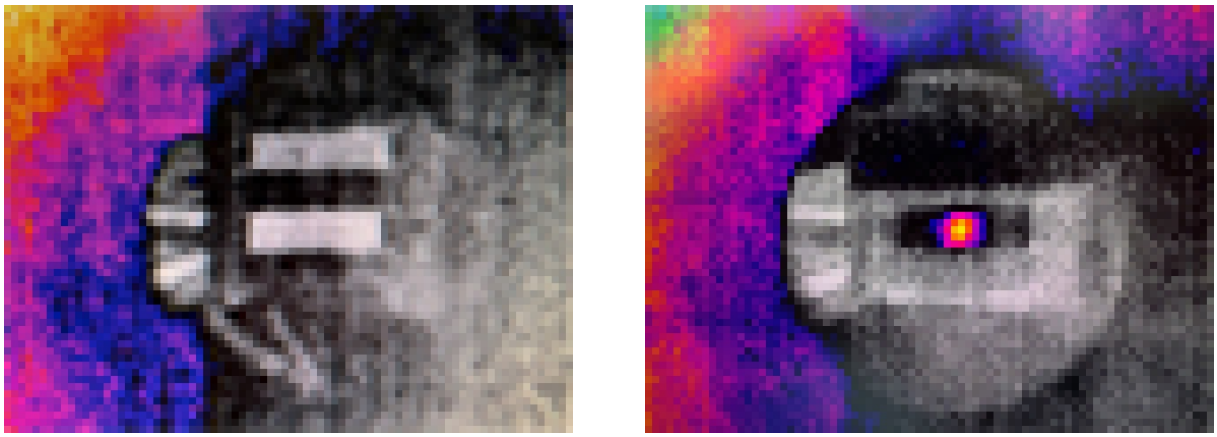

Figure 8.13.: Thermal images of the target ladder captured with the periscope camera. **Left:** two targets within their aluminum frame are visible just due to their different thermal emission behavior. **Right:** the electron beam is hitting a carbon target, so a warm spot is visible.

Motor test and rate maximization

Besides the thermal images also the count rates in the spectrometers give an indication of how the target is oriented with respect to the beam. These were used to cross check the motor movements for consistency and to align the target properly to the beam. In Figure 8.14 the results of two data taking campaigns are shown [109]. In the first, the position of the linear motor was varied, while the rotary motor was fixed. For the second, the opposite was performed. It is to be noted that earlier to that campaign a similar scan was already performed so that respectively the fixed motor was moved to its position of maximal rate before.
For both directions the raw trigger rates of SpekA and C were recorded. On the left, the linear motor was varied in steps of $80\,\mu\mathrm{m}$. A clear maximum in both spectrometers is found at the central of the figure. The curves have a FWHM of roughly $1\,\mathrm{mm}$ which matches the width of the target of $750\,\mu\mathrm{m}$ well. For both spectrometers the overall shape of the data appears continuous, no gaps or other artifacts were observed. This indicates that the motor neither got stuck nor lost steps while moving. For the right figure, the picture is almost the same. For geometrical reasons the shape of the peak is different, however also here a clear maximum without any artifacts is found. The FWHM here is about $4°$.
To summarize, both motors worked reliably. The challenge of the precise alignment of the target by a fraction of a millimeter and degree was handled successfully. The motors proved to offer enough sensitivity even inside the vacuum chamber. Also the rates in the spectrometers gave a fully sufficient accuracy to find the maximum rate.

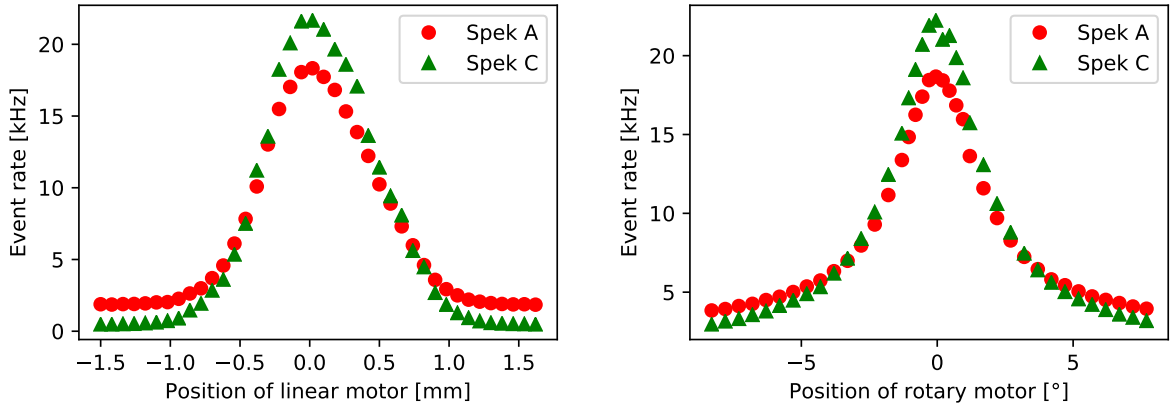

Figure 8.14.: Spectrometer rates in dependence of the position of the lithium target [109]. $855\,\mathrm{MeV}$ beam electrons with $3\,\mu\mathrm{A}$ beam current were used. **Left:** the linear position of the target parallel to the beam was changed. A clear maximum is seen in both the spectrometers A and C for the position around $0\,\mathrm{mm}$. **Right:** the rotary position was changed. A similar behavior compared to the linear motor was observed with small differences in the peak form due to geometrical reasons.

High current test

The final experiment to be performed within the test beamtime was a study with high beam currents. Its goal was to observe the behavior of the lithium in terms of temperature and rate. For the test, the target was moved to its position of maximized luminosity and the beam current was increased in $1\,\mu\mathrm{A}$ steps up to a maximum current of $14\,\mu\mathrm{A}$. The result of this test is shown in Figure 8.15. Here, in red and green the current dependent rates in SpekA and C are given.

In general, the behavior of the observed rates is very similar. It is continuously rising with the beam current. SpekC is a little higher since it features a larger momentum acceptance of 25% instead of 20% for SpekA. After all, there was no drop in the rate observed which could have indicated a meltdown of the target material. One issue was given during this test by the huge amounts of produced radiation, as the beam current was increased. For that reason, the thermal cameras were not able to determine the target temperature during this run. Anyhow, due to the stable rates and a later visual examination of the lithium plate, no melting had occurred. So even in this test, a failure of the cooling system was not observed.

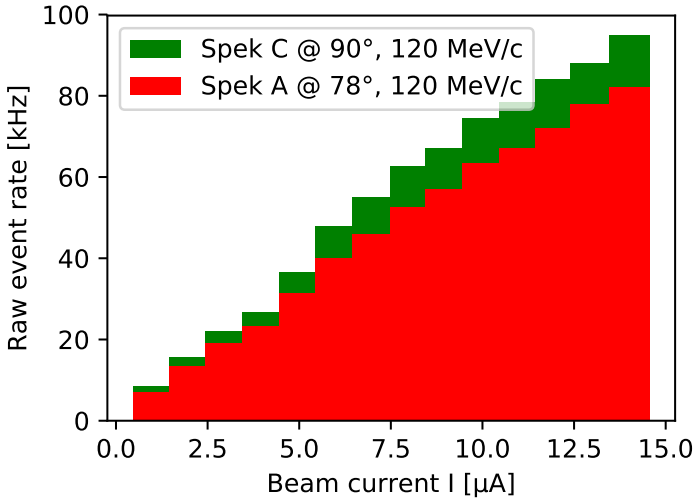

Figure 8.15.: High current test of the lithium target. For slowly increasing beam currents the raw rates of the spectrometers A and C were observed. At high currents, it would have been possible that the lithium melts and the rate suddenly drops. But as the rate kept rising continuously, that point was not yet reached.

Target summary

After this test beamtime, a series of minor changes was applied to the target setup, after which the system was ready to be used in the final experiments, as already depicted in Figure 8.11. A picture of the lithium after the irradiation is given in Figure 8.16. As one can see there, the overall shape of the target stayed intact. The only change are the black stripes on the lithium plate which were burned in by the beam. Here it is worth noticing, that the height position of the target had been changed during the studies, so multiple stripes are visible. They stretch evenly and continuously from the left to the right, again indicating that the target had been oriented properly.
During the studies, it was found, that the method of aligning the target via the spectrometer rates was far more reliable and quicker than the optical approach with the thermal cameras. The procedure involved the step-wise scan of one motor until a maximum was found. Then the other motor was maximized. The same was repeated in one more iteration until an optimal position was found. These steps took usually less than a minute. For this reason, the thermal camera setup was not used anymore for the second hypernuclear beamtime.
Also the periscope setup turned out to be a success. Though the exploration was not continued due to the lack of need during the following experiments, it still offers promising possibilities for future studies. It can be mounted with more degrees of freedom in terms of placement and

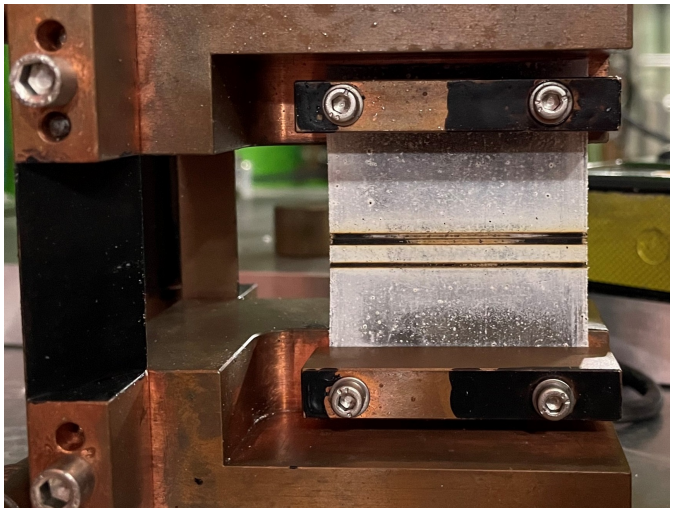

Figure 8.16.: Lithium target after the second hypernuclear beamtime. There are two marks observed, since the height of the target was changed after two weeks of operation. By that, fresh lithium could be used again. The stripes show a continuous discoloration along the complete length, so the target was aligned successfully, even over the coarse of weeks.

also gives more opportunities for radiation shielding of the camera.
Finally, the temperature behavior of the target could be observed via the thermal cameras. It is shown in Figure 8.17. The beam current was increased in steps of $0.1\,\mu\mathrm{A}$ and the maximum temperature was recorded. Starting from the $5°$ cooling water temperature, a linear transition was found to around $28°$ at $2\,\mu\mathrm{A}$. With the fit curve, an increase of $10.9°/\,\mu\mathrm{A}$ was extracted. By that, the maximum temperature during the high current test in Figure 8.15 can be estimated to around $150°$, still below lithium's melting point. The observed temperature behavior also highlights the capability of the thermal camera system in general. The scattering of the data points compared to the fit curve is moderate, it is observed to appear with a standard deviation of only $1.3°$.

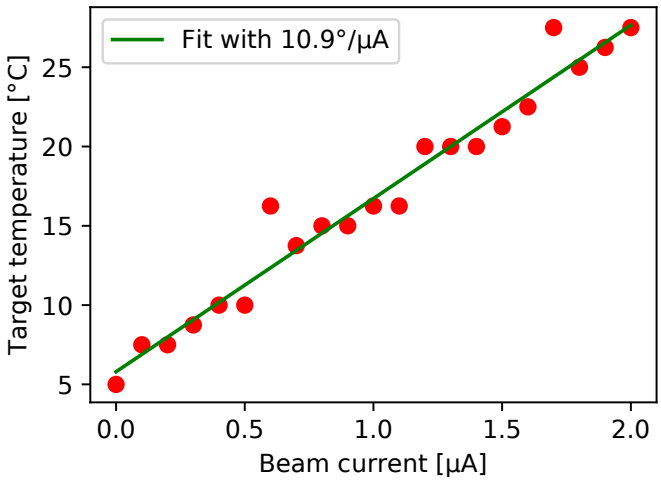

Figure 8.17.: Temperature behavior of the target measured with the thermal cameras. In steps of $0.1\,\mu\mathrm{A}$ the beam current was increased and a linear rise of the temperature was observed.

9. The Hypertriton Experiment

In this chapter the actual hypernuclear experiment is going to be described. Section **9.1** focuses on the general setup, involving the kinematic setting of the spectrometers, the used coincidence logic as well as the hyper-isotopes which can be observed in theory. Followed by **9.2**, the first hypernuclear beamtime is presented. It mostly acted as commissioning of the complete setup where many remaining issues were addressed. Finally, the data taking rate was maximized, so that in the second beam time, found in **9.3**, the actual data taking was performed. Also in this section, the present status of the data analysis is summarized.

9.1. Experimental Setup

The general setup in the A1 hall was strongly influenced by the previous decay pion spectroscopy experiments at MAMI [275, 116, 276]. The general principle and the past studies were already described in Chapter 7. Along with the improvements from Section 7.3 and the new lithium target from Chapter 8, the complete new setup is introduced in the following.
A sketch of the new experimental setup is provided in Figure 9.1 [215]. It depicts the A1-hall from a top view and shows the A1 spectrometers on their circular track. From the top, the electron beam enters the hall and is curved via two chicane magnets to an angle of $17°$. In the following, all spectrometer angles are going to be given in reference to this axis. Consequently, KAOS is placed at $0°$ forward angles. It bends the electrons into the beam dump and detects the emitted kaons. SpekA and C were placed orthogonally to the beam. While for C the exact $90°$ could be realized, the space was blocked by KAOS for SpekA. So here, $95°$ were chosen. As in the previous studies, both of them watch for decay pions. All spectrometers were directly connected to the target chamber. That way, they all shared the same vacuum system for a maximized momentum resolution.
The kinematic setting of the spectrometers is summarized in Table 9.1 Aside of the angle, also the momentum setting is found here. The state of KAOS was mainly determined by the restrictions given by the beam line. To guide the electron beam into the beam dump, the field had to be set to between 900 and $1000\,\mathrm{MeV}/c$. Finally, with $975\,\mathrm{MeV}/c$, the value from the previous experiments was chosen.
The central momentum of SpekA was set to $122\,\mathrm{MeV}/c$. That way, with the momentum acceptance of 20%, the momentum lines of ${}^{3}_{\Lambda}\mathrm{H}$ and ${}^{4}_{\Lambda}\mathrm{H}$ are both part of the spectrum. It ranged from $109.8\,\mathrm{MeV}/c$ to $134.2\,\mathrm{MeV}/c$. Spectrometer C, with a larger acceptance of 25%, was set to the slightly lower central momentum of $120\,\mathrm{MeV}/c$. The resulting acceptance is $[107.2, 137.2]\ \mathrm{MeV}/c$.

Table 9.1.: Kinematic spectrometer settings during both hypernuclear beamtimes.

Spectrometer	Central momentum	Angle	Particle
KAOS	$975\,\mathrm{MeV}/c$	$0°$	K^+
A	$122\,\mathrm{MeV}/c$	$95°$	π^-
C	$120\,\mathrm{MeV}/c$	$90°$	π^-

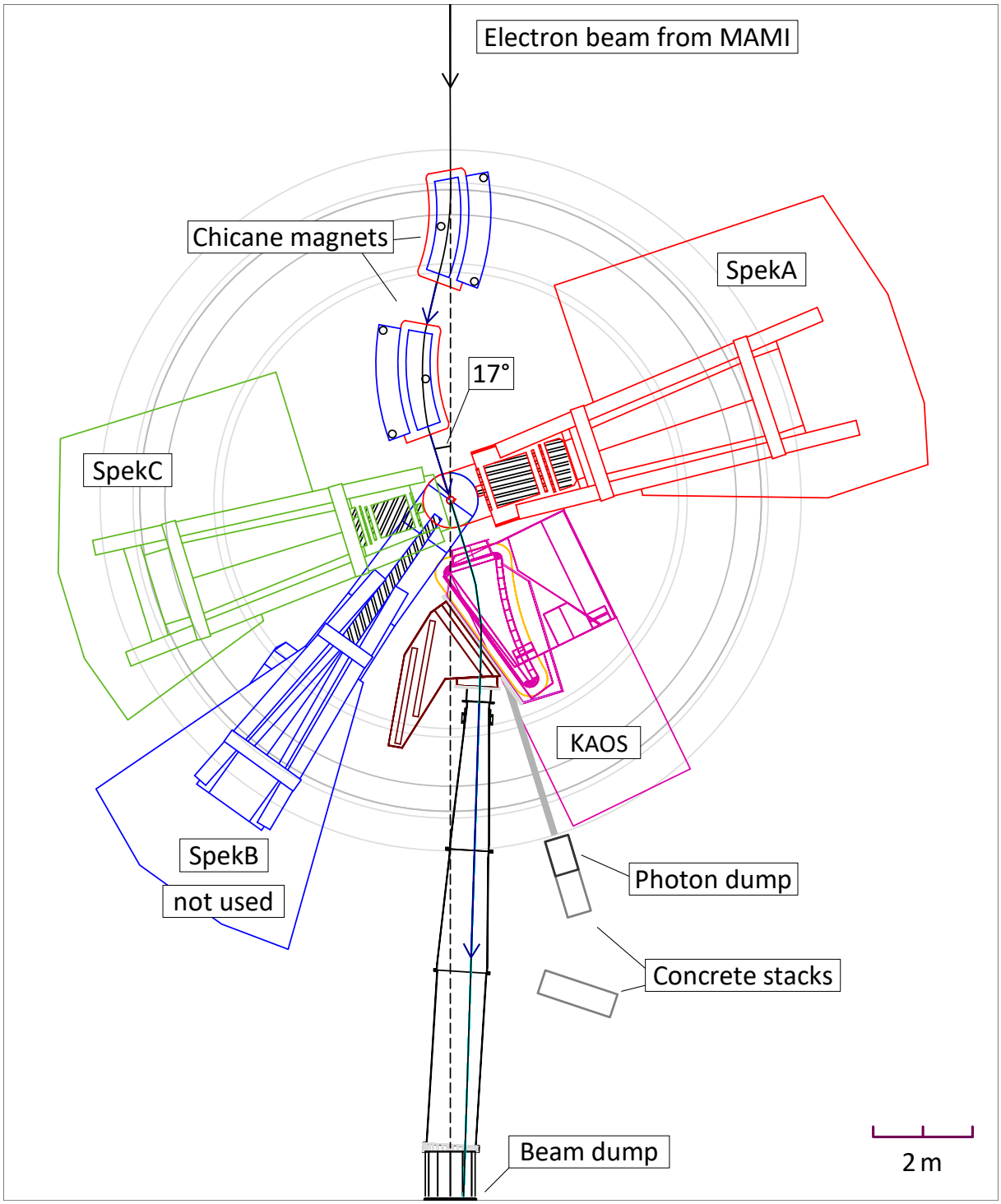

Figure 9.1.: Spectrometer setup of the hypernuclear beamtimes in 2022 [215] (modified). Like in the earlier experiments, the electron beam is deflected with the two chicanes to enter the target chamber under an angle of 17°. The vast majority of the beam will be bent back into the beam dump inside KAOS. Relative to the beam, spectrometer C is placed under 90° to detect decay pions. The same holds for spectrometer A. Due to the use of KAOS, its placement is limited to 95°. Spectrometer B doesn't fulfill any purpose during the beamtime. Additional concrete blocks were placed to shield KAOS from radiation coming from the beam dump.

Table 9.2.: Decay pion momentum of theoretically possible hyperfragments at a $^{7}\mathrm{Li}$ target.

Hypernucleus	Decay momentum	Decay products	Width
$^{3}_{\Lambda}\mathrm{H}$	$114.3\,\mathrm{MeV}/c$	$^{3}\mathrm{He}+\pi^{-}$	–
$^{4}_{\Lambda}\mathrm{H}$	$132.8\,\mathrm{MeV}/c$	$^{4}\mathrm{He}+\pi^{-}$	–
$^{5}_{\Lambda}\mathrm{H}$	$unknown$	$^{5}\mathrm{He}+\pi^{-}$	$0.6\,\mathrm{MeV}$
$^{6}_{\Lambda}\mathrm{H}$	$unknown$	$^{6}\mathrm{He}+\pi^{-}$	≈ 0
$^{4}_{\Lambda}\mathrm{He}$	$98.2\,\mathrm{MeV}/c$	$^{4}\mathrm{Li}+\pi^{-}$	$6.0\,\mathrm{MeV}$
$^{5}_{\Lambda}\mathrm{He}$	$99.3\,\mathrm{MeV}/c$	$^{5}\mathrm{Li}+\pi^{-}$	$1.5\,\mathrm{MeV}$
$^{6}_{\Lambda}\mathrm{He}$	$108.5\,\mathrm{MeV}/c$	$^{6}\mathrm{Li}+\pi^{-}$	–
$^{7}_{\Lambda}\mathrm{He}$	$115.7\,\mathrm{MeV}/c$	$^{7}\mathrm{Li}+\pi^{-}$	–

Observable hypernuclei

Off the lithium target, a reaction for the production of the hypertriton reads as follows,

$$\begin{aligned} {}^{7}\mathrm{Li}\,(e,e'K^{+})\,{}^{7}_{\Lambda}\mathrm{He}^{*} \quad &\rightarrow \quad X+{}^{3}_{\Lambda}\mathrm{H} \\ {}^{3}_{\Lambda}\mathrm{H} \quad &\rightarrow \quad {}^{3}\mathrm{He}+\pi^{-} \end{aligned}$$

Primarily, a highly excited helium hypernucleus is formed, which eventually de-excitates to a ground-state hypertriton. When looking back to the yield plots of hyperfragments at the lithium target in Figure 8.2 on page 92 though, a whole series of hypernuclei might be created instead of $^{3}_{\Lambda}\mathrm{H}$ alone. These are listed in Table 9.2. Theoretically, eight isotopes are possible, ranging from $^{3}_{\Lambda}\mathrm{H}$ to $^{7}_{\Lambda}\mathrm{He}$. The table also shows information about their mesonic two-body decay via the π^{-}, aside of the expected decay pion momentum and the decay reaction. In practice, not all of these hyper-isotopes can be observed via the decay pion spectroscopy, since some remaining nuclear fragments are unstable. Especially critical are $^{5}\mathrm{He}$, $^{4}\mathrm{Li}$ and $^{5}\mathrm{Li}$. They decay via nucleon emission and have therefore a lifetime of around $10^{-21}\,\mathrm{s}$. This leads to a width in the order of several MeV in their masses. This would then also broaden their decay pion peak, which then likely would go indistinct. For $^{6}_{\Lambda}\mathrm{H}$, the width is negligibly low, but here the expected decay momentum is simply unknown, so that the experiment cannot be tuned accordingly. Furthermore it is highly unlikely to transform the $^{7}\mathrm{Li}$ nucleus directly into a bound $^{7}_{\Lambda}\mathrm{He}$, so that also this hyper-isotope will not be observed in the experiment. The remaining isotopes are $^{3}_{\Lambda}\mathrm{H}$ and $^{4}_{\Lambda}\mathrm{H}$. In principle, $^{6}_{\Lambda}\mathrm{He}$ falls also into the acceptance of SpekC as well, but also here its production yield is expected to be very low, in fact by more than 3 orders of magnitude, compared to the hypertriton.

Coincidence logic

The three spectrometers were connected together logically, so that only coincidence events of SpekA with KAOS and SpekC with KAOS were recorded. The coincidence logic at A1 is realized via CAMAC crates with basic logic units from the manufacturers LeCroy and CAEN, but also some institute-specific modules are in use. Each spectrometer has its own logic to generate trigger signals and to perform the data readout. To be able to observe coincidence events though, the spectrometers need to be connected via an additional coincidence logic unit. For the hypernuclear beamtimes, this unit is placed on KAOS. Basically, this logic looks for trigger signals from one of A and C which arrive coincident with a trigger of KAOS. Only then the data readout will be initiated by signals sent back to the involved spectrometers.
In practice, a lot more steps have to be performed to achieve a properly working coincidence unit. The complete logic is depicted as a flow diagram in Figure 9.2. Here, all the involved modules

are depicted as rectangular boxed. Signals coming from (or going to) external modules are marked as rhombuses. Each module receives a letter which links to a short explanation in the box below.
In the figure, the three trigger signals enter from the left. Here, one can see already that SpekA and C are connected logically to act as only one spectrometer. This is desirable since for a proper hypernuclear event only one of them is supposed to detect a particle. By that, the coincidence logic is simplified to just work with the two spectrometers KAOS and A/C. Both of them have their own branch, the upper half for KAOS and the lower half for A/C. From their working principle, these two branches are almost identical. At first, the trigger is distributed via a fan-in-fan-out (FIFO), module A and V. From there, the trigger splits up to the VUCAMs D and U for single events and to a first AND module B and P which leads to the coincidence section. Both of these modules get a secondary input from a μBusy module, ζ for KAOS. For the A/C arm, the busy signals from the readout logic of A and C are taken explicitly. These are to block incoming triggers if already an event is in the readout process. If that is not the case, the trigger is forwarded to the next module. For the coincidence branch, the main coincidence module O is reached. Here, the triggers of both spectrometers are compared. The trigger signal of A/C was defined to have a length on $80\,\mathrm{ns}$. It opens the coincidence window, within that the module will wait until a trigger of KAOS arrives. This has a pulse length of $20\,\mathrm{ns}$. From there, an OR module is reached (F and Q) that triggers the data readout and sets the spectrometer to busy. Also the single branch enters here again, with the only difference, that just the one spectrometer is read out instead of both.
The following modules in the plan are not crucial for understanding the principle, in which the trigger system works. They ensure the proper data readout of KAOS and were kept analogously to the previous hypernuclear beamtimes. The same holds for the spectrometers A and C.

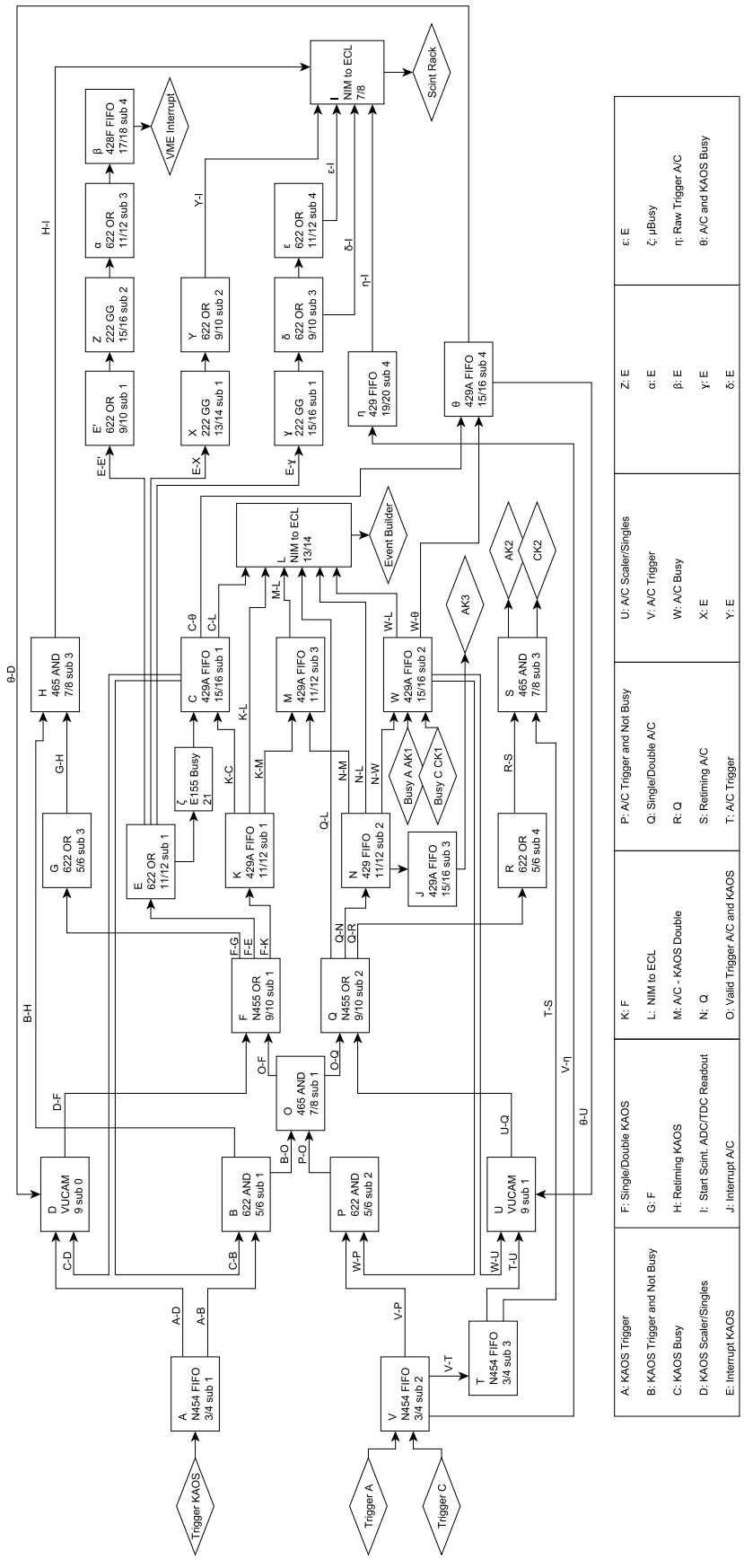

Figure 9.2.: Diagram of the coincidence logic on KAOS. It is the core of the event recognition and triggers the data readout.

9.2. The First Beamtime

From the 11$^{\text{th}}$ of July to the 1$^{\text{st}}$ of August 2022, the first beamtime with KAOS was performed. During that time, many adjustments were applied to bring the setup to a proper state for taking hypernuclear data. The end of that beamtime already allowed for the recording of test data, although without the NMR magnetic field probe in operation. The main adjustments which were performed during the first beamtime are explained in the following.

9.2.1. Finding the correct timing

The first main task was to find a proper coincidence timing between all spectrometers. Here, the path lengths of the particles in the spectrometers together with their respective momenta allowed for the estimation of flight time offsets. These lie in the order of several dozens of nanoseconds and need to be aligned for a proper functionality of the coincidence unit. These offsets were adjusted by sending the trigger signals through cables of different lengths, where $1\,\mathrm{m}$ of cable shifts the timing by $5\,\mathrm{ns}$. After the initial estimation, the timing was studied in more detail with a pulsed beam from MAMI. This allowed for the more precise alignment with actual data. The difference to the normal beam is, that here even random coincidences have to occur at the true coincidence timing due to the short pulse length.
Finally, the first coincidence spectra could be obtained. An example is shown in Figure 9.3 [181]. Here, the time difference of an event in KAOS to an event in SpekC is plotted as a histogram. A wide background plateau is observed together with a peak structure on top. One sharp peak is given by $\pi^+\pi^-$ coincidences. To the right, other structures are given. They consists of other coincidences with protons and muons. The actually desired $K^+\pi^-$ peak remains hidden in this figure. They are expected to be located in the right shoulder of the $\pi^+\pi^-$ peak. In the further analysis, they can be extracted via particle identification in the other detector systems, as going to be shown in Figure 9.5 on page 118.

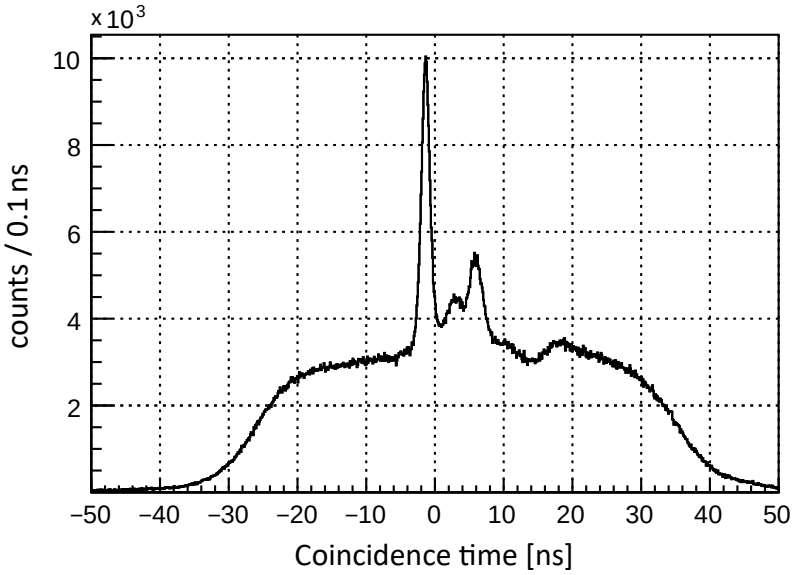

Figure 9.3.: Raw coincidence time spectrum between KAOS and SpekA [181]. On a plateau of background, a peak structure is observed. It is mainly given by $\pi^+\pi^-$ coincidences (sharp left peak) and a superposition of other combination possibilities, including protons and muons, compare to Figure 9.5 and 9.6. The desired $K^+\pi^-$ coincidences are expected to be contained in the right shoulder of the $\pi^+\pi^-$ peak.

9.2.2. Issues with data acquisition

The trigger timing was not the only issue to be considered during the beamtime. Two more problems needed to be solved. One was a missing retiming. The readout logic of SpekA and C contains a so called retiming coincidence, where the initial trigger is delayed and put to coincidence with the actual readout signal (sent from module S in Figure 9.2). It usually acts as defined time stamp for the involved TDCs. For the special setup with KAOS, where A and C are logically connected together, a trigger of SpekA will also try to initiate a readout of SpekC and vice versa. This resulted in problems with both the TDCs of A and C. The more drastic was SpekC, where the used TDC 2001 system needed to reboot every time, causing a dead time of $400\,\mathrm{ms}$. Therefore, an auto retiming was implemented, so that if the initial trigger was simply missing, the coincidence was made with a delayed version of the readout signal itself. By that, the TDC problems were reduced drastically.
Another issue was observed for single events. Indeed, the µBusy modules are in use to prevent new incoming events if one event is currently recorded (compare to Figure 9.2). But if a single event occurs, only the respective spectrometer is switched to being busy. Slightly later trigger signals can then cause a secondary readout process in the other spectrometer which crashes with the first one. To avoid this problem, the single events of A/C and KAOS were deactivated by removing their respective cable from the logic (D-F and U-Q) during the data taking.

9.2.3. Rate study

After improving the data acquisition itself, the data taking rate needed to be maximized. This question essentially boiled down to finding the maximum beam current to be handled properly by the spectrometers. At first, the raw trigger rates of all spectrometers were considered. This is seen in the left of Figure 9.4 [109]. SpekA and C observed quite moderate trigger rates up $50\,\mathrm{kHz}$ at $2\,\mu\mathrm{A}$. The dots are mostly overlapping and show a linear dependence to the beam current. For KAOS, the situation looks different. Here, rather a quadratic increase was observed

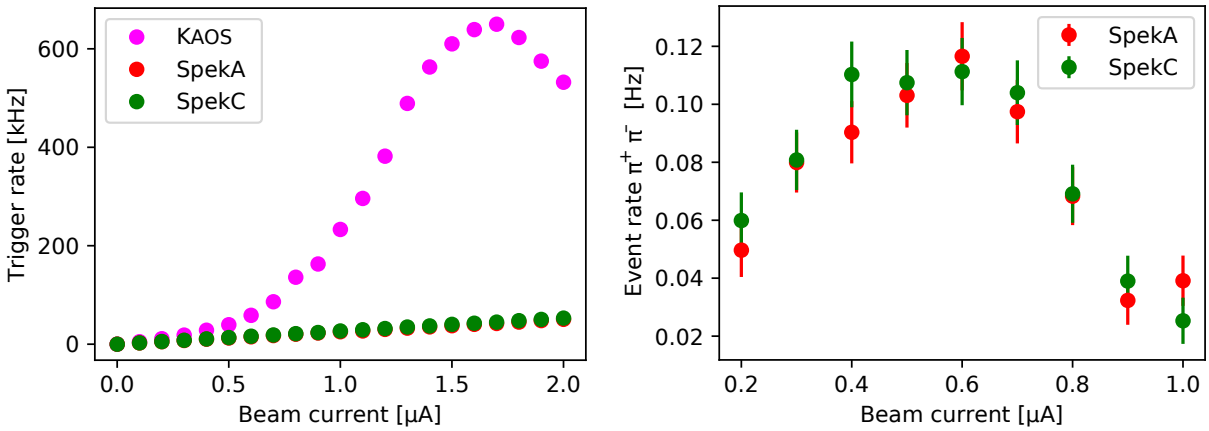

Figure 9.4.: Trigger and event rates of the spectrometers A, C and KAOS with the lithium target dependent on the beam current. **Left:** Trigger rate of the three spectrometers [109]. The points of SpekA and C, mostly overlapping, show a very similar behavior of moderate increase with the beam current. This looks different for KAOS. At around $0.5\,\mu\mathrm{A}$ the rate seems to increase stronger than the others until a maximum rate of more than $600\,\mathrm{kHz}$ is reached at $1.5\,\mu\mathrm{A}$. After that, overflow issues of the FPGA lower the resulting rate again. **Right:** rate of $\pi^+\pi^-$ coincidences of KAOS either with SpekA or SpekC. Contrary to the strongly increasing trigger rate the amount of these coincidences reached its maximum at around $0.6\,\mu\mathrm{A}$ and dropped from there again.

for lower beam currents. After $1.5\,\mu\mathrm{A}$ this trend was stopped by starting dead time effects of the KAOS trigger. A maximum of around $600\,\mathrm{kHz}$ was reached and then the rate was observed to decline again. While this test rather spotted the limits of the hardware, a second study focused more on the actual quality of the data.
As a measure of true coincidences in the data, the amount of $\pi^+\pi^-$ events in the coincidence spectra was evaluated. This was chosen due to the distinct peak form of these events (seen in Figure 9.3) and it was assumed that they scale linearly with the truly desired $K^+\pi^-$ coincidences. The resulting spectrum is found in the right of Figure 9.4 [109]. While from 0.2 to $0.6\,\mu\mathrm{A}$ a rising rate was observed, it rapidly dropped again when approaching $1\,\mu\mathrm{A}$. This can be explained by the high trigger rates which were observed in KAOS before. While true events are expected to be correlated with the beam current, the background level can increase with a higher order. This spoiled the data quality in KAOS and caused the decline of the true coincidences.
The reason for this behavior is mostly given by dead time effects. With increasing rate the chances are elevated that a true coincidence event cannot be observed because the data acquisition is still busy with another event. For a given dead time t_{dead} the amount of loss l is given by

$$l = t_{\mathrm{dead}} \cdot R_{\mathrm{DAQ}}, \tag{9.1}$$

as long as the DAQ rate R_{DAQ} does not exceed t_{dead}^{-1}. Consequently, the luminosity (calculated via (8.1) on page 93) will decrease by

$$\mathcal{L} = \mathcal{L}_{raw} \cdot (1 - l). \tag{9.2}$$

At A1, the dead time of the detectors ranges from 1 to $1.5\,\mathrm{ms}$. KAOS and SpekC belong to the faster spectrometers, while A is slower. Since A is read out for each event as well, $t_{\mathrm{dead}} = 1.5\,\mathrm{ms}$ needed to be assumed. To address these dead time issues, the first row of low momentum scintillators in KAOS was disabled. They saw the highest background rate compared to the others, compare to Chapter 7.3.2 on page 88.

9.3. The Second Beamtime

During the final days of this first beam time already the first sets of data could be collected. Since the NMR system was not yet in operation during that time, the data cannot be used for extracting hypernuclear binding energies with the desired resolution of $20\,\mathrm{keV}$. However, this data might be useful as training data for the upcoming analysis, so that an unbiased evaluation of the second beamtime data is possible.
The second KAOS beamtime started at the 16^{th} of September 2022, was interrupted at the 24^{th} due to repairs at MAMI and continued by the 30^{th} of September to run until the 16^{th} of October 2022. Before the data taking started, the new NMR device was brought to operation. More information in the appendix in Chapter B.4. Also during that time, the vacuum window in KAOS was replaced by an aluminum plate and the absorber wall was thickened (compare to Chapter 7.3.2).

9.3.1. Final data taking

Before the final data taking took place, the DAQ rate was assessed for the last time. The beam current was increased in steps of $0.1\,\mu\mathrm{A}$ and usually around one day of data was taken. This is summarized in Table 9.3. Here, the DAQ rate, the dead time and the integrated luminosity are shown. While at $0.5\,\mu\mathrm{A}$ a rate of $25.5\,\mathrm{Hz}$ was achieved, it had raised by a factor of 10, once the beam current was doubled. This seemed alarming in terms of elevated background levels, and the dead time losses reached 38%. At that time it was decided to also deactivate the second low momentum scintillators in KAOS, as described in Chapter 7.3.2. This strongly reduced the DAQ rate, seen in the $1.1\,\mu\mathrm{A}$ setting. Here, even with a higher beam current, the rate was less than half of the $1\,\mu\mathrm{A}$ value. Also the dead time losses were lowered to only 17%. In this setting, the final data taking took place. In summary, around 9 full days were taken here. Together with the other settings, nearly 15 days were acquired, resulting in an overall integrated luminosity of $1089\,\mathrm{fb}^{-1}$.

Table 9.3.: Amounts of collected data during the second beamtime with various beam currents. For the final acquisition $1.1\,\mu\mathrm{A}$ were used. It is to note, that for this setup hot trigger paddles from the low-momentum acceptance were switched off to suppress faulty events and preserve a moderate dead time.

Beam current $[\,\mu\mathrm{A}\,]$	**Measured time** $[\,\mathrm{days}\,]$	**DAQ rate** $[\mathrm{Hz}]$	**Dead time** $[\,\%\,]$	$\int \mathcal{L}\,\mathrm{d}t\ \left[\mathrm{fb}^{-1}\right]$
0.5	0.4	25.5	4 %	19
0.6	1.1	99.3	15 %	58
0.7	0.5	130.7	20 %	26
0.8	1.4	152.3	23 %	87
0.9	0.8	196.4	29 %	48
1.0	0.4	251.7	38 %	27
1.1	8.9	110.3	17 %	824
Sum	**14.8**			**1089**

9.3.2. Analysis status

The data analysis is currently performed by the PhD students Ryoko Kino and Tianhao Shao. So far, the spectra of the spectrometers have been investigated to obtain particle selection criteria. A first success was the decomposition of the raw coincidence spectrum between KAOS and the other spectrometers from Figure 9.3 on page 114. The result is shown in Figure 9.5 [280]. Here one can see the spectrum for three different particle selection criteria in the KAOS data. Here, mainly pions and protons were found, while the kaon events occurred rather rarely. Each of these particles was observed with pions, muons and electrons as coincidence partner in SpekA and C, generating a three peak structure. In the figure, the kaon spectrum was already scaled by a factor of 6 and still it is hardly visible compared to the other data, so a magnified version is plotted in Figure 9.6 [280]. Here, the desired $K^+\pi^-$ peak is clearly visible and also some coincidences with muons and electrons were found. The identification of the $K^+\pi^-$ peak offered the next selection criterion to further eliminate background events, so that already a preliminary decay pion momentum spectrum could be produced. It is given in Figure 9.7 [280] and is plotted analogously to the resulting spectra of the previous experiments in Figure 7.2 on page 83. Already at first glance the ${}^{4}_{\Lambda}\mathrm{H}$ peak at around $133\,\mathrm{MeV}/c$ is seen. It can be distinguished clearly from the background level. A signal to noise ratio of more than 4 is estimated, which is around twice as much than for the previous data. This may confirm the efforts of radiation shielding, the use of lower beam currents and the other measures to reduce background, which were described in Chapter 7.3 and 8.
However, for the hypertriton no indication was found so far. Still, with the clear observation of ${}^{4}_{\Lambda}\mathrm{H}$, the chances are greater than ever before, that a further analysis will be able to also extract hypertriton events. Up to now, around 60% of the complete data set were analysed and a more sophisticated suppression of background events is still to be elaborated.

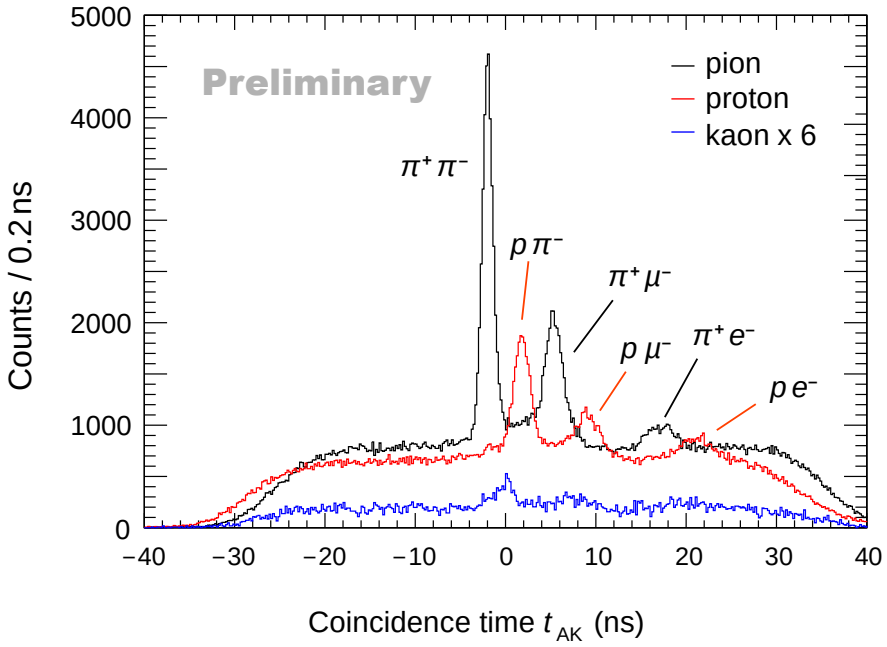

Figure 9.5.: Coincidence time spectrum between KAOS and SpekA after particle selection in KAOS [280] (modified). Mainly pions and protons were observed, kaons are comparably rare. Each of these particles was observed in coincidence with pions, muons and electrons in A/C respectively.

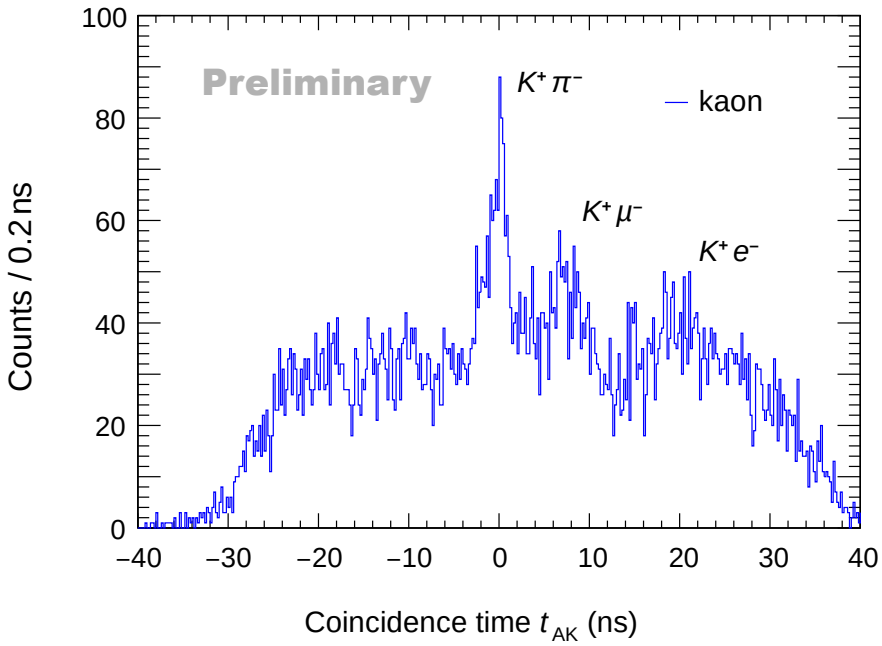

Figure 9.6.: Magnified version of the coincidence spectrum from Figure 9.5 for a detailed view of the kaon data [280]. In the center at around 0 the desired $K^+\pi^-$ coincidences are found. Besides that, also hints for coincidences with muons and electrons are present.

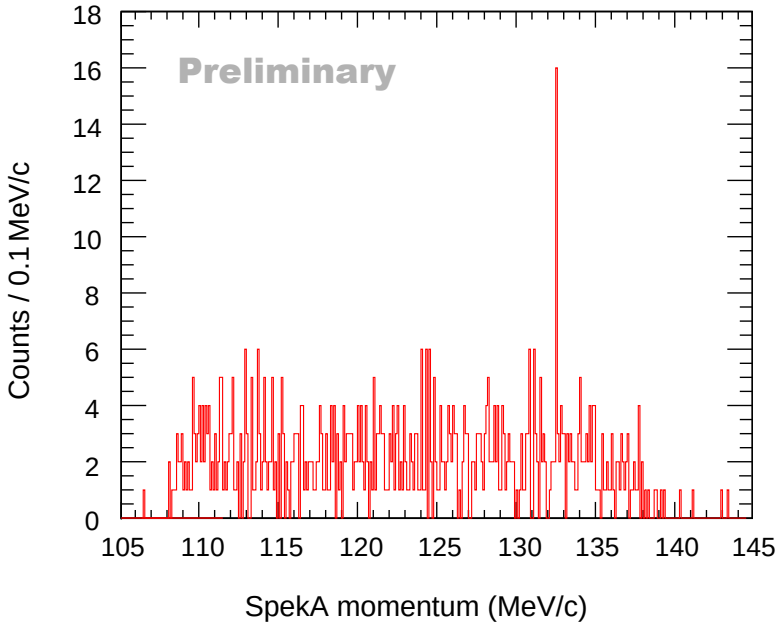

Figure 9.7.: Momentum spectrum of SpekA after the preliminary analysis by T. Shao [280]. The spectrum shows a strong ${}^{4}_{\Lambda}\mathrm{H}$ peak, while the hypertriton is yet to be discovered.

10. Summary and Outlook

Within this thesis, the data situation of the hypertriton has been reviewed and analysed. While with the most recent experiments – for example by ALICE and STAR – the discrepant data from the earlier heavy ion collision experiments was mostly rejected, the need for an independent remeasurement of its Λ binding energy was still confirmed. Consequently, a new hypernuclear experiment was prepared and finally conducted successfully at the Mainz Microtron.

The Chart of Hypernuclides

With the efforts put in the database project, an almost complete set of hypernuclear mass, lifetime and branching ratio data was gathered. Via the web interface, the platform is reachable around the globe and already found the attention of many hypernuclear physicists. The resulting average values proved to be crucial to unify the view on hypernuclear physics as well as being an objective foundation for discussions about ambiguities in discrepant data sets.
Throughout the implementation and testing of the averaging routines, they have been proven to be widely applicable without any artifacts or strange behavior observed. With these routines, a total of almost 100 averages was calculated reliably. These are based on around 600 experimental values out of 150 references. In the future, the main task about this project will be to maintain the web interface and to update the database with the upcoming experimental results.

The hypertriton experiment

Compared to the previous hypernuclear studies at A1, many improvements have been elaborated in order to achieve a higher data quality and a bigger hypertriton yield. This involved a whole set of changes in terms of radiation shielding and other minor revisions, but most importantly, a new high luminosity target system was developed and tested.
This target – consisting of pure lithium – needed to be treated carefully in order to protect it from corroding and melting, which was solved by an active cooling system and a thermal camera surveillance. During a test beamtime, the reliability of the target was demonstrated. This included its orientation process, cooling efficiency and durability during the irradiation with high beam currents. For the thermal cameras it was found that their application during experiments with the lithium target even is not necessary. Anyway, they delivered useful results, which could find their application in other experimental setups in the future.
Within the actual hypertriton experiment, more than $1000\,\mathrm{fb}^{-1}$ of data were taken successfully with the new setup. The evaluation was started recently by the PhD students Ryoko Kino and Tianhao Shao. Their analysis already revealed a promising ${}^{4}_{\Lambda}\mathrm{H}$ peak with a better signal-to-noise ratio than the previous end-results of 2016 [275]. This observation though only marked the starting point for the following in-depth analysis of the complete data set, so that with better background filtering and event selection also the hypertriton may finally be found.
For a highly accurate determination of the decay pion momentum a new set of NMR probes was installed in the spectrometer magnets to allow for a precise momentum calibration with the help of Pascal Klag's undulator light interference setup. This experiment is foreseen for the near future, to achieve the goal of $\pm 20\,\mathrm{keV}$ in the Λ binding energy.

A. Details about the Chart of Hypernuclides

A.1. The Website

The web interface is hosted by the Institute for Nuclear Physics Mainz and is found at `https://hypernuclei.kph.uni-mainz.de`. In this section, all characteristics of this interface are explained in detail.

A.1.1. The user interface – overview

A screenshot of the graphical user interface was already shown in Chapter 4, given in Figure 4.2 on page 41. It consists of a headline, an upper and a lower body as well as a footer. Besides the name of the website, the headline includes the logo of the Mainz university and the Strong2020 logo with the flag of the European Union by which the project was supported.
The **upper body** consists of three boxes. On the right, a chart of hypernuclei is shown, where analogous to a chart of nuclei all available hypernuclei are sorted by their proton and neutron number. The colors of the hyper-isotope buttons indicate the amount of stored measurements about each of them. By clicking one of these nuclei, basic properties as well as the stored measurements will be displayed. In the case of the screenshot, ${}^{4}_{\Lambda}\mathrm{H}$ was selected. Λ hypernuclei are the default to be shown in this chart, however it can be changed to other layers by clicking the *Hyperon Content* buttons below. This allows to also show double Λ, Σ^+, Ξ and $\bar{\Lambda}$ hypernuclei. In addition, there is the summary button, which will give access to the summary plot table, described in A.1.3. The center box contains basic properties about the clicked hyper-isotope such as its non-strange core and its hyperon content. It also defines the color scale for the chart in the left box. The right box is a placeholder for the ideograms which are generated after a physical property of the clicked element is selected. These are going to be described in further detail in Section A.2.
The **lower body** contains all the stored information about a hypernucleus in the form of a collapsible table. It encloses, depending on the data situation, the following categories, which are going to be explained in more detail in the following Section A.1.2:

- Ground State: Λ Binding Energy [1]
- Ground State: Lifetime
- Branching Ratios
- Ground State: Spin Parity
- Mesonic Two-Body Decays
- Fragmentation Thresholds
- Energy Levels

[1] The Λ is to be replaced by the respective hyperon(s).

The website's **footer** contains a set of buttons which are mainly used to display more general information. On the right, there is a note about the version number and links to navigate to legal notes and privacy statements as well as back to the website of the Mainz Institute for Nuclear Physics. *Guide and Procedures* opens up a window where a short summary of the averaging procedures and links to related publications can be found. Also used particle masses and information about the creators are listed there. *Export Data* will give access to a menu in which the user can select and download desired data sets stored in the database in the format of a text document. *Recommendations* shows a summary of data treatments which were applied to some data. In particular, an additional systematic error for old binding energy data from emulsion is described here, further information about this correction is found in Chapter 4.3.5. This correction can be dis-selected by clicking a checkbox. The website will then be reset and omit the correction. Finally, *Compilers* displays a list of people who contributed to the database by providing their own datasets.

A.1.2. Data table body

The data entries are represented as a table where each published value takes its own line, compare to Figure 4.2 on page 41. It consists of eight columns, starting with the reported value itself. The second and third column display its weight and χ^2 value from the average calculation, details about that are found in Chapter 4.3. Then, the first author and the year of publication are shown. The next two columns indicate the experimental technique used to obtain that value and an additional comment. The last column houses two buttons, *Info* and *Ref*. The first one will open a window, where all the available information about the measurement is displayed, while the latter will give access to references for citing the corresponding article.

Ground State: Λ Binding Energy

An example of the opened binding energy section is found in Figure A.1. It shows all available binding energy measurements for ${}^{4}_{\Lambda}\mathrm{He}$ sorted by their year of publication [101]. If reported values rely on other measurements, these are grouped together. For example, the value by Jurič contains two other values while one of them again consists of two further ones. These dependencies are indicated by shifting the values to the right. To avoid including the same data multiple times, the underlying measurements are not clickable as long as the top measurement is selected.
Also, some measurements may not be contributing to the average for various reasons. These will be listed at the bottom, shaded in gray and per default not selected. In this example, one measurement is excluded due to a weight of less than 2% making it obsolete. In contrast, here the measurement by Tamura is dis-selected arbitrarily to show the functionality of doing a customized selection of data. By that, the weights and the resulting average is re-calculated. It is shown as *evaluated value* in the top line, while the initial value *our value* still is displayed. Also the error scaling factor and the ideogram (not shown) are updated.
At the bottom of the table the *Display options* are found. These allow to change the values in the table from the hyperon binding energy to the total ground state mass of the hypernucleus via

$$m_{\mathrm{hyp}} = m_{\mathrm{ns}} + m_{\mathrm{Y}} - B_{\mathrm{Y}}, \tag{A.1}$$

with the mass of the non-strange core m_{ns} and the hyperon mass m_{Y}. A special case is given for ΛΛ hypernuclei. Here, also a third option is available to convert to the ΛΛ interaction energy. It describes the additional bond between the two hyperons apart from their bond to the non-

strange core, given by the binding energy of the respective single Λ hypernucleus ${}^{M-1}_{Y}Z$:

$$\Delta B_{\mathrm{YY}} = B_{\mathrm{YY}} - 2\,B_{\mathrm{Y}}\left({}^{M-1}_{Y}Z\right). \tag{A.2}$$

${}^{4}_{\Lambda}$He

Ground State: Λ Binding Energy	our value: 2.347 ± 0.036 MeV		evaluated value: 2.349 ± 0.043 MeV			(error scaled by 1.22, ndf = 4)	
B_Λ [MeV]	Weight	χ^2, Σ = 5.92	Author	Year	Method	Comment	More...
☐ 2.330 ± 0.100 (stat.)	0	0	H. Tamura	1994	(K-, pi-) Spectr.	(K^-stop, π^-)	Info Ref.
☑ 2.400 ± 0.100 (stat.)	0.12	0.26	R.S. Hayano	1988	Pion Spectroscopy	-	Info Ref.
☑ 2.390 ± 0.030 (stat.) ± *0.040 (syst.)*	0.50	0.66	M. Juric	1973	Emulsion	combined	Info Ref.
☐ 2.420 ± 0.040 (stat.) ± *0.040 (syst.)*	0	0	M. Juric	1973	Emulsion	combined	Info Ref.
☐ 2.440 ± 0.090 (stat.) ± *0.040 (syst.)*	0	0	M. Juric	1973	Emulsion	1H + 1H + 2H + π^-	Info Ref.
☐ 2.420 ± 0.050 (stat.) ± *0.040 (syst.)*	0	0	M. Juric	1973	Emulsion	1H + 3He + π^-	Info Ref.
☐ 2.360 ± 0.040 (stat.) ± *0.040 (syst.)*	0	0	G. Bohm	1968	Emulsion	-	Info Ref.
☑ 2.200 ± 0.060 (stat.) ± *0.040 (syst.)*	0.24	4.29	W. Gajewski	1967	Emulsion	-	Info Ref.
☑ 2.330 ± 0.210 (stat.) ± *0.040 (syst.)*	0.03	0.01	M. Raymund	1964	Emulsion	-	Info Ref.
☑ 2.440 ± 0.100 (stat.) ± *0.040 (syst.)*	0.11	0.71	N. Crayton	1962	Emulsion	-	Info Ref.
☐ 2.380 ± 0.240 (stat.) ± 0.130 (syst.)	0	0	Y. Prakash	1961	Emulsion	H + 3He + π^-	Info Ref.
Display options: ○ GS mass ◉ Binding energy B_Λ							
Ground State: Lifetime	our value: 250 ± 18 ps						
τ [ps]	Weight	χ^2, Σ = 0.09	Author	Year	Method	Comment	More...
☑ 245 ± 24 (stat.)	0.56	0.04	J. D. Parker	2007	(K-, pi-) Spectr.	(K^-stop, π^-)	Info Ref.
☑ 256 ± 27 (stat.)	0.44	0.05	H. Outa	1998	(K-, pi-) Spectr.	(K^-stop, π^-)	Info Ref.
☐ $228\,^{+233}_{-129}$ (stat.)	0	0	R. E. Phillips and J. Schneps	1969	Emulsion	-	Info Ref.
Display options: ◉ ps ○ relative to τ_Λ ○ decay width							

Figure A.1.: Example of the binding energy and lifetime data table [101]. Here, ${}^{4}_{\Lambda}$He is shown.

Ground State: Lifetime

The lifetime table is set up analogously to the binding energy table. Also here, different data representations can be chosen, the display options allow to switch between lifetime τ, the lifetime normalized to the free Λ lifetime $\frac{\tau}{\tau_\Lambda}$ and the decay width $\frac{\hbar}{\tau}$. Within the lifetime section, another body can be expanded which is a lifetime vs. binding energy contour plot. It illustrates their folded probability density distribution. An example is shown in Figure A.2 [101]. This plot also acted as foundation for Figure 5.9 on page 65.

Branching Ratios

The branching ratio section is the mother of various sub-sections for different decay modes which are again expandable. These are again designed analogously to the lifetime and binding energy sections. An overview about the available channels is given in Table A.1 [261]. These were designed together with Bachelor student Sabrina Ries. Furthermore, the elaborated branching ratio average values are going to be provided in Section A.4 on page 139.

Ground State: Spin Parity

This row shows the spin-parity assignment of a hypernucleus. If multiple sources are available, they will all be listed in the drop-down table. As long as there is a consistent agreement of these sources, the assignment is adopted as *our value*.

Mesonic Two-Body Decays

In this row, kinematical calculations are found. This includes decay pion momenta, nucleus momenta and Q values for the different pionic decay channels. These are based on the masses of the participating particles and assume a back to back decay at rest. The π^+ channel is suppressed compared to the π^- and π^0 channels but still was observed for ${}^{4}_{\Lambda}\mathrm{He}$ [175, 204, 240]. It is possible via the excitation of a Σ^+ baryon,

$$p\Lambda \rightarrow n\Sigma^+ \rightarrow nn\pi^+. \tag{A.3}$$

The released energy Q is calculated via

$$Q = m_{\mathrm{hyp}} - m_{\mathrm{nucl}} - m_{\pi}, \tag{A.4}$$

while the pion momentum is given by

$$p_{\pi} = \frac{1}{2\,m_{\mathrm{hyp}}}\sqrt{m^4_{\mathrm{nucl}} - 2\,m^2_{\mathrm{nucl}}m^2_{\pi} - 2\,m^2_{\mathrm{nucl}}m^2_{\mathrm{hyp}} + m^4_{\pi} - 2\,m^2_{\pi}m^2_{\mathrm{hyp}} + m^4_{\mathrm{hyp}}}. \tag{A.5}$$

Fragmentation Thresholds

This section is another calculator based area. It computes threshold energies for hypernuclei to split up into nuclear fragments while preserving the hyperon. These threshold are of interest especially for emulsion experiments like the one at J-PARC, which was described in Chapter 5.4.1 on page 66. Fragmentations like these often are visible in the emulsion plates and identifying the daughters may be crucial to extract information about the mother nucleus.
On the website – as shown for the case of ${}^{7}_{\Lambda}\mathrm{Li}$ in Figure A.3 – the various channels are sorted into two-body and three-body channels [101]. At the top of each column, a threshold plot is shown, where the threshold energy is found on the y axis, while on x the nuclear charge Z of the hyperon-containing fragment is shown. Below, the different channels are listed explicitly. Here the user can select the channels to be displayed in the figure by hand. Alternatively it is also possible to specify limits on the threshold energy to customize the plot. In addition, also the width of the different fragmentation channels is given. It is the width of the most unstable

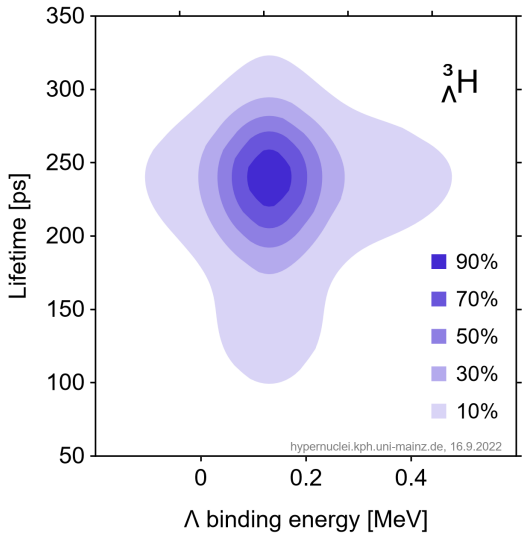

Figure A.2.: Folded lifetime and binding energy distribution for ${}^{3}_{\Lambda}\mathrm{H}$ [101]. The color scheme indicates the percentage of the 2D curve's total height.

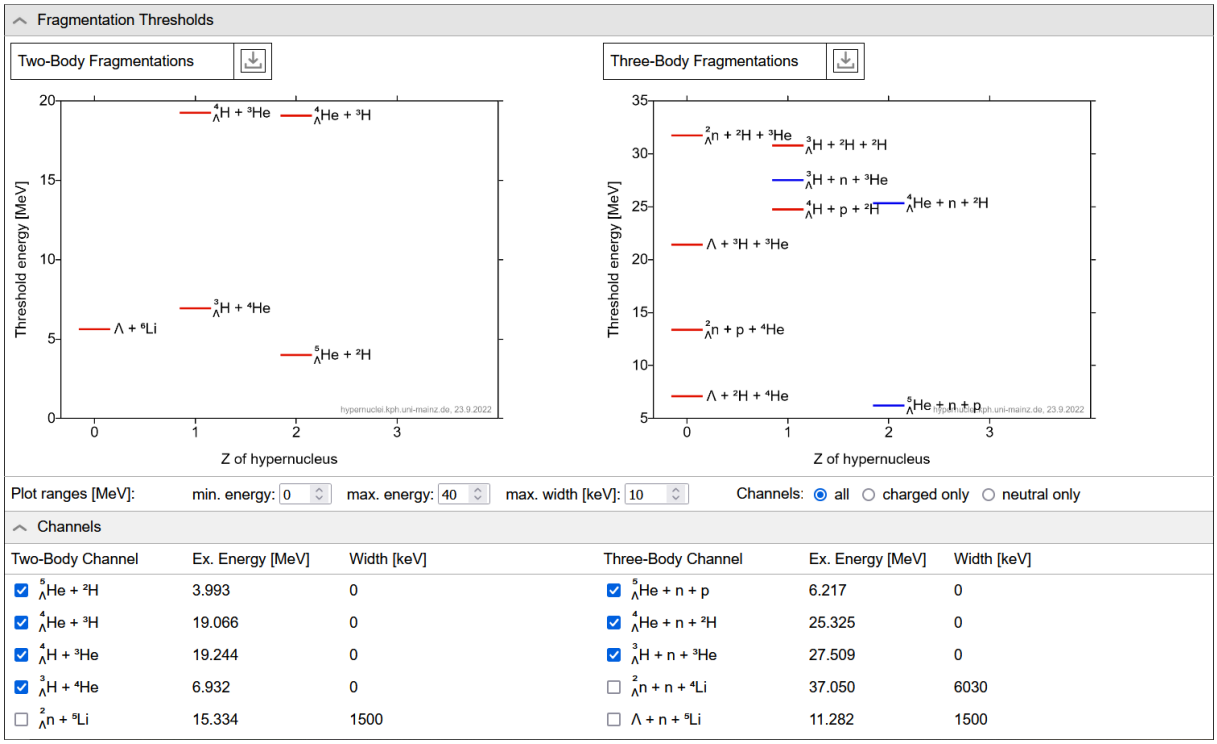

Figure A.3.: Fragmentation thresholds sub-table in the case of ${}^{7}_{\Lambda}\mathrm{Li}$ [101]. On the left, the two-body fragmentation channels are shown, on the right there are the three-body channels.

fragment in the reaction. For example, the isotope ${}^{4}\mathrm{Li}$ is very short lived, so its width is around $6\,\mathrm{MeV}$. Fragments like these can also be dis-selected by choosing a maximal width.
With the emulsion technique it is often impossible to detect uncharged particles, so also channels containing a single neutron are treated explicitly. They are displayed in blue while the other channels are red. With the dedicated *Channels* option their appearance can be adjusted.

Energy Levels

This section contains information on higher excited states of hypernuclei. This may include data from missing mass experiments as well as gamma ray spectroscopy. The sets of values for the different energy levels are averaged with the same methods as the lifetime and binding energy values. From that, the resulting level structure is displayed in the form of a level scheme plot as shown in Figure 4.1 on page 39.
If the spin parity information is given for all levels, the software tries to find a match to the corresponding state of the non-strange core. This is done by comparing their spin difference. Since the Λ is a spin $\frac{1}{2}$ particle, the hypernuclear spin can only differ by $\frac{1}{2}$. If a match is found, the hypernuclear and non-strange levels are connected by dotted lines to indicate the splitting of that level. The height of the non-strange ground state level is then calculated via

$$E_{\mathrm{ns}} = \frac{l+1}{2l+1}\,\Delta E, \tag{A.6}$$

with its spin quantum number l and the energy difference ΔE between the two hypernuclear levels.

A.1.3. Summary plots

This extra table is opened by clicking the *Summary* button in the hypernuclear chart box. This table summarizes the available information for the different characteristics which are then plotted against their mass number. In the following, the implemented sub tables will be described.

Λ binding energies

In this section, all the available Λ binding energies are displayed and plotted against their mass number. The resulting plot is shown in Figure A.4 [101]. Starting from ${}^{3}_{\Lambda}\mathrm{H}$ and reaching up to

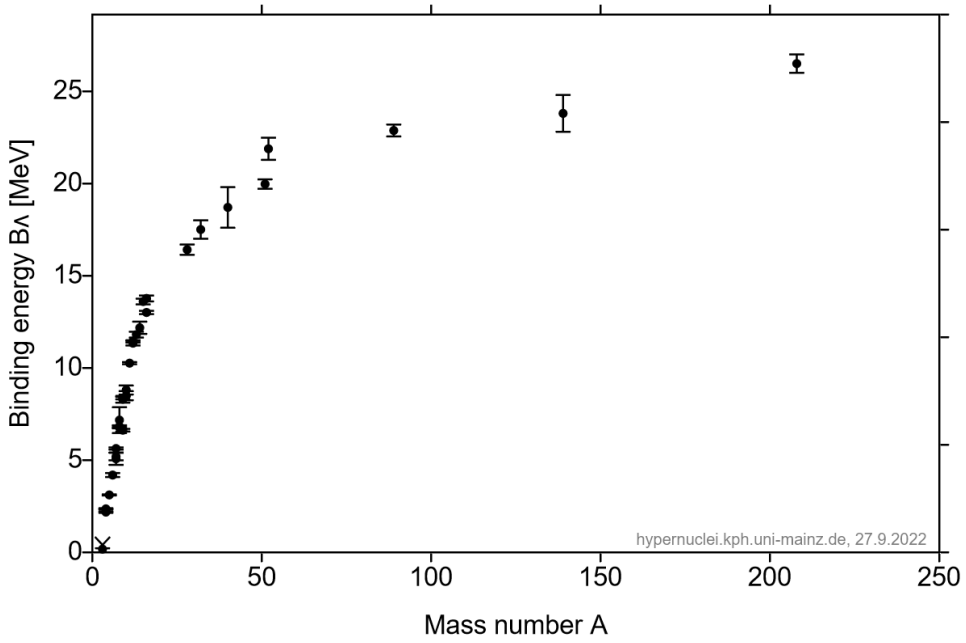

Figure A.4.: First version of the Λ binding energies summary plot [101]. The B_Λ values are plotted against the mass number of the hyper-isotopes. While for the first hypernuclei with $A \leq 10$ the binding energy seems to rise linearly, it quickly converges to a bit more than $25\,\mathrm{MeV}$.

${}^{208}_{\Lambda}\mathrm{Pb}$, all hypernuclei are included, where it was possible to calculate a reliable value for the Λ binding energy. It is observed that after a strong increase for $A < 20$, the binding energy tends to converge at higher A.
Also here different plotting options are available. The mass number scale can be changed to $A^{-\frac{2}{3}}$, which is shown in Figure A.5 [101]. This representation was chosen due to the nature of the binding energy for large nuclei. With growing mass number A also the radius of the nucleus is growing, $A \propto r^3$. Since the range of the Λ's interaction is limited, for large nuclei the potential depth becomes constant, $V_0 = \text{const.}$. The binding energy B_Λ then only depends on the Λ's kinetic energy,

$$B_\Lambda = V_0 - E_{\text{kin}}, \tag{A.7}$$

with $E_{\text{kin}} = \frac{p^2}{2m}$. The momentum p is then given by Heisenberg's relation of uncertainty,

$$p = \frac{\hbar}{r}. \tag{A.8}$$

Eliminating p and r from the equations leaves the expression

$$B_\Lambda = V_0 - \frac{\hbar^2}{2m} A^{-2/3}, \tag{A.9}$$

where B_Λ finally only depends on $A^{-2/3}$. By that, it is expected for this version of the plot in Figure A.5, that the binding energies for larger nuclei form a straight line. This behavior is indeed visible within the region from 0 to roughly 0.25. After that, the assumption of a large nucleus does not hold anymore and the binding energy gets larger than expected by the relation. Another conclusion from the observed trend is that the hypothetical infinitely large Λ hypernucleus, located at 0, would have a binding energy of $B_\Lambda \approx 30\,\mathrm{MeV}$.
A third plotting option is the *per nucleon* representation. Here, all the B_Λ values are divided by their mass number A. The resulting plot is shown in Figure A.6 [101]. It reveals a distinct maximum at $A = 12$. The normalized binding energy reaches $\approx 0.95\,\mathrm{MeV}$ there.

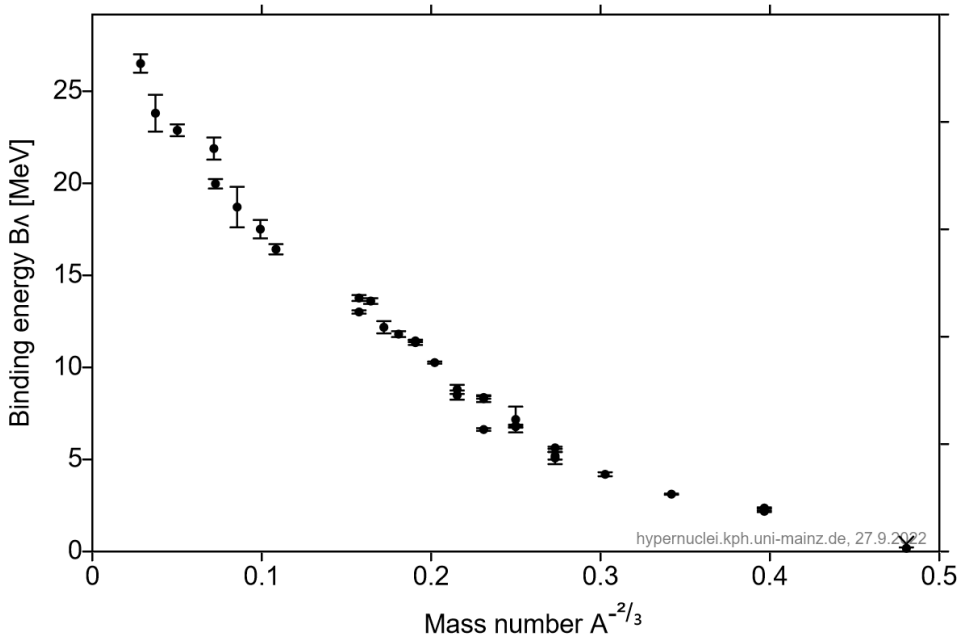

Figure A.5.: Second version of the binding energies summary plot [101]. This time, the mass number scale was changed to $A^{-\frac{2}{3}}$.

Further summary plots

A total of 4 more summary plot categories is given. These are **$\Lambda\Lambda$ interaction energies $\Delta B_{\Lambda\Lambda}$**, **Lifetimes**, **MWD branching ratios** and **NMWD branching ratios**. In principle, they are designed analogously to the binding energy summary, and to keep the focus on the characteristics of the user interface, they are not shown here in explicit detail.

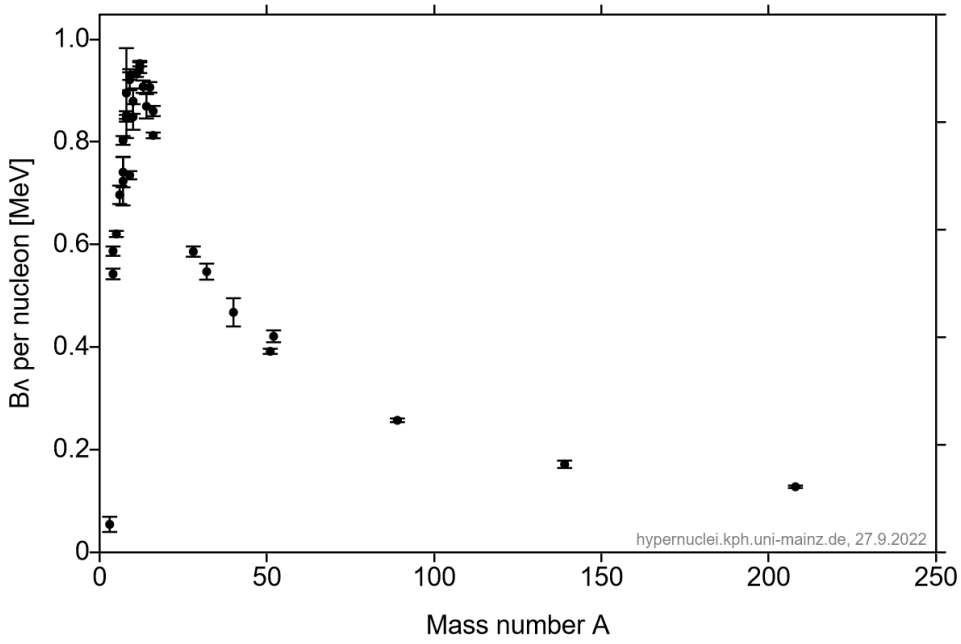

Figure A.6.: Third version, the summary plot of the Λ binding energies in *per nucleon* representation [101]. The binding energy values are divided by the respective mass number. By that, a clear maximum is formed at $A = 12$.

Table A.1.: Definition of the branching ratios which are available in the database with description [261]. Mesonic channels are listed in the top half, followed by the non-mesonic ones below.

No.	Symbol	Name in DB	Description
(1)	$\Gamma_\pi/\Gamma_\Lambda$	pi	all pionic decay channels normalized to free Λ width
(2)	$\Gamma_{\pi^-}/\Gamma_\Lambda$	pimall	all decay channels via π^- normed to free Λ width
(3)	$\Gamma_{\pi^-}/\Gamma_{\mathrm{tot}}$	pimtotot	all decay channels via π^- normed to total width of hypernucleus
(4)	$\Gamma^{2B}_{\pi^-}/\Gamma_\Lambda$	pim2B	two-body decay via π^- to free Λ
(5)	$\Gamma^{2B}_{\pi^-}/\Gamma_{\pi^-}$	2Bpimtoall	two-body decay via π^- to all decays via π^-, also known as R, equivalent to $(1)/(3)$
(6)	$\Gamma_{\pi^0}/\Gamma_\Lambda$	pi0all	all decay channels via π^0 normed to free Λ width
(7)	$\Gamma_{\pi^0}/\Gamma_{\pi^-}$	pi0topim	all decay channels via π^0 to all by π^-, equivalent to $(5)/(1)$
(8)	$\Gamma_{\pi^+}/\Gamma_{\pi^-}$	piptopim	all decay channels via π^+ to all by π^-
(9)	Γ_n/Γ_Λ	n	neutron induced decay to free Λ width
(10)	Γ_p/Γ_Λ	p	proton induced decay to free Λ width
(11)	$\Gamma_{\mathrm{nm}}/\Gamma_\Lambda$	nm	all non-pionic (non-mesonic) decay channels
(12)	Γ_n/Γ_p (1N)	np1	neutron induced to proton induced decay channels for one involved nucleon
(13)	Γ_n/Γ_p (1N & 2N)	np2	neutron induced to proton induced decay channels for one and two involved nucleons
(14)	Γ_2/Γ_{nm}	2Ntonm	all two nucleon induced decay channels to all non-mesonic channels
(15)	Γ_2/Γ_p	2Ntop	all two nucleon induced decay channels to all proton induced channels
(16)	$\Gamma_n/(\Gamma_n+\Gamma_p)$	ntonp	neutron induced decays to neutron and proton induced decays combined
(17)	$(\Gamma_n+\Gamma_p)/\Gamma_{\pi^-}$	Qm	neutron and proton induced decays to decay channels via π^-

A.2. Visualization in Ideograms

Data sets and their resulting averages are represented in the form of ideograms. These are auto generated plots analogous to e.g. the one shown in Figure 5.5 on page 60 to give a quick overview about the data situation. They contain all the contributing measurements of a physical property in form of a point with error bars. As for the averaging procedure, these errors are the quadratically added statistical and systematic error contributions. On the x axis the actual value of the physical property is given, in this case the binding energy of hypertriton, while the y coordinate is arbitrary. The values are just listed from top to bottom sorted by their year of publication. On the right of the ideogram all these values get a name tag with collaboration, or if not given, the first author, the year of publication as well as the experimental technique.
As described in Chapter 4.3, each of the contributing values receives a weight for the determination of the overall average. This weight is used to generate a distribution curve by assigning a Gaussian curve to every data point and adding these multiplied with their weight. Its value is shown on the y axis. The purpose of this curve is, again, to give a quantitative overview about the data situation. Several conclusions can be drawn from this curve: A sharp peak indicates the presence of a precise measurement which dominates the average. For example, it is easily seen in Figure 5.5 on page 60, that the data set is still dominated by Jurič's value from 1973. In other cases, the distribution curve can have a shoulder or even two peaks, an indication that either the errors of some data points were underestimated or that different experimental methods or collaborations have unknown systematic shifts. The latter can be cross-checked with the text labels.
Finally, the average value of the shown data points is displayed at the top left. It is visualized by a gray vertical line and a lighter gray bar to show the one-sigma interval around the average. In case of a used scaling factor – described in Eq. (4.23) – it will be noted next to the average value.

A.3. Database Structure

For the database, a structure was developed to fit the needs of the hypernuclear data collection as good as possible. This structure quickly became rather complex with more than 50 unique input fields. It is shown in form of a diagram in Figure A.7. A summary of all entities is given in the tables A.4 and A.5 starting on page 137. In the following, the structure is going to be explained in detail.

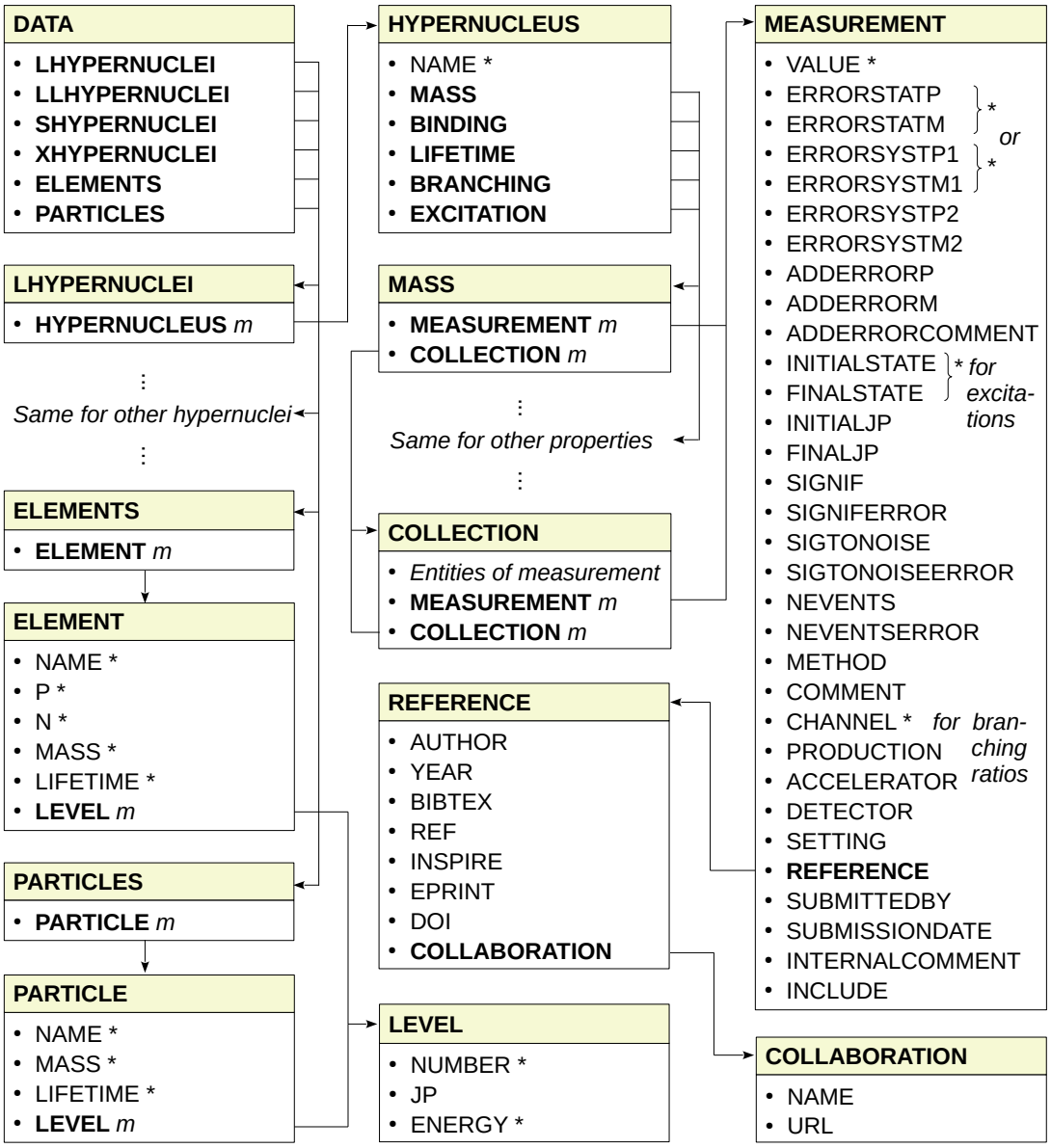

Figure A.7.: Entity structure of the database. The scheme consists of a set of complex elements, that can contain sub-elements. These can again be complex or just a simple text field. The complex elements are displayed bold faced. The * indicates the absolute minimal requirements for a database entry, while the m implies that this element may occur multiple times.

A.3.1. Hypernuclei

The root element of the database tree is simply called DATA. It contains everything what is stored in the database. From there, the data is sorted into several main categories. Each family of hypernuclei receives its own category. These are summarized in Table A.2. From there, every family is filled by the HYPERNUCLEUS element. Besides a NAME to specify the exact isotope, five further sub-elements for its physical properties are given. These are listed and briefly described in Table A.3. It was decided to implement the mass and the binding energy as separate categories although they are directly linked to each other and easily converted. The advantage of this way is that in any case, the originally published value can be saved. Aside from that, all categories are set up very similarly. The few exceptions will be explained in the following.

Table A.2.: List of hypernuclear entity names in the database.

Entity name	Description
LHYPERNUCLEI	Λ hypernuclei
LLHYPERNUCLEI	Double Λ hypernuclei
SHYPERNUCLEI	Σ^+ hypernuclei
XHYPERNUCLEI	Ξ^- hypernuclei

Table A.3.: List of entities addressing physical properties. While MASS and BINDING are in principle redundant, they were both adopted to the database to avoid the need for converting published values to the respective other form.

Entity name	Description
MASS	Mass values given in MeV/c^2.
BINDING	Binding energy values in MeV.
LIFETIME	Lifetimes given in ps.
BRANCHING	Branching ratios. All values are given in their normalized form. The database features 17 different channels to be averaged separately. These are listed in Table A.1. For the values to be interpreted correctly, their name has to be written explicitly to the CHANNEL element.
EXCITATION	Excitation energies given in MeV. An energy does not necessarily need to reference to the ground state, so to enable the database to calculate a proper level scheme, the initial and final levels have to be given in form of numbers at INITIALSTATE and FINALSTATE.

A.3.2. Measurements and collections

The most relevant database element is the MEASUREMENT entity. Its structure is seen on the right of Figure A.7. Far from any other entity, it contains the most sub-elements. These can be summarized into several categories.

The value itself

The basic information about a data point is given by the mean value and its error(s). The first is entered into the VALUE property while the latter are split up to statistical and systematic

sources ERRORSTATP/M and ERRORSYSTP1/M1. It is to note about these that they both have placeholders for the positive and negative part of an error separately. Also for symmetric errors, both components have to be set.
In Figure A.7, the VALUE receives a * to indicate its urgent need for a valid data point. In contrast, from the statistical and systematic errors, only one of them needs to be given to make a data point evaluable. To furthermore improve the versatility of the database, a second, optional systematic error may also be given. This is relevant, if a value was published with a more detailed listing of the systematic error components. In the end, this error will then be added quadratically to the first systematic error.
Finally, another set of fields is foreseen for an additional error ADDERRORP/M. It is to be used for the rare case, that a data point was obviously lacking a proper error analysis to some degree. So this error is not to be found in the initial publication but more of a subsequent correction. It has to be justified with the ADDERRORCOMMENT, a comment to explain the need and size of this error.

Additional properties for excitation energies

Besides, the value-error combination, some more crucial elements are to be filled for excitation energy values. Since they can give an energy difference between two arbitrary levels, the INITIALSTATE and FINALSTATE need to be defined. In the database, this is done by assigning simple integer numbers to each level, where the ground state starts with 0. Additional to that, also spin-parity information about both involved states can be given (INITIALJP and FINALJP) as well as a WIDTH of the initial state.

Statistical information

The following set of entities focuses on giving hints about the data quality for a certain data point. All these entities are optional, but still, if given, they can add plenty of background information to a value. The significance of a data point can be entered at SIGNIF, also, if provided, its error can be given at SIGNIFERROR. In a similar fashion, the signal to noise ratio and the number of observed events can be added, SIGTONOISE and NEVENTS. Both have an element for their errors as well.

About the experiment

Another set of entities is dedicated to the implementation of the experiment from which the data point originates. From all of them, the METHOD is the most meaningful. It indicates the experimental technique and by that gives a quick hint on how to classify it. The method is also to be displayed in the ideogram. Additional to that, the experiment is described furthermore by the used ACCELERATOR and DETECTOR, where simply their names are to be put. For a more detailed description, PRODUCTION is meant for naming a target nucleus, center of mass energy or similar properties. CHANNEL then specifies, if maybe for a data point only certain decay types were analyzed, two- or three-body decays for example. It is to be noted, that for branching ratio data, this field is solely meant for the explicit name of the branching ratio channel, the data point belongs to. These names are listed in Table A.1 on page 131. Finally, a COMMENT can be given, which maybe does not fit to the other categories properly. Inside the GUI, usually the COMMENT will be displayed in the data table. If it is left empty, the CHANNEL is displayed instead.

Other

Still, there are a few more entities left, which do not fit a proper category. The SUBMITTEDBY property is meant to acknowledge the help of other people, if they submitted a value to the database. The SUBMISSIONDATE then holds the date, where the value was submitted. INTERNALCOMMENT allows to put a note to the data point which is not going to be displayed anywhere. SETTING is a rather technical attribute, it is used to assign a setting name to a data set, meant to be assigned to other data sets as well, to indicate that they originate from the same experiment. As a consequence, the *treatment of shared systematic errors* will be triggered. This procedure is described in Chapter 4.3.5 on page 46. The final entity is INCLUDE. It is meant to contain a comment about why a data point is *not* to be included to the average. As a consequence, the value will appear gray in the GUI and be dis-selected by default. The comment will be found by clicking the *Info* button. This entity is meant to manually remove data from the averaging procedure, if it seems to be problematic. If nothing is added to INCLUDE, the data point will be processed as usual.

Collections

The concept of the collection allows to link several measurements to each other. A collection in general represents a value that was computed out of one or more previously published values. In such situations it is crucial to ensure that this data only appears once in the average, so either the older references or the new value would have to be excluded. Following the philosophy of maximal information, though, it is desirable to include all involved references to the database. The collection allows for that by linking all related values together in a form of tree. So in principle, a COLLECTION contains all the same entities as the MEASUREMENT, with the addition of multiple sub-MEASUREMENTs. Even other COLLECTIONs can be contained. That way, it is possible to clearly identify, which value inherits from others. Within the user interface it is then possible to switch between the different layers. Including the same data multiple times is still prohibited by the functionality of the interface.

A.3.3. References

The REFERENCE entity is part of the MEASUREMENT/COLLECTION main entity. It stores information about the papers first AUTHOR, the YEAR of publication and the involved COLLABORATION. The latter again has a NAME and a link to a website (URL). Besides that, also multiple ways to cite and find the article in other databases can be provided. BIBTEX contains the explicit BibTeX code, REF the minimal reference name in pure text form, while in INSPIRE, the ID of this paper inside the inspire hep database [161] can be stored. In the user interface, then a link to the according is available. The same holds for DOI and EPRINT, where the origin of the paper can be stored.

A.3.4. Elements and particles

ELEMENTS and PARTICLES are meant to store literature data about non-strange nuclear isotopes as well as several baryons and mesons. They both house self-explaining sub-entities. An ELEMENT is defined by its NAME, the numbers of protons P and neutrons N, its MASS and the LIFETIME. If available, also excitation levels can be added. Such a LEVEL consists of a NUMBER, its ENERGY above ground state and optional the spin-parity JP. PARTICLEs are defined quite similarly, they just are missing P and N. The LEVEL element is here mainly used to store the ground state JP. While the masses are given in MeV/c^2, the lifetimes are stored in seconds. A stable element or particle receives a lifetime of -1.

Table A.4.: Entities of the data table – Part 1. In the left column, the explicit entity name is given, in the right one, a brief description is found.

Entity name	Description
ADDERRORP	Additional error which was not reported in the cited reference based on later reports. Positive component.
ADDERRORM	Negative component.
ADDERRORCOMMENT	Comment about the source of the extra error.
MEASUREMENT	Set of entities to represent a measurement
COLLECTION	Set of measurements
VALUE	Published mean value of the data point.
ERRORSTATP	Positive component of the statistical error.
ERRORSTATM	Negative component of the statistical error.
ERRORSYSTP1	Positive component of the systematic error.
ERRORSYSTM1	Negative component of the systematic error.
ERRORSYSTP2	Extra systematic error in case of multiple error sources mentioned. Positive component.
ERRORSYSTM2	Negative component.
INITIALSTATE	Initial level for excitation and transition energies.
FINALSTATE	Final level for excitation and transition energies.
INITIALJP	Spin-parity information J^π for the initial state.
FINALJP	J^π for the final state.
WIDTH	Width of the initial state level.
SIGNIF	Significance of the reported data point.
SIGNIFERROR	Error of the significance.
SIGTONOISE	Signal to noise ratio of the data point.
SIGTONOISEERROR	Error of signal to noise.
NEVENTS	Number of events contributing to the data point.
NEVENTSERROR	Error of the number of events.
METHOD	Experimental method used to obtain the data.
CHANNEL	Comment about the observed channel, in case of branching ratio data the explicit name of the channel
PRODUCTION	Information about target, accelerated particles, energies, angles, etc.
ACCELERATOR	Name of the accelerator facility
DETECTOR	Name of the involved detector.
COMMENT	Free text to describe further characteristics.
SETTING	String to group measurements to a setting for treatment of shared systematics.
REFERENCE	Entity group to contain information about author, different reference types, etc.

Table A.5.: Entities of the data table - Part 2. In the left column, the explicit entity name is given, in the right one, a brief description is found.

Entity name	Description
AUTHOR	First author of the publication. In case of two first authors both of them.
YEAR	Year of the publication.
BIBTEX	BibTeX code to cite the article.
REF	Reference in compact text form.
INSPIRE	Link to the Inspire database.
EPRINT	Eprint number.
DOI	Doi link of the article.
COLLABORATION	Entity group for information about the collaboration.
NAME	Collaboration name.
URL	URL to the collaboration's web site.
SUBMITTEDBY	Name of external person who suggested to include the value into the database.
SUBMISSIONDATE	Date of the suggestion.
INTERNALCOMMENT	Internal note about the data point not to be displayed on the web page.
INCLUDE	String to explain why a data point was not included into the recommended average.

A.4. Branching ratio values

In this section, the chart's branching ratio results are going to be presented. For this category, 115 single values were found and entered into the database together with Bachelor student Sabrina Ries [261]. The results are separated into mesonic weak decays, where decay pions are involved, and non-mesonic weak decays, where interactions with other nucleons suppress the emission of pions. These are found in the tables A.6 and A.7 [101, 261]. An explanation of the various channels is given in Table A.1 on page 131.

Table A.6.: Branching ratio averages for mesonic weak decays [101, 261].

Channel	Isotope	Value	References	Comment
$\Gamma_{\pi^-}/\Gamma_\Lambda$	${}^{4}_{\Lambda}$He	0.282 ± 0.021	[235, 310, 228]	
	${}^{5}_{\Lambda}$He	0.342 ± 0.016	[168, 288]	
	${}^{11}_{\Lambda}$B	0.220 ± 0.044	[271, 222]	
	${}^{12}_{\Lambda}$C	0.116 ± 0.010	[48, 271, 151, 222, 288]	
	${}^{27}_{\Lambda}$Al	0.041 ± 0.021	[271]	
	${}^{28}_{\Lambda}$Si	0.040 ± 0.007	[271, 151]	
$\Gamma_{\pi^-}/\Gamma_{\text{tot}}$	${}^{5}_{\Lambda}$He	$0.323\ ^{+\ 0.067}_{-\ 0.065}$	[19]	
	${}^{7}_{\Lambda}$Li	$0.315\ ^{+\ 0.044}_{-\ 0.043}$	[19]	
	${}^{9}_{\Lambda}$Be	0.154 ± 0.041	[19]	
	${}^{11}_{\Lambda}$B	$0.199\ ^{+\ 0.057}_{-\ 0.043}$	[19]	
	${}^{15}_{\Lambda}$N	0.085 ± 0.030	[19]	
$\Gamma^{2B}_{\pi^-}/\Gamma_\Lambda$	${}^{4}_{\Lambda}$He	$0.690\ ^{+\ 0.120}_{-\ 0.100}$	[229]	
$\Gamma^{2B}_{\pi^-}/\Gamma_{\pi^-}$	${}^{3}_{\Lambda}$H	$0.357\ ^{+\ 0.028}_{-\ 0.027}$	[14, 174, 177, 176, 50, 28, 162, 29]	[46] excluded due to ambiguities and missing errors
	${}^{4}_{\Lambda}$H	0.690 ± 0.017	[46, 50, 162, 29]	
$\Gamma_{\pi^0}/\Gamma_\Lambda$	${}^{4}_{\Lambda}$He	0.571 ± 0.036	[235, 310, 228, 229]	
	${}^{5}_{\Lambda}$He	0.201 ± 0.011	[225]	
	${}^{11}_{\Lambda}$B	0.192 ± 0.066	[270]	
	${}^{12}_{\Lambda}$C	0.165 ± 0.008	[48]	
$\Gamma_{\pi^0}/\Gamma_{\pi^-}$	${}^{4}_{\Lambda}$He	1.970 ± 0.175	[235, 310, 228, 123, 50]	error scaled by 1.34, $ndf = 4$
$\Gamma_{\pi^+}/\Gamma_{\pi^-}$	${}^{4}_{\Lambda}$He	0.033 ± 0.016	[175, 240, 204]	error scaled by 1.68, $ndf = 2$

Table A.7.: Branching ratio averages for non-mesonic weak decays [101, 261].

Channel	Isotope	Value	References	Comment
Γ_n/Γ_Λ	${}^{4}_{\Lambda}$He	$0.034\ ^{+\ 0.020}_{-\ 0.019}$	[228, 310]	
	${}^{5}_{\Lambda}$He	0.200 ± 0.110	[288]	
	${}^{12}_{\Lambda}$C	0.230 ± 0.080	[178]	
Γ_p/Γ_Λ	${}^{4}_{\Lambda}$He	0.164 ± 0.013	[235, 228, 310]	
	${}^{5}_{\Lambda}$He	0.217 ± 0.041	[15, 288]	
	${}^{7}_{\Lambda}$Li	0.280 ± 0.070	[15]	
	${}^{9}_{\Lambda}$Be	0.300 ± 0.070	[15]	
	${}^{11}_{\Lambda}$B	$0.385\ ^{+\ 0.098}_{-\ 0.088}$	[15, 222]	error scaled by 1.09, $ndf = 1$
	${}^{12}_{\Lambda}$C	$0.446\ ^{+\ 0.064}_{-\ 0.082}$	[15, 178, 222]	
	${}^{13}_{\Lambda}$C	0.600 ± 0.140	[15]	
	${}^{15}_{\Lambda}$N	0.490 ± 0.110	[15]	
	${}^{16}_{\Lambda}$O	0.440 ± 0.120	[15]	
$\Gamma_{\mathrm{nm}}/\Gamma_\Lambda$	${}^{4}_{\Lambda}$He	0.175 ± 0.025	[235, 228]	
	${}^{5}_{\Lambda}$He	0.406 ± 0.020	[225, 288]	
	${}^{11}_{\Lambda}$B	0.891 ± 0.079	[271, 222]	
	${}^{12}_{\Lambda}$C	0.955 ± 0.031	[225, 222, 288]	
	${}^{27}_{\Lambda}$Al	1.230 ± 0.070	[271]	
	${}^{28}_{\Lambda}$Si	1.125 ± 0.125	[271]	
Γ_n/Γ_p (1N)	${}^{4}_{\Lambda}$He	$0.217\ ^{+\ 0.134}_{-\ 0.133}$	[228, 310]	
	${}^{5}_{\Lambda}$He	0.470 ± 0.112	[170, 288]	
	${}^{11}_{\Lambda}$B	$1.247\ ^{+\ 0.606}_{-\ 0.519}$	[222, 288]	
	${}^{12}_{\Lambda}$C	$0.782\ ^{+\ 0.199}_{-\ 0.195}$	[179, 271, 151]	error scaled by 2.09, $ndf = 2$
	${}^{28}_{\Lambda}$Si	$1.107\ ^{+\ 0.299}_{-\ 0.283}$	[271, 151]	error scaled by 1.50, $ndf = 1$
Γ_n/Γ_p (1&2N)	${}^{11}_{\Lambda}$B	$0.510\ ^{+\ 0.110}_{-\ 0.150}$	[40]	
	${}^{12}_{\Lambda}$C	$0.802\ ^{+\ 0.186}_{-\ 0.176}$	[271, 151]	error scaled by 1.05, $ndf = 1$
	${}^{28}_{\Lambda}$Si	$0.838\ ^{+\ 0.329}_{-\ 0.316}$	[271, 151]	error scaled by 1.56, $ndf = 1$
Γ_2/Γ_{nm}	${}^{12}_{\Lambda}$C	0.290 ± 0.130	[178]	
$\Gamma_n/(\Gamma_n + \Gamma_p)$	${}^{12}_{\Lambda}$C	$0.570\ ^{+\ 0.110}_{-\ 0.150}$	[40]	
$(\Gamma_n + \Gamma_p)/\Gamma_{\pi^-}$	${}^{4}_{\Lambda}$H	0.260 ± 0.130	[50]	
	${}^{4}_{\Lambda}$He	0.578 ± 0.054	[235, 228, 310, 50, 51]	
	${}^{5}_{\Lambda}$He	1.246 ± 0.085	[288, 82, 207]	
	${}^{11}_{\Lambda}$B	4.800 ± 1.100	[212]	

A.5. Further Notes about the Chart

A.5.1. Software implementation

The website is constructed via the interaction of a set of html, css and JavaScript files. The *index.html* is the root element of all files to set up an initial html frame for the web page as well as calling the connected .css and .js files. It can be opened by any modern web browser to display the web page. Opening it from a local file directory may result in conflicts with the CORS policy, which has to be disabled for development purposes. The routines of computing averages described in Chapter 4.3 are implemented within the *main.js* file. It is also responsible for most of the functionality regarding the various button actions as well as the transformation of the html document. This file was build up entirely from scratch. Besides that, *jquery.js* is a common library [164] which allows the interaction between js and html files and makes manipulating the latter a lot more convenient. The *chart.js* file is used for the generation of plots and graphics. It is also based on a well known library [74], but had to be modified at several places. Many further files are listed in Table A.8, together with a brief description.

Table A.8.: Involved files of the *Chart of Hypernuclides* website.

File name	Description
index.html	root element, design of the website's visual frame, call of other files, to be opened with the browser
style.css	main style sheet to specify the visual appearance of buttons, boxes, etc.
tooltip.css	additional tool-tip flags adapted from the bootstrap library [57]
tooltip.js	corresponding JavaScript file to allow for the tool-tip's functionality [57]
main.js	main JavaScript file to provide the data analysis, generation of data tables, etc.
Chart.js	library used for plotting [74], partly modified to generate the ideograms
chartjs-plugin-datalabels.js	plugin for Chart.js [75] to allow for data labels in the ideograms
dragscroll.js	library for improved drag-scrolling of the hypernuclear chart box [100]
error.js	small script for handling technical errors
jquery.min_3.6.js	versatile library to allow for the manipulation of elements, boxes, tables etc. in the websites body [164]
database.xml	database file to hold all information about hypernuclei etc.

A.5.2. Averaging with the linear variance model

This model offers, similar to the linear σ model described in Chapter 4.3.4 on page 43, the opportunity to calculate averages of data sets with asymmetric errors, where for each value $\mu\,^{+\sigma_+}_{-\sigma_-}$ is given [39]. While it was found to be less reliable than the linear σ model, especially with strongly asymmetric errors, its definition is a bit simpler. The variance is given by the function

$$V(x) = V_1 + V_2\,(x - \mu), \tag{A.10}$$

where $V_1 = \sigma_+\,\sigma_-$ and $V_2 = \sigma_+ - \sigma_-$ are directly given by the errors. Then, the resulting likelihood function is

$$\ln L(x) = -\frac{1}{2}\sum_{i=0}^{N}\frac{(x-\mu)^2}{V(x)}. \tag{A.11}$$

In the end, the more stable linear σ model was chosen for the averaging algorithm of the *Chart of Hypernuclides*.

B. Hardware at A1

Within this chapter, more information about the setup of the hypernuclear beamtime is found, especially about the installation process of KAOS and the measures to protect it from background radiation. Furthermore, the actual handling procedure of the lithium is described as well as the newly installed NMR system.

B.1. Installation of KAOS

Finding the in-beam-line position at 17°

Inside of the magnet's vacuum chamber of KAOS there are two white lines marking (i) the central line of the entry window and (ii) the 0° beam line. The second line is shifted by $100\,\mathrm{mm}$ towards the exit beam side and is used as the ideal particle entry into the spectrometer. This line also guides the uncharged particles into the additional 0° exit beam pipe where they are caught with an extra lead beam dump.
For the orientation of KAOS a rotational laser is mounted onto the flange of the photon beam line by using an aluminum holder, shown in Figure B.1. This laser generates a leveled plane which lies vertically along the length of the beam pipe. By that, a laser mark will be visible upstream at the target chamber as well as on the downstream side in the hall. At first, the laser is to be aligned to the spectrometer itself. Therefore, the holder allows for moving in two degrees of freedom. By that, an alignment to the second white line inside the spectrometer can be achieved. It is to be noted that this line doesn't hit the photon beam pipe in the center, but shifted by a few centimeters towards the electron arm.
Then, the laser mark upstream must be aligned to the beam line hole on the XYMO in front of the target chamber. This marks are clearly visible also with the spectrometer in its lowered height. To fix KAOS onto the 17° line, the laser mark downstream is to be brought to the $21.222\,\mathrm{m}$ mark on the circumference scale of A1's spectrometer track. Finally, the distance of KAOS to the target is the remaining dimension. To use the known transfer matrices for the KAOS magnet properly, the distance from target center to the entry into the magnet must be $1000\,\mathrm{mm}$. In practice though, it turned out to be more useful to take the distance between the outer target chamber with side walls to the KAOS nose, which is $180\,\mathrm{mm}$. In general it is not possible to align the three mentioned conditions one by one, since the directions KAOS can be pushed to are not free to choose. Rather than that, the final position is to be approximated in every dimension step by step.

Adjusting the height

KAOS rests on three feet which can be adjusted in their height via a hydraulic system. When the spectrometer finally arrived at the 17° position, it has to be brought to the correct height. Therefore, a leveling laser is placed inside the target chamber and adjusted to the exact height of the electron beam. Here, again, the XYMO hole in front of the chamber gives a good reference. This laser will then also radiate into the KAOS vacuum chamber via the entry flange, leaving a mark, where the spectrometer has to be aligned to. The dipole's shoe has a total height of

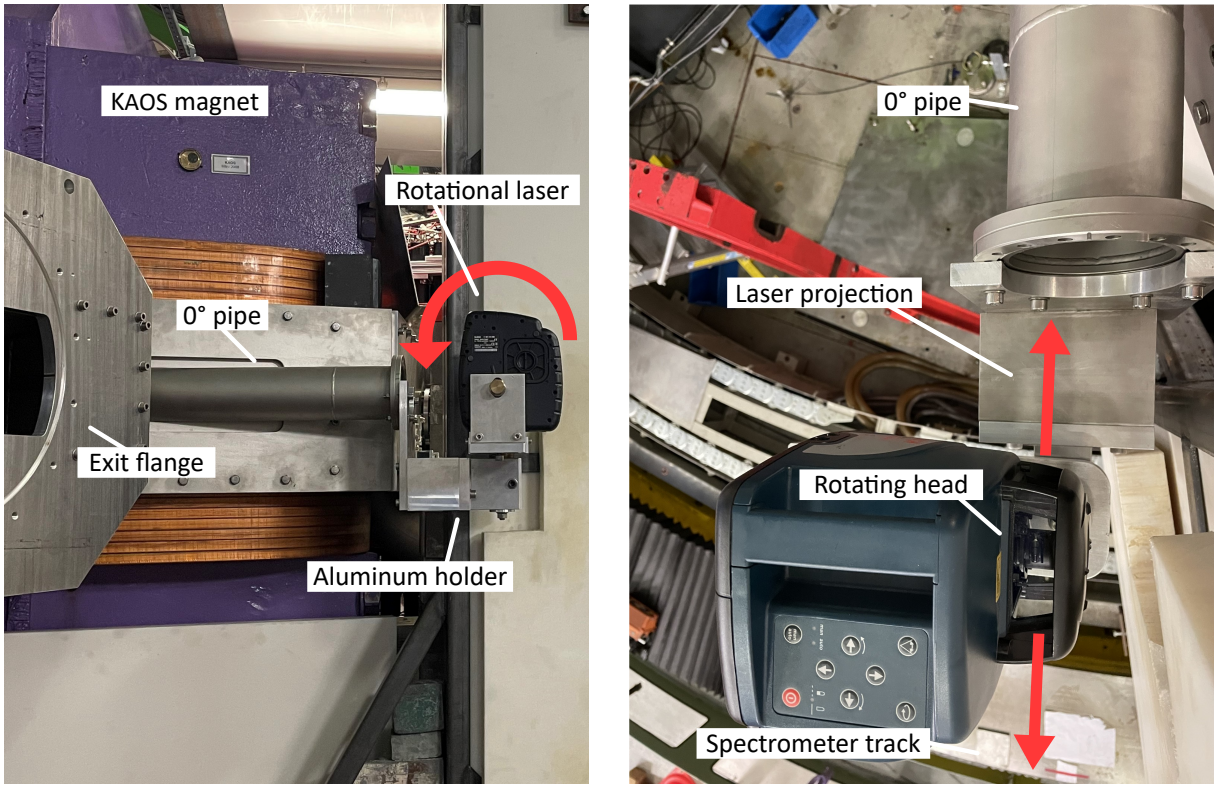

Figure B.1.: Installation of the Bosch BL 200 GC rotational laser to align KAOS. **Left:** the laser is installed to the 0° pipe at the spectrometer via a dedicated aluminum holder. The device will project a leveled plane by rotating a laser beam as indicated by the red arrow. **Right:** the laser will shine into the pipe, projecting a mark into the vacuum chamber of KAOS. Inside there, the laser has to be aligned to a white line mark by adjusting the holder. Afterwards, another mark of the laser can be found at the circular track of the spectrometers. This track has a millimeter scale to which KAOS finally has to be aligned.

$200\,\mathrm{mm}$ and to assure the particles entering centrally, a $100\,\mathrm{mm}$ mark was placed inside the shoe via KAOS' exit beam window and aligned to the laser.
For the final step, the leveling, two bubble levels with 1/10 degree accuracy were inserted into the shoe, one for the front-to-back level and one for left-right. A few additional millimeters at some of the feet were enough to bring KAOS into the desired position.

B.2. Protection against Radiation

Due to the forward angle design of KAOS, the spectrometer is closer to beam line and beam dump than the other A1 spectrometers. In addition, the shorter length of the central track brings the detectors even closer to the critical points. After all, several protection measures had to be installed to keep the disturbances by radiation at a moderate level.
The spectrometer is surrounded by boron containing plastic walls to especially absorb neutrons. For the back side of KAOS– which faces the A1 beam dump – these walls are also strengthened by an additional layer of lead. These walls can be seen on the left of Figure B.2. For the hypernuclear beamtimes of this thesis, two stacks of $50\,\mathrm{cm}$ thick concrete blocks were placed between KAOS and beam dump as shown, to improve the shielding even more. These stacks are also seen in Figure 9.1 on page 110. The stack closer to KAOS also acts as foundation for the dedicated photon

beam dump. This was designed by A. Esser to catch the uncharged particles coming from the 0° pipe [116]. It is seen on the right of Figure B.2. It mainly consists of lead bricks which are covered in metal plates. On the front side there is an entrance hole so that the particles are absorbed in the center of the lead block. To guide the particles to this dump, another pipe is connected to the 0° pipe. It then ends blindly in front of the dump.
Any radiation coming from this pipe and the dump is again caught as good as possible by another lead wall which is placed directly next to the photon dump. The whole construction rests on several lead bricks and aluminum plates to bring the dump setup to the correct height. Due to the asymmetric extra weight of the lead wall, some bricks were placed at the opposite side to act as counter weights. In addition, the plate was secured by crane cables to additionally prevent it from falling over.
During the experiment it was observed that especially the highest channels of the H wall saw a higher count rate compared to the other channels. This was due to a gap between the big absorber back walls of KAOS. It was then filled again by more concrete and lead bricks. With that, the installation of KAOS is complete, so that it can be connected to the vacuum system and is in working position for the hypernuclear experiments.

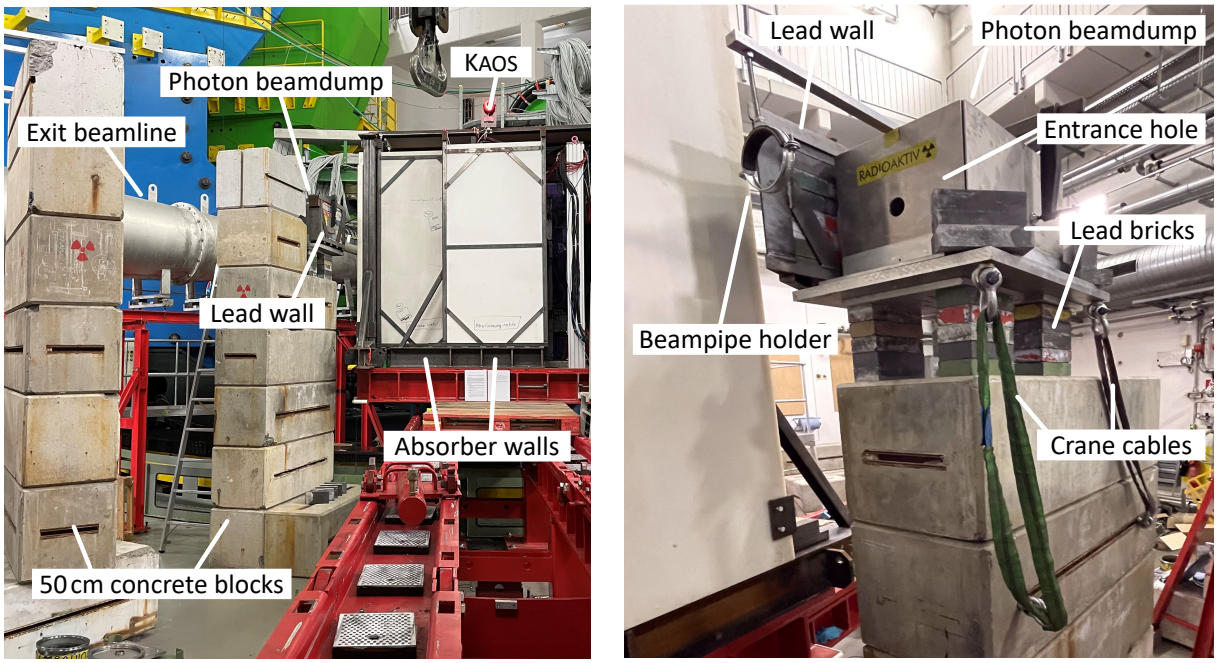

Figure B.2.: Absorbers against radiation around KAOS. **Left:** the spectrometer is seen from its back side, which faces the beam dump of A1. Here, absorber walls of Boron plastic and Lead are installed, which were supported furthermore by stacks of concrete bricks. One of these stacks also houses the photon beam dump. **Right:** close up of the photon dump. It consists mainly of lead. For more shielding, another lead wall was placed right next to it.

B.3. Preparation Procedure of the Lithium Target

For handling the lithium in the context of experiments like this, an argon filled glove box was used. Within this atmosphere, the working time with the lithium is vastly improved. In this box, the lithium is cut to size with a scalpel and flattened with a pair of aluminum plates. Also, it was mounted to the target frame inside there. To bring the equipped frame to the target chamber, it was put inside a transport box, which as well needed to be filled with argon before. Meanwhile,

the target chamber had initially to be evacuated to get rid of the ambient air inside the vacuum system. It was then flushed with argon to be ready to insert the lithium. That way, only a small amount of ambient air was present inside the system. After the insertion, this gas mixture was then pumped out as quick as possible to keep the surface corrosion of the lithium moderate.
This procedure does not allow for an accurate alignment of the target since the time is limited. In the usual cases, this would be done via a theodolite with which an accuracy of better than $100\,\mu\mathrm{m}$ is achieved. However, this is a very time consuming process and requires an opened vacuum system. This would leave plenty of time for the lithium to corrode. Therefore, the lithium target system was designed to be adjustable afterwards with a set of two step motors. These are explained in Chapter 8.2.4 on page 97.

B.4. Revised NMR Setup

The A1 spectrometers A, B and C consists of a total of 5 dipole magnets which are equipped with NMR probes. SpekA and SpekC both have two dipoles, SpekB only one. The old system was not operable anymore so it was replaced with the Caylar NMR 20 gaussmeter. The new system is set up by two probes for each dipole, covering a low field range $(0.1 - 0.5\,\mathrm{T})$ and a high field range $(0.45 - 2.1\,\mathrm{T})$. Each spectrometer has its own pre-amplifier.
It was observed that the NMR signal is easily disturbed by ground loops. To ensure a proper running, all cable connectors were covered with shrinking tube. Special care was also taken for the probes themselves, since they have a metal screw sitting on one side. Together with the old probe holders which were manufactured from aluminum, also there a ground loop could be established. Hence, the old holders were equipped with newly designed PVC parts and kapton foil. The goal of the device is to find the frequency at which the hydrogen atoms resonate. The value of **signal** has the strongest influence on the search for the resonance. It controls the amplification of the NMR signal. Internally, the device compares its amplitude to a fixed threshold, so changing the signal's amplification can easily fulfill the threshold condition at any frequency, or making it impossible to find the resonance at all. The **sweep** value controls the timing between the sent and received wave. If the signal suffers from outer disturbances, a **filter** can be chosen to perform a smoothing. In general, the lowest filter was preferred, yet some probes could only run reliably with higher filters. Finally, the **fieldtype** did not seem to have a reproducible influence on the resonance finding, so it was kept at *medium* for every

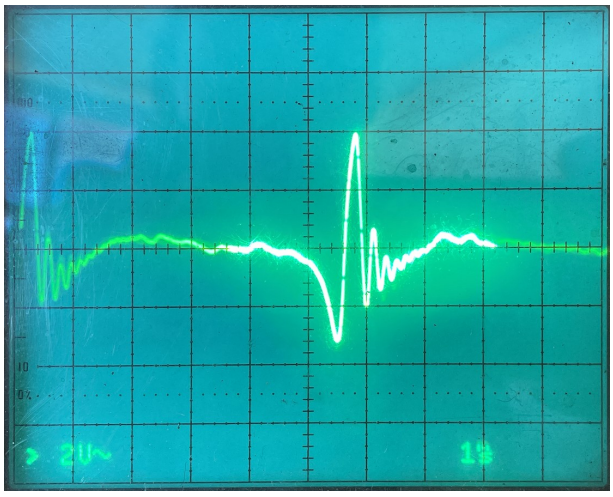

Figure B.3.: NMR resonance on an old-fashioned oscilloscope.

probe. For the experiment, the probe settings were chosen as noted in Table B.1. Here, also the enumeration of the probes is given. Finally, Table B.2 lists the commands to remotely steer the NMR device and the corresponding aliases in the control software Mezzo.

Table B.1.: Mapping of spectrometer magnets and NMR probes together with their setting.

Spectrometer magnet	Field region	Preamp	Probe	Signal	Sweep
A Dipole 1	low	1	1	3	1
A Dipole 1	high	1	2	3	1
A Dipole 2	low	1	3	3	1
A Dipole 2	high	1	4	3	1
B Dipole	low	2	1	3	1
B Dipole	high	2	2	3	1
C Dipole 1	low	3	1	5	3
C Dipole 1	high	3	2	3	1
C Dipole 2	low	3	3	3	1
C Dipole 2	high	3	4	3	1

Table B.2.: The NMR device's Mezzo aliases, raw commands and their use. The *x* in the commands has to be replaced by a desired number.

Mezzo alias	Command to device	Explanation
etc.nmr.value	READFIELDNMR	NMR value
etc.nmr.status	READ_STATUS1	Lock bit
etc.nmr.mode	SET_MANUMODE SET_AUTOFLAT DIGITAL_MODE HALLTRACKING	Manual mode: Field search by hand, Auto flat: automatic search without help, Digital mode: search around a rough estimation given by the user, Hall tracking: search around hall value
etc.nmr.hall	GETHALLVALUE	Field value of the included hall probe
etc.nmr.probe	SELECT_PR_0*x*	Select probe, 1 to 4 possible
etc.nmr.preamp	SELECT_PA_0*x*	Select preamp, 1 to 3 possible
etc.nmr.multiplexer	SELECT_SW_0*x*	Select multiplexer, always 1
etc.nmr.signal	SET_PRB_SIG*x*	Adjust signal amplification, 1 to 7 possible
etc.nmr.sweep	SET_PRB_SWE*x*	Adjust sweep, 1 to 7 possible
etc.nmr.filter	SET_PRB_FTR*x*	Apply filters, 1 to 3 possible
etc.nmr.fieldtype	SET_PRB_FLD*x*	Change field type, 1: medium, 2: low, 3: high

C. Literature

[1] *A1 website*.
wwwa1.kph.uni-mainz.de[Accessed: 01. June 2023].

[2] B. Abbott et al.:
GW151226: Observation of Gravitational Waves from a 22-Solar-Mass Binary Black Hole Coalescence.
In: *Phys. Rev. Lett.* 116 (24 2016), p. 241103.
DOI: 10.1103/PhysRevLett.116.241103.

[3] B. Abbott et al.:
GW170817: Observation of Gravitational Waves from a Binary Neutron Star Inspiral.
In: *Phys. Rev. Lett.* 119 (16 2017), p. 161101.
DOI: 10.1103/PhysRevLett.119.161101.

[4] B. Abbott et al.:
Observation of Gravitational Waves from a Binary Black Hole Merger.
In: *Phys. Rev. Lett.* 116 (6 2016), p. 061102.
DOI: 10.1103/PhysRevLett.116.061102.

[5] M. Abdallah et al.:
Measurements of ${}^{3}_{\Lambda}\mathrm{H}$ *and* ${}^{4}_{\Lambda}\mathrm{H}$ *Lifetimes and Yields in Au+Au Collisions in the High Baryon Density Region*.
In: (2021).
arXiv: 2110.09513 [nucl-ex].

[6] B. I. Abelev:
Observation of an Antimatter Hypernucleus.
In: *Science* 328.5974 (2010). Ed. by B. I. Abelev et al., pp. 58–62.
ISSN: 0036-8075.
DOI: 10.1126/science.1183980.
eprint: https://science.sciencemag.org/content/328/5974/58.full.pdf.

[7] V. Abgaryan et al.:
Status and initial physics performance studies of the MPD experiment at NICA.
In: *The European Physical Journal A* 58.7 (2022).
DOI: 10.1140/epja/s10050-022-00750-6.

[8] S. Acharya et al.:
${}^{3}_{\Lambda}\mathrm{H}$ *and* ${}^{3}_{\Lambda}\overline{\mathrm{H}}$ *lifetime measurement in Pb-Pb collisions at* $\sqrt{s_{\mathrm{NN}}} = 5.02$ *TeV via two-body decay*.
In: *Phys. Lett. B* 797 (2019), p. 134905.
DOI: 10.1016/j.physletb.2019.134905.
arXiv: 1907.06906 [nucl-ex].

[9] P. Achenbach.
Private communication.

[10] P. Achenbach:
The Kaos Spectrometer at the Mainz Microtron and first Measurements of Kaon Electroproduction.

Habilitation. Mainz: Johannes Gutenberg-Universität, 2010.

[11] P. Achenbach et al.:
High-precision measurement of the hypertriton mass.
In: *PoS* Hadron2017 (2018), p. 207.
DOI: 10.22323/1.310.0207.

[12] J. Adam et al.:
${}^{3}_{\Lambda}H$ and ${}^{3}_{\Lambda}\overline{H}$ production in Pb-Pb collisions at $\sqrt{s_{NN}}$ =2.76 TeV.
In: *Physics Letters B* 754 (2016), pp. 360 –372.
ISSN: 0370-2693.
DOI: http://dx.doi.org/10.1016/j.physletb.2016.01.040.

[13] J. Adam et al.:
Measurement of the mass difference and the binding energy of the hypertriton and antihypertriton.
In: *Nature Physics* 16.4 (2020), 409–412.
ISSN: 1745-2481.
DOI: 10.1038/s41567-020-0799-7.

[14] L. Adamczyk et al.:
Measurement of the ${}^{3}_{\Lambda}$H lifetime in Au+Au collisions at the BNL Relativistic Heavy Ion Collider.
In: *Phys. Rev. C* 97 (5 2018), p. 054909.
DOI: 10.1103/PhysRevC.97.054909.

[15] M. Agnello et al.:
First determination of the one-proton induced Non-Mesonic Weak Decay width of p-shell Λ-Hypernuclei.
In: *Physics Letters B* 738 (2014), pp. 499–504.
ISSN: 0370-2693.
DOI: https://doi.org/10.1016/j.physletb.2014.10.024.

[16] M. Agnello et al.:
First observation of the hyper superheavy hydrogen ${}^{6}_{\Lambda}$H.
In: *Nuclear Physics A* 881 (2012). Progress in Strangeness Nuclear Physics, pp. 269–287.
ISSN: 0375-9474.
DOI: https://doi.org/10.1016/j.nuclphysa.2012.02.015.

[17] M. Agnello et al.:
First results from the FINUDA experiment at DAPHNE.
In: *Nucl. Phys. A* 754 (2005). Ed. by A. Gal and E. Hungerford, pp. 399–409.
DOI: 10.1016/j.nuclphysa.2005.01.033.

[18] M. Agnello et al.:
Hypernuclear spectroscopy with K^- at rest on ${}^{7}Li$, ${}^{9}Be$, ${}^{13}C$ and ${}^{16}O$.
In: *Phys. Lett. B* 698 (2011), pp. 219–225.
DOI: 10.1016/j.physletb.2011.02.060.
arXiv: 1011.2695 [nucl-ex].

[19] M. Agnello et al.:
New results on mesonic weak decay of p-shell Λ-hypernuclei.
In: *Physics Letters B* 681.2 (2009), pp. 139–146.
ISSN: 0370-2693.
DOI: https://doi.org/10.1016/j.physletb.2009.09.061.

[20] J. K. Ahn et al.:

Double-Λ hypernuclei observed in a hybrid emulsion experiment.
In: *Phys. Rev. C* 88 (1 2013), p. 014003.
DOI: 10.1103/PhysRevC.88.014003.

[21] T. Akaishi et al.:
${}^{3}_{\Lambda}$H and ${}^{4}_{\Lambda}$H mesonic weak decay lifetime measurement with ${}^{3,4}He(K^-, \pi^0){}^{3,4}_{\Lambda}$H reaction.
http://j-parc.jp/researcher/Hadron/en/pac_1901/pdf/P73_2019-06.pdf.
2019.

[22] T. Akaishi et al.:
J-PARC E77 experiment: Feasibility study for ${}^{3}_{\Lambda}$H mesonic weak decay lifetime measurement with ${}^{4}He(K^-, \pi^0){}^{4}_{\Lambda}$H reaction.
http://j-parc.jp/researcher/Hadron/en/pac_2001/pdf/P77_2020-01.pdf.

[23] Alexandre Obertelli:
Hypernuclear halos with the HYDRA prototype at R3B.
Talk presented at the Joint THEIA-STRONG2020 and JAEA/Mainz REIMEI Web-Seminar 2021/2022.
2022.
URL: https://indico.gsi.de/event/14356/contributions/60538/attachments/38980/52705/HYDRA_THEIA_March2022.pdf (visited on 05/03/2022).

[24] ALICE Collaboration:
Measurement of the lifetime and Λ separation energy of ${}^{3}_{\Lambda}$H.
2022.
arXiv: 2209.07360 [nucl-ex].

[25] J. Alsing et al.:
Gravitational radiation from compact binary systems in the massive Brans-Dicke theory of gravity.
In: *Phys. Rev. D* 85 (6 2012), p. 064041.
DOI: 10.1103/PhysRevD.85.064041.

[26] V. A. Ambartsumyan and G. S. Saakyan:
The Degenerate Superdense Gas of Elementary Particles.
In: *Soviet Astronomy* 4 (1960), p. 187.

[27] R. Ammar et al.:
Mesic decays of hypernuclei from K^--capture.
In: *Il Nuovo Cimento (1955-1965)* 15.2 (1960), pp. 181–200.
ISSN: 1827-6121.
DOI: 10.1007/BF02860246.

[28] R. G. Ammar, W. Dunn, and M. Holland:
On the spin and binding of ${}^{3}H_{\Lambda}$.
In: *Il Nuovo Cimento (1955-1965)* 26.4 (1962), pp. 840–843.
ISSN: 1827-6121.
DOI: 10.1007/BF02781808.

[29] R. G. Ammar et al.:
Mesic Decays of Hypernuclei from K^--Capture.
In: *Il Nuovo Cimento* 19 (1961), pp. 20–35.

[30] A. Andronic et al.:
Production of light nuclei, hypernuclei and their antiparticles in relativistic nuclear collisions.
In: *Physics Letters B* 697.3 (2011), pp. 203 –207.

ISSN: 0370-2693.
DOI: http://dx.doi.org/10.1016/j.physletb.2011.01.053.

[31] R Armenteros et al.:
The properties of charged V-particles.
In: *The London, Edinburgh, and Dublin Philosophical Magazine and Journal of Science* 43.341 (1952), pp. 597–611.
DOI: 10.1080/14786440608520216.
eprint: https://doi.org/10.1080/14786440608520216.

[32] T. A. Armstrong et al.:
Measurements of light nuclei production in $11.5A\mathrm{GeV}/c$ *Au+Pb heavy-ion collisions*.
In: *Phys. Rev. C* 61 (6 2000), p. 064908.
DOI: 10.1103/PhysRevC.61.064908.

[33] Australian Telescope National Facility:
Pulsar Catalogue.
2022.
URL: https://www.atnf.csiro.au/research/pulsar/psrcat/ (visited on 05/01/2022).

[34] S. A. Avramenko et al.:
A Study of the production and lifetime of the lightest relativistic hypernuclei.
In: *Nucl. Phys. A* 547 (1992). Ed. by T. Fukuda et al., pp. 95C–100C.
DOI: 10.1016/0375-9474(92)90714-U.

[35] L. Baiotti:
Gravitational waves from neutron star mergers and their relation to the nuclear equation of state.
In: *Progress in Particle and Nuclear Physics* 109 (2019), p. 103714.
ISSN: 0146-6410.
DOI: https://doi.org/10.1016/j.ppnp.2019.103714.

[36] L. Baiotti and L. Rezzolla:
Binary neutron star mergers: a review of Einstein's richest laboratory.
In: *Reports on Progress in Physics* 80.9 (2017), p. 096901.

[37] T. Baker et al.:
Strong Constraints on Cosmological Gravity from GW170817 and GRB 170817A.
In: *Phys. Rev. Lett.* 119 (25 2017), p. 251301.
DOI: 10.1103/PhysRevLett.119.251301.

[38] H. Bandō, T. Motoba, and J. Žofka:
Production, structure and decay of hypernuclei.
In: *Int. J. Mod. Phys. A* 5 (1990), pp. 4021–4198.
DOI: https://doi.org/10.1142/S0217751X90001732.

[39] R. Barlow:
Asymmetric statistical errors.
In: *PHYSTAT (2005): Statistical Problems in Particle Physics, Astrophysics and Cosmology*. 2004,
Pp. 56–59.
arXiv: physics/0406120.

[40] P. D. Barnes:
Nonleptonic weak interactions in hypernuclei.
In: *Nuclear Physics A* 450 (1986), pp. 43–66.
ISSN: 0375-9474.
DOI: https://doi.org/10.1016/0375-9474(86)90541-5.

[41] J. Bernauer:
Measurement of the elastic electron-proton cross section and separation of the electric and magnetic form factor in the Q^2 range from 0.004 to 1 $(GeV/c)^2$. eng.
PhD thesis. Mainz, 2010.

[42] E. Berti et al.:
Testing general relativity with present and future astrophysical observations.
In: *Classical and Quantum Gravity* 32.24 (2015), p. 243001.

[43] R Bertini et al.:
A Full Set of Nuclear Shell Orbitals for the Λ Particle Observed in ^{32}S (Λ) and ^{40}Ca (Λ).
In: *Phys. Lett. B* 83 (1979), p. 306.
DOI: 10.1016/0370-2693(79)91113-4.

[44] R Bertini et al.:
Neutron hole states in ${}^{6}_{\Lambda}\mathrm{Li}$, ${}^{7}_{\Lambda}\mathrm{Li}$, ${}^{9}_{\Lambda}\mathrm{Be}$ and ${}^{1}2_{\Lambda}\mathrm{C}$ hypernuclei.
In: *Nuclear Physics A* 368.3 (1981), pp. 365–374.
ISSN: 0375-9474.
DOI: https://doi.org/10.1016/0375-9474(81)90761-2.

[45] G. Bertone and D. Hooper:
History of dark matter.
In: *Rev. Mod. Phys.* 90 (4 2018), p. 045002.
DOI: 10.1103/RevModPhys.90.045002.

[46] D. Bertrand et al.:
Branching ratios for the π^- mesonic decays of the hypernuclei ${}^{3}_{\Lambda}H$ and ${}^{4}_{\Lambda}H$.
In: *Nucl. Phys. B* 16 (1970), pp. 77–84.
DOI: https://doi.org/10.1016/0550-3213(70)90339-1.

[47] G. Bhamathi and K. Prema:
A note on the decay rates of $^3H_\Lambda$ and $^4H_\Lambda$.
In: *Il Nuovo Cimento A (1965-1970)* 63.2 (1969), pp. 555–558.
ISSN: 1826-9869.
DOI: 10.1007/BF02756232.

[48] H. Bhang et al.:
The Weak Decay Widths of Lambda Hypernuclei.
In: *J. Korean Phys. Soc.* 59 (2011), S1461–S1466.
DOI: 10.3938/jkps.59.1461.

[49] *Bicron Scintillators*.
crystals.saint-gobain.com[Accessed: 06. January 2023].

[50] M. M. Block et al.:
Hyperfragment studies in the helium bubble chamber.
In: *Proceedings of the International Conference on Hyperfragments, St. Cergue, Switzerland, 1963*.
1964,
Pp. 63–74.

[51] M. M. Block et al.:
Lifetime of the Λ^0 Hyperon.
In: *Phys. Rev.* 130 (2 1963), pp. 766–768.
DOI: 10.1103/PhysRev.130.766.

[52] K. Blomqvist et al.:

The three-spectrometer facility at the Mainz microtron MAMI.
In: *Nuclear Instruments and Methods in Physics Research Section A: Accelerators, Spectrometers, Detectors and Associated Equipment* 403.2 (1998), pp. 263–301.
ISSN: 0168-9002.
DOI: https://doi.org/10.1016/S0168-9002(97)01133-9.

[53] G. Bohm et al.:
A determination of the binding-energy values of light hypernuclei.
In: *Nucl. Phys. B* 4.6 (1968), pp. 511–526.
ISSN: 0550-3213.
DOI: https://doi.org/10.1016/0550-3213(68)90109-0.

[54] G. Bohm et al.:
On the lifetime of the ${}^{3}_{\Lambda}\mathrm{H}$ hypernucleus.
In: *Nuclear Physics B* 16.1 (1970), pp. 46–52.
ISSN: 0550-3213.
DOI: https://doi.org/10.1016/0550-3213(70)90335-4.

[55] J. Bondorf et al.:
Statistical multifragmentation of nuclei.
In: *Physics Reports* 257.3 (1995), pp. 133 –221.
ISSN: 0370-1573.
DOI: http://dx.doi.org/10.1016/0370-1573(94)00097-M.

[56] A. Bonetti et al.
In: *Nuovo Cimento* 11 (1954), p. 210.

[57] *Bootstrap library*.
getbootstrap.com[Accessed: 29. June 2023].

[58] E. Botta, T. Bressani, and A. Feliciello:
On the binding energy and the charge symmetry breaking in $A \leq 16$ Λ-hypernuclei.
In: *Nuclear Physics A* 960 (2017), pp. 165 –179.
ISSN: 0375-9474.
DOI: http://dx.doi.org/10.1016/j.nuclphysa.2017.02.005.

[59] A. S. Botvina, K. K. Gudima, and J. Pochodzalla:
Production of hypernuclei in peripheral relativistic ion collisions.
In: *Phys. Rev. C* 88 (5 2013), p. 054605.
DOI: 10.1103/PhysRevC.88.054605.

[60] A. S. Botvina et al.:
Relativistic ion collisions as the source of hypernuclei.
In: *The European Physical Journal A* 52.8 (2016), p. 242.
ISSN: 1434-601X.
DOI: 10.1140/epja/i2016-16242-7.

[61] A. Botvina, Y. Golubeva, and A. Iljinov:
Statistical simulation of the break-up of light nuclei in hadron-nucleus reactions.
In: *INR, P-0657, Moscow* (1990).

[62] A. Botvina and J. Pochodzalla:
Production of hypernuclei in multifragmentation of nuclear spectator matter.
In: *Phys. Rev. C* 76 (2 2007), p. 024909.
DOI: 10.1103/PhysRevC.76.024909.

[63] A. Botvina et al.:

Formation of hypermatter and hypernuclei within transport models in relativistic ion collisions.
In: *Physics Letters B* 742 (2015), pp. 7 –14.
ISSN: 0370-2693.
DOI: http://dx.doi.org/10.1016/j.physletb.2014.12.060.

[64] A. Botvina et al.:
Production of hypernuclei in peripheral collisions of relativistic ions.
In: *Nuclear Physics A* 881 (2012), pp. 228 –239.
ISSN: 0375-9474.
DOI: http://dx.doi.org/10.1016/j.nuclphysa.2012.01.015.

[65] A. Botvina et al.:
Production of spectator hypermatter in relativistic heavy-ion collisions.
In: *Phys. Rev. C* 84 (6 2011), p. 064904.
DOI: 10.1103/PhysRevC.84.064904.

[66] A. Botvina et al.:
Statistical simulation of the break-up of highly excited nuclei.
In: *Nuclear Physics A* 475.4 (1987), pp. 663 –686.
ISSN: 0375-9474.
DOI: http://dx.doi.org/10.1016/0375-9474(87)90232-6.

[67] W. Brückner et al.:
Hypercharge exchange reactions on nuclei.
In: *Physics Letters B* 55.1 (1975), pp. 107–110.
ISSN: 0370-2693.
DOI: https://doi.org/10.1016/0370-2693(75)90198-7.

[68] W. Brückner et al.:
Strangeness Exchange Reaction on Nuclei.
In: *Phys. Lett. B* 62 (1976), pp. 481–484.
DOI: 10.1016/0370-2693(76)90689-4.

[69] S. A. Bunyatov et al.:
Observation of the ${}^{12}_{\Lambda}C$ Hypernucleus in 250 GeV Proton Interaction with Photoemulsion Nuclei.
In: *Sov. J. Nucl. Phys.* 28 (1978), p. 222.

[70] M. Camenzind:
Faszination kompakte Objekte. Eine Einführung in die Physik der Weißen Zwerge, Neutronensterne und Schwarzen Löcher.
Second edition.
Springer Spektrum Berlin, Heidelberg, 2021.
ISBN: 978-3-662-62881-2.
DOI: https://doi.org/10.1007/978-3-662-62882-9.

[71] A. G. Cameron:
Neutron Star Models.
In: *APJ* 130 (1959). Provided by the SAO/NASA Astrophysics Data System, p. 884.
DOI: 10.1086/146780.

[72] T. Cantwell et al.:
On the binding energy values and excited states of some $A \leq 10$ hypernuclei.
In: *Nucl. Phys. A* 236 (1974), pp. 445–456.

[73] CBM Collaboration:
Challenges in QCD matter physics –The scientific programme of the Compressed Baryonic Matter experiment at FAIR.

In: *The European Physical Journal A* 53.3 (2017), p. 60.
ISSN: 1434-601X.
DOI: 10.1140/epja/i2017-12248-y.

[74] *Chartjs library*.
chartjs.org[Accessed: 02. September 2022].

[75] *Chartjs-plugin datalabels library*.
chartjs-plugin-datalabels.netlify.app[Accessed: 29. June 2023].

[76] K. N. Chaudhari et al.:
Binding energy and π^+ decay of light hyperfragments.
In: *Proceedings of the Indian Academy of Sciences - Section A* 68 (1968), pp. 228–243.

[77] H. R. Choudhury and V. P. Gautam:
$\Lambda - d$ Bound States ($J = \frac{1}{2}, \frac{3}{2}$) and Faddeev's Approach to the Three-Body Problem.
In: *Phys. Rev. C* 7 (1 1973), pp. 74–79.
DOI: 10.1103/PhysRevC.7.74.

[78] R. E. Chrien et al.:
States of ^{12}C (Λ) Formed in the Reaction ^{12}C (K^-, π^-).
In: *Phys. Lett. B* 89 (1979), p. 31.
DOI: 10.1016/0370-2693(79)90069-8.

[79] P. Ciok, M. Danysz, and J. Gierula:
Delayed decay of heavy fragments ejected from cosmic ray stars.
In: *Nuovo Cimento* 11 (1954), p. 436.

[80] Z. Citron et al.:
Future physics opportunities for high-density QCD at the LHC with heavy-ion and proton beams.
2019.
arXiv: 1812.06772 [hep-ph].

[81] T. Clifton et al.:
Modified gravity and cosmology.
In: *Physics Reports* 513.1 (2012). Modified Gravity and Cosmology, pp. 1 –189.
ISSN: 0370-1573.
DOI: https://doi.org/10.1016/j.physrep.2012.01.001.

[82] G. Coremans et al.:
The non-mesonic decay of helium hypernuclei.
In: *Nuclear Physics B* 16.1 (1970), pp. 209–220.
ISSN: 0550-3213.
DOI: https://doi.org/10.1016/0550-3213(70)90351-2.

[83] N. Crayton et al.:
Compilation of Hyperfragment Binding Energies.
In: *Rev. Mod. Phys.* 34 (2 1962), pp. 186–189.
DOI: 10.1103/RevModPhys.34.186.

[84] P. Creminelli and F. Vernizzi:
Dark Energy after GW170817 and GRB170817A.
In: *Phys. Rev. Lett.* 119 (25 2017), p. 251302.
DOI: 10.1103/PhysRevLett.119.251302.

[85] H. T. Cromartie et al.:
Relativistic Shapiro delay measurements of an extremely massive millisecond pulsar.
In: *Nature Astronomy* 4 (21 2020), pp. 72–76.

DOI: 10.1038/s41550-019-0880-2.

[86] J. Crussard and D. Morellet:
Emission probable d'un fragment nucléaire contenant une particule V^0.
In: *Comptes Rendus* 236 (1953), p. 64.

[87] C. O. Curceanu and J. Pochodzalla:
Meeting Reports: HYP2015: From Particles and Nuclei to the Stars: Strangeness Investigators Met in Sendai.
In: *Nuclear Physics News* 26.2 (2016), pp. 27–34.
DOI: 10.1080/10619127.2016.1140997.
eprint: https://doi.org/10.1080/10619127.2016.1140997.

[88] F. Cusanno et al.:
High-Resolution Spectroscopy of $^{16}_{\Lambda}\mathbf{N}$ *by Electroproduction*.
In: *Phys. Rev. Lett.* 103 (20 2009), p. 202501.
DOI: 10.1103/PhysRevLett.103.202501.

[89] R. H. Dalitz:
Parity Nonconservation in the Decay of Free and Bound Λ *Particles*.
In: *Phys. Rev.* 112.2 (1958), pp. 605–613.
DOI: 10.1103/PhysRev.112.605.

[90] R. H. Dalitz and L. Liu:
Pionic Decay Modes of Light Λ *Hypernuclei*.
In: *Phys. Rev.* 116 (5 1959), pp. 1312–1321.
DOI: 10.1103/PhysRev.116.1312.

[91] R. Dalitz and G. Rajasekharan:
The spins and lifetimes of the light hypernuclei.
In: *Physics Letters* 1.2 (1962), pp. 58 –60.
ISSN: 0031-9163.
DOI: http://dx.doi.org/10.1016/0031-9163(62)90437-7.

[92] M. Danysz and J. Pniewski:
Delayed disintegration of a heavy nuclear fragment: I.
In: *The London, Edinburgh, and Dublin Philosophical Magazine and Journal of Science* 44.350 (1953), pp. 348–350.
DOI: 10.1080/14786440308520318.
eprint: http://dx.doi.org/10.1080/14786440308520318.

[93] D. H. Davis:
50 years of hypernuclear physics – I. The early experiments.
In: *Nucl. Phys. A* 754 (2005), pp. 3c–13c.
DOI: 10.1016/j.nuclphysa.2005.01.002.

[94] D. H. Davis:
Hypernuclei – The early days.
In: *Nucl. Phys. A* 547 (1992), pp. 369–378.
DOI: 10.1016/0375-9474(92)90746-7.

[95] V. Dexheimer and S. Schramm:
Proto-Neutron and Neutron Stars in a Chiral SU(3) Model.
In: *The Astrophysical Journal* 683.2 (2008), p. 943.
DOI: 10.1086/589735.

[96] P. Dłuzewski et al.:

On the binding energy of the ${}^{12}_{\Lambda}C(g.s.)$ hypernucleus.
In: *Nucl. Phys. A* 484 (1988), pp. 520–524.
ISSN: 0375-9474.
DOI: https://doi.org/10.1016/0375-9474(88)90307-7.

[97] F. Dohrmann et al.:
Angular distributions for ${}^{3,4}_{\Lambda}H$ bound states in the ${}^{3,4}He(e, e'K^+)$ reaction.
In: *Phys. Rev. Lett.* 93 (2004), p. 242501.

[98] F. Dohrmann et al.:
Quasifree Λ, Σ^0, and Σ^- electroproduction from ${}^{1,2}H$, ${}^{3,4}He$, and carbon.
In: *Phys. Rev. C* 76 (2007), p. 054004.

[99] B. W. Downs and R. H. Dalitz:
Analysis of the Λ-Hypernuclear Three-Body Systems.
In: *Phys. Rev.* 114 (2 1959), pp. 593–602.
DOI: 10.1103/PhysRev.114.593.

[100] *Dragscroll library*.
github.com/asvd/dragscroll[Accessed: 29. June 2023].

[101] P. Eckert, P. Achenbach, et al.:
Chart of Hypernuclides — Hypernuclear Structure and Decay Data.
hypernuclei.kph.uni-mainz.de[Accessed: 01. June 2023].

[102] P. Eckert et al.:
Octagonal-shaped scintillation counter as position detector for low-intensity electron beams.
In: *Nuclear Instruments and Methods in Physics Research Section A: Accelerators, Spectrometers, Detectors and Associated Equipment* 1041 (2022), p. 167357.
ISSN: 0168-9002.
DOI: https://doi.org/10.1016/j.nima.2022.167357.

[103] P. Eckert:
Commissioning of the hypertriton binding energy measurement at MAMI.
https://indico.cern.ch/event/896088/contributions/4748938/attachments/2470586/4238471/HYP2022.pptx.
Talk presented at HYP2022 Conference.
2022.

[104] P. Eckert:
Hypernuclear Database.
https://indico.gsi.de/event/11181/contributions/47174/attachments/34188/44588/eckert_slides.pdf.
Talk presented at THEIA-REIMEI 2021 meeting.
2021.

[105] P. Eckert:
Preparation of the hypertriton binding energy measurement at MAMI.
https://indico.lip.pt/event/592/contributions/3318/attachments/2680/4149/PANIC2021.pdf.
Talk presented at PANIC2021 Conference.
2021.

[106] P. Eckert:
Systematic treatment of hypernuclear data and application to the hypertriton.
https://indico.nucleares.unam.mx/event/1541/session/36/contribution/21/material/slides/0.pdf.

Talk presented at HADRON2021 Conference.
2021.

[107] P. Eckert:
Systematic treatment of hypernuclear data on a new publicly available website.
https://indico.rcnp.osaka-u.ac.jp/event/1640/contributions/9058/.
Talk presented at SNP school 2021.
2021.

[108] P. Eckert:
Untersuchung der $^{12}C(e,e'\pi^+\pi^+)^{12}Be$ - Reaktion am MAMI-C.
Master Thesis. Johannes Gutenberg-Universität Mainz, (2019).

[109] P. Eckert et al.:
Commissioning of the hypertriton binding energy measurement at MAMI.
In: *EPJ Web Conf.* 271 (2022), p. 01006.
DOI: 10.1051/epjconf/202227101006.

[110] P. Eckert et al.:
Preparation of the hypertriton binding energy measurement at MAMI.
In: *PoS* PANIC2021 (2022), p. 201.
DOI: 10.22323/1.380.0201.

[111] P. Eckert et al.:
Systematic treatment of hypernuclear data and application to the hypertriton.
In: *Rev. Mex. Fis. Suppl.* 3.3 (2022), p. 0308069.
DOI: 10.31349/SuplRevMexFis.3.0308069.
arXiv: 2201.02368 [physics.data-an].

[112] Ekawa, Hiroyuki:
WASA-FRS HypHI experiment at GSI for studying light hypernuclei.
In: *EPJ Web Conf.* 271 (2022), p. 08012.
DOI: 10.1051/epjconf/202227108012.

[113] A. Esser et al.:
Beam-normal single spin asymmetry in elastic electron scattering off ^{28}Si and ^{90}Zr.
In: *Phys. Lett. B* 808 (2020), p. 135664.
DOI: 10.1016/j.physletb.2020.135664.
arXiv: 2004.14682 [nucl-ex].

[114] A. Esser et al.:
Observation of $^{4}_{\Lambda}H$ hyperhydrogen by decay-pion spectroscopy in electron scattering.
In: *Phys. Rev. Lett.* 114 (2015), p. 232501.
DOI: 10.1103/PhysRevLett.114.232501.

[115] A. Esser et al.:
Pioneering experiment for high resolution decay pion spectroscopy of light hypernuclei at MAMI.
In: *Proceedings of the 50th International Winter Meeting on Nuclear Physics, Bormio, Italy, 23–27 Jan. 2012*.
PoS (Bormio2012).
2012,
P. 038.

[116] A. Esser:
Zerfallspionenspektroskopie leichter Hyperkerne in der Elektroproduktion. ger.
PhD thesis. Mainz: Johannes Gutenberg-Universität, 2013.

[117] J. M. Ezquiaga and M. Zumalacárregui:
Dark Energy After GW170817: Dead Ends and the Road Ahead.
In: *Phys. Rev. Lett.* 119 (25 2017), p. 251304.
DOI: 10.1103/PhysRevLett.119.251304.

[118] M. Faessler et al.:
Spectroscopy of the hypernucleus ${}^{12}_{\Lambda}C$.
In: *Physics Letters B* 46.3 (1973), pp. 468–470.
ISSN: 0370-2693.
DOI: https://doi.org/10.1016/0370-2693(73)90168-8.

[119] P. Fecchio:
Studying hypertriton production, lifetime, and binding in different collision systems with ALICE.
indi.to/3MvSH.
2021.

[120] D. Fedorov, A. Jensen, and K. Riisager:
General properties of halos.
In: *Physics Letters B* 312.1 (1993), pp. 1 –5.
ISSN: 0370-2693.
DOI: http://dx.doi.org/10.1016/0370-2693(93)90476-X.

[121] Z.-Q. Feng:
Formation and dynamics of exotic hypernuclei in heavy-ion collisions.
In: *Phys. Rev. C* 102 (4 2020), p. 044604.
DOI: 10.1103/PhysRevC.102.044604.

[122] E. Fermi:
High Energy Nuclear Events.
In: *Progress of Theoretical Physics* 5.4 (1950), p. 570.
DOI: 10.1143/ptp/5.4.570.
eprint: /oup/backfile/Content_public/Journal/ptp/5/4/10.1143/ptp/5.4.570/2/5-4-570.pdf.

[123] J. G. Fetkovich et al.:
Properties of ${}_{\Lambda}\mathrm{He}^{4}$.
In: *Phys. Rev. D* 6 (11 1972), pp. 3069–3085.
DOI: 10.1103/PhysRevD.6.3069.

[124] *Flir Lepton Thermal Camera Module*.
flir.eu/products/lepton/.

[125] E. Fonseca et al.:
Refined Mass and Geometric Measurements of the High-mass PSR J0740+6620.
In: *The Astrophysical Journal Letters* 915.1 (2021), p. L12.
DOI: 10.3847/2041-8213/ac03b8.

[126] E. Fonseca et al.:
Fundamental Physics with Radio Millisecond Pulsars.
2019.
arXiv: 1903.08194 [astro-ph.HE].

[127] M. Fortin et al.:
Relativistic hypernuclear compact stars with calibrated equations of state.
In: *Phys. Rev. D* 101 (3 2020), p. 034017.
DOI: 10.1103/PhysRevD.101.034017.

[128] L Fortney:
Lifetime measurements of ${}_{\Lambda}H^3$ and ${}_{\Lambda}H^4$.
In: *Proceedings of the International Conference on Hyperfragments*.
1964,
Pp. 85–88.
DOI: 10.5170/CERN-1964-001.85.

[129] P. Freire:
Pulsar mass measurements.
2023.
URL: https://www3.mpifr-bonn.mpg.de/staff/pfreire/NS_masses.html (visited on 07/20/2023).

[130] A. G. Frodesen, T. Røe, and O. Skjeggestad:
A systematic study of hypernuclei from Σ- captures in nuclear emulsions.
In: *Nuclear Physics* 68.3 (1965), pp. 575 –581.
ISSN: 0029-5582.
DOI: DOI:10.1016/0029-5582(65)90391-3.

[131] W. Fry, J. Schneps, and M. Swami:
Disintegration of Hyperfragments.
In: *Phys. Rev.* 99.5 (1955), pp. 1561–1572.
DOI: 10.1103/PhysRev.99.1561.

[132] W. Gajewski et al.:
A compilation of binding energy values of light hypernuclei.
In: *Nuclear Physics B* 1.3 (1967), pp. 105 –113.
ISSN: 0550-3213.
DOI: DOI:10.1016/0550-3213(67)90095-8.

[133] A. Gal and H. Garcilazo:
Towards resolving the ${}^{3}_{\Lambda}H$ lifetime puzzle.
In: *Physics Letters B* 791 (2019), pp. 48 –53.
ISSN: 0370-2693.
DOI: https://doi.org/10.1016/j.physletb.2019.02.014.

[134] A. Gal and J. Pochodzalla:
Foreword.
In: *Nuclear Physics A* 954 (2016). Recent Progress in Strangeness and Charm Hadronic and Nuclear Physics, pp. 1 –2.
ISSN: 0375-9474.
DOI: http://dx.doi.org/10.1016/j.nuclphysa.2016.06.009.

[135] H. Garcilazo:
Non-existence of Λnn or $\Sigma^- nn$ bound states.
In: *Journal of Physics G: Nuclear Physics* 13.5 (1987), p. L63.

[136] H. Garcilazo, T. Fernández-Caramés, and A. Valcarce:
ΛNN and ΣNN systems at threshold.
In: *Phys. Rev. C* 75 (3 2007), p. 034002.
DOI: 10.1103/PhysRevC.75.034002.

[137] C. A. A. Gayoso:
The scintillating fiber focal plane detector for the use of Kaos as a double arm spectrometer. eng. PhD thesis. Mainz, 2012.
DOI: http://doi.org/10.25358/openscience-2042.

[138] J. Geratz.
Bachelor Thesis. Mainz: Johannes Gutenberg-Universität, 2021.

[139] Glöckle, W. and Miyagawa, K. and Kamada, H. and Golak, J. and Witala, H.:
The hypertriton and its decays.
In: *Nuclear Physics A* 639.1 (1998), pp. 297c –306c.
ISSN: 0375-9474.
DOI: http://dx.doi.org/10.1016/S0375-9474(98)00287-5.

[140] T. Gogami et al.:
High resolution spectroscopic study of ${}^{10}_{\Lambda}\mathrm{Be}$.
In: *Phys. Rev. C* 93 (3 2016), p. 034314.
DOI: 10.1103/PhysRevC.93.034314.

[141] T. Gogami et al.:
Proposal to JLAB PAC48, C12-19-002: High accuracy measurement of nuclear masses of Λ *hyperhydrogens*.
https://indico.jlab.org/event/394/contributions/6380/attachments/5334/6632/e12-19-002_JLab-PAC48_gogami_20200811.pdf.

[142] T. Gogami et al.:
Spectroscopy of $A = 9$ *hyperlithium with the* $(e, e' K^+)$ *reaction*.
In: *Phys. Rev. C* 103 (4 2021), p. L041301.
DOI: 10.1103/PhysRevC.103.L041301.

[143] T. Gogami et al.:
Spectroscopy of the neutron-rich hypernucleus ${}^{7}_{\Lambda}\mathrm{He}$ *from electron scattering*.
In: *Phys. Rev. C* 94 (2 2016), p. 021302.
DOI: 10.1103/PhysRevC.94.021302.

[144] T. Gogami:
High accuracy measurement of nuclear masses of hyperhydrogens.
https://www-nh.scphys.kyoto-u.ac.jp/~gogami/e12-19-002/opensrc/Proposal-C12-19-002_PAC49_submitted.pdf.
PROPOSAL TO JLAB PAC49 C12-19-002.
2021.

[145] T. Gogami:
Spectroscopic research of Lambda hypernuclei up to medium-heavy mass region with the (*e,e'*K^+) *reaction*.
PhD thesis. Tohoku U., 2014.
DOI: 10.2172/1351527.

[146] J. G. Gongleton:
A simple model of the hypertriton.
In: *Journal of Physics G: Nuclear and Particle Physics* 18.2 (1992), pp. 339–357.
DOI: 10.1088/0954-3899/18/2/015.

[147] R. Grace et al.:
Weak Decay of ${}^{12}_{\Lambda}\mathrm{C}$ *and* ${}^{11}_{\Lambda}\mathrm{B}$ *Hypernuclei*.
In: *Phys. Rev. Lett.* 55 (10 1985), pp. 1055–1058.
DOI: 10.1103/PhysRevLett.55.1055.

[148] *Hallym – Pulsars*.
web.hallym.ac.kr[Accessed: 13. March 2023].

[149] T. Hasegawa et al.:

Spectroscopic study of (Lambda) B-10, (Lambda) C-12, (Lambda) Si-28, (Lambda) Y-89, (Lambda) La-139, and (Lambda) Pb-208 by the (pi+, K+) reaction.
In: *Phys. Rev. C* 53 (1996), pp. 1210–1220.
DOI: 10.1103/PhysRevC.53.1210.

[150] O. Hashimoto and H. Tamura:
Spectroscopy of Λ hypernuclei.
In: *Progress in Particle and Nuclear Physics* 57.2 (2006), pp. 564 –653.
ISSN: 0146-6410.
DOI: http://dx.doi.org/10.1016/j.ppnp.2005.07.001.

[151] O. Hashimoto et al.:
Proton Energy Spectra in the Nonmesonic Weak Decay of ${}^{12}_{\Lambda}C$ and ${}^{28}_{\Lambda}$Si Hypernuclei.
In: *Phys. Rev. Lett.* 88 (4 2002), p. 042503.
DOI: 10.1103/PhysRevLett.88.042503.

[152] S. H. Hayakawa et al.:
Observation of Coulomb-Assisted Nuclear Bound State of Ξ−N14 System.
In: *Phys. Rev. Lett.* 126.6 (2021), p. 062501.
DOI: 10.1103/PhysRevLett.126.062501.
arXiv: 2010.14317 [nucl-ex].

[153] R. S. Hayano et al.:
Observation of a Bound State of ^{4}He (Σ) Hypernucleus.
In: *Phys. Lett. B* 231 (1989), pp. 355–358.
DOI: 10.1016/0370-2693(89)90675-8.

[154] P. Herrmann:
Vorarbeiten für genaue und präzise Messungen leichter Hyperkernmassen mit der A1-Spektrometeranlage am MAMI. ger.
PhD thesis. Mainz: Johannes Gutenberg-Universität, 2021.
DOI: 10.25358/openscience-6299.

[155] A. Hewish et al.:
Observation of a Rapidly Pulsating Radio Source.
In: *Nature* 217.5130 (1968), pp. 709–713.
ISSN: 1476-4687.
DOI: 10.1038/217709a0.

[156] F. Hildenbrand and H.-W. Hammer:
Lifetime of the hypertriton.
In: *Phys. Rev. C* 102 (6 2020), p. 064002.
DOI: 10.1103/PhysRevC.102.064002.

[157] R. Honda et al.:
Missing-mass spectroscopy with the ^{6}Li$(\pi^-, K^+)X$ reaction to search for ${}^6_{\Lambda}$H.
In: *Phys. Rev. C* 96 (1 2017), p. 014005.
DOI: 10.1103/PhysRevC.96.014005.

[158] V. D. Hopper and S. Biswas:
Evidence Concerning the Existence of the New Unstable Elementary Neutral Particle.
In: *Phys. Rev.* 80 (6 1950), pp. 1099–1100.
DOI: 10.1103/PhysRev.80.1099.

[159] H. Hotchi et al.:
Spectroscopy of medium-heavy Λ hypernuclei via the (π^+, K^+) reaction.

In: *Phys. Rev. C* 64 (4 2001), p. 044302.
DOI: 10.1103/PhysRevC.64.044302.

[160] M. Ilieva et al.:
A feasibility study of hypernuclei reconstruction at NICA/MPD.
In: *Journal of Physics: Conference Series* 668.1 (2016), p. 012104.

[161] *INSPIRE HEP — Discover High-Energy Physics Content*.
inspirehep.net/[Accessed: 04. December 2022].

[162] A. Z. Ismail et al.:
Study of hyperfragments produced in 800 MeV/c K^- interactions. I. Mesonic decays.
In: *Nuovo Cimento (Italy) Divided into Nuovo Cimento A and Nuovo Cimento B* 10 (27 1963).
DOI: 10.1007/BF02813099.

[163] JINA-CEE:
NICER Measures the Radius of the Most Massive Neutron Star.
2021.
URL: https://www.jinaweb.org/news/nicer-measures-radius-most-massive-neutron-star (visited on 04/01/2022).

[164] *jQuery library*.
jquery.com/[Accessed: 02. September 2022].

[165] M. Jurić et al.:
A new determination of the binding-energy values of the light hypernuclei ($A \leq 15$).
In: *Nucl. Phys. B* 52 (1973), pp. 1–30.
DOI: 10.1016/0550-3213(73)90084-9.

[166] K.-H. Kaiser et al.:
The 1.5GeV harmonic double-sided microtron at Mainz University.
In: *Nuclear Instruments and Methods in Physics Research Section A: Accelerators, Spectrometers, Detectors and Associated Equipment* 593.3 (2008), pp. 159–170.
ISSN: 0168-9002.
DOI: https://doi.org/10.1016/j.nima.2008.05.018.

[167] H. Kamada et al.:
π-mesonic decay of the hypertriton.
In: *Phys. Rev. C* 57 (4 1998), pp. 1595–1603.
DOI: 10.1103/PhysRevC.57.1595.

[168] S. Kameoka et al.:
Measurement of the pi- decay width of hyper He-5 (Lambda).
In: *Nucl. Phys. A* 754 (2005). Ed. by A. Gal and E. Hungerford, pp. 173–177.
DOI: 10.1016/j.nuclphysa.2005.03.016.
arXiv: nucl-ex/0402023.

[169] Kamiya, Yuki:
Study on hadron-hadron interaction with femtoscopic technique.
In: *EPJ Web Conf.* 271 (2022), p. 05002.
DOI: 10.1051/epjconf/202227105002.

[170] B. H. Kang et al.:
Exclusive Measurement of the Nonmesonic Weak Decay of the ${}^{5}_{\Lambda}\mathrm{He}$ Hypernucleus.
In: *Phys. Rev. Lett.* 96 (6 2006), p. 062301.
DOI: 10.1103/PhysRevLett.96.062301.

[171] Y. W. Kang et al.:
Lifetimes of Light Hyperfragments.
In: *Phys. Rev.* 139 (2B 1965), B401–B406.
DOI: 10.1103/PhysRev.139.B401.

[172] M. Kapishin:
The fixed target experiment for studies of baryonic matter at the Nuclotron (BM@N).
In: *The European Physical Journal A* 52.8 (2016), p. 213.
ISSN: 1434-601X.
DOI: 10.1140/epja/i2016-16213-0.

[173] T. Katayama, T. Miyatsu, and K. Saito:
Equation of state for massive neutron stars.
In: *The Astrophysical Journal Supplement Series* 203.2 (2012), p. 22.
DOI: 10.1088/0067-0049/203/2/22.

[174] G. Keyes et al.:
A measurement of the lifetime of the ${}^{3}_{\Lambda}\mathrm{H}$ hypernucleus.
In: *Nuclear Physics B* 67.2 (1973), pp. 269 –283.
ISSN: 0550-3213.
DOI: https://doi.org/10.1016/0550-3213(73)90197-1.

[175] G. Keyes et al.:
Measurement of Decay Branching Ratios for the He-4 (Lambda) Hypernucleus.
In: *Nuovo Cim. A* 31 (1976), p. 401.
DOI: 10.1007/BF02734263.

[176] G. Keyes et al.:
New Measurement of the ${}_{\Lambda}\mathrm{H}^{3}$ Lifetime.
In: *Phys. Rev. Lett.* 20 (15 1968), pp. 819–821.
DOI: 10.1103/PhysRevLett.20.819.

[177] G. Keyes et al.:
Properties of ${}^{3}_{\Lambda}\mathrm{H}$.
In: *Phys. Rev. D* 1 (1 1970), pp. 66–77.
DOI: 10.1103/PhysRevD.1.66.

[178] M. Kim et al.:
Three-Body Nonmesonic Weak Decay of the ${}^{12}_{\Lambda}\mathbf{C}$ Hypernucleus.
In: *Phys. Rev. Lett.* 103 (18 2009), p. 182502.
DOI: 10.1103/PhysRevLett.103.182502.

[179] M. Kim et al.:
Coincidence measurement of the nonmesonic weak decay of ${}^{12}_{\Lambda}\mathrm{C}$.
In: *Physics Letters B* 641.1 (2006), pp. 28–33.
ISSN: 0370-2693.
DOI: https://doi.org/10.1016/j.physletb.2006.08.012.

[180] J. Kingelhöfer and C. Helmel:
Optimierung eines Linsensystem für eine Thermalkamera.
Report of the practical lab course.
2022.

[181] R. Kino.
Private communication.

[182] V. Kireyeu:

Study of clusters and hypernuclei production with the NICA/MPD experiment.
In: *Physics of Atomic Nuclei* 78.13 (2015), pp. 1508–1510.
ISSN: 1562-692X.
DOI: 10.1134/S1063778815130189.

[183] P Klag et al.:
High accuracy synchrotron radiation interferometry with relativistic electrons.
In: *Journal of Physics: Conference Series* 2482.1 (2023), p. 012016.
DOI: 10.1088/1742-6596/2482/1/012016.
arXiv: 2212.11139 [physics.ins-det].

[184] P. Klag et al.:
Novel optical interferometry of synchrotron radiation for absolute electron beam energy measurements.
In: *Nucl. Instrum. Methods Phys. Res. A* 910 (2018), pp. 147–156.
DOI: 10.1016/j.nima.2018.09.072.

[185] P. Klag:
Measurement of the electron beam energy at the Mainz microtron via interference of undulator radiation – under preparation.
PhD thesis. Mainz: Johannes Gutenberg-Universität.

[186] T. Kolar et al.:
Measurement of polarization transfer in the quasi-elastic $^{40}\mathrm{Ca}(\vec{e}, e'\vec{p})$ *process*.
2023.
arXiv: 2306.05565 [nucl-ex].

[187] N. N. Kolesnikov and V. A. Kopylov:
Meson decays of hypertritium.
In: *Soviet Physics Journal* 31.3 (1988), pp. 210–213.
ISSN: 1573-9228.
DOI: 10.1007/BF00898225.

[188] R. Konoplya and A. Zhidenko:
Detection of gravitational waves from black holes: Is there a window for alternative theories?
In: *Physics Letters B* 756 (2016), pp. 350 –353.
ISSN: 0370-2693.
DOI: https://doi.org/10.1016/j.physletb.2016.03.044.

[189] K. Koyama:
Cosmological tests of modified gravity.
In: *Reports on Progress in Physics* 79.4 (2016), p. 046902.
DOI: 10.1088/0034-4885/79/4/046902.

[190] M. Leon:
Decay of $_{\Lambda}\mathrm{H}^3$ *and the Spin Dependence of the* Λ*-Nucleon Interaction*.
In: *Phys. Rev.* 113 (6 1959), pp. 1604–1607.
DOI: 10.1103/PhysRev.113.1604.

[191] E. Liu et al.:
Revisiting the former nuclear emulsion data for hypertriton.
In: *Eur. Phys. J. A* 57.12 (2021), p. 327.
DOI: 10.1140/epja/s10050-021-00649-8.

[192] P. Liu et al.:
Recalibration of the binding energy of hypernuclei measured in emulsion experiments and its implications.

In: *Chinese Phys. C* 43 (2019), p. 124001.
DOI: 10.1088/1674-1137/43/12/124001.

[193] W. O. Lock, ed.:
International Conference on Hyperfragments, St. Cergue, Switzerland, 28-30 March, 1963: Proceedings.
CERN Yellow Reports: Conference Proceedings.
1964.
DOI: 10.5170/CERN-1964-001.

[194] D. Logoteta:
Hyperons in Neutron Stars.
In: *Universe* 7.11 (2021), p. 408.
ISSN: 2218-1997.
DOI: 10.3390/universe7110408.

[195] S. Lokanathan, D. K. Robinson, and S. J. S. Lorant:
Hypernucleus Studies. I. Mesonically Decaying Hypernuclei.
In: *Proceedings of the Royal Society of London. Series A, Mathematical and Physical Sciences* 254.1279 (1960), pp. 470–486.
ISSN: 00804630.

[196] R. J. Lombard and C. Volpe:
Size of Two-Body Weakly Bound Objects: Short Versus Long Range Potentials.
In: *Phys. Rev. Lett.* 88 (19 2002), p. 190402.
DOI: 10.1103/PhysRevLett.88.190402.

[197] D. Lonardoni, S. Gandolfi, and F. Pederiva:
Effects of the two-body and three-body hyperon-nucleon interactions in Λ hypernuclei.
In: *Phys. Rev. C* 87 (4 2013), p. 041303.
DOI: 10.1103/PhysRevC.87.041303.

[198] A. S. Lorente, A. S. Botvina, and J. Pochodzalla:
Production of excited double hypernuclei via Fermi breakup of excited strange systems.
In: *Physics Letters B* 697.3 (2011), pp. 222 –228.
ISSN: 0370-2693.
DOI: http://dx.doi.org/10.1016/j.physletb.2011.02.002.

[199] Y. Ma:
Current status of hypertriton lifetime measurement with J-PARC E73 experiment.
https://indico.cern.ch/event/896088/contributions/4787824/attachments/2468893/4234954/HYP2022_yue_ma.pdf.
Talk presented at HYP Conference 2022.
2022.

[200] Y. Ma:
Result of J-PARC E73 initial run on observation of weak decay of hypertriton and ${}^{4}_{\Lambda}\mathrm{H}$ lifetime.
Talk presented at the Joint THEIA-STRONG2020 and JAEA/Mainz REIMEI Web-Seminar 2021/2022.
2022.
URL: https://indico.gsi.de/category/571/ (visited on 05/03/2022).

[201] H. Mansour and K. Higgins:
The decay rate of ${}^{3}H_{\Lambda}$.
In: *Il Nuovo Cimento A (1965-1970)* 51.2 (1979), pp. 180–186.
ISSN: 1826-9869.

DOI: 10.1007/BF02775419.

[202] T. Mart et al.:
Electromagnetic production of the hypertriton. English.
In: *Nuclear Physics A* 640.2 (1998), pp. 235–258.
ISSN: 0375-9474.
DOI: 10.1016/S0375-9474(98)00441-2.

[203] M. May et al.:
Observation of Levels in ${}^{13}_{\Lambda}\mathrm{C}$, ${}^{14}_{\Lambda}\mathrm{N}$, *and* ${}^{18}_{\Lambda}\mathrm{O}$ *Hypernuclei*.
In: *Phys. Rev. Lett.* 47 (16 1981), pp. 1106–1109.
DOI: 10.1103/PhysRevLett.47.1106.

[204] C. Mayeur et al.:
A determination of the B_Λ *values of light hypernucleivalues of light hypernuclei*.
In: *Il Nuovo Cimento A (1971-1996)* 43 (1966), pp. 180–192.

[205] M. Mildeberger:
Entwicklung eines Li-Targets für die Pion-Spektroskopie von Hyperkernen.
Bachelor Thesis. Johannes Gutenberg-Universität Mainz, 2019.

[206] M. Milgrom:
MOND vs. dark matter in light of historical parallels.
In: *Studies in History and Philosophy of Science Part B: Studies in History and Philosophy of Modern Physics* 71 (2020), pp. 170 –195.
ISSN: 1355-2198.
DOI: https://doi.org/10.1016/j.shpsb.2020.02.004.

[207] H. G. Miller et al.:
Nonmesonic Decay of Helium Hyperfragments.
In: *Phys. Rev.* 167 (4 1968), pp. 922–932.
DOI: 10.1103/PhysRev.167.922.

[208] C. Milner et al.:
Observation of Λ*-Hypernuclei in the Reaction* ${}^{12}\mathrm{C}(\pi^+, K^+){}^{12}_{\Lambda}\mathrm{C}$.
In: *Phys. Rev. Lett.* 54 (12 1985), pp. 1237–1240.
DOI: 10.1103/PhysRevLett.54.1237.

[209] K. Miyagawa et al.:
Properties of the bound $\Lambda(\Sigma)NN$ *system and hyperon-nucleon interactions*.
In: *Phys. Rev. C* 51 (6 1995), pp. 2905–2913.
DOI: 10.1103/PhysRevC.51.2905.

[210] T. Miyatsu, T. Kambe, and K. Saito:
Equation of state for hybrid stars with strangeness.
In: *PoS* INPC2016 (2017), p. 135.
DOI: 10.22323/1.281.0135.
arXiv: 1702.05871 [nucl-th].

[211] T. Miyoshi et al.:
High resolution spectroscopy of the B-12(Lambda) hypernucleus produced by the (e, e-prime K+) reaction.
In: *Phys. Rev. Lett.* 90 (2003), p. 232502.
DOI: 10.1103/PhysRevLett.90.232502.
arXiv: nucl-ex/0211006.

[212] A. Montwill et al.:

The non-mesonic to π^- mesonic decay ratio and Λ-neutron stimulation fraction for p-shell hypernuclei.
In: *Nuclear Physics A* 234.2 (1974), pp. 413–428.
ISSN: 0375-9474.
DOI: https://doi.org/10.1016/0375-9474(74)90572-7.

[213] T. Nagae et al.:
Observation of a ${}^{4}_{\Sigma}$He Bound State in the ${}^{4}He(K^-, \pi^-)$ Reaction at $600MeV/c$.
In: *Phys. Rev. Lett.* 80 (8 1998), pp. 1605–1609.
DOI: 10.1103/PhysRevLett.80.1605.

[214] S. Nagao.
Private communication.

[215] S. Nagao:
Decay pion spectroscopy of electro-produced hypernuclei. eng.
PhD thesis. Sendai, Japan: Department of Physics, Graduate School of Science, Tohoku University, 2015.

[216] S. Nagao:
Design of an experiment for hypernuclear lifetime measurement with photon beam.
In: *International Workshop on Strangeness Nuclear Physics 2017*.
Ekimae Campus, Osaka Electro-communication University, 2017.

[217] M. M. Nagels, T. A. Rijken, and Y. Yamamoto:
Extended-soft-core baryon-baryon model ESC16. II. Hyperon-nucleon interactions.
In: *Phys. Rev. C* 99 (4 2019), p. 044003.
DOI: 10.1103/PhysRevC.99.044003.

[218] Nakagawa, Manami et al.:
Unique approach for precise determination of binding energies of hypernuclei with nuclear emulsion and machine learning.
In: *EPJ Web Conf.* 271 (2022), p. 11006.
DOI: 10.1051/epjconf/202227111006.

[219] S. N. Nakamura et al.:
Observation of the ${}^{7}_{\Lambda}He$ hypernucleus by the $(e, e'K^+)$ reaction.
In: *Phys. Rev. Lett.* 110 (2013), p. 012502.

[220] K. Nakazawa et al.:
The first evidence of a deeply bound state of Xi–14N system.
In: *Progress of Theoretical and Experimental Physics* 2015.3 (2015). 033D02.
ISSN: 2050-3911.
DOI: 10.1093/ptep/ptv008.
eprint: https://academic.oup.com/ptep/article-pdf/2015/3/033D02/9720010/ptv008.pdf.

[221] H. Nemura et al.:
Study of Light Λ- and $\Lambda\Lambda$-Hypernuclei with the Stochastic Variational Method and Effective ΛN Potentials.
In: *Progress of Theoretical Physics* 103.5 (2000), pp. 929–958.
ISSN: 0033-068X.
DOI: 10.1143/PTP.103.929.
eprint: https://academic.oup.com/ptp/article-pdf/103/5/929/5113992/103-5-929.pdf.

[222] H. Noumi et al.:
Hypernuclear weak decay of ${}^{12}_{\Lambda}$C and ${}^{11}_{\Lambda}$B.
In: *Phys. Rev. C* 52 (6 1995), pp. 2936–2945.
DOI: 10.1103/PhysRevC.52.2936.

[223] L. Nungesser:
Aufbau und Simulation des KAOS-Spektrometers für Koinzidenzmessungen in der assoziierten Kaosproduktion.
PhD thesis. Johannes Gutenberg-Universität Mainz, (2010).

[224] K. Ogawa, H. Narumi, and Y. Sunami:
Binding Energy of Hypertriton by Solving the Faddeev Equation in Coordinate Space.
In: *Progress of Theoretical Physics* 63.2 (1980), pp. 533–541.
ISSN: 0033-068X.
DOI: 10.1143/PTP.63.533.
eprint: https://academic.oup.com/ptp/article-pdf/63/2/533/5334289/63-2-533.pdf.

[225] S. Okada et al.:
π^0 decay branching ratios of ${}^{5}_{\Lambda}$He and ${}^{12}_{\Lambda}$C hypernuclei.
In: *Nuclear Physics A* 754 (2005). Proceedings of the Eighth International Conference on Hypernuclear and Strange Particle Physics, pp. 178–183.
ISSN: 0375-9474.
DOI: https://doi.org/10.1016/j.nuclphysa.2005.02.128.

[226] J. R. Oppenheimer and G. M. Volkoff:
On Massive Neutron Cores.
In: *Phys. Rev.* 55 (4 1939), pp. 374–381.
DOI: 10.1103/PhysRev.55.374.

[227] H. Outa et al.:
Lifetime measurement of H-4 (Lambda) hypernucleus.
In: *Nucl. Phys. A* 547 (1992). Ed. by T. Fukuda et al., pp. 109C–114C.
DOI: 10.1016/0375-9474(92)90716-W.

[228] H. Outa et al.:
Mesonic and non-mesonic decay widths of ${}^{4}_{\Lambda}$H and ${}^{4}_{\Lambda}$He.
In: *Nuclear Physics A* 639.1 (1998). Proceedings of the International Conference on Hypernuclear and Strange Particle Physics, pp. 251c–260c.
ISSN: 0375-9474.
DOI: https://doi.org/10.1016/S0375-9474(98)00281-4.

[229] H. Outa et al.:
Mesonic weak decay of ${}^{4}_{\Lambda}$H and ${}^{4}_{\Lambda}$He.
In: *Nuclear Physics A* 585.1 (1995). Hypernuclear and Strange Particle Physics, pp. 109–112.
ISSN: 0375-9474.
DOI: https://doi.org/10.1016/0375-9474(94)00552-X.

[230] H. Outa et al.:
Formation and Decay of Σ Hypernuclei in (Stopped K^-, $\pi^{\pm}$) Reactions.
In: *Progress of Theoretical Physics Supplement* 117 (1994), pp. 177–199.
ISSN: 0375-9687.
DOI: 10.1143/ptp.117.177.

eprint: https://academic.oup.com/ptps/article-pdf/doi/10.1143/ptp.117.177/5421307/117-177.pdf.

[231] O. E. Overseth and R. F. Roth:
Time Reversal Invariance in Λ^0 Decay.
In: *Phys. Rev. Lett.* 19 (7 1967), pp. 391–393.
DOI: 10.1103/PhysRevLett.19.391.

[232] *PANDA website*.
panda.gsi.de[Accessed: 23. April 2023].

[233] K. Pardo and D. N. Spergel:
What is the price of abandoning dark matter? Cosmological constraints on alternative gravity theories.
2020.
arXiv: 2007.00555 [astro-ph.CO].

[234] H. Park et al.:
Lifetime measurements of medium-heavy Λ hypernuclei.
In: *Phys. Rev. C* 61 (5 2000), p. 054004.
DOI: 10.1103/PhysRevC.61.054004.

[235] J. D. Parker et al.:
Weak decays of ${}^{4}_{\Lambda}\mathrm{He}$.
In: *Phys. Rev. C* 76 (3 2007), p. 035501.
DOI: 10.1103/PhysRevC.76.035501.

[236] Particle Data Group:
Review of Particle Physics.
In: *Prog. Theor. Exp. Phys.* 2020 (2020), p. 083C01.
DOI: 10.1093/ptep/ptaa104.

[237] *Particle Data Group, Review of Particle Physics Archive*.
pdg.lbl.gov/rpp-archive/index-2022.html[Accessed: 12. December 2022].

[238] Pawlowska, Diana:
Femtoscopic measurements of two-kaon combinations in Au+Au collisions at the RHIC energies.
In: *EPJ Web Conf.* 271 (2022), p. 08009.
DOI: 10.1051/epjconf/202227108009.

[239] A. Pérez-Obiol et al.:
Revisiting the hypertriton lifetime puzzle.
In: *Phys. Lett. B* 811 (2020), p. 135916.
DOI: 10.1016/j.physletb.2020.135916.
arXiv: 2006.16718 [nucl-th].

[240] R. E. Phillips and J. Schneps:
Lifetimes of Light Hyperfragments. II.
In: *Phys. Rev.* 180 (5 1969), pp. 1307–1318.
DOI: 10.1103/PhysRev.180.1307.

[241] P. H. Pile et al.:
Study of hypernuclei by associated production.
In: *Phys. Rev. Lett.* 66 (20 1991), pp. 2585–2588.
DOI: 10.1103/PhysRevLett.66.2585.

[242] J. D. H. Pilkington et al.:
Observations of some further Pulsed Radio Sources.

In: *Nature* 218.5137 (1968), pp. 126–129.
ISSN: 1476-4687.
DOI: 10.1038/218126a0.

[243] J. Pniewski and D. Ziemińska.
In: *Proc. of the Seminar on Kaon-Nuclear Interaction and Hypernuclei, Zvenigorod, September 12–14, 1977* (1979), p. 33.

[244] J. Pniewski et al.:
Final state interactions in the decay of the hypernucleus ${}^{9}_{\Lambda}$Li and a reappraisal of the binding energies of A = 9 hypernuclei.
In: *Nucl. Phys. A* 443 (1985), pp. 685–690.
DOI: 10.1016/0375-9474(85)90218-0.

[245] J. Pochodzalla:
Study of $A = 3$ Hypernuclei.
Tech. rep.
White paper, representing the networking activity THEIA (WP16) within STRONG-2020.
Institute for Nuclear Physics, Mainz Germany, 2022.

[246] J. Pochodzalla.
Private communication.

[247] J. Pochodzalla:
From Neutron Stars to Strange Nuclei: strongly interacting matter on scales from kilometers to femtometers.
https://zhuanlan.zhihu.com/p/615690528.
Talk presented at Fudan.
2023.

[248] B. Povh:
Nuclear physics with hyperons.
In: *Progress in Particle and Nuclear Physics* 5 (1981), pp. 245–268.
ISSN: 0146-6410.
DOI: https://doi.org/10.1016/0146-6410(81)90051-X.

[249] B. Povh et al.:
Teilchen und Kerne. Eine Einführung in die physikalischen Konzepte.
Ninth edition.
Springer-Verlag GmbH, 2014.
ISBN: 978-3-642-37821-8.

[250] Y. Prakash et al.:
On the binding energies of mesic hypernuclei.
In: *Il Nuovo Cimento (1955-1965)* 21 (1961), pp. 235–248.
DOI: 10.1007/BF02832551.

[251] R. J. Prem and P. H. Steinberg:
Lifetimes of Hypernuclei, ${}_{\Lambda}\mathrm{H}^{3}$, ${}_{\Lambda}\mathrm{H}^{4}$, ${}_{\Lambda}\mathrm{H}^{5}$.
In: *Phys. Rev.* 136 (6B 1964), B1803–B1806.
DOI: 10.1103/PhysRev.136.B1803.

[252] D. Psaltis:
Probes and Tests of Strong-Field Gravity with Observations in the Electromagnetic Spectrum.
In: *Living Reviews in Relativity* 11.9 (2008).
DOI: 10.1007/lrr-2008-9.

[253] B. Ram and W. Williams:
Decay rate and branching ratio $(\pi^- {}^3He)/(all\ \pi^-\ modes)$ of ${}^3_\Lambda H$.
In: *Nuclear Physics B* 28.2 (1971), pp. 566 –572.
ISSN: 0550-3213.
DOI: http://dx.doi.org/10.1016/0550-3213(71)90017-4.

[254] C. Rappold et al.:
Hypernuclear production cross section in the reaction of ${}^6Li + {}^{12}C$ at 2 A GeV.
In: *Physics Letters B* 747 (2015), pp. 129 –134.
ISSN: 0370-2693.
DOI: https://doi.org/10.1016/j.physletb.2015.05.059.

[255] C. Rappold et al.:
Hypernuclear spectroscopy of products from ${}^6Li$ projectiles on a carbon target at 2 A GeV.
In: *Nuclear Physics A* 913 (2013), pp. 170 –184.
ISSN: 0375-9474.
DOI: http://dx.doi.org/10.1016/j.nuclphysa.2013.05.019.

[256] C. Rappold et al.:
On the measured lifetime of light hypernuclei ${}^3_\Lambda H$ and ${}^4_\Lambda H$.
In: *Physics Letters B* 728 (2014), pp. 543 –548.
ISSN: 0370-2693.
DOI: http://dx.doi.org/10.1016/j.physletb.2013.12.037.

[257] C. Rappold et al.:
Search for evidence of ${}^3_\Lambda n$ by observing $d + \pi^-$ and $t + \pi^-$ final states in the reaction of ${}^6Li + {}^{12}C$ at $2A$ GeV.
In: *Phys. Rev. C* 88 (4 2013), p. 041001.
DOI: 10.1103/PhysRevC.88.041001.

[258] P. S. Ray et al.:
STROBE-X: X-ray Timing and Spectroscopy on Dynamical Timescales from Microseconds to Years.
2019.
arXiv: 1903.03035 [astro-ph.IM].

[259] M. Rayet and R. H. Dalitz:
The lifetime of ${}^3H_\Lambda$.
In: *Il Nuovo Cimento A (1971-1996)* 46.4 (1966), pp. 786–794.
ISSN: 1826-9869.
DOI: 10.1007/BF02857527.

[260] M. Raymund:
The binding energy difference between the hypernuclides ${}^4He_\Lambda$ and ${}^4H_\Lambda$.
In: *Nuovo Cimento* 32 (1964), pp. 555–587.

[261] S. Ries:
Systematische Sammlung und Verarbeitung von Daten aus Hyperkernexperimenten. ger.
Bachelor Thesis. Mainz: Johannes Gutenberg-Universität, 2022.

[262] K. Riisager, D. V. Fedorov, and A. S. Jensen:
Quantum halos.
In: *Europhysics Letters* 49.5 (2000), p. 547.
DOI: 10.1209/epl/i2000-00180-y.

[263] T. E. Riley et al.:

A NICER View of the Massive Pulsar PSR J0740+6620 Informed by Radio Timing and XMM-Newton Spectroscopy.
In: *The Astrophysical Journal Letters* 918.2 (2021), p. L27.
DOI: 10.3847/2041-8213/ac0a81.

[264] G. Rochester and C. Butler:
Evidence for the existance of new unstable elementary particles.
In: *Nature* 160 (1947), pp. 855–857.
DOI: doi:10.1038/160855a0.

[265] P. K. Saha et al.:
Production of the Neutron-Rich Hypernucleus ${}^{10}_{\Lambda}\mathrm{Li}$ *in the* (π^-, K^+) *Double Charge-Exchange Reaction*.
In: *Phys. Rev. Lett.* 94 (5 2005), p. 052502.
DOI: 10.1103/PhysRevLett.94.052502.

[266] T. R. Saito:
Hypernuclear studies with the WASA-FRS experiment and nuclear emulsions + machine learning.
Talk presented at EMMI Workshop *4th Workshop on Anti-Matter, Hyper-Matter and Exotica Production at the LHC*, 13-17 February 2023.
2023.

[267] T. R. Saito:
Studies of hypernuclei with heavy-ion beams, nuclear emulsions and machine learning.
In: *EPJ Web Conf.* 271 (2022), p. 08003.
DOI: 10.1051/epjconf/202227108003.

[268] T. R. Saito et al.:
New directions in hypernuclear physics.
In: *Nature Reviews Physics* 3.12 (2021), pp. 803–813.
DOI: 10.1038/s42254-021-00371-w.

[269] T. Saito et al.:
Production of hypernuclei in peripheral HI collisions: The HypHI project at GSI.
In: *Nuclear Physics A* 881 (2012), pp. 218 –227.
ISSN: 0375-9474.
DOI: http://dx.doi.org/10.1016/j.nuclphysa.2012.02.011.

[270] A. Sakaguchi et al.:
π^0 *decay process of* ${}^{12}_{\Lambda}\mathrm{C}$ *and* ${}^{11}_{\Lambda}\mathrm{B}$ *hypernuclei*.
In: *Phys. Rev. C* 43 (1 1991), pp. 73–81.
DOI: 10.1103/PhysRevC.43.73.

[271] Y. Sato et al.:
Mesonic and nonmesonic weak decay widths of medium-heavy Λ *hypernuclei*.
In: *Phys. Rev. C* 71 (2 2005), p. 025203.
DOI: 10.1103/PhysRevC.71.025203.

[272] M. Schäfer et al.:
Nature of the $\Lambda nn(J^\pi = 1/2^+, I = 1)$ *and* ${}^{3}_{\Lambda}\mathrm{H}^*(J^\pi = 3/2^+, I = 0)$ *states*.
In: *Phys. Rev. C* 103 (2 2021), p. 025204.
DOI: 10.1103/PhysRevC.103.025204.

[273] M. Schäfer et al.:
The continuum spectrum of hypernuclear trios.

In: *Physics Letters B* 808 (2020), p. 135614.
ISSN: 0370-2693.
DOI: https://doi.org/10.1016/j.physletb.2020.135614.

[274] B. S. Schlimme et al.:
Operation and characterization of a windowless gas jet target in high-intensity electron beams.
In: *Nucl. Instrum. Meth. A* 1013 (2021), p. 165668.
DOI: 10.1016/j.nima.2021.165668.
arXiv: 2104.13503 [physics.ins-det].

[275] F. Schulz et al.:
Ground-state binding energy of ${}^{4}_{\Lambda}H$ from high-resolution decay-pion spectroscopy.
In: *Nuclear Physics A* 954 (2016). Recent Progress in Strangeness and Charm Hadronic and Nuclear Physics, pp. 149 –160.
ISSN: 0375-9474.
DOI: http://dx.doi.org/10.1016/j.nuclphysa.2016.03.015.

[276] F. Schulz:
Präzisionsmessung der Λ-Separationsenergie von ${}^{4}_{\Lambda}H$ am Mainzer Mikrotron. ger.
PhD thesis. Mainz: Johannes Gutenberg-Universität, 2016.
DOI: 10.25358/openscience-4548.

[277] P. Senger:
Nuclear matter physics at NICA.
In: *The European Physical Journal A* 52.8 (2016), p. 217.
ISSN: 1434-601X.
DOI: 10.1140/epja/i2016-16217-8.

[278] P. Senger et al.:
The kaon spectrometer at SIS.
In: *Nuclear Instruments and Methods in Physics Research Section A: Accelerators, Spectrometers, Detectors and Associated Equipment* 327.2 (1993), pp. 393–411.
ISSN: 0168-9002.
DOI: https://doi.org/10.1016/0168-9002(93)90706-N.

[279] A. J. Seriff et al.:
Cloud-Chamber Observations of the New Unstable Cosmic-Ray Particles.
In: *Phys. Rev.* 78 (3 1950), pp. 290–291.
DOI: 10.1103/PhysRev.78.290.

[280] T. Shao.
Private communication.

[281] C. Skordis and T. Złosnik:
A new relativistic theory for Modified Newtonian Dynamics.
2020.
arXiv: 2007.00082 [astro-ph.CO].

[282] A. Sorin et al.:
Heavy-ion program at NICA/MPD at JINR.
In: *Nuclear Physics A* 855.1 (2011), pp. 510 –513.
ISSN: 0375-9474.
DOI: http://dx.doi.org/10.1016/j.nuclphysa.2011.02.118.

[283] M. Steinen:
Feasibility studies for the high precision X-ray spectroscopy of heavy Ξ^- hyperatoms at Panda using the PANda GErmanium Array PANGEA.

PhD thesis. Johannes Gutenberg-Universität Mainz, (2020).

[284] J. Steinheimer et al.:
Hypernuclei, dibaryon and antinuclei production in high energy heavy ion collisions: Thermal production vs. coalescence.
In: *Physics Letters B* 714.1 (2012), pp. 85 –91.
ISSN: 0370-2693.
DOI: http://dx.doi.org/10.1016/j.physletb.2012.06.069.

[285] C. Stoll and A. Meseck:
Optics of a Recirculating Beamline for MESA.
In: *JACoW* IPAC2022 (2022), MOPOTK014.
DOI: 10.18429/JACoW-IPAC2022-MOPOTK014.

[286] D. Suvarieva et al.:
A Feasibility Study of Hyperon and Hypernuclei Reconstruction at NICA with BM@N Detector.
In: *Journal of Physics: Conference Series* 668.1 (2016), p. 012121.

[287] K. N. Suzuki et al.:
The cross-section measurement for the ${}^3H(e,e'K^+)nn\Lambda$ *reaction*.
In: *Progress of Theoretical and Experimental Physics* 2022.1 (2021). 013D01.
ISSN: 2050-3911.
DOI: 10.1093/ptep/ptab158.
eprint: https://academic.oup.com/ptep/article-pdf/2022/1/013D01/42902111/ptab158.pdf.

[288] J. J. Szymanski et al.:
Nonleptonic weak decay of ${}^5_\Lambda\mathrm{He}$ *and* ${}^{12}_\Lambda\mathrm{C}$.
In: *Phys. Rev. C* 43 (2 1991), pp. 849–862.
DOI: 10.1103/PhysRevC.43.849.

[289] H. Takahashi et al.:
Observation of a ${}^6_{\Lambda\Lambda}He$ *Double Hypernucleus*.
In: *Phys. Rev. Lett.* 87 (21 2001), p. 212502.
DOI: 10.1103/PhysRevLett.87.212502.

[290] H. Tamura et al.:
Formation of ${}^4_\Lambda\mathrm{H}$ *hypernuclei from* K^- *absorption at rest on light nuclei*.
In: *Phys. Rev. C* 40 (2 1989), R479–R482.
DOI: 10.1103/PhysRevC.40.R479.

[291] H. Tamura et al.:
Study of Λ*-Hypernuclei with Stopped* K^- *Reaction*.
In: *Progress of Theoretical Physics Supplement* 117 (1994), pp. 1–15.
ISSN: 0375-9687.
DOI: 10.1093/PTPS.117.1.
eprint: https://academic.oup.com/ptps/article-pdf/doi/10.1093/PTPS.117.1/32881723/117-1.pdf.

[292] M. Tanabashi et al.:
The Review of Particle Physics.
In: *Phys. Rev. D* 98 (2018), p. 030001.

[293] L. Tang et al.:
The experiments with the High Resolution Kaon Spectrometer at JLab Hall C and the new spectroscopy of ${}^{12}_\Lambda B$ *hypernuclei*.
In: *Phys. Rev. C* 90 (2014), p. 034320.

[294] B. Taylor:
Numerical Comparisons of Several Algorithms for Treating Inconsistent Data in a Least-Squares Adjustment of the Fundamental Constants.
U.S. National Bureau of Standards NBSIR 81-2426, 1982.

[295] D. Tidman et al.:
Delayed disintegration of a heavy nuclear fragment: II.
In: *The London, Edinburgh, and Dublin Philosophical Magazine and Journal of Science* 44.350 (1953), pp. 350–352.
DOI: 10.1080/14786440308520319.
eprint: http://dx.doi.org/10.1080/14786440308520319.

[296] A. J. Toepfer and L. H. Schick:
$\Lambda - \Sigma$ *Conversion and* Λnp *Isospin-Zero Bound States*.
In: *Phys. Rev.* 175 (4 1968), pp. 1253–1256.
DOI: 10.1103/PhysRev.175.1253.

[297] A. Toia:
Participants and spectators at the heavy-ion fireball.
In: *CERN Courier* 53.4 (2013), pp. 31 –33.
ISSN: 0304-288X.

[298] S. Trogolo:
Addressing the hypertriton lifetime puzzle with ALICE at the LHC.
In: *Nuclear Physics A* 982 (2019). The 27th International Conference on Ultrarelativistic Nucleus-Nucleus Collisions: Quark Matter 2018, pp. 815 –818.
ISSN: 0375-9474.
DOI: https://doi.org/10.1016/j.nuclphysa.2018.11.016.

[299] G. M. Urciuoli et al.:
Spectroscopy of ${}^{9}_{\Lambda}\mathrm{Li}$ *by electroproduction*.
In: *Phys. Rev. C* 91 (3 2015), p. 034308.
DOI: 10.1103/PhysRevC.91.034308.

[300] A. O. Vaisenberg and V. A. Smirnitskii:
Mesonic Decay of a Tritium Hyperfragment.
In: *Soviet Physics JETP* 5.4 (1957), pp. 607–608.

[301] Y. Wang et al.:
Low-Q2 elastic electron-proton scattering using a gas jet target.
In: *Phys. Rev. C* 106.4 (2022), p. 044610.
DOI: 10.1103/PhysRevC.106.044610.
arXiv: 2208.13689 [nucl-ex].

[302] A. L. Watts et al.:
Dense matter with eXTP.
In: *Science China Physics, Mechanics and Astronomy* 62 (2017), p. 029503.
ISSN: 0146-6410.
DOI: https://doi.org/10.1007/s11433-017-9188-4.

[303] N. Wex and M. Kramer:
Generic Gravity tests with the double pulsar.
In:
The Twelfth Marcel Grossmann Meeting.
World Scientific Publishing Company, 2012,
Pp. 1574–1576.

DOI: 10.1142/9789814374552_0275.
eprint: http://www.worldscientific.com/doi/pdf/10.1142/9789814374552_0275.

[304] K. Yagi, L. C. Stein, and N. Yunes:
Challenging the presence of scalar charge and dipolar radiation in binary pulsars.
In: *Phys. Rev. D* 93 (2 2016), p. 024010.
DOI: 10.1103/PhysRevD.93.024010.

[305] T. O. Yamamoto et al.:
Observation of Spin-Dependent Charge Symmetry Breaking in ΛN Interaction: Gamma-Ray Spectroscopy of ${}^{4}_{\Lambda}He$.
In: *Phys. Rev. Lett.* 115.22 (2015), p. 222501.
DOI: 10.1103/PhysRevLett.115.222501.
arXiv: 1508.00376 [nucl-ex].

[306] T. Yamamoto:
Gamma ray spectroscopy of Λ hypernuclei at the HIHR/K1.1 beamlines.
Talk presented at International Workshop on the Extension Project for the J-PARC Hadron Experimental Facility.
2021.
URL: https://indico2.riken.jp/event/3773/contributions/16399/attachments/10275/14509/HDext_WS_20210708_yamamoto.pdf (visited on 05/10/2022).

[307] L. Yordanova and V. Vasendina:
MPD Detector at NICA.
In: *Journal of Physics: Conference Series* 503.1 (2014), p. 012041.

[308] M. Yoshimoto et al.:
First observation of a nuclear s-state of a Ξ hypernucleus, ${}^{15}_{\Xi}\mathrm{C}$.
In: *PTEP* 2021.7 (2021), p. 073D02.
DOI: 10.1093/ptep/ptab073.
arXiv: 2103.08793 [nucl-ex].

[309] N. Yunes and X. Siemens:
Gravitational-Wave Tests of General Relativity with Ground-Based Detectors and Pulsar-Timing Arrays.
In: *Living Reviews in Relativity* 16.1 (2013), p. 9.
ISSN: 1433-8351.
DOI: 10.12942/lrr-2013-9.

[310] V. Zeps:
The weak decays of light hypernuclei.
In: *Nuclear Physics A* 639.1 (1998). Proceedings of the International Conference on Hypernuclear and Strange Particle Physics, pp. 261c–268c.
ISSN: 0375-9474.
DOI: https://doi.org/10.1016/S0375-9474(98)00282-6.

[311] ZGS group:
The Argonne ZGS in retrospect.
In: *CERN Courier* 7 (1980), pp. 293–297.

[312] X. Zhang et al.:
Optimization design and test of the Booster Ring dipole magnet in HIAF.
In: *Journal of Instrumentation* 17.03 (2022), P03024.
DOI: 10.1088/1748-0221/17/03/P03024.

[313] Z. Zhang and C. M. Ko:
Hypertriton production in relativistic heavy ion collisions.
In: *Physics Letters B* 780 (2018), pp. 191–195.
ISSN: 0370-2693.
DOI: https://doi.org/10.1016/j.physletb.2018.03.003.

List of Abbreviations

ADC	Analog to Digital Converter
AGS	Alternating Gradient Synchrotron
BNL	Brooklyn National Lab
CAT7	Category 7 Ethernet Cable
CBM	Compressed Baryonic Matter experiment
CCD	Charge-Coupled Device
CFD	Constant Fraction Discriminator
CMOS	Complementary Metal-Oxide-Semiconductor
CSS	Cascading Style Sheet
DAC	Digital to Analog Converter
DAQ	Data Acquisition
DOI	Digital Object Identifier system
ELPH	Research center for ELectron PHoton science
EOS	Equation Of State
FAIR	Facility for Antiproton and Ion Research
FIFO	Fan In Fan Out
FPGA	Field-Programmable Gate Array
FWHM	Full Width Half Maximum
GPIO	General-Purpose Input/Output
GR	General Relativity
GSI	Gesellschaft für Schwerionenforschung
GUI	Graphical User Interface
HDC	Horizontal Drift Chamber
HDSM	Harmonic Double Sided Microtron
HKS	High resolution Kaon Spectrometer
HRS	High Resolution Spectrometer
HTML	Hyper Text Markup Language
HV	High Voltage
I2C	Inter-Integrated Circuit
JLab	Jefferson Lab
J-PARC	Japan Proton Accelerator Research Complex
KAOS	Kaon Spectrometer
KEK	High Energy Accelerator Research Organization (Japanese abbreviation)
LHC	Large Hadron Collider
LIGO	Laser Interferometer Gravitational-wave Observatory
LISA	Laser Interferometer Space Antenna

LVDS	Low Voltage Differential Signals
MAMI	Mainz Microtron
MESA	Mainz Energy-recovering Superconducting Accelerator
MPD	Multi Purpose Detector
NICA	Nuclotron-based Ion Collider Facility
NICER	Neutron star Interior Composition ExploreR
ndf	Number of Degrees of Freedom
NMR	Nuclear Magnetic Resonance
PANDA	Antiproton Annihilation at Darmstadt
PCS	Pair of Charge Separation dipole magnets
PDF	Probability Density Function
PDG	Particle Data Group
PMT	Photo Multiplier Tube
PVC	Poly-Vinyl-Chloride
RTM	Race Track Microtron
SIS	Schwerionensynchrotron
SKS	Superconducting Kaon Spectrometer
STM	ST Microelectronics, Company
TDC	Time to Digital Converter
ToF	Time of Flight
TOV	Tolman–Oppenheimer–Volkoff equation
URL	Uniform Resource Locator, web address
VDC	Vertical Drift Camber
WASA	Wide Angle Shower Apparatus
XYMO	X-Y MOnitor

List of Tables

List of Figures

D. Note of Thanks

Mein persönlicher Dank gilt allen Personen, die mir bei der Realisierung dieser Doktorarbeit behilflich waren.

Dies umfasst die Mitglieder der A1-Kollaboration, denen ich zunächst für das ermöglichte Experiment am A1-Aufbau danken möchte. Darüber hinaus bin ich auch für die freundliche Hilfe bei der Vorbereitung und der Durchführung der Messung dankbar.

Auch den Mitarbeitern der MAMI-Gruppe möchte ich in diesem Sinne danken.

Ebenso erwähnenswert sind die Werkstätten TBB, TBE, TBM, TBV und das Detektorlabor, die bei der Installation des Experiments, der Wartung und der Reparatur entstandener Schäden unverzichtbar waren und große Dienste geleistet haben.

Im Hinblick auf das Datenbank-Projekt bin ich der EDV-Gruppe dankbar, ohne die die Einrichtung der Website nicht möglich gewesen wäre.

Besonderen Dank möchte ich an Prof. Dr. J. P. für die Betreuung dieser Doktorarbeit richten, ebenso an die langjährigen Kollegen P. K., Dr. P. H. und Prof. Dr. P. A.. Auch den japanischen Kollegen der Tohoku-Universität und dem neuen Doktoranden T. S. möchte ich für die tatkräftige Unterstützung während des Experiments danken.

Zu guter Letzt möchte ich mich auch bei meiner Frau und meiner Familie für den herzlichen Beistand während allen Phasen meines Studiums bedanken.